



The  
University  
Of  
Sheffield.

*III-V Semiconductor Nano-Photonic Devices  
for Integrated Quantum Optical Circuits*

**Zofia Katarzyna Bishop**

Submitted for the degree of  
Doctor of Philosophy

Department of Physics and Astronomy  
University of Sheffield

December 2018



# Abstract

The work presented in this thesis is motivated by the ultimate goal of realizing a fully integrated quantum optical circuit (IQOC), based on a III-V semiconductor, specifically gallium arsenide (GaAs), in a planar architecture with embedded indium arsenide (InAs) quantum dots as single photon sources. Technological challenges involved with achieving a scalable quantum photonic circuit are addressed through the design, development and testing of controllable on-chip nano-photonic elements, such as nanobeam photonic crystal filters and electro-mechanical actuators. The research into both of these types of devices presented here represents the first work of this kind that has been carried out in the LDS group at the University of Sheffield. The majority of the measurements that have been undertaken and which are presented here are of an optical spectroscopic nature.

An on-chip optical filter based on a one-dimensional photonic crystal structure has been modelled and demonstrated experimentally. Such devices can be integrated with other circuit elements in order to achieve a purely electrically driven IQOC. Tuning the resonant wavelength of the device in order to attain control over the filtering parameters has also been investigated.

Control over the splitting ratio of an on-chip optical beam splitter operating at the single photon level has been achieved through an electro-mechanical cantilever based system for the first time on the GaAs platform. This technology, which can be used for switching and phase shifting, now paves the way towards the physical realization of reconfigurable IQOCs.

Other more efficient and versatile electro-mechanical systems that could be used to provide greater control over a variety of optical circuit elements, such as filters and beam splitters, have also been investigated experimentally. Comb-drive actuators, which are well established on silicon based platforms, have been developed for use in the GaAs based quantum optical architecture.



# Acknowledgments

I was very fortunate to study with so many intelligent and unique individuals in the LDSD group. I wish to thank all the current and ex members who made those several years particularly colourful and/or from whom I have learnt a great deal about the mysterious art of lab work. I would also like to thank my supervisor Luke Wilson for his guidance and Maurice Skolnick for giving me the opportunity to go through that journey. I also owe much to Ben Royall, who patiently and tirelessly continued to provide me with increasingly complicated samples. Of course I would also like to acknowledge Chris Vickers and Phil Taylor for keeping it all going by guarding the never-ending process of liquefying, storing, boiling and recovering helium.

I would also like to thank my other friends and family for their support and for not making me explain the subject of my research too many times. Finally, the warmest and biggest gratitude goes to my beloved husband Ray, who kept me sane through all the ups and downs, and provided irreplaceable support throughout the years. This document would not be the same without him.



# Publications and Conferences

## Articles:

**Z.K. Bishop**, A.P. Foster, B. Royall, C. Bentham, E. Clarke, M.S. Skolnick, and L.R. Wilson, "Electro-mechanical control of an on-chip optical beam splitter containing an embedded quantum emitter", *Opt. Lett.* **43**, 2142-2145 (2018).

## Contributed Talks:

**Z.K. Bishop**, A.P. Foster, B. Royall, C. Bentham, E. Clarke, M.S. Skolnick, and L.R. Wilson, "On-chip electro-mechanical routing of single photons from an embedded quantum emitter", *Quantum Dot Day 2018*, Sheffield; January 2018.

**Z.K. Bishop**, A.P. Foster, B. Royall, C. Bentham, E. Clarke, M.S. Skolnick, and L.R. Wilson, "On-chip electro-mechanical routing of single photons from an embedded quantum emitter", *Northern Quantum Meeting 2*, Lancaster; December 2017.

**Z.K. Bishop**, A.P. Foster, B. Royall, C. Bentham, E. Clarke, M.S. Skolnick, and L.R. Wilson, "Electro-mechanical control of an on-chip beam splitter with an embedded single photon source", *International Conference on Integrated Quantum Photonics*, Rome; September 2017.

**Z.K. Bishop**, A.P. Foster, B. Royall, C. Bentham, E. Clarke, M.S. Skolnick, and L.R. Wilson, "On-chip electro-mechanical routing of single photons from an embedded quantum emitter", *Quantum Light Matter Interactions in Solids: towards integrated quantum photonics*, London; September 2017.

## **Poster Presentations:**

**Z.K. Bishop**, A.P. Foster, B. Royall, C. Bentham, E. Clarke, M.S. Skolnick, and L.R. Wilson. "On-chip electro-mechanical routing of single photons from an embedded quantum emitter", *Conference on Lasers and Electro-Optics (CLEO)*, San Jose, California; May 2018.

# Contents

<b>Abstract</b>	<b>iii</b>
<b>Acknowledgments</b>	<b>v</b>
<b>Publications and Conferences</b>	<b>vii</b>
<b>List of Figures</b>	<b>xii</b>
<b>Glossary of Acronyms</b>	<b>xxiii</b>
<b>Glossary of Symbols</b>	<b>xxv</b>
<b>1 Introduction</b>	<b>1</b>
1.1 Outline and Scope of this Thesis . . . . .	3
<b>2 Background</b>	<b>5</b>
2.1 Semiconductor Quantum Dots . . . . .	5
2.1.1 Optical and Electronic Properties of InAs Quantum Dots	6
2.1.2 Quantum Dots as Qubits . . . . .	9
2.1.3 Quantum-Confined Stark Effect . . . . .	9
2.2 Guiding of Light in a Photonic Integrated Circuit . . . . .	11
2.2.1 Nanobeam Waveguides . . . . .	11
2.2.2 Photonic Crystal Waveguides . . . . .	13
2.3 Cavity Quantum Electrodynamics . . . . .	16
2.3.1 Weak Coupling: The Purcell Effect . . . . .	18
2.3.2 Strong Coupling: Rabi Splitting . . . . .	19
2.3.3 Photonic Crystal Cavities . . . . .	20
<b>3 Methods</b>	<b>23</b>
3.1 Wafer Growth . . . . .	23

3.1.1	Quantum Dot Growth . . . . .	24
3.1.2	Wafer Structure . . . . .	26
3.2	Device Design and Fabrication . . . . .	27
3.2.1	Design for Fabrication of On-Chip Devices . . . . .	27
3.2.2	Fabrication of Photonic Structures . . . . .	34
3.2.3	Diode Structure Fabrication . . . . .	40
3.3	Optical Device Characterisation . . . . .	44
3.3.1	Cryogenic Measurements . . . . .	44
3.3.2	Micro-Photoluminescence Spectroscopy . . . . .	48
3.3.3	Time-Correlated Single Photon Counting . . . . .	52
3.4	Computational Methods . . . . .	54
3.4.1	Electromagnetic Simulations . . . . .	54
3.4.2	Electro-Mechanical Modelling . . . . .	61
<b>4</b>	<b>Nanobeam Photonic Crystal Cavities for On-Chip Spectral Filtering and Cavity QED Applications</b>	<b>65</b>
4.1	Principles of Operation . . . . .	67
4.2	On-Chip Spectral Filtering . . . . .	68
4.2.1	Design Requirements . . . . .	68
4.2.2	Modelling and Optimization of the Filter . . . . .	69
4.2.3	Fabrication . . . . .	74
4.2.4	Filtering of QD Emission Using Nanobeam PhCCs . . . . .	75
4.2.5	Conclusions and Further Development . . . . .	78
4.3	Cavity QED Effects . . . . .	79
4.3.1	Design Requirements . . . . .	79
4.3.2	Modelling and Optimization of the Filter . . . . .	80
4.3.3	Fabrication . . . . .	83
4.3.4	Cavity QED Effects in Nanobeam PhCCs with Tunable QD Emission . . . . .	85
4.3.5	High-Q Cavity Design . . . . .	91
4.3.6	Conclusions and Further Development . . . . .	92
4.4	Summary and Outlook . . . . .	94
<b>5</b>	<b>Electro-Mechanical Control of an On-Chip Optical Beam Splitter</b>	<b>95</b>
5.1	Principle of Operation . . . . .	96
5.2	Modelling of the System . . . . .	97
5.2.1	Modelling of a Directional Coupler . . . . .	97
5.2.2	Modelling of a Cantilever . . . . .	100

5.3	Device Design and Fabrication . . . . .	104
5.3.1	Device Design . . . . .	104
5.3.2	Sample Fabrication . . . . .	106
5.4	Electro-Mechanical Testing of the Device . . . . .	107
5.4.1	Room Temperature Testing . . . . .	107
5.4.2	Cryogenic Temperature Testing . . . . .	107
5.5	Tuning of the Optical Properties of a Directional Coupler by Electro-Mechanical Control of a Cantilever . . . . .	110
5.5.1	Experimental Setup . . . . .	110
5.5.2	Results and Discussion . . . . .	111
5.6	Summary and Outlook . . . . .	121
<b>6</b>	<b>Development of Electro-Mechanical In-Plane Actuators for the On- Chip Tuning of Photonic Devices</b>	<b>123</b>
6.1	Control of Optical Properties Using In-Plane Actuation . . . . .	125
6.1.1	Directional Couplers . . . . .	125
6.1.2	Nanobeam Photonic Crystal Cavities . . . . .	127
6.2	Metal Rail Actuators . . . . .	135
6.2.1	Electro-Mechanical Modelling . . . . .	136
6.2.2	Device Design, Fabrication and Testing . . . . .	139
6.3	Comb-Drive Actuators . . . . .	149
6.3.1	Electro-Mechanical Modelling . . . . .	150
6.3.2	Device Design, Fabrication and Testing . . . . .	153
6.4	Summary and Outlook . . . . .	160
<b>7</b>	<b>Summary and Future Directions</b>	<b>161</b>
7.1	Summary . . . . .	161
7.2	Further Work . . . . .	162
	<b>Appendix: List of Wafers</b>	<b>165</b>
	<b>Bibliography</b>	<b>167</b>



# List of Figures

2.1	Diagram of the energy levels of a neutral exciton state within a QD . . . . .	8
2.2	Schematic diagram of the electronic band structure of a quantum dot under (a) flat-band condition (zero electric field, $\mathcal{E} = 0$ ), and (b) non-zero electric field within the structure ( $\mathcal{E} \neq 0$ ) . . . .	10
2.3	Angled scanning electron microscope image of a typical GaAs nanobeam waveguide . . . . .	12
2.4	1D, 2D and 3D photonic crystal lattices with materials of different refractive indices indicated with dark and light shades of blue . . . . .	14
2.5	Scanning electron microscope image of a typical GaAs photonic crystal waveguide . . . . .	14
2.6	Types of photonic crystal cavities: (a) H1 and (b) L3 are (2D) planar periodic structures with 1 and 3 holes omitted to create a defect respectively, while (c) the nanobeam is a 1D array with a changed spacing between the two centre holes . . . . .	21
3.1	Schematic diagram of the Stranski-Krastanov epitaxial method for growing self-assembled InAs QDs (purple) on a GaAs substrate (blue) . . . . .	25
3.2	Schematic diagram of an MBE chamber . . . . .	25
3.3	Typical structure of a GaAs wafer with (a) an intrinsic, and (b) a doped QD membrane structure . . . . .	27
3.4	Digital image of a cantilever device design in GDS format, used for the electro-mechanical control of an optical beam splitter in Chapter 5 . . . . .	29

3.5	SEM image of two suspended nanobeam waveguides joined during the fabrication process . . . . .	29
3.6	Angled SEM image of the cantilever based electro-mechanical system with the cantilever still attached at its centre to the substrate . . . . .	30
3.7	Digital image of an electro-mechanical system in GDSII format designed for the tuning of a nanobeam photonic crystal cavity . . . . .	30
3.8	SEM image of a nanobeam photonic crystal cavity that has broken due to a smaller waveguide width and larger hole sizes than designed . . . . .	31
3.9	Digital image of a comb-drive actuator in GDSII format designed for the electro-mechanical control of a beam splitter . . . . .	32
3.10	SEM image of a comb-drive actuator with its fixing columns attached to the substrate . . . . .	33
3.11	Schematic diagram of the fabrication process of suspended photonic structures . . . . .	35
3.12	Schematic diagram of the critical point drying process . . . . .	38
3.13	SEM images of a suspended GaAs photonic device fabricated (a) with, and (b) without the critical point drying process . . . . .	39
3.14	SEM images of a nanobeam photonic crystal filter fabricated (a) with an e-beam resist, and (b) with a silicon dioxide mask . . . . .	41
3.15	Schematic diagram of the fabrication process for diodes . . . . .	43
3.16	Schematic diagram of a continuous flow cryostat . . . . .	46
3.17	Schematic diagram of a liquid helium bath cryostat . . . . .	47
3.18	Schematic diagram of (a) non-resonant, and (b) quasi-resonant and resonant quantum dot excitation methods . . . . .	48
3.19	Schematic diagram of a spatially selective $\mu$ -PL experimental setup with two optical collection paths . . . . .	50
3.20	(a) Schematic diagram of the experimental arrangement for the Hanbury Brown and Twiss measurement. (b) Typical $g^{(2)}(\tau)$ results for an antibunched (solid line), a coherent (diamonds), and a bunched (dashed line) light source . . . . .	53
3.21	Schematic diagram illustrating an arbitrary dielectric map $\epsilon_r(\mathbf{r})$ and its equivalent when mapped onto the Yee lattice to produce $\epsilon_r(\Delta\mathbf{r})$ . . . . .	56

3.22	Schematic diagram of a single voxel of the Yee lattice used for calculating the electromagnetic fields in the FDTD simulations . . . . .	56
3.23	Simulation of light propagation along a nanobeam waveguide performed using the Lumerical FDTD Solutions package . . . . .	58
3.24	(a) 3D image of a meshed model created in Comsol Multiphysics software to study the electro-mechanical behaviour of a cantilever. (b) Results from the simulation showing the displacement of the cantilever towards the ground terminal (substrate) at 0 V and 7 V . . . . .	63
4.1	Schematic diagram of a nanobeam photonic crystal cavity . . . . .	67
4.2	Spectrum from a typical GaAs wafer containing a high density of self-assembled InAs QDs, obtained using non-resonant photo-luminescence excitation . . . . .	69
4.3	Simulation results showing the percentage of light with a wavelength range of 200 nm transmitted through the nanobeam PhC filters with waveguide thickness $t = 140$ nm, number of holes on each side of the cavity $n = 3$ , and (a) other parameters as chosen by Chen et al., and (b) other parameters rescaled with respect to the initial values . . . . .	71
4.4	Simulation results showing the percentage of light with a wavelength range of 900 – 950 nm transmitted through nanobeam PhC filters with filling fraction, $f$ , held constant, thickness $t = 140$ nm, width $w = 350$ nm, diameter of holes $d = 200$ nm, period $a = 263$ nm, cavity width $c = 413$ nm and different number of holes on either side of the cavity $n = 3, 4, 5$ . . . . .	72
4.5	Simulation results for the designed filter showing how the quality factor of the cavity, $Q$ , and the maximum transmissivity of light through the filter, $T$ , vary with respect to the number of holes on each side of the cavity, $n$ . . . . .	72
4.6	Top-view scanning electron microscope (SEM) images of typical nanobeam PhC filters with filling fraction, $f$ , held constant and (a) $n = 3$ , and (b) $n = 4$ . . . . .	74

4.7	Experimental results showing the routed QD emission in the wavelength range of 840 – 1000 nm collected from the through and normalization OCs for a filter with $n = 3$ . . . . .	76
4.8	Experimental results for filters with $n = 3, 4, 5$ . The data show the percentage of light transmitted to the through OC with respect to that collected from the normalisation OC for the wavelength range of 925 – 975 nm . . . . .	76
4.9	Modelling results demonstrating how small changes to the waveguide width, $w$ , and hole diameter, $d$ , affect the resonance wavelength of the filters . . . . .	78
4.10	Simulation results showing the percentage of light within the wavelength range of 800 – 1000 nm transmitted through a nanobeam PhC filter with $n = 3$ , $d = 200$ nm, $a = 263$ nm, width $c = 413$ nm, and different values of $w$ and $t$ . . . . .	81
4.11	Simulation results showing the percentage of light within the wavelength range of 800 – 1000 nm transmitted through a nanobeam PhC filter with $t = 170$ nm, $w = 280$ nm, $d = 125$ nm, $a = 250$ nm, $c = 335$ nm, and $n = 4$ . . . . .	81
4.12	Schematic diagram of a nanobeam PhC filter with decreasing FF realized through (a) decreasing hole diameter, and (b) increasing waveguide width . . . . .	83
4.13	Simulation results showing the percentage of light within the wavelength range of 900 – 920 nm transmitted through a nanobeam PhC filter with $t = 170$ nm, $w = 280$ nm, $d_0 = 125$ nm, $a = 250$ nm, $c = 335$ nm, and either $n = 4$ with filling fraction, $f$ , held constant or $n = 10$ with $f$ decreasing linearly from the centre of the cavity . . . . .	84
4.14	Simulation results showing the $Q$ -factor and transmissivity, $T$ , for a nanobeam PhC filter with $t = 170$ nm, $w = 280$ nm, $d_0 = 125$ nm, $a = 250$ nm, $c = 335$ nm, and either filling fraction, $f$ , held constant or with $f$ decreasing linearly from the centre of the cavity . . . . .	84
4.15	Top-view scanning electron microscope (SEM) images of typical nanobeam PhCCs with decreasing hole diameter from the centre and $n = 20$ . . . . .	85

4.16	Results obtained by exciting with different powers and collecting from the centre of one of the devices with a cavity mode (at 933.3 nm) close to the emission wavelength of the QDs . . . . .	87
4.17	I-V characteristic of the measured diode structure . . . . .	89
4.18	Photoluminescence emission spectra obtained while exciting and collecting from the centre of one of the filters, as a function of forward bias applied to the diode structure . . . . .	90
4.19	Schematic diagram of a nanobeam PhCC with filling fraction, $f$ , increasing from the centre of the cavity, realized through increasing hole diameter . . . . .	91
4.20	Digital image of a high- $Q$ nanobeam PhCC with filling fraction, $f$ , increasing linearly from the centre of the cavity over $n_c = 15$ , and with a further number of holes with $f$ held constant at the waveguide end, $n_w = 15$ , ready for fabrication . . . . .	92
4.21	Simulation results showing the $Q$ -factor versus the number of holes in the near-cavity tapered region, $n_c$ , for the nanobeam PhCC with filling fraction, $f$ , increasing linearly from the centre of the device in both directions until $d_{\text{end}} = 125$ nm, followed by $n_w = 15$ holes with constant $f$ . . . . .	93
5.1	Schematic diagram of a directional coupler . . . . .	97
5.2	Results of the optical modelling of a directional coupler consisting of 160 nm thick and 280 nm wide waveguides with a $7 \mu\text{m}$ long coupling region and varied out-of-plane waveguide separation . . . . .	98
5.3	Relationship between the square of the actuation voltage and the distance between the cantilever and the substrate derived from Equation (5.2). . . . .	100
5.4	Displacement of the free end of a cantilever with different dimensions $z_0$ , $L$ and $w$ as the actuation voltage is increased, found using FEA . . . . .	102

5.5	Displacement of the free end of a $30\ \mu\text{m}$ long, $10\ \mu\text{m}$ wide, and $160\ \text{nm}$ thick cantilever with $z_0 = 2\ \mu\text{m}$ with and without $9\ \mu\text{m}$ long and $300\ \text{nm}$ wide supportive struts, located on either side of the end of the cantilever, as the actuation voltage is increased, found using FEA . . . . .	102
5.6	The profile and deformation of a cantilever as modeled using the FEA software at $V_{\text{act}} = 0\ \text{V}$ and $V_{\text{act}} = 7\ \text{V}$ for (a) a cantilever without struts, (b) a cantilever with $9\ \mu\text{m}$ long and $300\ \text{nm}$ wide struts . . . . .	103
5.7	Displacement of the free end of the $35\ \mu\text{m}$ long, $7.5\ \mu\text{m}$ wide, and $160\ \text{nm}$ thick cantilever with $z_0 = 2\ \mu\text{m}$ as actuation voltage is increased, calculated using analytical modelling . . . . .	103
5.8	SEM images of the opto-electro-mechanical system used for single photon routing . . . . .	105
5.9	Schematic diagram of the wafer structure . . . . .	106
5.10	SEM image of a device actuated electro-mechanically at room temperature at (a) $0\ \text{V}$ , (b) $16\ \text{V}$ , and (c) $16.5\ \text{V}$ . . . . .	108
5.11	Images of the device actuated electro-mechanically at cryogenic temperature as $V_{\text{act}}$ is increased up to $13\ \text{V}$ and then decreased back to $0\ \text{V}$ , demonstrating the hysteresis behaviour of the cantilever . . . . .	109
5.12	SEM image of the device which collapsed irrevocably at cryogenic temperature . . . . .	109
5.13	QD $\mu\text{-PL}$ emission spectra obtained when exciting the wetting layer at the input OC and collecting the signals from the input, through and drop OCs . . . . .	112
5.14	Filtered $\mu\text{-PL}$ collection maps of the device with an overlaid device contour with (a) $V_{\text{act}} = 0\ \text{V}$ , and (b) $V_{\text{act}} = 12.5\ \text{V}$ . . . . .	113
5.15	Normalized second-order correlation function obtained by exciting the QD from above and collecting the spectrally filtered $\mu\text{-PL}$ signal from the input OC using two collection paths . . . . .	115
5.16	Measured changes to the QD signal collected from the through (fixed) and drop (moving) OCs independently, as the actuation voltage is increased. . . . .	115

5.17	Theoretical changes to the reflection from an OC as its distance from the substrate decreases (with increasing displacement), based on the TMM . . . . .	116
5.18	Measured changes to the emission wavelength of the QD as the actuation voltage is increased and then decreased, demonstrating the hysteresis in the electro-mechanical behaviour of the cantilever . . . . .	116
5.19	Comparison of the cantilever displacement as a function of actuation voltage (up to the pull-in displacement of $z_0/3$ ), found using: analytical modelling (solid line) as shown previously in Figure 5.7, FEA (dotted line), and that derived using Equation (5.5) with $X_{\text{mod}} = 4750$ (dashed line) . . . . .	118
5.20	Estimated experimental cantilever displacement as a function of actuation voltage based on the observed pull-in voltage . . . .	118
5.21	Percentage change of the QD signal collected from the drop OC with respect to the signal recorded from that OC at 0V (red empty circles). The continuous purple line shows the expected reflection changes (already shown in Figure 3.4.1) but as a function of actuation voltage (converted from displacement using the derived relationship in Figure 5.20) . . . . .	120
5.22	Experimental results (empty squares) for the through OC from the graph in Figure 5.16 as a function of displacement converted from actuation voltage using the relationship in Figure 5.20. The other three lines are theoretical curves for $s_{\text{in}}$ of 80, 82, and 84 nm normalized to the initial signal at zero displacement . . .	120
5.23	Schematic diagram of the suggested improved wafer structure .	122
6.1	Schematic diagram of a directional coupler consisting of two single-mode waveguides separated laterally by distance $s_{\text{in}}$ in the coupling region of length $l_c$ . . . . .	125
6.2	Results of the optical modelling of a directional coupler consisting of 160 nm thick and 280 nm wide coplanar waveguides with a $7 \mu\text{m}$ long coupling region as a function of their in-plane separation . . . . .	126

6.3	Schematic diagrams of the proposed systems for the tuning of a nanobeam photonic crystal cavity by varying the in-plane separation between the device and (a) a perturbing nanobeam waveguide, and (b) a perturbing nanobeam PhC . . . . .	129
6.4	Transmissivity of light through a PhC filter (with the following parameters: $t = 140$ nm, $w = 280$ nm, $a = 240$ nm, $d = 100$ nm, $c = 360$ nm and $n = 6$ ) versus wavelength . . . . .	129
6.5	Simulation results showing how the mode wavelength of the nanobeam photonic crystal filter varies with respect to the in-plane separation, $s_{in}$ , from both a perturbing nanobeam photonic crystal and a perturbing nanobeam waveguide . . . . .	131
6.6	Simulation results demonstrating how the full-width at half-maximum of the spectral peak of the nanobeam photonic crystal filter varies with respect to the in-plane separation, $s_{in}$ , from both a perturbing nanobeam photonic crystal and a perturbing nanobeam waveguide . . . . .	131
6.7	Modelling results for the $E_y$ component of the electromagnetic mode of the PhC filter separated laterally from a coplanar nanobeam (a) waveguide by $s_{in} = 40$ nm, (b) PhC by $s_{in} = 40$ nm, (c) waveguide by $s_{in} = 120$ nm, and (d) PhC by $s_{in} = 120$ nm . . .	132
6.8	Simulation results showing the dependency of the $Q$ -factor of the nanobeam photonic crystal cavity on the in-plane separation, $s_{in}$ , from both a perturbing nanobeam photonic crystal and a perturbing nanobeam waveguide . . . . .	134
6.9	Simulation results showing the relationship between the transmissivity of resonant light through the nanobeam photonic crystal filter and its in-plane separation, $s_{in}$ , from both a perturbing nanobeam photonic crystal and a perturbing nanobeam waveguide . . . . .	134
6.10	Schematic diagram of the profile of two fixed-fixed nanobeam structures with an actuation voltage applied between them . . .	136
6.11	(a) Bottom- and (b) side-view schematic diagrams of the modelled electro-mechanical metal rail system . . . . .	137
6.12	Results of the electro-mechanical simulations of the rail system presented in Figure 6.11 . . . . .	138

6.13 (a) Original design in GDSII format, and (b) SEM image of the fabricated metal rail actuator for the tuning of directional couplers . . . . .	141
6.14 SEM images showing examples of problems occurring during fabrication of the original metal rail actuator for the tuning of directional couplers . . . . .	143
6.15 Improved design of a metal rail actuator for the tuning of directional couplers, in GDSII format . . . . .	145
6.16 SEM images of the improved metal rail actuator for the tuning of directional couplers . . . . .	146
6.17 Images of the electro-mechanical in-plane actuator for the tuning of a nanobeam photonic crystal cavity . . . . .	147
6.18 Images of the fabricated metal rail actuators showing problems with lifting metal off the sample from in between rails . . . . .	148
6.19 Schematic diagram of a comb-drive actuator . . . . .	151
6.20 Displacement of the rotor versus actuation voltage for comb-drive actuators . . . . .	152
6.21 Digital image (in GDSII format) of an initial design of a comb-drive actuator for controlling the SR of a DC . . . . .	154
6.22 Schematic diagram of the wafer structure used for comb-drive actuators . . . . .	154
6.23 Angled SEM images showing fabricated comb-drive actuators . . . . .	156
6.24 Digital image (in GDSII format) of an improved design of a comb-drive actuator for controlling the SR of a DC . . . . .	157
6.25 SEM images showing fabricated improved comb-drive actuators . . . . .	158
6.26 SEM images of the electro-mechanical diode structure reported in Chapter 5 demonstrating the changes to image brightness due to applied voltage . . . . .	159



# Glossary of Acronyms

<b>APD</b>	Avalanche photo-diode
<b>BZ</b>	Brillouin zone
<b>CCD</b>	Charge-coupled device
<b>CDA</b>	Comb-drive actuator
<b>CPD</b>	Critical point drying
<b>DC</b>	Directional coupler
<b>EBL</b>	Electron-beam lithography
<b>FDTD</b>	Finite-difference time-domain
<b>FEA</b>	Finite element analysis
<b>FF</b>	Filling fraction
<b>FWHM</b>	Full-width at half-maximum
<b>GDSII</b>	Graphic database system II
<b>HBT</b>	Hanbury Brown and Twiss
<b>HF</b>	Hydrofluoric acid
<b>ICP</b>	Inductively coupled plasma
<b>IQOC</b>	Integrated quantum optical circuit
<b>LDSD</b>	Low dimensional structures and devices
<b>LO</b>	Longitudinal optical

<b>MBE</b>	Molecular beam epitaxy
<b>MOEMS</b>	Micro-opto-electro-mechanical system
<b>MOVPE</b>	Metalorganic vapour phase epitaxy
<b><math>\mu</math>-PL</b>	Micro-photo-luminescence
<b>OC</b>	Output-coupler
<b>PECVD</b>	Plasma-enhanced chemical vapour deposition
<b>PhC</b>	Photonic crystal
<b>PhCC</b>	Photonic crystal cavity
<b>RHEED</b>	Reflection high-energy electron diffraction
<b>RF</b>	Radio-frequency
<b>QCSE</b>	Quantum-confined Stark effect
<b>QD</b>	Quantum dot
<b>QIP</b>	Quantum information processing
<b>SAQD</b>	Self-assembled quantum dot
<b>SEM</b>	Scanning electron microscope
<b>SNSPD</b>	Superconducting nanowire single photon detectors
<b>SPCM</b>	Single photon counting module
<b>SR</b>	Splitting ratio
<b>TCSPC</b>	Time-correlated single photon counting
<b>TE</b>	Transverse electric (mode)
<b>TM</b>	Transverse magnetic (mode)
<b>TMM</b>	Transfer-matrix method
<b>UHV</b>	Ultra-high vacuum
<b>WL</b>	Wetting layer

# Glossary of Symbols

$a$	Photonic crystal period
$A$	Area
$\mathbf{B}$	Magnetic displacement field vector
$c$	Width of a photonic crystal cavity
$C$	Capacitance
$d$	Diameter of air holes
$\mathbf{D}$	Electric displacement field vector
$\mathcal{E}$	Electric field intensity
$E$	Energy
$\mathbf{E}$	Electric field vector
$f$	Filling fraction
$F$	Electrostatic force
$F_p$	Purcell factor
$g$	Air gap between opposing teeth of a CDA
$g_0$	Emitter-photon coupling rate
$g^{(2)}(\tau)$	Second order correlation function
$\mathbf{H}$	Magnetic field vector
$\hbar$	Dirac constant

$J$	Current density vector
$k$	Wave number
$k_B$	Boltzmann constant
$k_s$	Stiffness constant
$l_c$	Coupling length
$l_s$	Strut length
$L$	Cantilever length
$L(\omega)$	Spectral lineshape of the cavity
$n$	Number of holes
$n_{\text{eff}}$	Effective refractive index
$n_i(t)$	Number of counts
$p$	Permanent electric dipole moment
$Q$	Quality factor (Q-factor)
$r$	Computational unit cell size
$s_{\text{in}}$	In-plane separation
$s_{\text{out}}$	Out-of-plane separation
$t$	Thickness
$T$	Transmissivity
$v_g$	Group velocity
$V_{\text{act}}$	Actuation voltage
$V_{\text{eff}}$	Effective modal volume
$V_{\text{pull}}$	Pull-in voltage
$w$	Width

$x$	In-plane displacement
$Y$	Young's modulus
$z$	Distance in the out-of-plane direction
$\alpha$	Polarisability
$\gamma$	Non-resonant emission rate of an emitter
$\Gamma_{\text{cav}}$	Transition rate of an emitter within a cavity
$\Gamma_{\text{FS}}$	Transition rate of an emitter in free space
$\Delta\omega$	Full width at half-maximum
$\epsilon_0$	Permittivity of free space
$\epsilon_{\text{max}}$	Relative permittivity at the location of the maximum $\mathcal{E}$
$\epsilon_r$	Relative permittivity
$\theta_c$	Critical angle of refraction
$\kappa$	Optical loss rate
$\lambda$	Wavelength of light in vacuum
$\mu$	Electric dipole matrix element of the emitter transition
$\mu_0$	Permeability of free space
$\mu_r$	Relative permeability
$\xi$	Normalized dipole orientation
$\rho$	Free electric charge density
$\tau$	Delay time
$\tau_d$	Exciton lifetime
$\omega$	Angular frequency



# Chapter 1

## Introduction

The idea of quantum computers was first proposed by Richard Feynman in 1982 [1] as a way of simulating complex quantum many-body problems and quantum electrodynamical systems, which cannot be solved using current *classical* computers. However, since then it has been realized that quantum computers also offer additional advantages over their classical counterparts, such as the ability to solve specific problems exponentially faster by making use of the quantum effects of superposition and entanglement, on which quantum information processing inherently relies. Examples include the factorisation of large prime numbers [2] and searching unordered lists [3]. The former is currently used in encryption protocols for securing digital information, for example, on the web. This has caused interest in the physical implementation of a universal quantum computer to grow, and in 2000 David DiVincenzo formalised the necessary requirements for its realization [4]. A large variety of architectures, based on several different physical principles, each with their own advantages and disadvantages, has been proposed since. Examples include systems based on superconducting junctions and trapped ions [5]. However, using the polarization of single photons to encode information (in so called quantum bits, or qubits) has been shown to be particularly promising for scalable systems, due to photons being both relatively easy to manipulate and comparatively free from decoherence issues [6]. The idea of an optical quantum information processing circuit was further reinforced when in 2001 it was demonstrated that efficient quantum computation could be achieved using linear optics with only single photons, phase shifters, beam splitters

and single-photon detectors [7].

In this context it is important to realize that it was not until the invention of integrated circuits that a real breakthrough occurred in the utilization of what we now call classical computers, which allowed personal computers to become both technologically feasible and widely available, and which thereafter completely revolutionised the modern world by ushering in what has become known as the Information Age. This significant discovery has indeed been acknowledged through the Nobel Prize in Physics being awarded in 2000 "for basic work on information and communication technology" with one half jointly to Zhores I. Alferov and Herbert Kroemer "for developing semiconductor heterostructures used in high-speed- and opto-electronics" and the other half to Jack S. Kilby "for his part in the invention of the integrated circuit"[8]. It is interesting to note too that while the integrated circuits of Kilby were germanium-based, others based on silicon were invented contemporaneously by R. N. Noyce, who would have had an equal claim to Kilby to a share in the 2000 Nobel Prize, had he not died ten years earlier. Thus, while it was the breakthrough in the silicon-based microchips driven by Noyce, who became one of the founders of Intel Corporation in 1968, that fuelled the personal computer revolution, the work on semiconductor heterostructures revolutionized opto-electronics, paving the way towards realization of a variety of semiconductor devices, such as light-emitting diodes, lasers and compact discs. Consequently, both of the two inventions were essential ingredients for the information revolution.

Accordingly, it seems reasonable to assume that in order to have a similar impact on the world, quantum computers might similarly need to be integrated on a semiconductor chip. Hence, III-V semiconductor systems have quickly become the promising frontrunners for the development of quantum optical circuits, due both to their proven optical and electronic properties as well as to the already existing well-developed semiconductor fabrication technologies. Therefore, integrating linear optical elements together with single photon emitters (semiconductor heterostructures) and their detectors on-chip has become the ultimate goal in the physical realization of an efficient quantum optical information processing circuit. It is the purpose of this thesis to further the state-of-the-art integration methods, as well as to develop on-chip electro-mechanical systems that would allow for III-V semiconductor optical circuits to be reconfigured and controlled in-situ.

## 1.1 Outline and Scope of this Thesis

The focus of this thesis is thus to contribute to the further technological progress in realising a controllable and fully integrated gallium arsenide (GaAs) based quantum optical circuit, using embedded indium arsenide (InAs) quantum dots (QDs) as single photon emitters, and nano-photonic devices, such as beam splitters and filters, as information processing elements. The QDs are used as static qubits, which store the information (equivalent to bits in a classical computer realized through capacitors), and photons are used as flying qubits, which send the information around the chip and on which the processing is realized through optical elements (equivalent to current flow in a classical computer, where the processing is realized through transistors).

Background information on the proposed solid-state quantum optical information processing system is provided in Chapter 2. This includes descriptions of quantum dots, methods of waveguiding the single photons emitted by them within a planar architecture, and the essential elements of cavity quantum electrodynamics, which finds applications in many on-chip optical elements, such as filters and routers. The experimental and computational methods used throughout this thesis in order to design, make and test the proposed integrated photonic devices are then explained in detail in Chapter 3.

Chapters 4-6 present the results of the original research that has been undertaken for this thesis. Chapter 4 demonstrates on-chip optical filtering using one-dimensional photonic crystal cavity structures for the first time in the LDS group at the University of Sheffield. Embedded QDs are used as photon sources to measure the relative transmissivity of light through the filter. Further improvements to the cavity design are also proposed. In addition, electrical control of the device's operation, by tuning the emission wavelength of the QDs into resonance with the cavity mode, is also investigated for the first time. This could lead in future to novel integration of fully electrically controlled optical circuits.

Chapter 5 demonstrates the electro-mechanical control of an on-chip optical beam splitter containing embedded single-photon sources for the first time. The system is realised through two nanobeam waveguides whose out-of-plane separation determines the splitting ratio of the device. Applying an actuation voltage to a cantilever to which one of the waveguides is attached

permits control of the operation of the beam splitter. Emission from the embedded QD used to measure the optical properties of the device is confirmed to be of single-photon nature through a second-order correlation measurement.

Chapter 6 presents the development of two other electro-mechanical systems that use in-plane actuation to control a variety of on-chip photonic elements, such as beam splitters and photonic crystal cavities. This method is shown to be able to provide greater and more efficient control over the optical properties of these devices. Metal-rail systems and comb-drive actuator structures, which have both been demonstrated on silicon, but not on GaAs so far, are designed, developed and tested, with the latter found to be more versatile, more efficient and somewhat easier to realize in practice.

Finally, a summary of the work achieved in this thesis is presented in Chapter 7, where directions for further research, based on the results reported here, are also discussed.

# Chapter 2

## Background

This chapter discusses the essential theoretical background that underpins the research undertaken for this thesis. It begins with a detailed explanation of what semiconductor quantum dots (QDs) are and what are the electronic and optical properties of the InAs QDs studied throughout this thesis. Their suitability for qubits in solid-state quantum information processing (QIP) systems is also addressed. The chapter then goes on to explain how single photons (flying qubits) emitted by the QDs (static qubits) are guided in an integrated quantum optical circuit to enable information transfer and processing. Finally, the field of cavity quantum electrodynamics (cQED) is introduced, which finds applications in many aspects of QIP, such as efficient single photon generation, optical filtering, switching, routing and the creation of logic gates.

### 2.1 Semiconductor Quantum Dots

Quantum dots (QDs) are nanometer-sized semiconductor structures within which the carriers of charge are confined in all three spatial directions. Due to this three-dimensional confinement the electronic levels in QDs are discrete. QDs are often referred to as artificial atoms due to the fact that their emission is quantized like that of an atom. They can be grown in a variety of ways, but the InAs QDs incorporated in a GaAs matrix reported throughout this thesis have all been grown through self-assembly. Details of the growth procedure are discussed in Section 3.1.1. Any variation in the sizes of the QDs that occurs naturally during the growth will affect their emission wavelength [9].

The QDs studied here operate in the near infrared spectrum of  $\sim 890\text{--}970\text{ nm}$ . Using GaAs as a host material for InAs QDs is advantageous for two reasons. Firstly, standard nano-fabrication techniques can be used with GaAs, and secondly GaAs is transparent for this wavelength range, thereby allowing the emitted photons to propagate through the GaAs without reabsorption. In addition, InAs is a direct semiconductor, which ensures efficient radiative recombination of charge carriers within the QD [10]. Self-assembled QDs (SAQDs) have been successfully studied in other material systems, such as CdSe QDs in ZnS [11, 12], CdTe QDs in ZnTe [13] and SiGe QDs in Si [14]. However, InAs QDs approximate two-level emitters particularly effectively, thereby making them highly efficient for the single-photon generation required for QIP applications [15–18].

### 2.1.1 Optical and Electronic Properties of InAs Quantum Dots

The band gaps of GaAs and InAs at room temperature are 1.42 eV and 0.35 eV respectively. This large step difference in the band gaps between the two materials, in combination with InAs being formed into nanometer-sized islands surrounded by GaAs, gives rise to the three-dimensional potential confinement of charge carriers, and hence to discrete energy levels within the QD. However, due to strain within the structure and diffusion of Ga into the InAs QD during the growth process, the actual band gap within the QD is much closer to that of GaAs, typically around 1.35 eV [19–21]. Due to this small difference between the two band gaps, which is close to the thermal energy of electrons at room temperature ( $k_B T$ ), the carriers of charge can be scattered out of the QD through phonon interactions. In addition, the thermal energy of the system affects the coherence of the quantum states, which is extremely important for QIP applications. The higher is the temperature of the system the faster the decoherence time of the quantum states is expected to be. In order to minimise these effects the QDs studied in this thesis are cooled to below 5 K using liquid helium cryostats, which are described in Section 3.3.1. This also ensures that when a single electron (or hole) is added to the QD it populates only the first level in the conduction (or valence) band. This discrete behaviour creates the two-level system required for QIP [22].

Electrons and holes trapped within a QD are attracted to each other through

the electrostatic Coulomb force, and hence they form bound states called excitons. A typical QD contains only one or two energy levels for electrons and holes, which means there is a finite number of different excitonic states that can exist within a QD. The most elementary of these is a neutral exciton state. A neutral exciton is formed when a single electron and a single hole are trapped within a QD. Both carriers of charge have spin  $s = 1/2$ , but their orbital angular momentum,  $l$ , differs. The conduction band has the form of an s-type wavefunction ( $l = 0$ ) and is therefore degenerate with respect to spin (*i.e.*,  $m_s = \pm 1/2$ ). By contrast, the valence band has a p-type orbital ( $l = 1$ ), and hence has three distinct sub-states (*i.e.*,  $m_l = -1, 0, 1$ ). These combine with the spin sub-states to give  $3 * 2 = 6$  sub-states. An alternative way of describing these is in terms of the total angular momentum given by  $\mathbf{j} = \mathbf{l} + \mathbf{s}$ . In the case when  $l = 1$  and  $s = 1/2$  the two possible values of  $j$  are  $1/2$  and  $3/2$ . The  $j = 1/2$  state has two sub-states (*i.e.*,  $m_j = -1/2, +1/2$ ), while the  $j = 3/2$  state has 4 sub-states (*i.e.*,  $m_j = -3/2, -1/2, +1/2, +3/2$ ) again giving a total number of sub-states of  $2 + 4 = 6$ . The resulting hole states are known as the heavy hole band ( $j = 3/2, m_j = \pm 3/2$ ), the light hole band ( $j = 3/2, m_j = \pm 1/2$ ) and the split-off band ( $j = 1/2, m_j = \pm 1/2$ ).

The split-off band typically has a large energy offset from the heavy and light hole bands of  $\approx 350$  meV, and can therefore be neglected when considering the lowest energy states of a neutral exciton [23]. The remaining degeneracy between the heavy and light hole bands is typically lifted due to strain within the QD caused by the lattice mismatch between the two semiconductors giving  $\approx 30$  meV energy difference between the two bands [24]. This means that the light hole band can also be omitted from further considerations. Therefore, the total angular momentum projections for neutral exciton states of the lowest energy (which comprise an electron and a heavy-hole) are  $m_j^x = m_s^e + m_j^h = \pm 1, \pm 2$ . Since a photon carries a spin projection of  $\pm 1$ , only those exciton states with  $m_j^x = \pm 1$  are optically allowed, and these are called bright excitons. The states with  $m_j^x = \pm 2$  require an angular momentum transfer of twice that of a photon. Therefore, these states are optically forbidden and are called dark excitons.

The degeneracy between both bright and both dark states can also be lifted by the asymmetry of the QD. The energy level difference between the two bright (or dark) states is known as fine structure splitting (FSS) [25, 26]. The

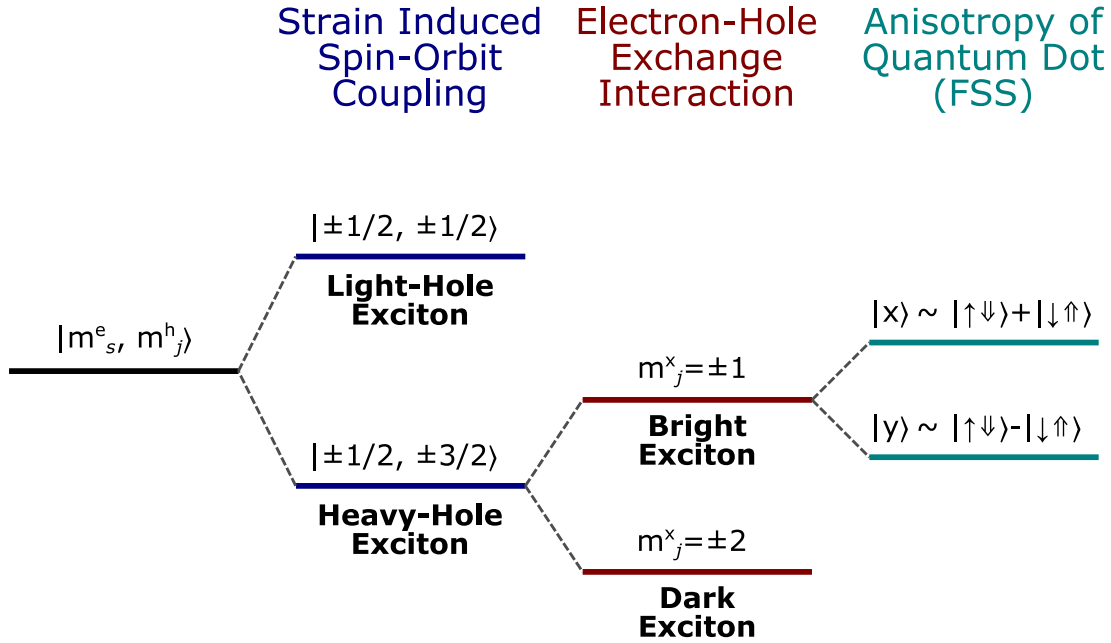


**Figure 2.1:** Schematic diagram of the energy levels of a neutral exciton state within a QD.

two bright states decay radiatively by emitting photons which are orthogonally polarised to one another. This property can be utilized for directional emission of a single photon on a chip. If a QD is located in a structure exhibiting polarised optical modes, such as a 2D photonic crystal cavity (discussed in Section 2.6) or a nanobeam waveguide (see Section 2.2.1), only the excited bright state of the matching polarisation will couple to the structure modes, and hence emit light in the preferential direction on a chip [27, 28]. A schematic diagram of the energy levels of a neutral exciton state within a QD is presented in Figure 2.1.

As mentioned before, other excitonic states (apart from a neutral exciton) can exist within a QD. If a QD is populated with more holes than electrons (or the other way round), the bound state becomes charged and is known as a positive (or negative) exciton. These states are optically active with different energy levels from each other and the neutral exciton state due to the modified strength of the Coulomb interactions between the carriers. Similarly, a QD could be populated by two electrons and two holes forming a biexciton. The two electron-hole pairs can recombine to emit two photons successively [29]. This so-called biexciton cascade can be used for the generation of polarization-

entangled photons on a chip, which is another essential component of QIP systems [30–32]. However, coupling two photons of different polarization to the same direction in a waveguide remains a technological challenge.

### 2.1.2 Quantum Dots as Qubits

The reasons behind QDs being good contenders for optical qubits are twofold. Firstly, as discussed above, the two-level system of an exciton in a QD allows for the creation of qubits. Secondly, the ability of the QDs (static qubits) to couple efficiently to single photons (flying qubits) facilitates transfer and storage of quantum information on a chip [33, 34]. However, as this is a solid-state system, the difficulty in achieving it experimentally arises from the inevitable interactions with the environment that result in the dephasing of the quantum states. Examples of processes causing the decoherence of the system in time are crystal lattice vibrations (phonons), nuclear spin interactions and charge fluctuations [35]. These effects can be mitigated by reducing the emitter lifetime so that it is lower than the dephasing time. By so doing, the quantum state can be recovered from the QDs through photons before it collapses. This can be achieved by embedding a quantum emitter inside an optical microcavity, which increases its emission rate through the so-called Purcell effect, which is discussed further in Section 2.3.

### 2.1.3 Quantum-Confined Stark Effect

The emission wavelength of a QD depends on both the energy level difference between the electron and hole states and the exciton binding energy. Due to this binding energy, the exciton has a lower energy than an unbound electron and hole pair. The band structure of the device can be modified by the application of an electric field. Schematic diagrams of both an unbiased and biased QD populated by one neutral exciton are presented in Figure 2.2. As voltage is applied across the device the band structure is modified, decreasing the energy separation between the electron and hole states, thereby reducing the energy of the photon emitted upon recombination. The resulting QD emission is thus at a longer wavelength than under the flat-band conditions. This modification of the emission energy,  $\Delta E$ , due to an electric field,  $\mathcal{E}$ , is known as the

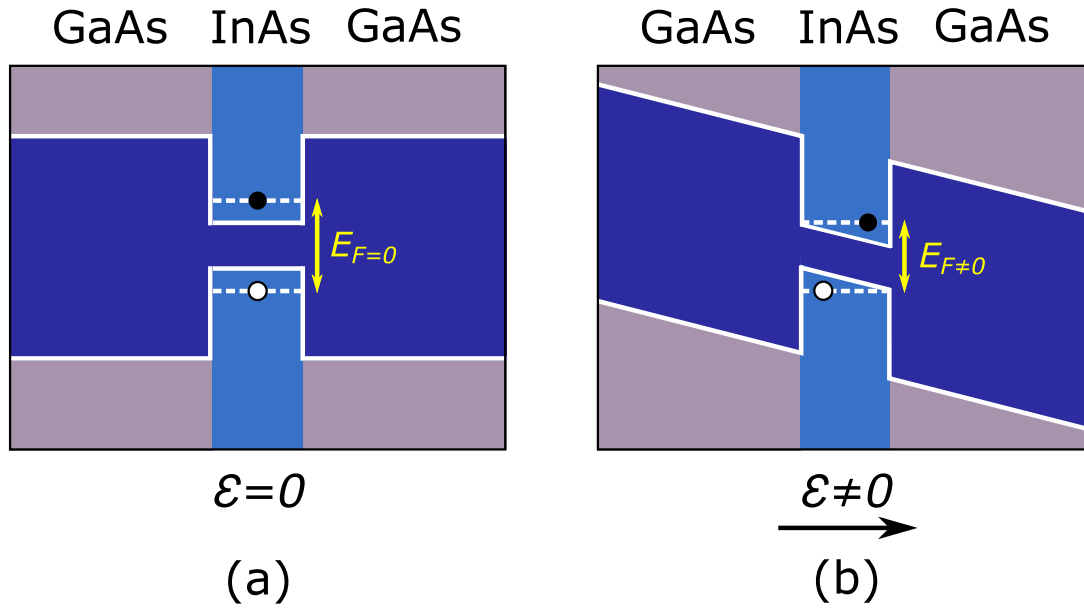


**Figure 2.2:** Schematic diagram of the electronic band structure of a quantum dot under (a) flat-band condition (zero electric field,  $\mathcal{E} = 0$ ), and (b) non-zero electric field within the structure ( $\mathcal{E} \neq 0$ ). The application of an electric field reduces the energy difference between the electron and hole energy states.

quantum-confined Stark effect (QCSE), and is given by [36, 37]:

$$\Delta E = -p\mathcal{E} - \alpha\mathcal{E}^2, \quad (2.1)$$

where  $p$  and  $\alpha$  are the permanent electric dipole moment and the polarisability of the material respectively, in the direction of the electric field,  $\mathcal{E}$ .

The range of QD emission tuning that can be achieved through the QCSE depends on the rate at which the charge carriers tunnel out from the QD. If the rate of tunnelling is faster than the radiative recombination rate the emission efficiency is quenched. One of the factors affecting the tunnelling rate is the energetic barrier height between the electron and hole energy states of the QD and the surrounding material [38]. The application of a large electric field changes the shape of the band structure to triangular, which hence reduces the energy offset between the electron (or hole) and the GaAs, thereby leading to quenched emission. The amount of tuning can, hence, be maximized by careful design of the wafer structure. Bennett *et al.* [39] have shown a giant QCSE tuning of InAs QD emission of 25 meV by introducing AlGaAs barriers on either side of the thin GaAs layers surrounding the InAs

QD layer. The QCSE provides a promising alternative to other QD emission tuning methods, such as temperature control. By contrast with temperature tuning, QCSE control does not affect other properties of the QD emission, such as spectral coherence [40], nor of the semiconductor devices, such as optical cavity modes [41, 42]. It also has the potential to be scalable and to provide local control over different QDs on a chip. This is an important capability for enabling QIP on integrated circuits. An example is the two-photon interference effect emitted from two remote QDs, observed experimentally by Patel *et al.* [43] due to local QCSE tuning.

## 2.2 Guiding of Light in a Photonic Integrated Circuit

Guiding light in a photonic integrated circuit is essential for achieving optical QIP on a chip. Two commonly used methods that accomplish this are through the so-called nanobeam and photonic crystal (PhC) waveguides. Even though it is only the former approach that has been used for all of the research reported in this thesis, both of the mechanisms are now briefly described. The short introduction to PhCs here will also be useful later in this thesis, particularly when PhC cavities are introduced in Section 2.3.3 and then modelled and studied experimentally in Chapters 4 and 6.

### 2.2.1 Nanobeam Waveguides

Perhaps the easiest method of guiding light in a dielectric medium such as a GaAs chip is through total internal reflection (TIR). GaAs is a transparent material for QD emission wavelengths, with a refractive index of  $n \approx 3.4$  at cryogenic temperatures. For a nanobeam waveguide a large refractive index difference that minimises the critical angle of refraction,  $\theta_c$ , is provided through air cladding. This is achieved by simply etching away the GaAs material around a rectangular structure, as shown in Figure 2.3. Light is then confined through TIR in two directions: out-of-plane and one in-plane, with  $\theta_c \approx 17^\circ$  according to Snell's Law. This means that QD emission can propagate in one direction along the waveguide only.

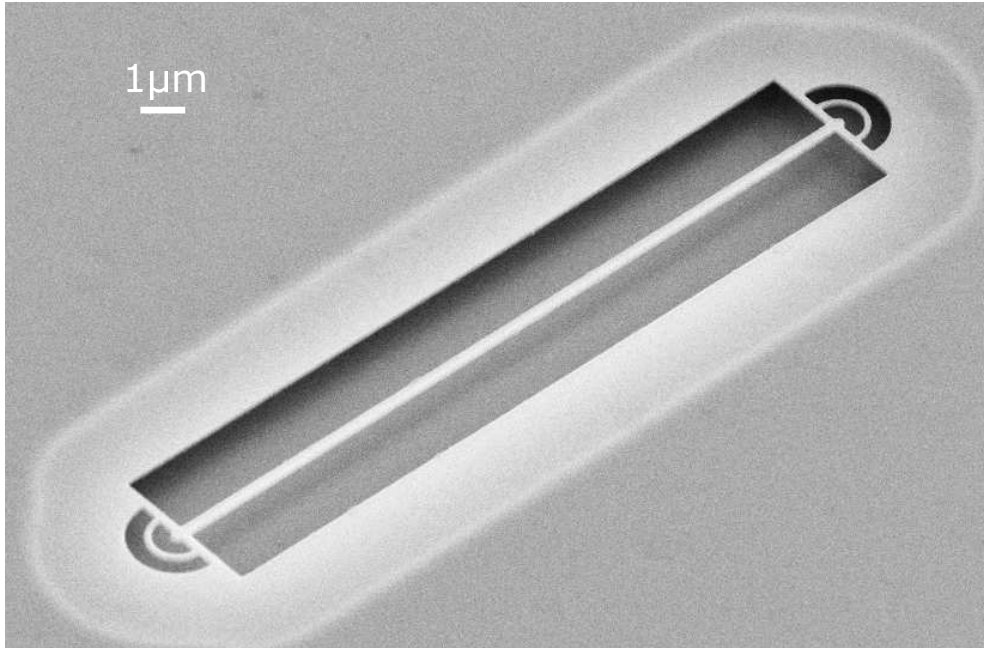


**Figure 2.3:** Angled scanning electron microscope image of a typical GaAs nanobeam waveguide.

Another important aspect of light propagation for optical QIP applications is single mode operation. The group velocity of a light wave,  $v_g$ , depends on the wave number,  $k$ , in which certain frequencies of light,  $\omega$ , can propagate, according to:

$$v_g = \frac{d\omega}{dk}. \quad (2.2)$$

Hence, if the energy of an optical pulse at a single frequency (such as the QD emission) spreads over several optical modes, parts of the pulse will travel at different speeds. This will result in broadening of the initial short pulse in time. This so-called intermodal dispersion is particularly problematic for light propagation over long distances.

In addition, the overall efficiency of on-chip single-photon sources depends on the number of possible modes to which each photon can be coupled. If this number is large the probability of a photon being emitted to the desired waveguide mode (known as the  $\beta$ -factor) is low, making the source inefficient [44]. Therefore, on-chip waveguides are designed to operate in a single-mode regime (similarly to industry standard single-mode fibres). To confine the light to a single vertical (out-of-plane) mode a waveguide thickness

of 140 nm is used. This corresponds to the  $\lambda/2n$  constraint for a QD emission wavelength of 950 nm. This dimension is fixed during the epitaxial growth of the GaAs membrane on top of the sacrificial AlGaAs layer, the etching of which allows the suspension of the nanobeam waveguide (see Section 3.1). With the waveguide thickness now set, its width will affect the number of transverse electric (TE) and transverse magnetic (TM) modes that are allowed to propagate. As QD emission is known to couple well to the TE modes [45], the waveguide width has been chosen so that it results in the strong confinement of a single TE mode. In order to find the appropriate dimension finite-difference time-domain (FDTD) or frequency domain electromagnetic modelling had to be undertaken (see Section 3.4.1). In our case an FDTD solver was used by Dr Rikki J. Coles to determine that a waveguide with a width equal to twice its thickness will confine 95 % of the light in a single TE mode. For this reason, the width of the waveguide that is intended to be achieved during sample fabrication is  $\sim 280$  nm.

### 2.2.2 Photonic Crystal Waveguides

Photonic crystal (PhC) confinement is perhaps most easily described through an analogy to semiconductor physics. The periodic alignment of atoms and molecules in a crystal lattice of a material gives rise to a periodic potential experienced by the electrons travelling through the material. This may result in an energy gap in the band structure of the crystal in which electrons are prohibited to propagate through the lattice. Photonic crystals are the optical analogue of this phenomenon. Instead of the atomic lattice, a macroscopic lattice of materials with different dielectric constants is used, replacing a periodic potential with a periodic refractive index. If the refractive index contrast is large enough and if the absorption of light in the materials is small, then the various reflections and refractions of light from the periodic interfaces can give rise to an energy band gap for photons (known as a photonic band gap) [46–48], just like the atomic lattice does for electrons. Therefore, we can engineer PhCs in order to prevent light of particular frequencies from propagating in certain directions.

Hence, there exist 1D, 2D and 3D PhCs depending on the number of forbidden directions within the crystal. Figure 2.4 illustrates the three different

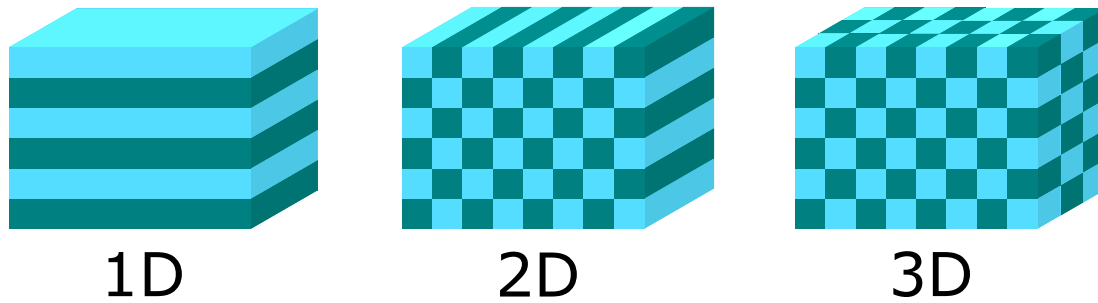


**Figure 2.4:** 1D, 2D and 3D photonic crystal lattices with materials of different refractive indices indicated with dark and light shades of blue.

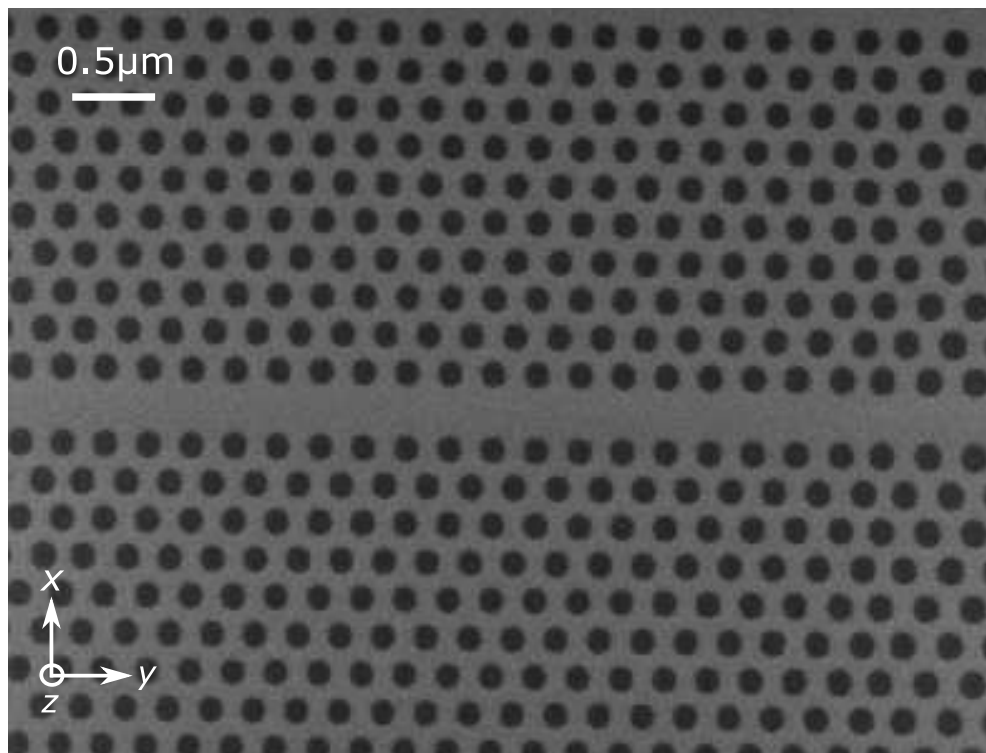


**Figure 2.5:** Scanning electron microscope image of a typical GaAs photonic crystal waveguide.

lattice types that give different spatial confinements. An example of a 1D PhC is a distributed Bragg reflector, where thin layers of materials with varying refractive index act as a mirror for light propagating perpendicular to the layers. A 2D PhC can be engineered by simply making periodic holes in a dielectric material. Truly 3D PhCs with complete photonic band gaps in all three spatial dimensions are very challenging to achieve experimentally. In 1998 Lin *et al.* [49] demonstrated such a structure using polysilicon 1D rods carefully positioned in a face-centred tetragonal lattice using a four-layered stacking sequence. It required a complicated and cumbersome fabrication process especially developed for this purpose where each layer had to be deposited, patterned and etched consecutively. They have achieved a large 3D photonic band gap for wavelengths of 10 – 14.5  $\mu\text{m}$ .

2D PhCs can be realised on a chip through a triangular lattice of holes created in a GaAs membrane. This results in a photonic band gap for certain wavelengths of light in two in-plane directions. Eventually it is desirable for the QD emission to propagate in one in-plane direction as in the case of the nanobeam waveguides discussed above. Therefore, the out-of-plane confinement is again realized by suspending the 2D PhC structure created in a GaAs membrane by removing the sacrificial AlGaAs layer from beneath it. This results in an overall 3D confinement of light at the QD emission frequencies: two in-plane directions through PhC confinement and one out-of-plane direction through TIR. In order then to create a waveguide, one row of holes is omitted in the 2D PhC lattice, as shown in Figure 2.5. Light is still prohibited from propagating in the  $x$  direction, and can only travel in the  $+y$  or  $-y$  direction through the line defect at its centre. The resulting so-called W1 PhC waveguides are of great interest to researchers in the field of optical QIP as they integrate well with other important circuit components, such as PhC cavities [50] (discussed in Section 2.3.3).

Furthermore, PhC waveguides can be used to study the so-called slow light phenomenon. As the optical modes propagating through the waveguide approach the Brillouin zone (BZ) boundary, backscattered light interferes with the original rays, thereby reducing the group velocity of the travelling wave. Further away from the BZ boundary the backscattered light is more out-of-phase with the propagating wave, and hence the two interfere less with each other, resulting in the mode being dominated by TIR within the waveguide [51].

The larger is the refractive index contrast, the more intense are the backscattered waves, and hence the bigger is the slow-down factor of the propagating wave [52]. For this reason PhCs are promising media for studying the slow light phenomenon.

The slow light regime can occur due to any resonances within the structure, and therefore does not have to occur only near the edge of the BZ. Careful adjustment to the design of the W1 PhC waveguide can move the slow light region away from the BZ boundary, as demonstrated by Petrov *et al.* [53]. The bandwidth for slow light operation can also be increased, for example, by increasing the diameter of the holes in the row closest to the line defect [54]. Similarly, the slow-down factor can be greatly enhanced by decreasing the width of the waveguide by bringing two parts of the 2D PhC lattice closer together [55]. Engineering of the slow light phenomenon within the PhC structures provides opportunities for the realization of tunable and compact integrated delay lines [56, 57], as well as optical storage and switching applications [58, 59].

## 2.3 Cavity Quantum Electrodynamics

An optical microcavity is an optical resonator whose linear dimensions are of the order of or smaller than the wavelength of the light to be confined within it. Standing waves are formed in a cavity by an arrangement of optical elements, such as mirrors. A basic example is a Fabry-Perot cavity made of two parallel mirrors. As the two mirrors are highly reflective, the light will continuously reflect off of them, resulting in the formation of standing waves for certain resonant frequencies of the cavity,  $\omega$ , which depend on the geometry of the cavity and the medium within it. For an ideal cavity, the resonant light waves should remain trapped between the mirrors for an infinite amount of time. However, in reality, imperfections in the cavity design or in the mirrors lead to photons having a finite lifetime within the cavity. The optical loss rate of the cavity,  $\kappa$ , is often described in terms of the quality factor (or  $Q$ -factor) of the cavity, as follows:

$$Q = \frac{\omega}{\kappa}. \quad (2.3)$$

The photon loss rate manifests itself through spectral characteristics of the cavity. A lossless cavity would have an emission line of infinitesimal width, while an imperfect one manifests itself through a broadened emission spectrum. The  $Q$ -factor can, therefore, also be defined as:

$$Q = \frac{\omega}{\Delta\omega}, \quad (2.4)$$

where  $\Delta\omega$  is the full-width at half-maximum (FWHM) of the resonant peak of the cavity.

When a quantum emitter, such as a QD, is placed inside an optical cavity, the two interact with each other. If the emitter and the cavity are in resonance, the rate of transition between the ground and excited QD states is modified due to light-matter interactions. This interesting phenomenon is known as cavity quantum electrodynamics (cQED). It is characterised by three parameters: the above-mentioned photon loss rate of the cavity,  $\kappa$ , the non-resonant emission rate of the emitter,  $\gamma$ , and the emitter-photon coupling rate,  $g_0$ .

The parameter  $\gamma$  includes the effects of emission into modes that are not the resonant frequency modes of the cavity, as well as any non-radiative recombination processes. The former can be suppressed by reducing the spectral density of non-resonant cavity modes. This can be achieved by optical band gap engineering through, for example, PhCs described in Section 2.2.2. The non-radiative recombination processes are typically negligible for InAs QDs at low temperatures ( $\sim 5$  K) [44].

The parameter  $g_0$  describes the rate of exchange of energy between the emitter and the cavity mode while in resonance, and is defined as follows [60]:

$$g_0 \equiv \left( \frac{\mu^2 \omega}{2\epsilon_0 \hbar V_{\text{eff}}} \right)^{1/2}, \quad (2.5)$$

where  $\mu$  is the electric dipole matrix element of the emitter transition,  $\omega$  is the angular frequency,  $\epsilon_0$  is the permittivity of free space,  $\hbar$  is the Dirac constant and  $V_{\text{eff}}$  is the effective modal volume. While  $\mu$  depends mostly on the size of the emitter, which is largely fixed,  $V_{\text{eff}}$  is defined to be [61]:

$$V_{\text{eff}} \equiv \frac{\int_V \epsilon |\mathcal{E}|^2 dV}{\max(|\mathcal{E}|^2) \epsilon_{\text{max}}}, \quad (2.6)$$

where  $\mathcal{E}$  is the electric field,  $\epsilon$  is the dielectric permittivity and  $\epsilon_{\max}$  is the dielectric permittivity at the location of the maximum electric field intensity. Typically,  $V_{\text{eff}}$  is given in the convenient units of  $(\lambda/n)^3$ , where  $\lambda$  is the wavelength of light in vacuum and  $n$  is the refractive index of the material. Therefore, by decreasing the size of the cavity, the emitter-photon coupling rate can be increased. For this reason PhC cavities (further discussed in Section 2.3.3), whose effective modal volumes are of the order of  $10^{-2}(\lambda/n)^3$  or smaller are of great interest for studying cQED effects.

The light-matter interaction between the emitter and the cavity can be classified into two regimes: the weak and strong coupling regimes. If the photons are lost from the cavity before the emitter can reabsorb them, *i.e.*  $g_0 \ll (\kappa, \gamma)$ , the system is weakly coupled. Conversely, in the strongly coupled case, the photons are reabsorbed by the emitter and re-emitted several times before leaving the cavity, *i.e.*  $g_0 \gg (\kappa, \gamma)$ .

### 2.3.1 Weak Coupling: The Purcell Effect

Even though photons are not reabsorbed by the quantum emitter in the weak coupling regime of light-matter interaction, an interesting phenomenon takes place. According to Fermi's Golden Rule the rate of transition between the ground and excited states of the emitter is proportional to the density of available states as well as to the strength of interaction between the emitter and the environment for this transition frequency. Therefore, for the emitter resonant with the cavity mode the interaction strength is increased, in comparison to the free space, resulting in the enhanced emission rate of the quantum emitter. This effect was first observed by Edward Mills Purcell in 1946 [62] and has since become known as the Purcell effect. It can be quantified by the Purcell factor, which is defined as the ratio of transition rates for an emitter within a cavity,  $\Gamma_{\text{cav}}$ , to that in free space,  $\Gamma_{\text{FS}}$ , and is given by:

$$F_P = \frac{\Gamma_{\text{cav}}}{\Gamma_{\text{FS}}} = \frac{3}{4\pi^2} \left(\frac{\lambda}{n}\right)^3 \left(\frac{Q}{V_{\text{eff}}}\right) \xi^2 L(\omega), \quad (2.7)$$

where  $\xi$  is the normalized dipole orientation defined below,  $L(\omega)$  is the spectral lineshape of the cavity and the other parameters are as defined previously. The factor  $\xi$  describes the spatial and polarisation alignment between the emitter

and the cavity mode fields, and is given by:  $\xi \equiv |\mathbf{p} \cdot \mathbf{E}|/|\mathbf{p}||\mathbf{E}|$ , where  $\mathbf{p}$  is the dipole moment of the emitter and  $\mathbf{E}$  is the electric field in the cavity. The parameter  $L(\omega)$  represents the spectral overlap between the emitter's frequency,  $\omega_0$ , and that of the cavity,  $\omega$ , with a Lorentzian lineshape, and can be written as  $L(\omega) \equiv \Delta\omega^2/[4(\omega_0 - \omega)^2 + \Delta\omega^2]$ .

The Purcell factor indicates either an enhancement (for  $F_P > 1$ ) or a suppression (for  $F_P < 1$ ) of the transition rate of the quantum emitter from ground to excited states due to the light-matter coupling between the emitter and the cavity. As the Purcell factor depends not only on the Q-factor and the effective modal volume of the cavity but also on the spectral and spatial alignment between the emitter and the cavity, high Purcell factor values are very challenging to achieve experimentally.

In addition, experimental determination of the Purcell factor is not straightforward. Time-resolved photo-luminescence spectroscopy can be used to determine the radiative lifetime of an emitter. However, to compare directly cavity and free space transition rates, the cavity would have to be placed around the emitter following the free space measurement. For this reason experimental values of the Purcell factor are typically found through statistical means, where an average radiative lifetime of a set of emitters in free space is compared to that of an emitter in a cavity [63].

### 2.3.2 Strong Coupling: Rabi Splitting

In the strong coupling regime of the cQED effect, the emitted photon remains in the cavity for a long enough period of time to be reabsorbed by the emitter. This exchange between the cavity photon and the emitter exciton is known as Rabi oscillation [64]. The system is well described by the Jaynes-Cummings Hamiltonian [65], the solutions of which are two energy eigenstates whose difference,  $\Delta E$ , depends on the strength of the coupling as follows:

$$\Delta E = 2\sqrt{g_0^2 - \frac{(\kappa - \gamma)^2}{16}}. \quad (2.8)$$

When  $g_0 \ll (\kappa, \gamma)$ ,  $\Delta E$  is imaginary and the emitter and the cavity states are degenerate. This is the case in the weak coupling regime, where the Purcell effect is the dominant phenomenon as discussed above. By contrast, when

$g_0 \gg (\kappa, \gamma)$ ,  $\Delta E$  is real and the degeneracy is lifted. The cavity photon and the emitter exciton form a quasiparticle known as an exciton-polariton [66], forming two states, and with the magnitude of the energy splitting between them being  $\Delta E$ . Experimentally, the strong coupling regime is observed through the splitting between the cavity mode and the emission wavelength spectral peaks at resonance. The transition between the weak and strong coupling regimes is confirmed by an anti-crossing of the two emission peaks as one is tuned across the resonance of the other [67–69]. Quantum emitters, such as QDs, embedded in microcavities and operating in the strong coupling regime are compelling contenders for the provision of efficient on-demand single photon sources [70, 71].

### 2.3.3 Photonic Crystal Cavities

As discussed briefly in Section 2.2.2, 2D and 1D photonic crystal (PhC) confinement can be integrated in a planar semiconductor architecture to be used for controlling the propagation of light in quantum optical circuits. The remaining directions are forbidden through total internal reflection. However, defects can be introduced to the PhC periodic structure in order to allow a proportion of the spectrum inside the photonic band gap to be allowed through. An example given earlier was the linear propagation defect where, by removing one row of holes in a 2D PhC, a single mode waveguide can be formed. However, localized point defects can also be used to create optical microresonators.

The most widely studied PhC cavities (PhCCs) are the so-called H1 and L3 cavities [48]. Both of these are based on the same 2D PhC structure as in Section 2.2.2. An H1 cavity is created by omitting one hole, while an L3 cavity is made by removing three nearest-neighbour holes in a row (*i.e.*, along one of the triangular-lattice directions) from the periodic array. They can be optimized further in order to decrease out-of-plane scattering losses by slightly shifting and/or altering the diameter of the holes immediately surrounding the defect, thereby achieving very high experimental Q-factors of over 40,000 [72, 73]. Nanobeam PhCCs, which are based on 1D PhCs are currently attracting increasing attention from the quantum optical community as they can be easily integrated with other circuit components, such as nanobeam wa-

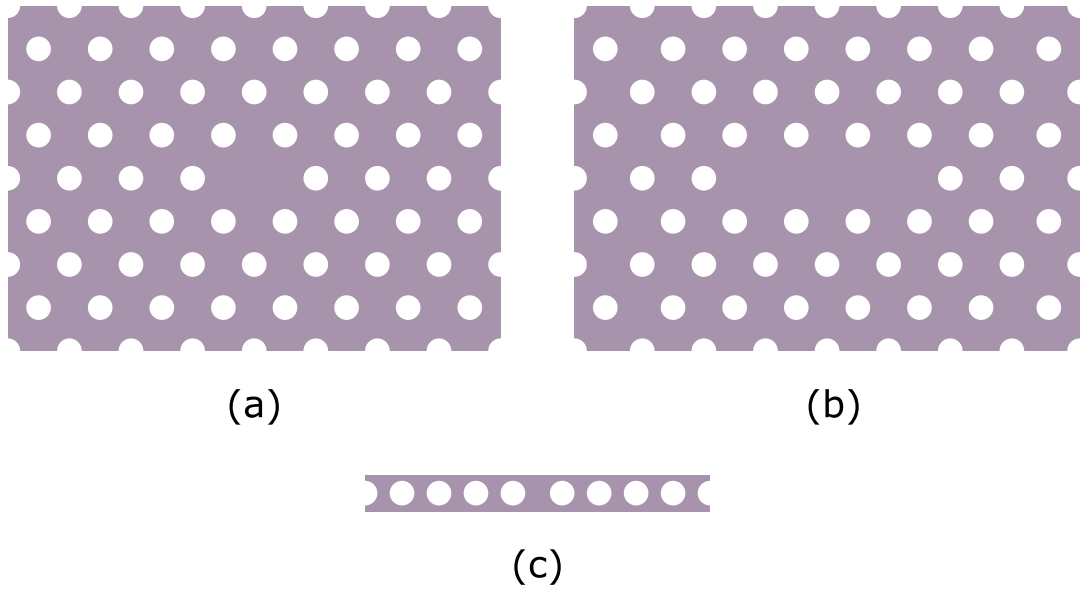


**Figure 2.6:** Types of photonic crystal cavities: (a) H1 and (b) L3 are (2D) planar periodic structures with 1 and 3 holes omitted to create a defect respectively, while (c) the nanobeam is a 1D array with a changed spacing between the two centre holes.

veguides (see Section 2.2.1) and beam splitters. In addition, there exist promising electro-mechanical in-plane actuators, which can be used to tune the optical properties of these cavities in situ (see Chapter 6). Defect states in the nanobeam PhCCs can be created in a variety of ways, some of which are further discussed in Chapter 4. However, the simplest case is to displace half of the PhC array closer to or further away from the other half, so that the distance between the two centre holes is different to the periodic spacing between all the other holes. The three types of PhCCs discussed here are presented schematically in Figure 2.6.

PhCCs are very promising platforms for studying cQED effects as they have very low effective modal volumes,  $V_{\text{eff}}$ . This is due to their inherent size, with cavities of dimensions of the order of the wavelength of light for which they are designed to operate, so that  $V_{\text{eff}} \sim (\lambda/n)^3$ . This means that even PhCCs with low  $Q$ -factors can achieve a large Purcell enhancement of the emission rate of the emitter embedded within them. In addition, these structures have found numerous applications in a variety of nanophotonic devices, such as switches, logic gates and memory storage [74].



# Chapter 3

## Methods

This chapter outlines the experimental and computational methods that have been used in order to obtain the results presented in this thesis. It begins with a description of the molecular beam epitaxy (MBE) technique used to grow quantum dots (QDs) and an overview of a typical structure of the GaAs-based wafers. The subsequent fabrication techniques for the placement of diodes and various photonic structures on those wafers are then discussed. The chapter continues with an outline of the optical device characterisation methods that have been utilized. These include a micro-photoluminescence setup employed with two types of cryostats and a time-correlated single-photon counting technique used to verify the single-photon nature of the emission from the QDs. Finally, the chapter concludes with a description of the computational methods used to simulate the optical and electro-mechanical behaviour of the structures studied in this thesis.

### 3.1 Wafer Growth

In this section the principles behind the growth of self-assembled QDs are explained. The technique that was used to grow the InAs QDs for all the samples is also described. Finally, the typical structures of the doped (electrically active) and intrinsic (electrically inactive) wafers are presented.

All of the wafers used for the experiments reported in this thesis were grown by Dr Edmund Clarke in the National Epitaxy Facility in Sheffield, UK.

### 3.1.1 Quantum Dot Growth

A semiconductor QD is a structure with the charge carriers quantum confined in all three spatial dimensions (as discussed in Section 2.1). In order to achieve such confinement the sizes of the QDs have to be no larger than the de Broglie wavelength of electrons (50 nm in GaAs) [75]. Therefore, a fabrication method is required that allows precise control over the dimensions and shapes of the nanostructures, as these will affect the optical properties of the QDs [76]. Several advanced crystal growth techniques fulfil these criteria. Natural or self-assembled QDs can be produced using heteroepitaxial methods. Natural QDs are made by the deposition of 2D semiconductor layers of different bandgaps on top of each other to create a two-dimensional confinement of charge known as a quantum well. The remaining in-plane confinement necessary for QD formation arises naturally in the system from monolayer thick fluctuations in the quantum well width [77]. On the other hand, QDs formed by self-assembly offer higher yield and better control over their sizes and shapes [22].

It is the self-assembled InAs QDs that were used throughout this thesis, and hence the Stranski-Krastanow growth mode [78] used for their formation is discussed here in detail. This method relies on the lattice mismatch between the two compound semiconductors. In the case of InAs QDs formed on a GaAs substrate, this amounts to 7% [79]. As a thin layer of InAs is deposited on top of GaAs at first a layer is formed with the lateral lattice constant of GaAs, known as the wetting layer. However, as the InAs layer thickness is increased to above a critical value (typically  $\sim 1.7$  monolayers [77]), the stored compressive strain leads to instability. In order to relieve the built-up energy InAs relaxes to its original lateral lattice dimensions forming small islands of the order of 10 nm in size. Their exact size and shape can be controlled through various growth parameters, such as temperature, pressure and deposition time [80]. A final layer of GaAs is then grown on top of the formed islands in order to remove any surface effects from the formed QDs. In particular, this minimises the carriers' non-radiative recombination caused by the InAs-air interface, thereby resulting in improved optical quality of the QDs [81]. A diagram of the Stranski-Krastanow growth mode is presented in Figure 3.1.

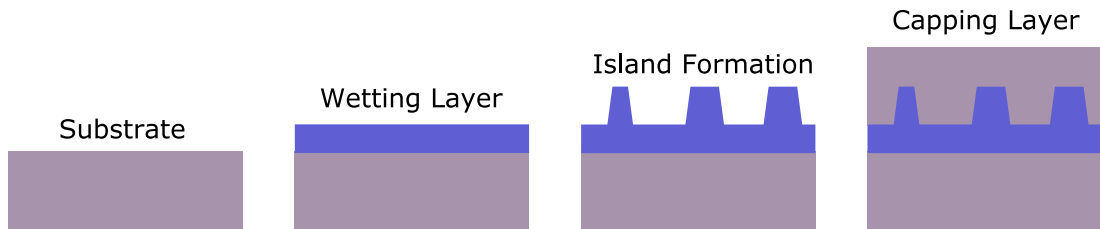


**Figure 3.1:** Schematic diagram of the Stranski-Krastanov epitaxial method for growing self-assembled InAs QDs (blue) on a GaAs substrate (purple).

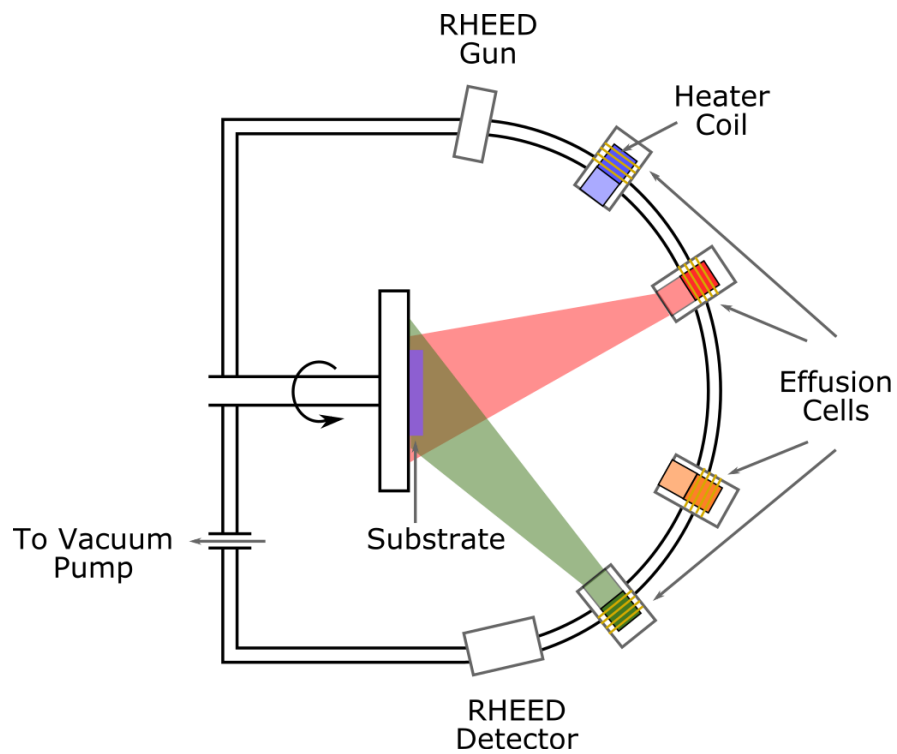


**Figure 3.2:** Schematic diagram of an MBE chamber.

Self-assembled QDs can be grown either by molecular beam epitaxy (MBE) or metalorganic vapour phase epitaxy (MOVPE). The main difference between the two techniques is that MBE uses elemental sources that are directed onto a substrate in an ultra-high vacuum (UHV) environment (down to  $10^{-12}$  Pa) ensuring material purity, whereas MOVPE uses compound sources that require the use of a carrier gas (typically hydrogen) to enable them to flow across the substrate surface [82]. The QDs used in this thesis were all grown using MBE. A schematic diagram of an MBE chamber is presented in Figure 3.2. Solid sources of each element, such as gallium or arsenic, are stored in separate effusion cells. These are heated to their evaporation temperatures and their deposition on a heated substrate is controlled by mechanical shutters. By opening several shutters at a time compound semiconductors, such as InAs, can be grown by condensing on and reacting with the pre-cleaned substrate [83]. The reflection high-energy electron diffraction (RHEED) technique is often used to monitor the growth of the thin layers. In this method an electron gun releases a beam of high-energy electrons, which strike the surface of the sample at an angle. The diffracted electrons then interfere constructively at specific angles depending on the crystal structure of the sample, and the resulting diffraction pattern is detected. The fringe spacing of the pattern then helps to determine the thickness of the deposited layer in-situ [84].

### 3.1.2 Wafer Structure

For the experimental results reported in this thesis two types of GaAs wafers have been used: intrinsic and doped. Their general layout is presented in Figure 3.3. A buffer layer of GaAs is first grown, using MBE, on top of a commercial epi-ready wafer to level out the substrate. An  $\text{Al}_{0.6}\text{Ga}_{0.4}\text{As}$  layer (typically  $1\ \mu\text{m}$  thick) is then deposited to allow fabrication of suspended GaAs devices (as discussed in Section 3.2). The final layer is the GaAs membrane with a thin (less than 1 nm) InAs QD layer grown in its centre. For samples that do not require electrical connections the top GaAs layer is intrinsic. It is typically of a thickness  $h \approx 140\ \text{nm}$ , so that a single optical mode of the QD emission (usually around a wavelength of 950 nm) can be vertically confined in the membrane (according to:  $h \approx \lambda/2n$ , where  $n = 3.4$  is the refractive index of GaAs at 4 K). For electrical samples the typically 110 nm thick intrinsic GaAs

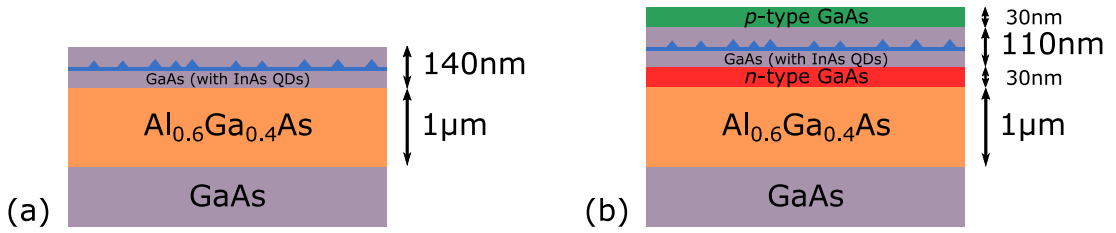


**Figure 3.3:** Typical structure of a GaAs wafer with (a) an intrinsic, and (b) a doped QD membrane structure.

layer with embedded InAs QDs is sandwiched between an  $n$ -type and a  $p$ -type doped GaAs layers, each of 30 nm thickness (giving a membrane thickness of about 170 nm). The  $n$ -type layer is created through doping of GaAs with silicon, while the  $p$ -type layer is achieved through beryllium doping. Upon deposition of contacts on these two layers, QCSE (see Section 2.1.3) can be used to tune the QD emission wavelength. For the electro-mechanical structure studied in Chapter 5 the GaAs substrate is also doped, so that a potential difference between the substrate and the membrane can be achieved.

## 3.2 Device Design and Fabrication

This section outlines the design and fabrication techniques used to make the devices reported in this thesis. The creation of the desired pattern that is used to fabricate the samples is first explained. Then the fabrication of suspended photonic integrated structures is discussed. This is followed by a description of the procedure used for diode fabrication for doped wafers.

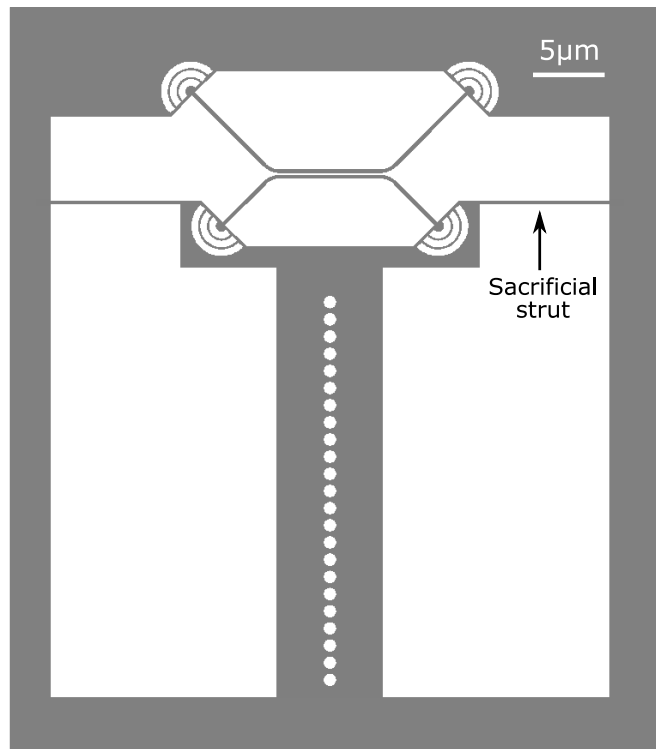
The devices studied experimentally and presented in subsequent chapters have been designed by myself and fabricated mostly by Dr Ben Royall, but together with some contribution from Dr Deivis Vaitiekus and myself, in the National Epitaxy Facility in Sheffield, UK.

### 3.2.1 Design for Fabrication of On-Chip Devices

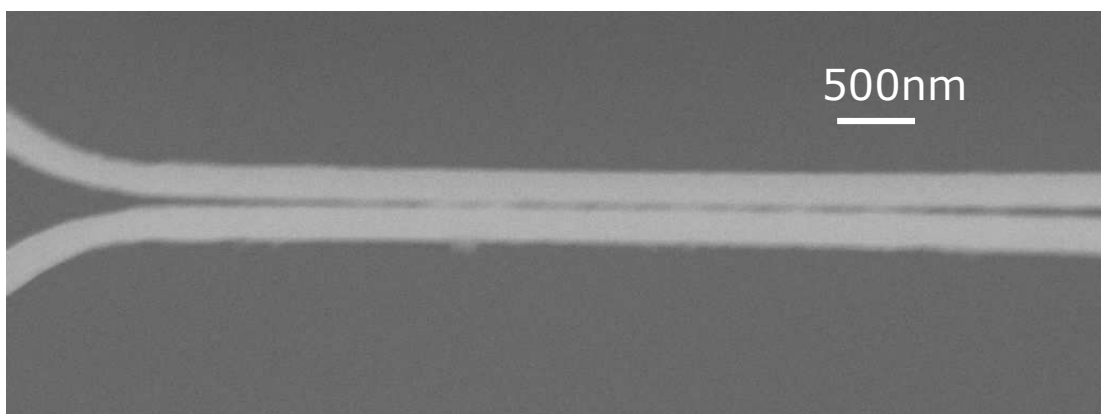
In order to fabricate the integrated photonic devices and study them experimentally they have to be designed first. The modelling of the structures through computational methods is described in Section 3.4. After the required systems have been designed and their parameters chosen carefully the struc-

tures have to be created in a Graphic Database System II (GDSII) format used for fabrication. This is the conventional industrial format for integrated circuitry design. It contains all necessary information about a device, such as planar geometric shapes, text labels and the hierarchical layout, when several separate fabrication steps are required. Examples of three system designs in GDSII format are shown in Figures 3.4, 3.7 and 3.9. These designs have to be modified from the original models so that they properly take into consideration the fabrication procedures or the fragility of these devices. For example, the optimized fabrication method for the creation of suspended structures in GaAs consistently results in smaller GaAs features, larger separations between them and larger etched features. This information has to be fed back into the GDSII design, so that the required device parameters can be reproduced during sample processing. For example, nanobeam waveguides like those located at the end of the cantilever in Figure 3.4 are usually separated by a 20 – 30 nm larger distance after processing than in the GDSII file. Hence, the GDSII file has to contain smaller separations than those required in an actual device. However, small separations are very difficult to achieve in practice and if one attempts to be make them very small (less than 60 nm) the nanobeam waveguides may actually become joined during the fabrication process, as seen, for example, in the scanning electron microscope (SEM) image shown in Figure 3.5. In addition, the cantilever structure in Figure 3.4 was found to be very fragile, such that it often collapsed onto the substrate during transportation and installation. Therefore, supporting struts had to be added on either side of the cantilever's end to prevent that, and a subsequent process to remove them post-installation was developed.

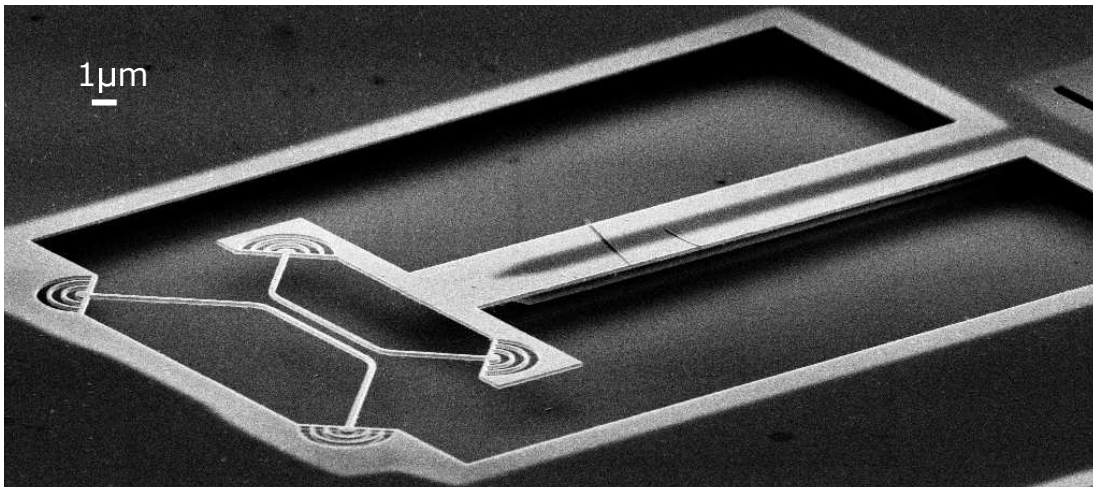
The time needed to etch the structure is also crucial. The device is suspended using a wet etch procedure (described in the following section) resulting in different parts of the structure etching at different rates depending on their sizes. For example, the Bragg gratings at the ends of the waveguides are very narrow and will etch much faster than a wide cantilever. If the etch lasts long enough to fully suspend the cantilever, the gratings might totally disappear. By contrast, if gratings are etched for the optimal time, the cantilever may still be connected to the substrate at its centre, as shown on the angled SEM image in Figure 3.6. This is the reason for introducing the holes in the centre of the cantilever to increase its etch rate.



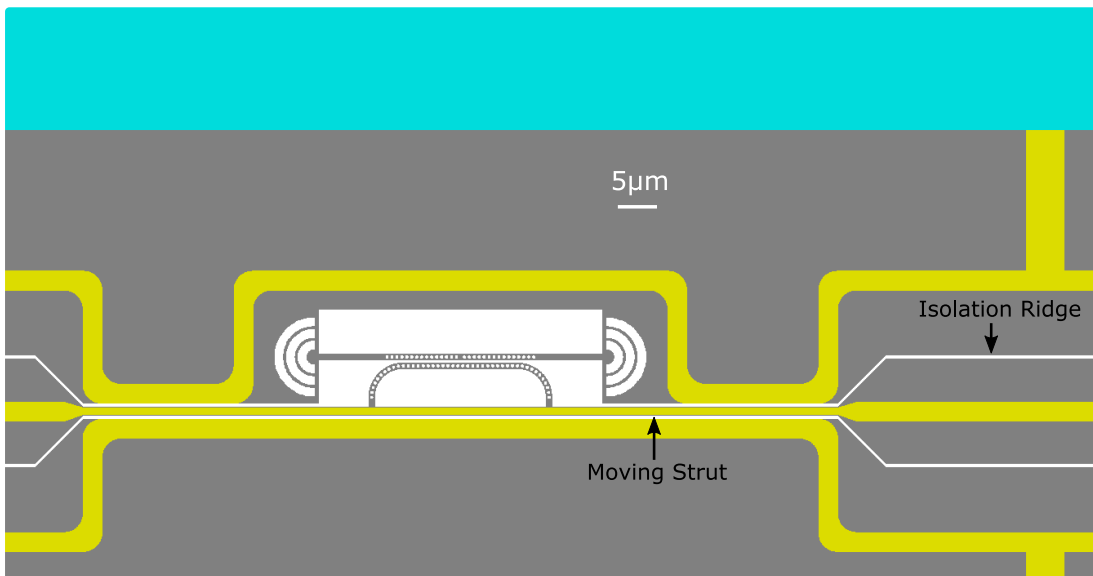
**Figure 3.4:** Digital image of a cantilever device design in GDSII format, used for the electro-mechanical control of an optical beam splitter in Chapter 5. Etched areas are shown in white.



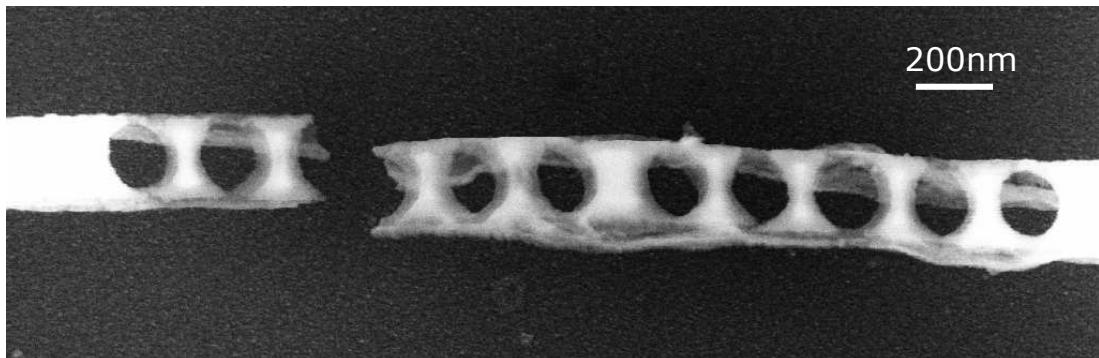
**Figure 3.5:** SEM image of two suspended nanobeam waveguides joined during the fabrication process.



**Figure 3.6:** Angled SEM image of the cantilever based electro-mechanical system with the cantilever still attached at its centre to the substrate (noticeable by the grey stripe along its length).



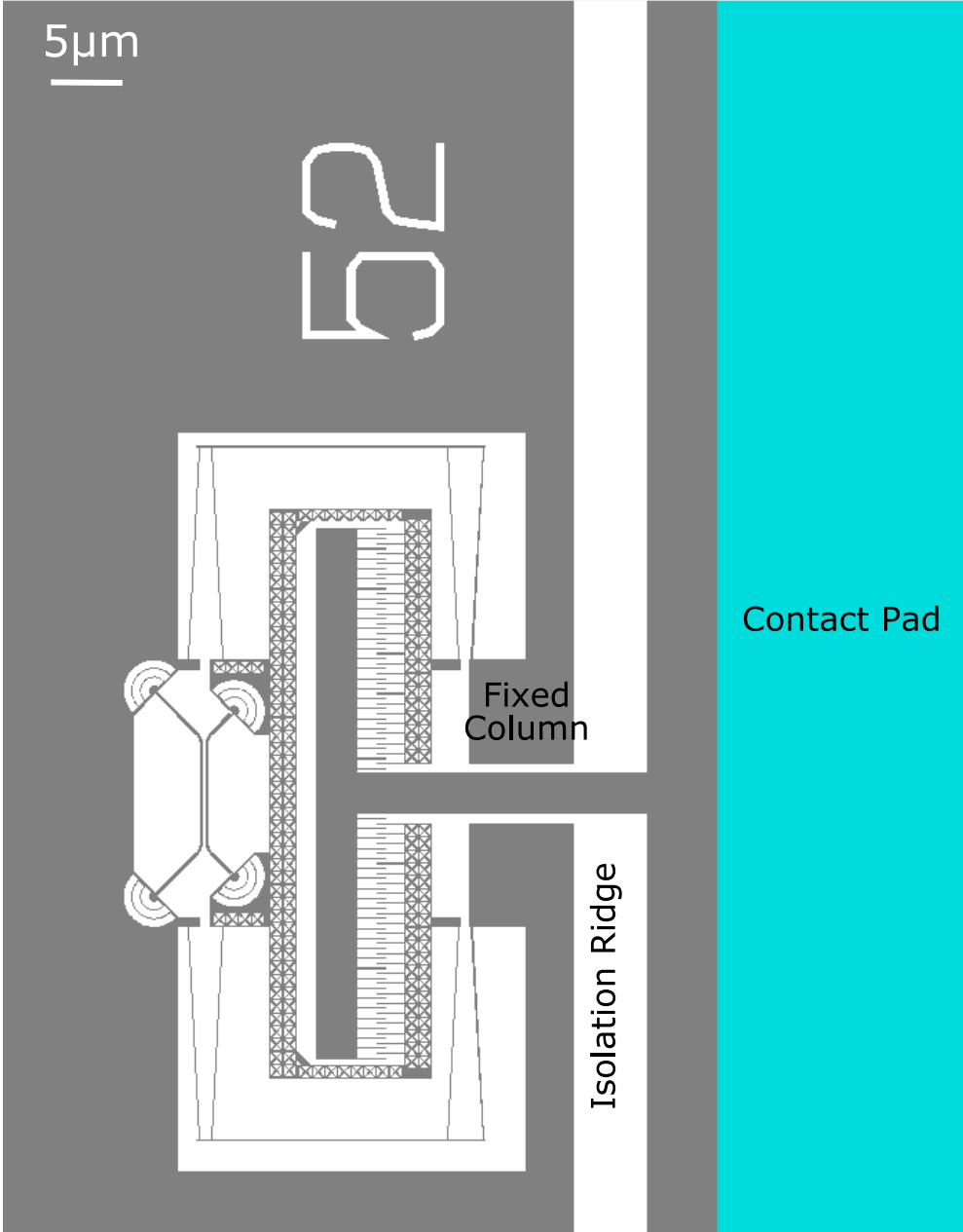
**Figure 3.7:** Digital image of an electro-mechanical system in GDSII format designed for the tuning of a nanobeam photonic crystal cavity. Etched areas are shown in white, the metal contact rail in gold and the large electrical contact pad in blue.



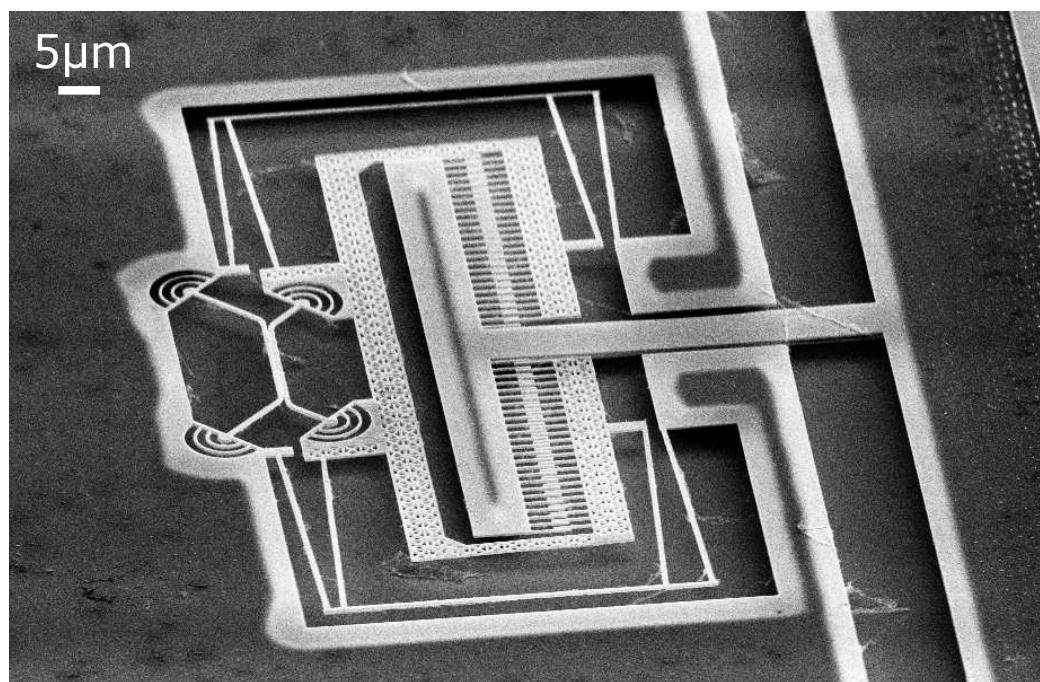
**Figure 3.8:** SEM image of a nanobeam photonic crystal cavity that has broken due to a smaller waveguide width and larger hole sizes than designed.

Figure 3.7 shows another electro-mechanical system in GDSII format. It has been designed for tuning a nanobeam photonic crystal cavity and its development is discussed in detail in Chapter 6. The GDSII file design for this system demonstrates the need for different layers within the device, which represent different parts of the system that have to be fabricated consecutively. For example, the gold rails, which represent metal contacts, need to be patterned separately from the white (etched) parts of the structure as different steps are involved in their processing. The gold layer, in contrast to the white one, is not etched away from the GaAs but instead a thin layer of metal is deposited onto the sample. The large blue rectangle represents an electrical contact pad, through which voltage can be applied to the smaller metal rails. Contact pads had to be incorporated into this device design as a typical contact photo-mask used for diode fabrication (see Section 3.2.3) could not be used for this system, which is made to operate on an intrinsic wafer. The contact pad had to be fabricated in a separate fabrication step from the metal rail, as it requires a thicker, and therefore stronger, metal layer to which wires can be bonded. It is also advantageous to use a faster processing rate during patterning and metal deposition of the contact pad due to its size.

For this system there were two important design factors to consider. The first one, already mentioned earlier, is that the widths of the fabricated waveguides are usually about 30 – 40 nm narrower and the diameters of the etched holes in those waveguide are usually about 40 – 50 nm larger than in the GDSII file. This can have dire consequences for the nanobeam photonic crystal structures, as demonstrated in Figure 3.8, where the combination of narrower wa-



**Figure 3.9:** Digital image of a comb-drive actuator in GDSII format designed for the electro-mechanical control of an optical beam splitter.



**Figure 3.10:** SEM image of a comb-drive actuator with its fixing columns attached to the substrate.

veguide and larger holes has led to breakage of the entire nanobeam structure. It is, therefore, important to correct for the expected fabrication imperfections in the GDSII design.

Another issue that could be solved through a proper design of the GDSII file was the observed current flow between different metal rails, despite them being deposited on an intrinsic GaAs wafer. This was a problem because the device was to operate based on an induced electro-static attraction between the rails at different potentials. The issue was resolved by adding isolation ridges between the rails, which could be fabricated at the same time as the etched GaAs structure (see Figure 3.7).

The third example device in GDSII format is the comb-drive actuator shown in Figure 3.9. This design demonstrates the identification marks that allow the easy recognition of which particular device, from among a large number of similar structures on the sample, is being investigated experimentally at any given time. In this case the identifier is the number 52. It provides information on the particular device parameters that may be varied amongst the large ensemble of devices on a chip. For the comb-drive actuator a range of numbers

or lengths of the teeth, or lengths of the struts, can be produced on a sample in order to study the effect they have on the electro-mechanical behaviour of the device. A crucial element for this particular design of the comb-drive actuator is the size of the fixed columns. These need to remain attached to the substrate during the wet etch that removes the AlGaAs sacrificial layer from beneath the other parts of the device. This is an opposite requirement to the above-mentioned cantilever system, which needed to be fully suspended. If the columns become suspended the entire moving side of the device will be attached to the rest of the wafer at only two points on the left-hand side. This would result in the system not working properly and the possibility of the moving side of the device totally detaching from the rest of the device. An angled SEM image of a comb-drive actuator with properly attached columns is shown in Figure 3.10.

### 3.2.2 Fabrication of Photonic Structures

The fabrication procedure of suspended photonic structures on a typical intrinsic GaAs wafer (see Section 3.1.2) is described below. The steps are also illustrated in Figure 3.11. Before the fabrication can begin a small piece of wafer (usually about 1 cm<sup>2</sup>) has to be cleaved from the as-grown wafer (which is typically 2 inch in diameter) after the QD growth has been completed. This is done by scribing the wafer, turning it over and gently rolling the scribing tool over the marked area. Then any surface contaminants are removed from the sample through the so-called three-solvent clean, using n-butyl acetate, acetone, and isopropyl alcohol.

The sample thus prepared is then spin-coated with CSAR 62 - a positive electron-beam (e-beam) resist. A few drops of the resist are deposited onto the surface and the sample is then spun around its centre at 4000 rpm for 30 s. This results in a uniform coating, approximately 360 nm thick. In order to enhance the adhesion of the resist to the wafer, the sample is then baked on a hot plate at 180 °C for 3 minutes.

The following e-beam lithography (EBL) step transfers the required pattern of photonic structures from GDSII format onto the resist by directing the beam of high-energy (~ 50 keV) electrons around the sample to expose only the areas that will eventually be etched away from the wafer. The EBL step is capable of

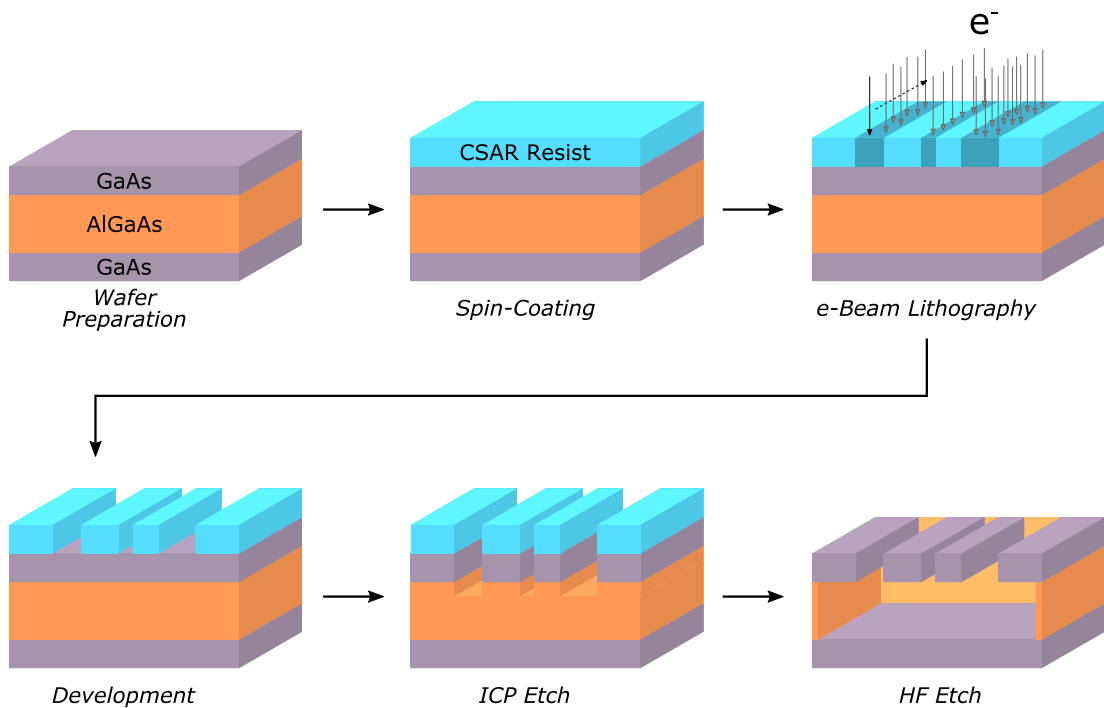


**Figure 3.11:** Schematic diagram of the fabrication process of suspended photonic structures. A positive e-beam resist (CSAR 62) is spin-coated onto a cleaved and cleaned GaAs wafer with embedded QDs. The device pattern is then transferred onto the resist using electron-beam lithography and developed using xylene. The photonic structure is then etched into the wafer using an inductively coupled plasma with the resist as a mask, which is afterwards decomposed using ultraviolet light and removed chemically. The last step is a wet hydrofluoric acid etch, which removes the sacrificial AlGaAs layer from beneath the device, thereby creating a suspended structure.

producing feature sizes as small as 10 nm. Exposure to the e-beam changes the solubility of the resist and by immersing the sample in the xylene developer afterwards the exposed areas of the resist are removed from the surface. The developed resist pattern creates a mask used for the transfer of the structure onto the wafer using an inductively coupled plasma (ICP) etch.

ICP etching is a highly anisotropic dry etch process, which can provide extremely smooth and vertical sidewalls (with a wall tilt of less than  $4^\circ$ ). This is essential for achieving the low-loss high-confinement photonic crystal cavities studied in Chapter 4 [85–87]. During an ICP etch a charged chlorine/argon-based plasma is created in a vacuum chamber with the imposition of a strong radio-frequency (RF) field. A secondary RF field is then used to accelerate electrons to high velocities, which then collide with the chamber, and hence charge the wafer platter. As the walls of the chamber are grounded, a large voltage difference causes the ions to bombard the wafer vertically. This changes the volatility of the GaAs wafer areas not protected by the mask, hence transferring the device pattern into the sample. The etching lasts typically about 90 s, until the sacrificial AlGaAs layer is reached. The CSAR 62 resist is then removed from the surface of the sample by first decomposing it through exposure to ultraviolet light and then soaking it in *N*-methyl-2-pyrrolidinone for several minutes.

The last step in the fabrication process is a wet hydrofluoric (HF) acid etch. The sample is submerged in a 5:2 mixture of water and HF acid for about 10–20 s in order to remove the sacrificial AlGaAs layer from beneath the GaAs membrane, thereby creating a suspended photonic structure. This is due to the selectivity ratio of  $10^5:1$  in the etching process with HF between  $\text{Al}_{0.6}\text{Ga}_{0.4}\text{As}$  and GaAs [88]. When the under-etching is completed the sample is rinsed with water and dried.

However, as the aspect ratios of the suspended photonic devices tend to be high, the surface tension present when drying the structure can have dire consequences. As the sample is dried the surface tension of the water droplets remaining between the GaAs membrane and the substrate increases, resulting in the suspended device being pulled down towards the substrate, potentially collapsing it irreversibly. In order to avoid that, a critical point drying (CPD) procedure can be used. This relies on the fact that a supercritical fluid does not have any surface tension, due to the lack of a liquid/gas phase boundary [89].

Water and liquid carbon dioxide are the most commonly used CPD fluids, but both the critical temperature and pressure of CO<sub>2</sub> are considerably lower, and hence easier to achieve, than that of H<sub>2</sub>O. Therefore, a CPD procedure with CO<sub>2</sub> has been used for the fabrication of the devices studied in subsequent chapters in this thesis.

The CPD procedure is illustrated in Figure 3.12. After the sample is rinsed with water following the HF etch, it is purged with acetone. As acetone is miscible with both water and liquid CO<sub>2</sub>, it can be used to remove the former. The sample is then placed in a chamber whose temperature and pressure can be controlled. Initially the pressure is set to 1 atmosphere and the temperature to 278 K and liquid CO<sub>2</sub> is added, which dissolves the acetone. Then the temperature and pressure are raised to above the critical values for CO<sub>2</sub> (over 304 K and 73 atmospheres), so that the CO<sub>2</sub> becomes a supercritical fluid. Once this transition is completed, the pressure is decreased back to 1 atmosphere, while keeping the temperature at 304 K, allowing the CO<sub>2</sub> to transform from a supercritical phase to a gaseous phase without any surface tension present. Finally, the chamber is vented, leaving the suspended GaAs photonic structure dried at room temperature and pressure.

The effect of using the CPD process on a fabricated suspended device is demonstrated in Figure 3.13. It shows two SEM images of the same photonic network prepared with and without CPD. The structure dried in air has clearly collapsed down onto the substrate due to surface tension, while that fabricated with the CPD procedure remains suspended.

### **Development of Silicon Dioxide Mask**

An additional complication in the fabrication procedure of nano-optical devices arises when photonic crystal (PhC) structures are made. These devices require precise reproduction of the size and shape of the periodically repeated pattern. As will be discussed in Chapter 4, the optical properties of PhC devices can vary considerably with just a few nanometers deviation from the required feature sizes. Unfortunately, the e-beam resist typically used for the fabrication of other less demanding nano-photonic structures, such as waveguides (discussed in Chapter 5), has a tendency to peel off slightly during the ICP etching procedure. This results in a somewhat rougher surface and rand-

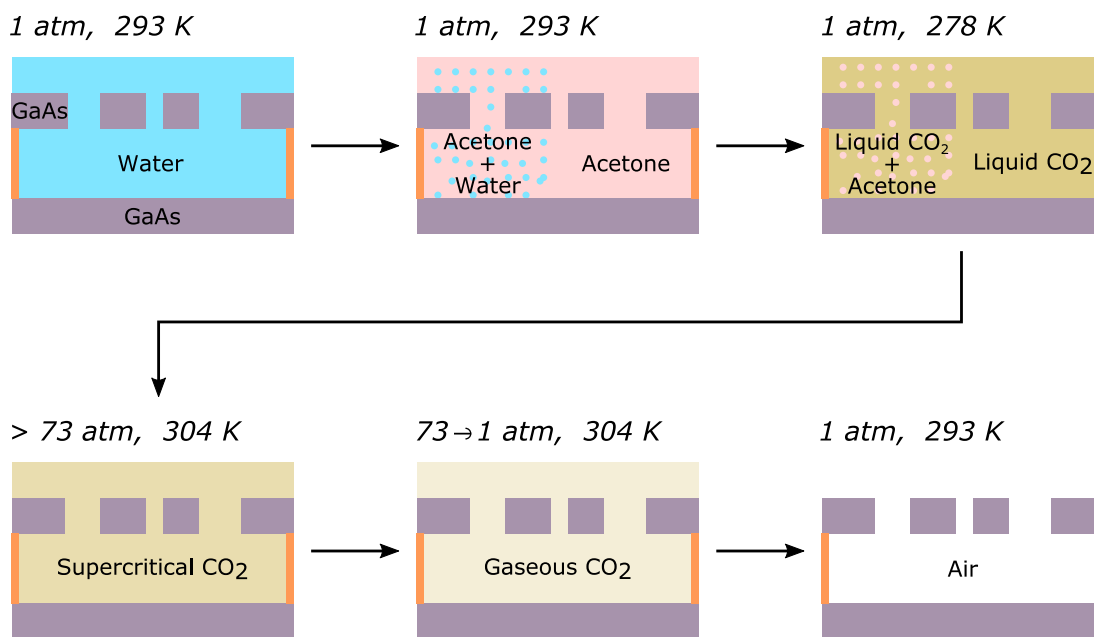


**Figure 3.12:** Schematic diagram of the critical point drying process. The rinsed under-etched device is purged with acetone to remove water. Then the liquid CO<sub>2</sub> is added to dissolve the acetone. This is followed by an increase in both temperature and pressure to the critical values for CO<sub>2</sub>, inducing its transition into a supercritical fluid phase. The pressure is then decreased, allowing the CO<sub>2</sub> to become gaseous. Finally, the chamber is vented leaving the GaAs photonic structure dried and suspended.

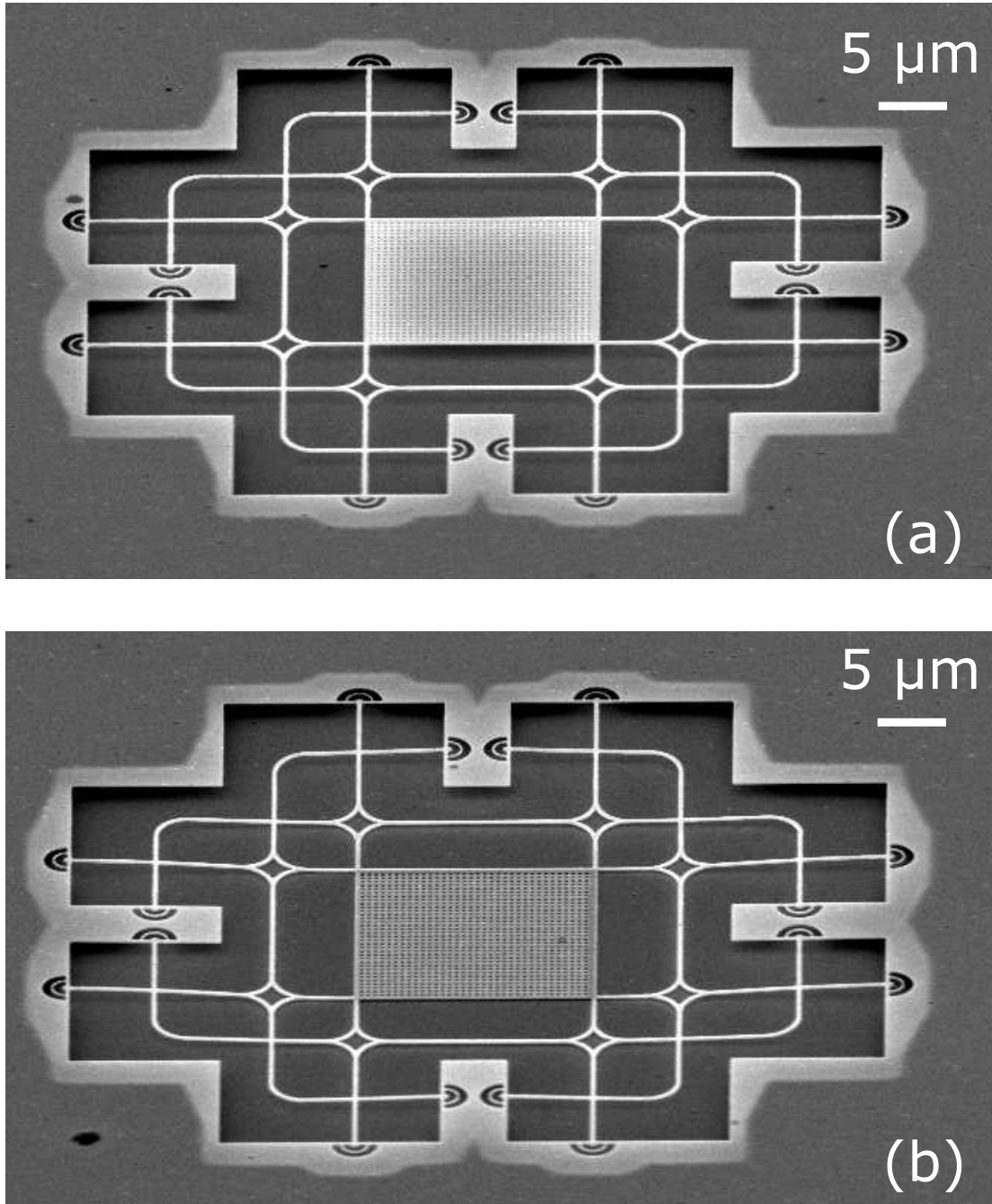


**Figure 3.13:** SEM images of a suspended GaAs photonic device fabricated (a) with, and (b) without the critical point drying process.

only spaced few-nanometer sized differences in the periodic patterns. This effect is particularly more pronounced for nanobeam PhC structures as opposed to 2D ones, such as PhC waveguides or 2D PhC cavities (see Sections 2.2.2 and 2.3.3 respectively). The combination of periodically etched holes in a narrow strip of material, as is the case for a nanobeam waveguide, exacerbates the problem of the resist peeling off from the GaAs during etching. For this reason a new fabrication procedure that achieves the required reproducibility levels of the nanobeam PhC devices was developed. It uses a more robust, silicon dioxide ( $\text{SiO}_2$ ) mask for the etching, which reduces the problem of irregular shapes of these structures [90]. This requires two additional steps in the fabrication process shown in Figure 3.11. Firstly, a 100 nm layer of  $\text{SiO}_2$  is deposited onto the prepared wafer using plasma-enhanced chemical vapour deposition (PECVD), described below, before the CSAR 62 resist is spin-coated on top of it. The PhC structure is then transferred into the resist as usual using EBL and xylene. Then the pattern needs to be also created in the  $\text{SiO}_2$  mask beneath it. This is done with an ICP etch which uses trifluoromethane ( $\text{CHF}_3$ ) plasma, rather than the chlorine/argon-based plasma used in the GaAs etching. Next, the resist is removed using ultraviolet light and acetone as usual and the  $\text{SiO}_2$  mask alone is used for the ICP etching of the wafer. Finally, two HF acid etch steps, of 10 % and 40 % concentrations, remove the  $\text{SiO}_2$  mask and the AlGaAs layer respectively, before the sample is finished with a CPD step. Figure 3.14 demonstrates the difference between the nanobeam PhC filter fabricated with an e-beam resist and a  $\text{SiO}_2$  mask.

The PECVD process mentioned above is one that allows deposition of thin films of material. In this procedure, a sample is placed in a vacuum chamber and reactant gases - in this case silane ( $\text{SiH}_4$ ) and nitrous oxide ( $\text{N}_2\text{O}$ ) - are fed into it as required. Plasma is then created from the gases using a strong RF field. The ionized gases react with the heated sample, allowing the material to be deposited. The process lasts until the required thickness of the  $\text{SiO}_2$  layer is reached.

### 3.2.3 Diode Structure Fabrication

For the electrical samples studied in this thesis a diode structure needs to be produced in addition to the photonic device, in order to allow the application

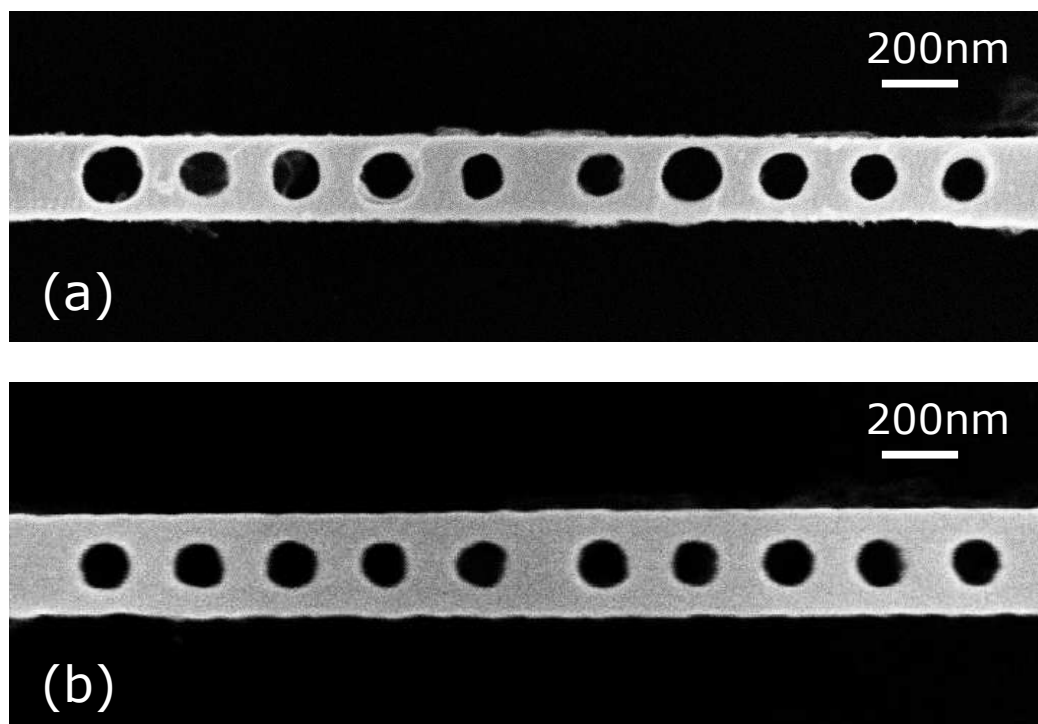


**Figure 3.14:** SEM images of a nanobeam photonic crystal filter fabricated (a) with an e-beam resist, and (b) with a silicon dioxide mask.

of voltage to the doped layers of the wafer. This can be done either before or after the photonic structure fabrication, but in either case it needs to be in advance of the final steps of HF etch and CPD, in order to avoid damage to the suspended devices by the subsequent processing.

The fabrication of the diode structure is very similar to that of the photonic devices themselves. The main differences are that photo-lithography can be used instead of e-beam lithography, and a wet (acid) etch can be used instead of an ICP etch. Both lithography techniques have their advantages and disadvantages. The main benefit of using photo-lithography is that it is much faster. It takes only several seconds of exposure to ultraviolet light, instead of hours of e-beam patterning, to transfer the structure into the resist. The disadvantages of photo-lithography are twofold. Firstly, an expensive hard mask (as opposed to a soft one, such as a computer-generated pattern that can be easily adjusted) has to be made in advance. Therefore, it is typically only used when a large quantity of samples with exactly the same pattern is needed. Secondly, the minimum feature sizes that can be produced using photo-lithography are

about 100 times larger than those made using EBL. However, whereas this has no appreciable effect on the quality of the diode structures, which are typically several microns in size, it would not be possible to resolve the nanometre-sized features of the photonic devices using photo-lithography.

Similarly, the two etching methods have their own advantages and disadvantages. As mentioned before, ICP etching produces smooth and vertical walls, which are essential in achieving high-quality photonic devices, but which are not so important for simple contact deposition on the diode structure of the wafer. Wet etching, on the other hand, does not require expensive equipment, and hence it is faster and cheaper. Therefore, wet etching is the technique of choice for fabricating diode structures.

The full fabrication procedure for diodes is shown schematically in Figure 3.15. A doped GaAs wafer is prepared by cleaving (if the diode is to be fabricated first) and cleaning. This time the sample is spin-coated with a positive photo-resist SPR350. The diode structure is then transferred onto the resist using photo-lithography. The mask is brought into contact with the sample's surface in a mask aligner and then exposed to ultraviolet light. The uncovered areas of the resist are then removed using MF26a developer. The wafer is then etched in a mixture of sulphuric acid ( $\text{H}_2\text{SO}_4$ ), hydrogen peroxide ( $\text{H}_2\text{O}_2$ ) and water in the respective concentration 1:8:80 until the desired doped layer is reached. For example, if the electrical sample is used for the tuning of the QD emission wavelength it is the  $n$ -type GaAs layer of the membrane that needs to be reached (as indicated in the diagram). Conversely, if the wafer is used for electro-mechanical actuation of the membrane (as in Chapter 5), then the GaAs substrate, beneath the sacrificial AlGaAs layer, needs also to be doped and reached by etching. Finally, a Ni:Au contact layer can be deposited on the doped layer using evaporation. Nickel is used as it offers superior adhesion to the GaAs surface, while gold is a better conductor. Solid Ni is first heated through high-resistance metallic coils until it evaporates. This allows deposition of Ni on top of the cooler sample, typically to a thickness of about 20 nm. Then about 200 nm of Au is deposited on top of the Ni layer in the same manner. This results in the entire surface of the wafer being covered in the metal contact. However, as the resist is removed afterwards with acetone, the contact remains only on the desired doped layer of the wafer. The whole procedure is then repeated with a different hard mask in order to deposit a

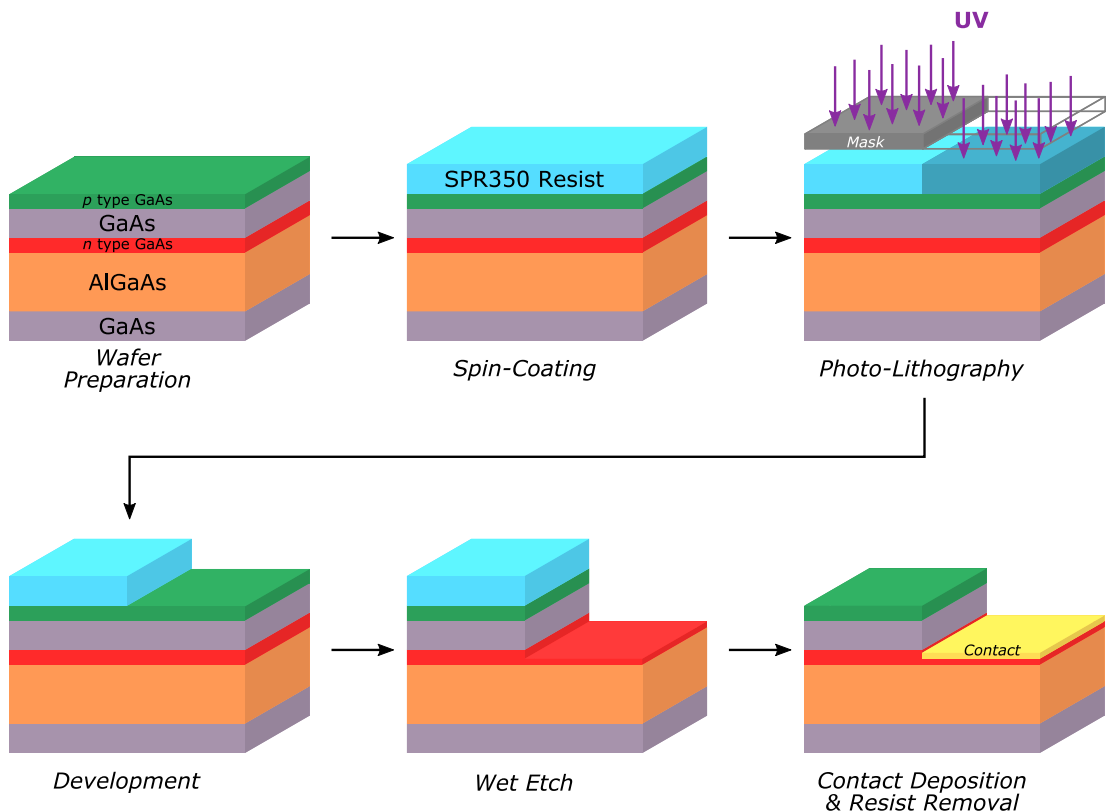


**Figure 3.15:** Schematic diagram of the fabrication process for diodes. SPR350 resist is spin-coated onto a cleaved and cleaned doped GaAs wafer with embedded QDs. A contact pattern is then transferred onto the resist using a hard mask and ultraviolet light. The exposed areas are removed using MF26a developer. The wafer is then etched with the resist as a mask by soaking it in sulphuric acid until the  $n$  contacting layer is reached. Finally, a Ni:Au contact layer is deposited and the resist is removed with acetone.

second contact, this time on the top  $p$ -type layer. In this case the wet etch is not necessary as the  $p$ -type layer is the surface of the wafer.

An electrical sample prepared in this way is then mounted with gold epoxy to either a 12-pin TO-5 header for use in a flow cryostat, or a 20-pin ceramic chip carrier for use in a bath cryostat (see Section 3.3.1). The electrical connections between the wafer and the mount are then made using a gold wire ball bonder. This technique involves feeding a thin, approximately  $15\ \mu\text{m}$  diameter, gold wire through a capillary tool and heating it by the application of electrical current. This causes the wire to melt at its tip forming a ball due to surface tension. The capillary is then pressed down onto the sample's contact and as the gold solidifies it forms a weld with the sample. The wire is then passed through the capillary until enough length is achieved to reach the contact on the mount, and the procedure is repeated. This time a weld is created by bending the wire as it is pressed down onto the holder's contact. Due to the increased resistance in the defect, the heat dissipation increases melting the bent area of the wire, forming a weld with the mount as it solidifies. The wire is then cut behind the second weld, and the process can be repeated to create more connections.

## 3.3 Optical Device Characterisation

### 3.3.1 Cryogenic Measurements

The great majority of the experiments reported in this thesis have been performed on samples held at a temperature of approximately 5 K in cryostats cooled by liquid helium ( $^4\text{He}$ ). While the temperature of liquid helium is 4.2 K, the samples are never in direct contact with it, and hence the assumption of slightly higher sample temperature. Two types of cryogenic systems have been used depending on the mode of cooling: continuous flow and bath cryostats. Both types, together with their corresponding advantages and disadvantages, are briefly described below.

### Continuous Flow Cryostat

In a continuous flow cryostat, the sample is mounted on top of a copper cold finger within a vacuum chamber. The cold finger provides a thermal contact between the sample and the heat exchanger outside the vacuum chamber. Liquid helium is pumped continuously through the heat exchanger to cool the sample down to a temperature of  $\sim 5$  K. The micro-photo-luminescence ( $\mu$ -PL) setup (discussed later and presented in Figure 3.19) is positioned on a bench above the cryostat, and the glass window on the top of the chamber allows optical access to the sample. The cryostat is located on top of a translation stage that enables coarse adjustments to the position of the sample in the  $X$  and  $Y$  directions. The optical setup is used to control focus ( $Z$  direction) and fine-tune the sample position. A schematic diagram of the continuous flow cryostat is shown in Figure 3.16.

The main advantage of this system is that samples can be exchanged rapidly. Mounting a new sample in the cryostat, evacuating the chamber and cooling it down can all take less than 4 hours. However, due to the continuous pumping of liquid helium through the cryostat, mechanical vibrations can be a major problem, especially for measurements requiring long timescales and hence long positional stability, such as the HBT experiment. In addition, due to safety and environmental concerns, the liquid helium flow is stopped overnight and during weekends, causing the sample to be cooled down to  $\sim 5$  K and then warmed up to room temperature many times. This thermal cycling has been found to cause deterioration of some photonic structures, especially the electro-mechanical devices (reported in Chapters 5 and 6). Despite these disadvantages, the continuous flow cryostat is a good choice for sample characterisation and spectral measurements that can be performed on shorter timescales (such as those presented in Chapter 4), due to its relatively simple and rapid operation.

### Bath Cryostat

The main advantages of a bath cryostat over a continuous flow cryostat are its positional and thermal stability. As the sample (located inside an evacuated insert) is immersed in a dewar containing liquid helium, no pumping is required. The dewar is also positioned on a vibrational damping platform, which

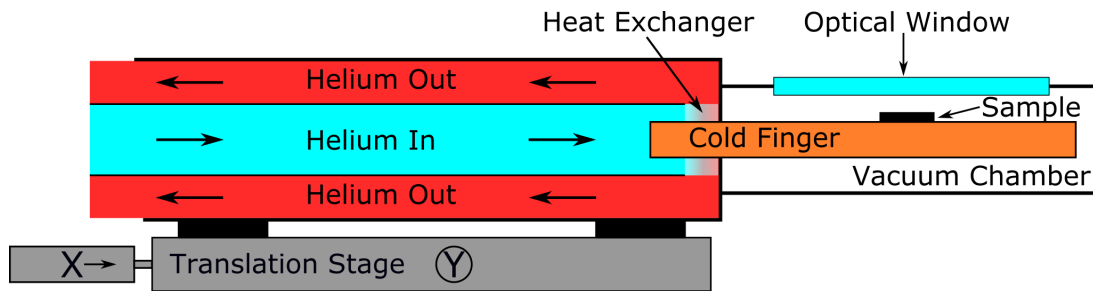


**Figure 3.16:** Schematic diagram of a continuous flow cryostat. The microphotoluminescence system shown in Figure 3.19 is positioned on a bench above the cryostat.

keeps any mechanical vibrations to a minimum, thereby providing a long term positional stability, often lasting days. The sample is also kept at a constant temperature of  $\sim 5$  K for weeks and even months. If the dewar is refilled with liquid helium fortnightly, there is no need for the sample to be warmed up to room temperature until all measurements are complete. This is why a bath cryostat provides ideal conditions for second-order correlation measurements (discussed in Section 3.3.3) and experiments on the electro-mechanical devices. On the other hand, the mounting of the sample in the bath cryostat is much more complicated, and hence can take much longer, than that for the continuous flow system. The schematic diagram of the bath cryostat is shown in Figure 3.17.

The sample is mounted in a chip carrier, which itself is attached to the top of the piezoelectric translation stage, which allows fine positioning and focus of the sample. This structure together with an aspheric objective lens and an achromatic doublet are installed in a cage system inside the insert tube. The two lenses positioned in a  $4f$  configuration increase the scanning range of the microscope without compromising image quality [91]. Electrical leads are fed from the top to the very bottom of the insert to enable both the control of the piezoelectric positioner and the electrical properties of the sample. The insert tube is evacuated and a little helium gas is fed inside it in order to achieve better heat transfer between the sample and the liquid helium outside the insert. The glass window on top of the tube allows optical access to the sample. The optical measurement system shown in Figure 3.19 is mounted on a breadboard directly on top of the dewar.

Exchanging the sample involves removing the  $\mu$ -PL setup from the top of

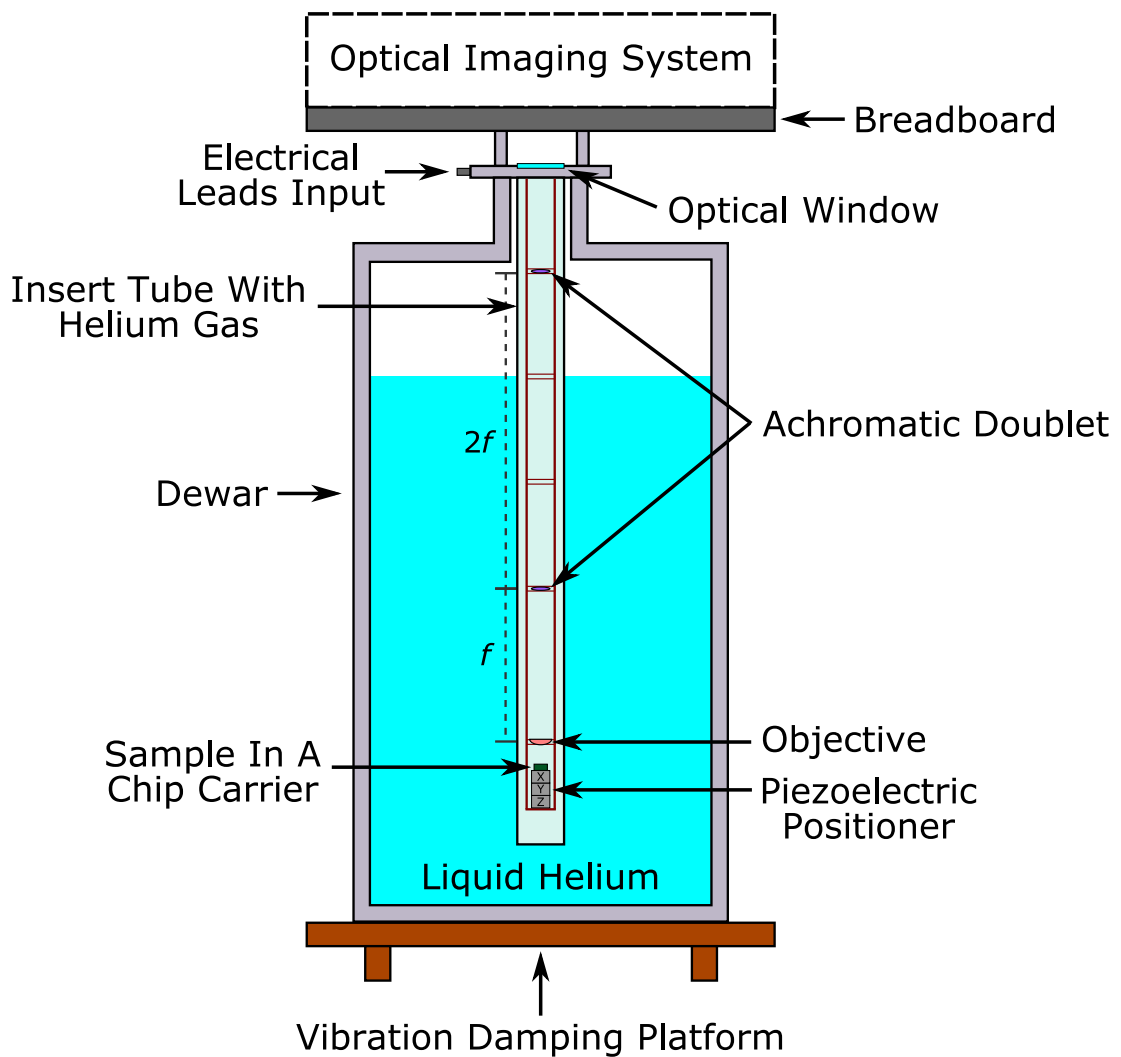


**Figure 3.17:** Schematic diagram of a liquid helium bath cryostat. The micro-photoluminescence system shown in Figure 3.19 is mounted on the top of the dewar as indicated.

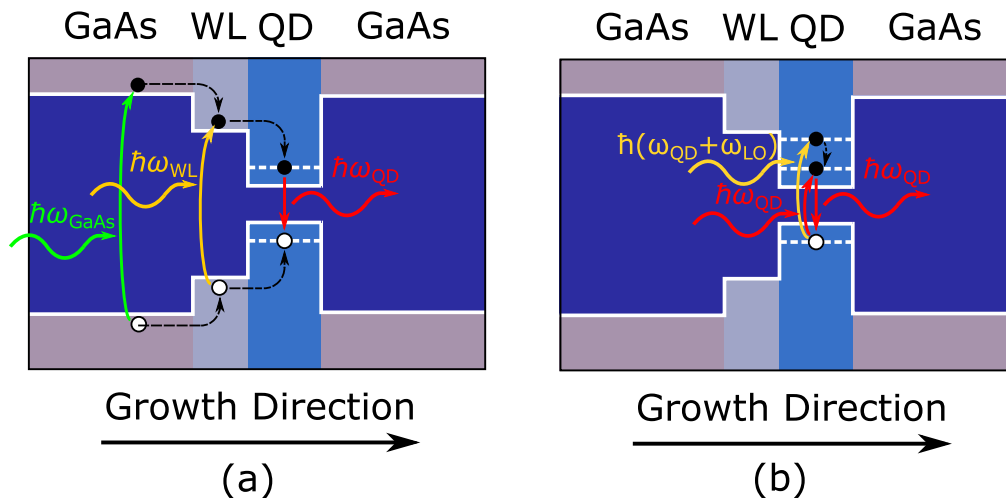


**Figure 3.18:** Schematic diagram of (a) non-resonant, and (b) quasi-resonant and resonant quantum dot excitation methods.

the dewar and taking out the insert tube. The apparatus then needs to be allowed to warm up to room temperature before the chip carrier can be detached from the piezoelectric positioner and up to 14 electrical contacts from the sample. This is a very delicate task, which often leads to necessary repairs of various parts of the system. Moving the imaging system can also result in misalignment, which then requires further adjustments to be made. The entire process can last several days.

### 3.3.2 Micro-Photoluminescence Spectroscopy

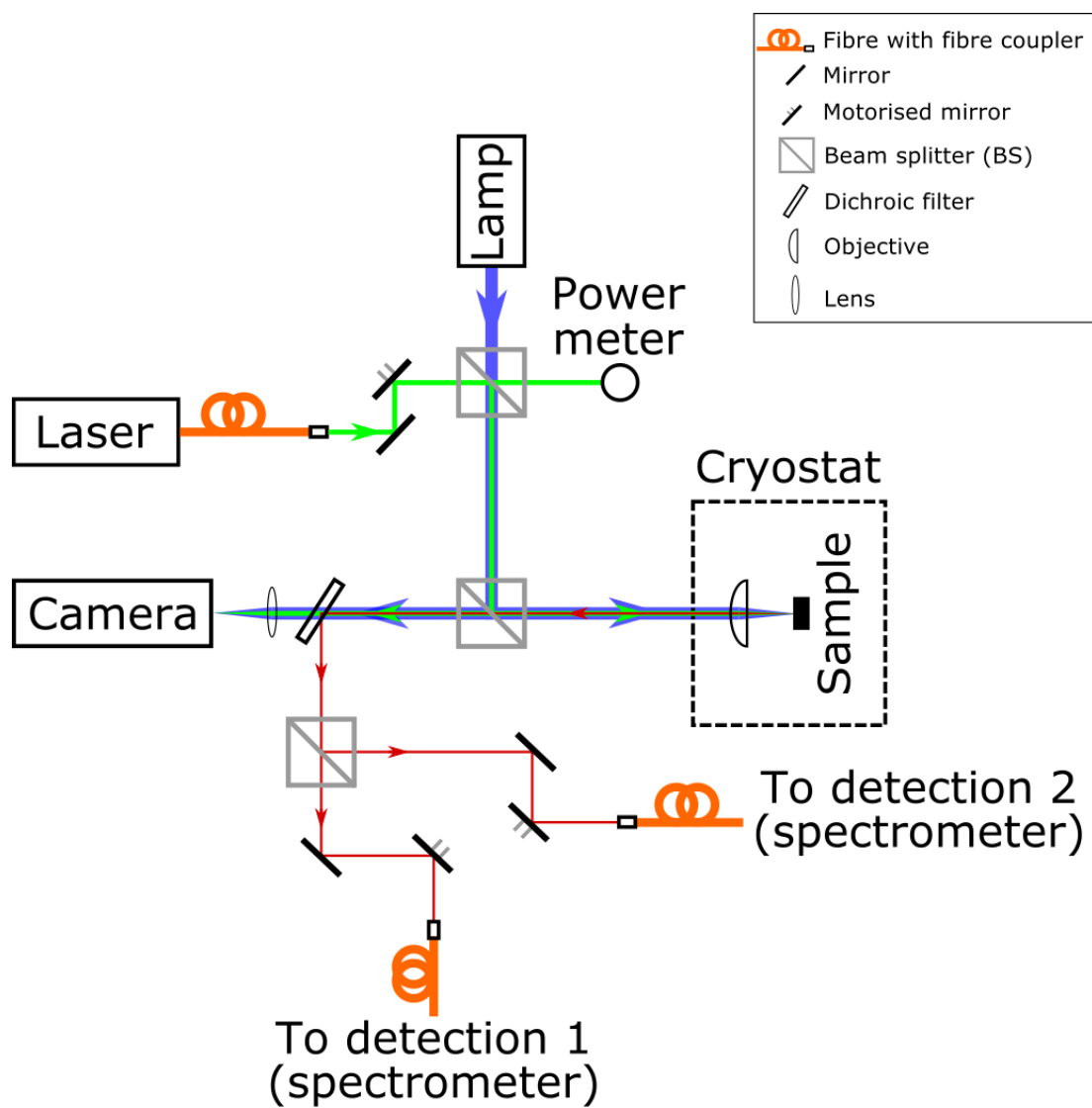
Quantum dots can be made to emit single photons by means of electrical (electro-luminescence) or optical (photo-luminescence) excitation [92]. All the experiments reported in this thesis have been performed using the latter. Photo-luminescence (PL) is the processes of delivering enough energy in the form of light to the semiconductor in order to promote electrons to the conduction band, thereby creating electron-hole pairs, which can then recombine emitting photons. Analysis of the light emitted from a QD during the radiative recombination of the electron-hole pair can reveal information about its properties, such as energy level structure and coherence (see Sections 2.1.1,2.1.2).

Figure 3.18 presents three distinct optical excitation schemes that exist for QDs: non-resonant, quasi-resonant, and resonant. Two different non-resonant QD excitation processes can be used [see Figure 3.18(a)]. One involves exciting

the QDs with light of energy equal to or larger than the band gap of the wetting layer (WL) but smaller than the GaAs band gap. The other approach is to supply light of energy equal to or larger than the GaAs band gap. An electron-hole pair created in this way will either emit a photon at the WL or GaAs band gap energies correspondingly, or will relax to the lower energy level of the QD, where it will be captured by the 3D potential confinement. The non-radiative relaxation processes that take place are carrier scattering and phonon interactions [93]. These occur on the timescale of a few pico-seconds, and they remove any coherence between the excitation source and photons emitted by the QD.

The quasi-resonant and resonant excitation schemes are illustrated in Figure 3.18(b). The quasi-resonant process involves exciting QDs with an energy equal to either the p-like first excited state of the QD [94] or to a longitudinal optical (LO) phonon-assisted transition [95, 96]. An exciton in QD's first excited state will decay to the ground state (s-like) within a few tens of pico-seconds. The LO phonon excitation scheme requires for the light of energy equal to the sum of the QD and LO phonon energies to be absorbed, generating a ground-state exciton within the QD and an LO phonon. By contrast, resonant excitation directly drives the QD ground-state transition at the Rabi frequency [97, 98]. The main difficulty in realising quasi-resonant or resonant PL measurements is that the photons emitted by the QD maintain some degree of coherence with the excitation source due to relatively few non-radiative relaxation processes being involved. In order to be able to distinguish between the excitation and emission photons experimentally the sample and/or setup designs require careful arrangement [99].

All the experiments undertaken for this thesis have used non-resonant QD excitation schemes. The above GaAs band gap excitation method was achieved through a He:Ne laser emitting at 632.8 nm, while for the WL excitation scheme a Ti:Sapphire continuous-wave laser with a tunable emission wavelength of 800 – 860 nm was used. A typical spatially selective micro-PL ( $\mu$ -PL) setup that has been used for most of the experiments reported in this thesis is presented in Figure 3.19. Two key attributes of this arrangement that are necessary for most of the experiments presented in the following chapters are the ability to excite and collect light from small defined areas of the sample, and to be able to do so selectively so that the two paths are independent from



**Figure 3.19:** Schematic diagram of a spatially selective micro-photoluminescence experimental setup with two optical collection paths (marked in red). The excitation path is shown in green, while the white light illumination beam is marked in blue.

each other. This allows excitation of one part of the device and collection from another for the measurements of the transmissivity of the photons emitted by QDs through the integrated optical devices, such as waveguides (in Chapter 5) and filters (in Chapter 4).

The excitation laser is fed to the  $\mu$ -PL setup through a single-mode optical fibre, which is then coupled out of the fibre in order to be directed onto the sample using a system of mirrors and beam splitters, as shown. It is then focused to a spot of  $\sim 2 \mu\text{m}$  in diameter on the sample using an objective lens. In the bath cryostat configuration that lens is positioned inside the cryostat  $\sim 6 \text{ mm}$  above the sample, while in the flow cryostat the Mitutoyo near-infrared objective (NA= 0.42) is situated on top of the breadboard with the rest of the imaging system and remains at room temperature during the optical measurements. The first beam splitter incorporates a power meter and a white light source (lamp), in order to monitor the excitation power and illuminate the sample inside the cryostat for imaging, respectively. The purpose of the second beam splitter is to separate the excitation laser from the QD PL signal, so that they are independent from each other. The dichroic filter behind the second beam splitter lets through shorter wavelengths, such as those from the white light source and the excitation laser reflected from the sample, so that these can be observed with the camera. The longer, infrared signal emitted by the QDs are reflected by the filter and directed onto another beam splitter. This enables PL signal collection from two different areas of the sample at the same time. The two collection paths are controlled through their own two mirrors and are coupled into separate single-mode fibres for detection. The signal from each of the collection paths is then passed to its own 0.75 m Princeton Instruments (SP2750i) spectrometer, as shown. The dispersed signal is either directed onto a PyLoN nitrogen-cooled coupled charged device (CCD) for spectral measurements or filtered through a side exit and passed onto a Thorlabs silicon avalanche photo-diode (APD) for time-correlated single photon counting (TCSPC) experiments [discussed below]. The motorised mirrors in each of the three optical paths are used to control the position of the excitation and collection spots on the sample via a computer. They also enable automated raster scanning of a defined area of the sample in order to create PL maps of the measured photonic device (used in Chapter 5). Such maps are useful to illustrate the propagation of QD emission around the sample.

### 3.3.3 Time-Correlated Single Photon Counting

The spectral measurements of the PL signal allow identification of the transition energies of optically active excitonic states within QDs. However, they are unable to provide information about photon statistics of the emitted light. Many applications of quantum optics require a single photon source, which will emit only one photon in a well-defined interval. This differs from, for example, laser sources, which emit photons at random intervals, and thermal sources, which emit photons in bunches. The second-order correlation function,  $g^{(2)}(\tau)$ , can be used to identify light sources as anti-bunched, coherent (random) and bunched [100]. It can be measured using a Hanbury Brown and Twiss (HBT) experiment presented schematically in Figure 3.20(a). In this procedure, the investigated light is passed through a 50:50 beam splitter and each resulting path is directed to an APD. When a photon arrives at a detector it sends an electrical pulse to the single photon counting module (SPCM). Detector D1 triggers the SPCM to start counting the delay time,  $\tau$ , at time  $t$  until detector D2 stops the count at time  $(t + \tau)$  as it registers the arrival of a second photon at a time  $\tau$  later. Many such events (coincidence counts) are accumulated by the SPCM, which then produces a histogram of the number of events recorded depending on the elapsed time  $\tau$  between the pulses arriving at D1 and D2. The second-order correlation function for this measurement system is given by:

$$g^{(2)}(\tau) = \frac{\langle n_1(t)n_2(t + \tau) \rangle}{\langle n_1(t) \rangle \langle n_2(t + \tau) \rangle}, \quad (3.1)$$

where  $n_i(t)$  denotes the number of counts registered by detector  $i$  at time  $t$ , and the angled brackets indicate time-averaged values. Clearly,  $g^{(2)}(t, \tau) \equiv g^{(2)}(\tau)$  is independent of the starting time  $t$ .

Anti-bunched light sources emit single photons at long, defined time intervals. When one photon enters the beam splitter it will either travel to D1 or D2 with equal probability. If it is recorded at D1 the probability of detecting a photon at the same time ( $\tau = 0$ ) at D2 is zero, as only one photon is available at a time. This means the SPCM will not register any coincidence counts. At longer timescales, the second photon will have a 50% probability of arriving at D2. If it arrives at D2 the timer is stopped and the SPCM records an

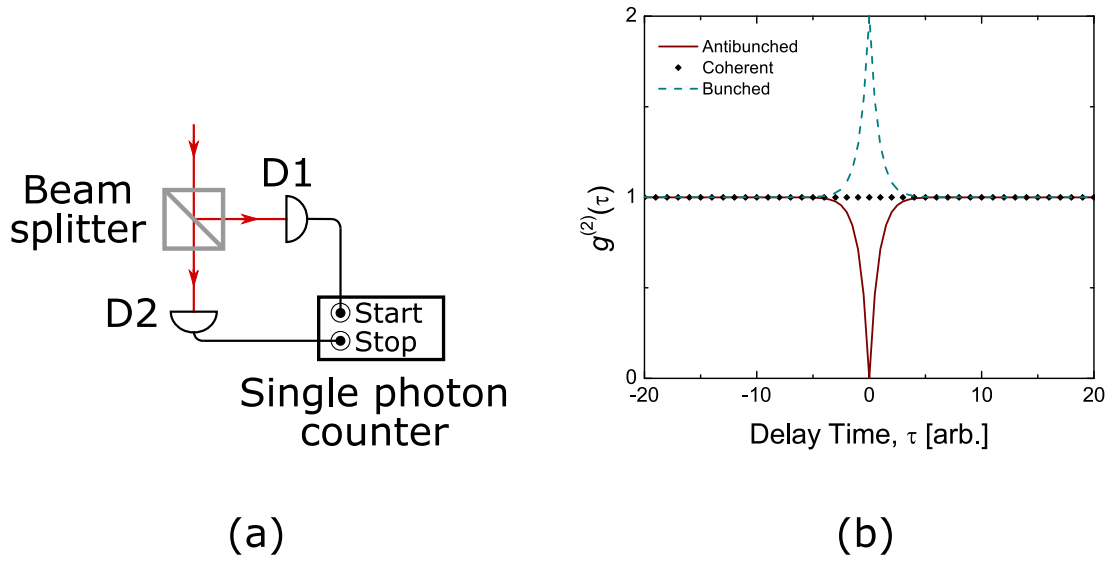


**Figure 3.20:** (a) Schematic diagram of the experimental arrangement for the Hanbury Brown and Twiss measurement. (b) Typical  $g^{(2)}(\tau)$  results for an antibunched (solid line), a coherent (diamonds), and a bunched (dashed line) light source.

event. If it arrives at D1 nothing happens and the timer continues running until another photon strikes D2. Therefore, for anti-bunched (single photon) sources  $g^{(2)}(0) = 0$ , and at long timescales  $g^{(2)}(\tau) = 1$ .

Coherent light sources on the other hand emit photons at random time intervals. Hence, the probability of detecting a photon at D2 is independent of  $\tau$  giving  $g^{(2)}(\tau) = 1$  for any value of  $\tau$ . Finally, and by contrast, bunched sources emit photons in batches. Therefore, if one photon is detected there is a higher probability of detecting another one at shorter rather than longer time scales. This leads to  $g^{(2)}(\tau) > 1$  for  $\tau$  near zero and  $g^{(2)}(\tau) = 1$  for larger  $\tau$ . Thermal light possesses the highest photon correlations of any naturally occurring light sources with  $g^{(2)}(\tau) = 2$  [101]. All classical sources of light, including thermal sources, are bunched. Anti-bunching is only possible for quantum sources. A typical result of a second-order correlation measurement for each light source classification is presented in Figure 3.20(b).

The histogram obtained from the accumulated HBT measurements can be fitted with the function  $g^{(2)}(\tau) = 1 - [1 - g^{(2)}(0)]e^{-|\tau|/\tau_d}$ , where  $\tau_d$  is the lifetime of the exciton (*i.e.*, the source of the photons). In practice,  $g^{(2)}(0)$  never reaches zero for anti-bunched light sources mainly due to the response time of the detectors, which is typically of the order of 400 ps. This effectively smooths the

results for very short timescales. However, this measurement inaccuracy can be removed from the data by deconvolving the fit to the experimental results with the known characteristics of the detection system (as demonstrated in Figure 5.15).

## 3.4 Computational Methods

The two main types of computational methods used to design the GaAs-based devices reported in this thesis are electromagnetic and electro-mechanical simulations. The former were used to investigate the propagation of QD emission through photonic structures, such as waveguides (in Chapter 5) and photonic filters (in Chapter 4), while the latter were used to study the behaviour of mechanical devices, such as cantilevers (in Chapter 5), metal rail systems and comb-drive actuators (in Chapter 6), upon the introduction of a capacitive force to the system. Both of the modelling methods are briefly outlined below.

### 3.4.1 Electromagnetic Simulations

The electromagnetic simulations solve Maxwell's equations in order to model the propagation of light around photonic structures. Two distinct computational techniques were used for this purpose in this thesis: time and frequency domain methods.

#### Finite-Difference Time-Domain

The time-domain approach investigates the field evolution within a photonic structure in time. Thus, the time-dependent Maxwell's equations:

$$\nabla \times \mathbf{E} = -\frac{\partial \mathbf{B}}{\partial t}, \quad (3.2)$$

$$\nabla \times \mathbf{H} = \mathbf{J} + \frac{\partial \mathbf{D}}{\partial t}, \quad (3.3)$$

are solved directly at finite time intervals, together with the remaining time-independent Maxwell's equations:

$$\nabla \cdot \mathbf{D} = \rho, \quad (3.4)$$

$$\nabla \cdot \mathbf{B} = 0, \quad (3.5)$$

where  $\mathbf{E}$ ,  $\mathbf{H}$  are the electric and magnetic fields,  $\mathbf{D}$ ,  $\mathbf{B}$  are the electric displacement and magnetic induction fields with  $\mathbf{D} = \epsilon_0 \epsilon_r \mathbf{E}$  and  $\mathbf{B} = \mu_0 \mu_r \mathbf{H}$  (where  $\epsilon_0$  and  $\mu_0$  are respectively the dielectric permittivity and permeability of free space, and  $\epsilon_r$  and  $\mu_r$  are respectively the relative permittivity and permeability of the medium), and  $\rho$ ,  $\mathbf{J}$  are the free electric charge and current densities.

Central to the finite-difference time-domain (FDTD) method is the device structure, which is represented as a dielectric map,  $\epsilon_r(\mathbf{r})$ , and a light source. These are defined within a simulation domain, which is then divided into small cubic cells of size  $\Delta \mathbf{r}$ . The device shape is then mapped onto this computational voxel array, known as a Yee lattice, to give  $\epsilon_r(\Delta \mathbf{r})$ , as illustrated in Figure 3.21. During the modelling the electromagnetic fields are propagated from the light source at time  $t = 0$  through the Yee lattice in discrete time steps,  $\Delta t$ . The electric fields are evaluated along the edges of each voxel and the magnetic fields are defined on the faces. A single cubic cell (voxel) of the Yee lattice is shown schematically in Figure 3.22. The simulation can end either at the defined maximum time limit,  $T$ , or a minimum energy threshold remaining within the simulation domain [102]. Various flux monitors can be placed throughout the simulation domain in order to record the propagation of light at different positions within the structure. The accuracy of the simulations will obviously depend on the size of the voxels. The smaller the computational unit is made, the higher the accuracy of the mapped device structure and the calculations, but the larger the computer power and time required. This trade-off also holds for the monitors that record the data. When setting up simulations care must be taken not to mismatch a high-accuracy simulation with low-resolution monitors or vice versa. The overall size of the simulation domain, which is mainly determined by the size of the photonic structure of interest, can be the defining factor for the maximum possible computational accuracy that can be reached for a given system.

The time-domain method has been employed in the work reported in this thesis when the temporal response of a photonic device is of interest, for example, for the investigation of light transmission through photonic crystal filters and the resonance decay times within them (in Chapter 4). These simulations have been performed by myself using a commercial-grade FDTD software: Lu-

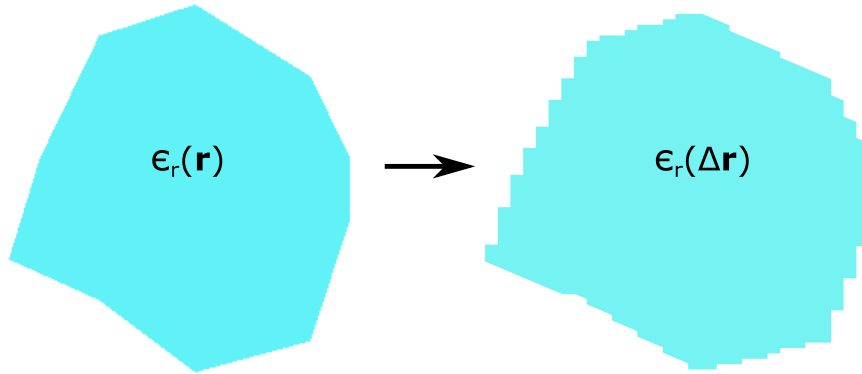


**Figure 3.21:** Schematic diagram illustrating an arbitrary dielectric map  $\epsilon_r(\mathbf{r})$  and its equivalent when mapped onto the Yee lattice to produce  $\epsilon_r(\Delta\mathbf{r})$ .

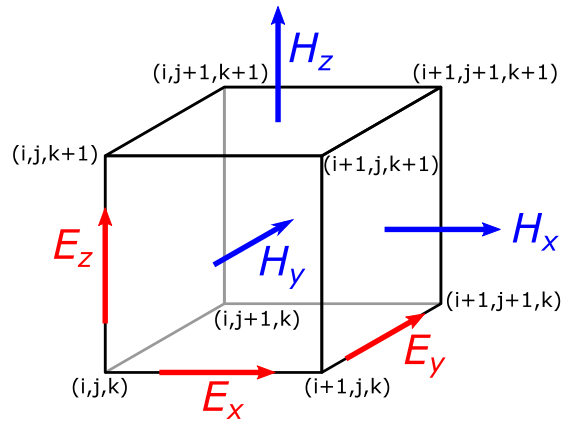


**Figure 3.22:** Schematic diagram of a single voxel of the Yee lattice used for calculating the electromagnetic fields in the FDTD simulations. The electric fields are calculated along the edges, while the magnetic fields are calculated normal to the faces.

merical FDTD Solutions [103].

An example of the FDTD model simulated using the above mentioned software is presented in Figure 3.23, where the behaviour of light with time in a nanobeam waveguide with a quantum dot (*i.e.*, light source) located in its centre is under investigation. Figure 3.23(a) illustrates the 3D model with the waveguide shown in blue, the dipole source indicated by an arrow, the computational domain filled with air shown in orange, and two data monitors marked in yellow. The  $z$ -normal monitor located above the waveguide is a so-called time monitor, as it records electro-magnetic fields as a function of time. Two data sets from this monitor are presented in Figure 3.23(b). At time  $t = 0$  the electro-magnetic fields are accumulated in the centre of the waveguide as the dipole is turned on. Light emitted by the dipole travels in both directions,  $-y$  and  $y$ , along the waveguide, and hence at time  $t = 11$  fs the total power of the source is now split between two positions, as shown. The  $y$ -normal monitor located by the right end of the waveguide is used to record the electro-magnetic fields propagating along the waveguide as a function of wavelength. The results are shown in Figure 3.23(c). The transmissivity is defined as a percentage of the total dipole intensity, and hence can be no greater than 50% since half of the light has travelled in the opposite direction along the waveguide. In a large wavelength range of 200 nm the efficiency of light propagation changes by only  $\sim 10\%$ .

### Frequency-Domain Eigenmode Solver

The frequency-domain approach, on the other hand, works by finding the frequency modes,  $\omega$ , of a periodic structure, from which the associated electric and magnetic fields can be derived. Various assumptions need to be made in order to derive an eigenvalue equation based on frequency from the two time-dependent Maxwell's equations in Equations (3.2) and (3.3). These include: no sources of free charge or free current present in the system ( $\rho = 0, J = 0$ ), the materials under investigation being isotropic and non-dispersive (so that  $\epsilon_r$  depends only on the position,  $\mathbf{r}(x, y, z)$ , within the system), as well as transparent (so that  $\epsilon_r(\mathbf{r})$  is real and positive), and finally  $\mu_r \sim 1$  for most materials of interest [47]. In general  $\mathbf{E}$  and  $\mathbf{H}$  are functions of both space and time, but because Maxwell's equations are linear we can separate these dependencies as

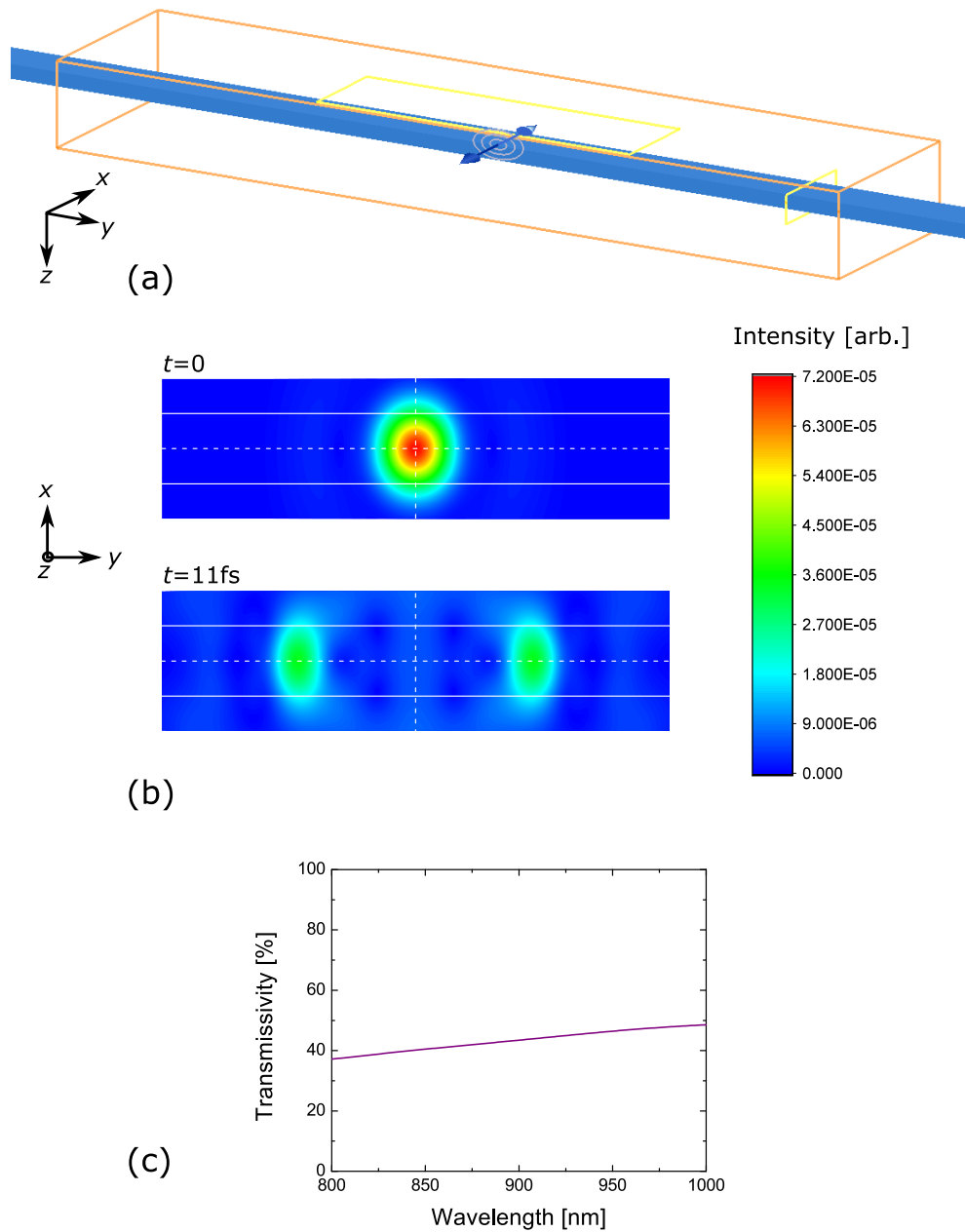


**Figure 3.23:** FDTD simulation of light propagation along a nanobeam waveguide performed using the Lumerical FDTD Solutions package. (a) 3D model showing the waveguide in blue, the computational domain in orange, the data monitors in yellow, and the dipole source in the centre of the waveguide as an arrow. (b) Results from the  $z$ -normal monitor, showing the electro-magnetic fields at the two times  $t = 0$  and  $t = 11\text{fs}$ . Edges of the waveguide are indicated by the continuous white lines, and the centres of symmetry by the dashed ones. (c) Results from the  $y$ -normal monitor, showing the total amount of light transmitted to the right end of the waveguide as a function of wavelength.

follows:  $\mathbf{E}(\mathbf{r}, t) = \mathbf{E}(\mathbf{r})e^{-i\omega t}$  and  $\mathbf{H}(\mathbf{r}, t) = \mathbf{H}(\mathbf{r})e^{-i\omega t}$  for monochromatic sources. With all these assumptions in place, Equations (3.2) and (3.3) become:

$$\nabla \times \mathbf{E}(\mathbf{r}) = i\omega\mu_0\mathbf{H}(\mathbf{r}), \quad (3.6)$$

$$\nabla \times \mathbf{H}(\mathbf{r}) = -i\omega\epsilon_0\epsilon_r(\mathbf{r})\mathbf{E}(\mathbf{r}). \quad (3.7)$$

Decoupling these equations by eliminating  $\mathbf{E}(\mathbf{r})$  from Equation (3.7) and using  $c = 1/\sqrt{\epsilon_0\mu_0}$ , where  $c$  is the speed of light in vacuum, we obtain the following eigenvalue equation:

$$\nabla \times \left( \frac{1}{\epsilon_r(\mathbf{r})} \nabla \times \mathbf{H}(\mathbf{r}) \right) = \left( \frac{\omega}{c} \right)^2 \mathbf{H}(\mathbf{r}). \quad (3.8)$$

The frequency-domain method of simulating electromagnetic problems involves solving the eigenvalue problem defined in Equation (3.8), and then finding the corresponding field  $\mathbf{E}(\mathbf{r})$  using Equation (3.7). The frequency-domain calculations require smaller simulation volumes and less time in comparison to time-domain methods, and are therefore less computationally intensive. This approach was hence used when the temporal response of the system was not under consideration, for example, for the coupling efficiency of light between two parallel waveguides in Chapter 5. These simulations were carried out with an open-source software: MIT Photonic Bands [104, 105], using a program written by Dr Rikki J. Coles.

### Transfer-Matrix Method

In addition to full 3D electromagnetic modelling in the two different domains described above, a simpler 1D method has also been used to model the propagation of light through a multilayer medium. In particular, this was essential for the analysis of the results reported in Chapter 5, where a cantilever is displaced downwards towards a substrate using electro-mechanical actuation. This movement causes changes to the optical interference pattern of light emitted from the device and that reflected from the substrate, thereby influencing the measurement from the waveguide attached to the cantilever. In principle, the whole system could be modelled using the FDTD method, but in practice the required size of the simulation meant that the model would be extremely

computationally intensive. Instead frequency domain simulations were performed on the waveguide system and a Transfer Matrix Method (TMM) was used to identify separately the changing optical interference pattern affecting measurements.

The TMM approach is based on the facts that the Maxwell's equations (3.2) and (3.3) imply that the tangential components of  $\mathbf{E}$  and  $\mathbf{H}$  are continuous across layer boundaries carrying zero current ( $\mathbf{J} = 0$ ), and the Maxwell's equations (3.4) and (3.5) imply that the normal components of  $\mathbf{D}$  and  $\mathbf{B}$  are continuous across layer boundaries carrying zero free charge ( $\rho = 0$ ). This, together with the known reflectance and transmittance coefficients between different material layers, can be used to calculate the total amount of light reflected from a multilayered medium, which takes into account any constructive or destructive interference between the reflected and transmitted rays within the system. The reflection,  $r$ , and transmission,  $t$ , coefficients between the incident layer (1), and the subsequent layer (2) are defined to be the ratios of the amplitudes of the complex electric field of the reflected and transmitted waves respectively, to that of the incident wave. They may be found using the following Fresnel equations [106]:

$$r_{\text{TE(TM)}} = \frac{n_1 \cos(\theta_{1(2)}) - n_2 \cos(\theta_{2(1)})}{n_1 \cos(\theta_{1(2)}) + n_2 \cos(\theta_{2(1)})}, \quad (3.9)$$

$$t_{\text{TE}} = 1 + r_{\text{TE}}, \quad (3.10)$$

$$t_{\text{TM}} = (1 + r_{\text{TM}}) \frac{\cos \theta_1}{\cos \theta_2}, \quad (3.11)$$

where TE and TM denote transverse electric (s-polarised) and transverse magnetic (p-polarised) waves respectively,  $n_1$  and  $n_2$  are the refractive indices of layers 1 and 2 respectively, and  $\theta_1$  and  $\theta_2$  are incident (reflection) and refraction angles respectively measured from normal of the boundary between the two layers (with  $n_1 \sin \theta_1 = n_2 \sin \theta_2$ ). The total transfer matrix for a light wave propagating through multiple layers is a multiplication of matrices describing the continuities of electromagnetic fields across each of the layer boundaries using Fresnel coefficients, and those defining the propagation of light through each of the media depending on their refractive indices, the thickness-

ses of the layers, and the wavelength of light propagating through the medium [107]. The reflection and transmission coefficient for the entire layered structure can then be derived from the total transfer matrix.

The TMM calculations were performed using an open-source programming language Python with its specialised TMM package developed by Steven Byrnes [108].

### 3.4.2 Electro-Mechanical Modelling

Part of the research reported in this thesis focuses on using so-called Micro-Electro-Mechanical Systems (MEMS) in order to control the optical properties of GaAs-based devices. This is an emerging field of interest to the applied quantum optics community. These systems combine electrostatics with mechanics, as parts of the devices are displaced mechanically on-chip upon the application of voltage between two terminals, which introduces a capacitive force between them. For this reason it is beneficial to use modelling tools that allow the simulation of the entire system, rather than to separate artificially the electrostatic and mechanical problems. That is why the electro-mechanical simulations were performed using a commercial-grade software: Comsol Multiphysics, which provides a specialized MEMS module [109] for exactly these purposes. The systems that integrate photonic devices with MEMS have been named MOEMS or NOEMS, Micro(Nano)-Opto-Electro-Mechanical Systems. However, no modelling tool is yet available that treats these structures as a whole integrated system. For this reason the electromagnetic simulations had to be done separately from the electro-mechanical modelling to analyse NOEMS.

Comsol Multiphysics is a user-friendly Finite-Element-Analysis (FEA) tool. It enables the modelling of complex systems that otherwise might be unsolvable due to the number of coupled differential equations that describe them. Once the 3D model is created, and various boundary conditions prescribed (such as terminals, voltages, displacements, materials) the model is divided into small sections (finite-elements). These are then described by linear equations instead, which give approximate solutions to the problem, and the final result is the sum of the solutions from all finite-elements within the model. The smaller the individual elements are made, the smaller the approximati-

ons. As usual, there is thus a trade-off between accuracy and the computer power and time needed to achieve it.

An example of a simulation set up for the electro-mechanical analysis of a cantilever (further discussed in Chapter 5) is illustrated in Figure 3.24. In this model the cantilever is positioned in a 3D simulation volume that is filled with air, as shown in Figure 3.24(a). The automatic non-uniform mesh of the computational finite-elements allows an increased resolution of the simulation at the interfaces and at the objects of interest, while decreasing it for those parts of the model that do not have significant influence over the final result. This is very advantageous as higher accuracy can be achieved for shorter simulation times. For example, the air volume has a coarser mesh than the cantilever, and the face of the simulation domain to which the cantilever is fixed has the finest mesh at the interface between them, which then gets coarser further away from it. The fixed end of the cantilever is defined through the prescribed zero displacement at its vertical short side where the cantilever meets with the face of the simulation domain (marked in red). The bottom face of the simulation volume is used as an electrical ground - plate of zero potential (marked in green), while the bottom face of the cantilever is used as an electrical terminal to which different potentials can be applied (marked in orange). By applying a voltage to the terminal a capacitive force between the cantilever and the bottom of the simulation domain is induced, which causes the cantilever to displace in the  $+z$  direction towards the ground. As the cantilever is fixed at one end to the side of the simulation domain the displacement will be largest at its free end and smallest (zero) at the other, as illustrated in Figure 3.24(b). The image shows the profiles of the cantilever at applied actuation voltages of 0 V and 7 V, as determined by the simulation.

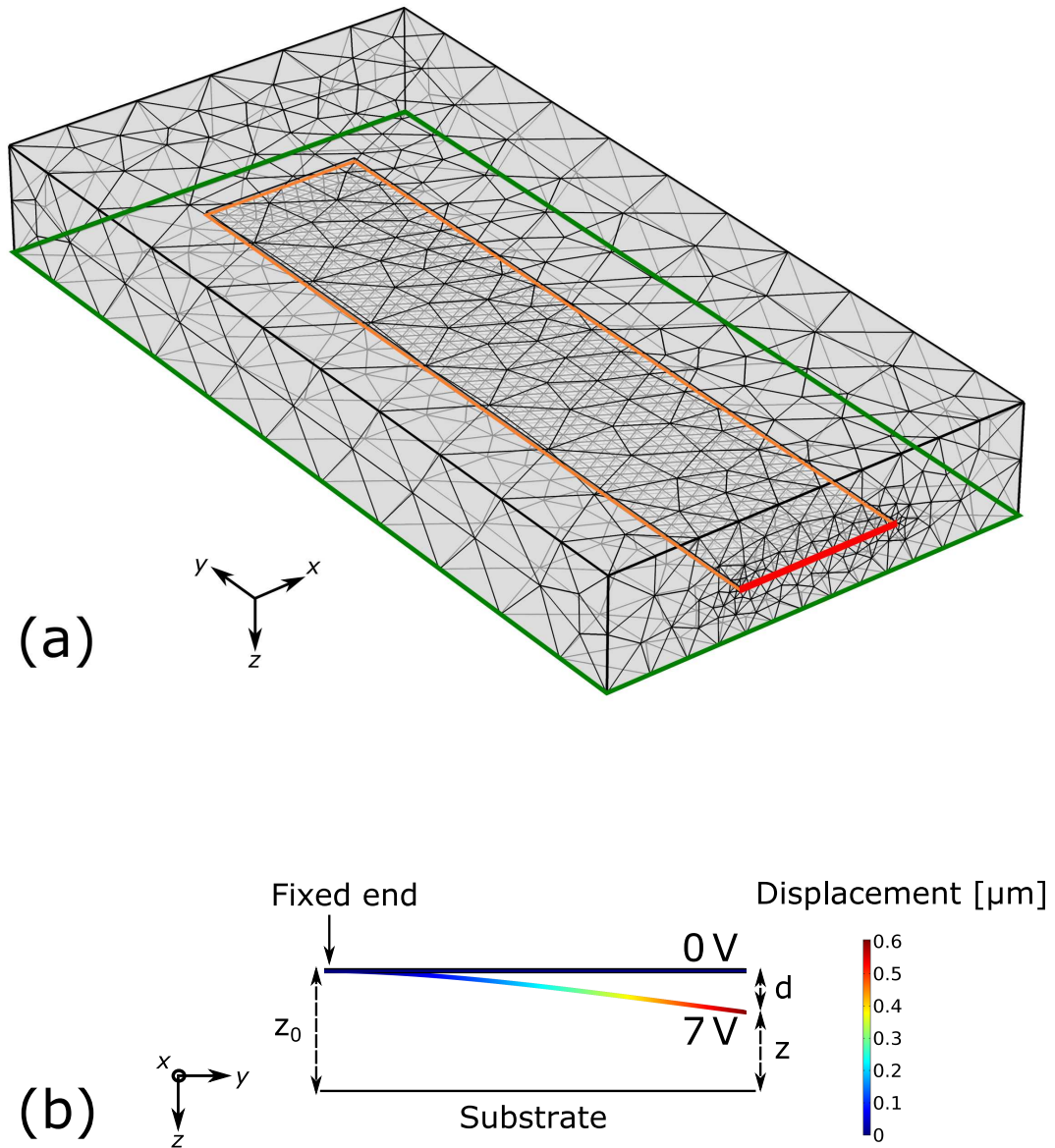


**Figure 3.24:** (a) 3D image of a meshed model created in Comsol Multiphysics software to study the electro-mechanical behaviour of a cantilever. The fixed face of the cantilever is marked in red, the bottom face of the cantilever used as a voltage terminal is marked in orange, and the bottom face of the simulation volume used as a ground terminal is marked in green. (b) Results from the simulation showing the displacement of the cantilever towards the ground terminal (substrate) at actuation voltages applied to it of 0 V and 7 V.



## Chapter 4

# Nanobeam Photonic Crystal Cavities for On-Chip Spectral Filtering and Cavity QED Applications

Nanobeam photonic crystal cavities (PhCCs) are of increasing interest to the quantum optical community as they are readily integrable with other on-chip photonic elements essential for QIP, such as nanobeam waveguides and beam splitters. In addition, these optical microcavities offer high  $Q$ -factors and low effective modal volumes,  $V_{\text{eff}}$ , [110] which means they are a highly suitable platform for cavity QED (cQED) studies (see Section 2.3) [111]. They can also be used as optical filters, and even as switches [112, 113]. Other semiconductor structures exist that can be used for similar purposes, such as whispering gallery resonators [114, 115], 2D PhCCs [116–119], 2D PhC heterostructures [120] and micropillars [41, 121]. However, these are typically not as straightforward to integrate with other circuit components.

On-chip filtering is now gaining greater significance as the realization of a fully integrated quantum optical circuit is becoming within our reach. The filtering in III-V optical circuits with embedded single photon sources is essential for non-resonant excitation techniques, which result in emission from a large number of semiconductor structures. As previously discussed in Section 3.1 the QDs studied in this thesis are grown epitaxially and form through self-

assembly. This implies that if such QDs are excited non-resonantly either through photo-luminescence or electro-luminescence the optical signal from the sample will consist of emission from many QDs, as well as potentially from the wetting layer and the GaAs itself [122]. For this reason, in order to be able to perform operations on single photons, any emissions from other QDs, the wetting layer and the GaAs need to be filtered out. Currently such filtering is mostly done externally by collecting the entire signal from the sample and then using a spectrometer to filter out the single QD emission. This filtering method was used, for example, for the second-order correlation measurements reported in Chapter 5. However, in order for quantum optical circuits to be fully integrated, such filtering needs to be performed on-chip [123, 124] together with all other necessary operations.

Most of the nanobeam PhCC studies reported in the literature so far are concerned with telecommunication wavelength operation [110, 112, 125–131], and hence are not compatible with the emission of the QDs studied in this thesis. Therefore, these structures had to be designed from scratch in order to match the emission from the available GaAs-based wafers used for the experiments reported here.

In this chapter the design, optimization and performance of nanobeam PhCCs is demonstrated through both modelling and experimental results. The chapter begins with a brief discussion of how the structures operate and how their performance is measured. It then goes on to demonstrate experimentally on-chip filtering of QD emission with a passband of  $\Delta\omega = 1 - 3$  nm. The expected trade-off of the device between a narrow passband and a high transmissivity is also explained and illustrated through experimental results. The chapter then goes on to discuss ways of minimising the spectral extent of the cavity mode (and hence of maximising the respective  $Q$ -factors) through slight alterations to the design of the structure.  $Q$ -factors of  $\sim 2800$  ( $\Delta\omega \approx 0.34$  nm) are achieved experimentally and further improvements are suggested, which are shown theoretically to achieve very high  $Q$ -factors of  $\sim 850,000$  ( $\Delta\omega \approx 1$  pm). The possibility of tuning the QD emission wavelength into resonance with the cavity mode using the quantum-confined Stark effect (QCSE), discussed in Section 2.1.3, for cQED applications is also examined experimentally. The chapter ends with a summary of the work achieved so far and offers recommendations for future directions of study in this area.

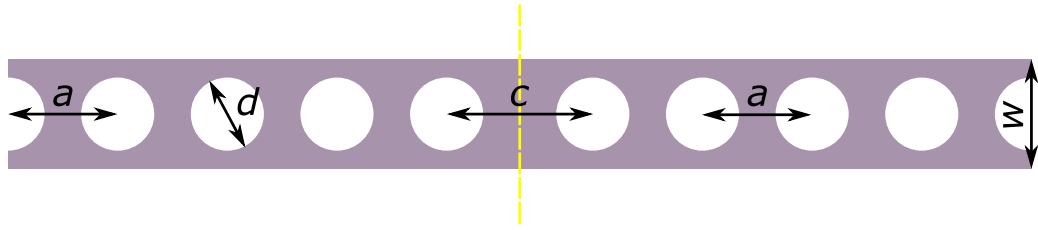


**Figure 4.1:** Schematic diagram of a nanobeam photonic crystal cavity created by increasing the distance between the two central air holes to be  $c > a$ , where  $a$  is the periodic distance between the remaining holes. The dashed yellow line indicates the centre of symmetry of the device.

## 4.1 Principles of Operation

Nanobeam PhC cavities are based on the 1D PhCCs discussed in Section 2.6 that are created through periodic positioning,  $a$ , of air holes of diameter,  $d$ , along a nanobeam waveguide (see Section 2.2.1), with width,  $w$ , and thickness,  $t$ . While the QD emission is confined in two dimensions inside the nanobeam waveguide by total internal reflection, the PhC structure provides the confinement in the remaining direction along the nanobeam waveguide for the parts of the light spectrum within its photonic band gap. By introducing a defect inside the PhC structure an optical cavity can be formed. This can be achieved in several different ways, of which the simplest is to adjust the distance between the two central holes of the PhC,  $c$ , leaving all the other parameters unchanged. Increasing or decreasing this dimension breaks the periodicity of the PhC, and hence creates an optical resonator between the two central holes, whilst ensuring the PhC structure (and hence its band gap) on either side of the cavity remains unaffected. A schematic diagram of such a nanobeam PhCC is presented in Figure 4.1.

As discussed previously in Section 2.3, the  $Q$ -factor is the figure of merit for optical microcavities as it is inversely proportional to the cavity's loss rate, which determines the full-width at half-maximum (FWHM),  $\Delta\omega$ , of the resonant peak of the cavity. The decay mechanisms of the nanobeam PhCC (neglecting absorption) are twofold. The light can either couple to the waveguide or radiate into the surrounding air. Therefore, the total loss rate of the

cavity can be expressed as follows [47]:

$$\frac{1}{Q} = \frac{1}{Q_w} + \frac{1}{Q_r}, \quad (4.1)$$

where  $Q_w$  and  $Q_r$  are the  $Q$ -factors associated with the waveguide and radiation losses respectively. The fraction of light,  $T$ , transmitted in resonance with the cavity mode through the resonator, as derived using coupled-mode theory, depends on both of these parameters through:

$$T = \left( \frac{Q_r}{Q_r + Q_w} \right)^2. \quad (4.2)$$

This means that in order to achieve near unity transmission (*i.e.*  $T \approx 100\%$ )  $Q_r$  needs to be much larger than  $Q_w$  (*i.e.*,  $Q_r \gg Q_w$ ). However, according to Equation 4.1, increasing  $Q_r$  will result in the total  $Q$ -factor of the resonator to be dominated by the lower  $Q_w$ . For this reason a trade-off between a good transmissivity through the cavity and a high  $Q$ -factor is expected in these structures.

The following section of this Chapter reports detailed studies of this phenomenon through both electromagnetic modelling and experimental measurements in the context of integrating narrow-band optical filters on a chip. The next Section 4.3 then explores ways of further optimizing the parameters  $Q_r$  and  $Q_w$  through resonator design in order to achieve higher  $Q$ -factors, both through modelling and experimentally. The possibility of tuning the QD emission wavelength using QCSE (see Section 2.1.3) into resonance with the cavity mode for cQED applications is also investigated, and some initial experimental results are reported.

## 4.2 On-Chip Spectral Filtering

### 4.2.1 Design Requirements

In a typical wafer used in this thesis (see Section 3.1.2) the QD emission wavelength is in the range of  $\sim 900 - 960$  nm, while that of the wetting layer is in the range of  $\sim 820 - 860$  nm. GaAs itself emits at around 815 nm. Therefore, a filter with a photonic band gap in the range of  $\sim 800 - 980$  nm and with a cavity

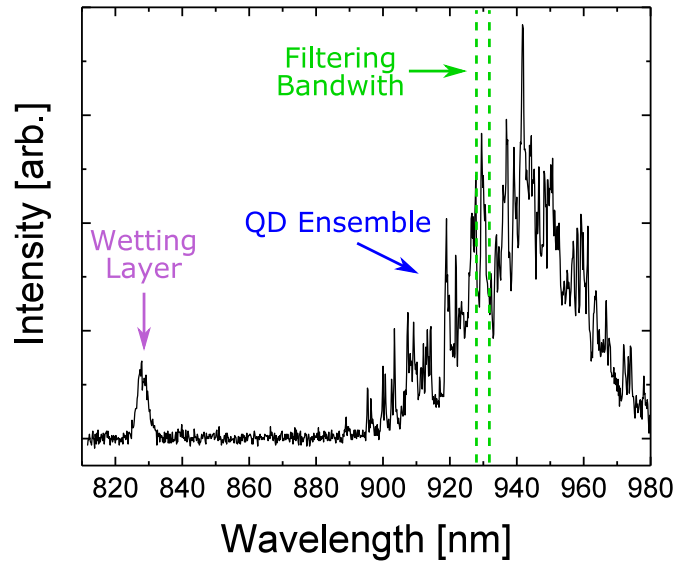


**Figure 4.2:** Spectrum from a typical GaAs wafer containing a high density of self-assembled InAs QDs, obtained using non-resonant photo-luminescence excitation. The two green dashed lines indicate the required filtering bandwidth.

mode at  $\sim 930$  nm (*i.e.*, the middle of the QD emission range) is required. This will lead to the transmission of only a small proportion of the QD emission spectrum (ideally a single QD) through a nanobeam PhC filter, while blocking a large range of other emissions from the wafer. The spectral response of a typical wafer containing a high density of QDs excited non-resonantly through photo-luminescence is shown in Figure 4.2. The two green dashed lines indicate the desired bandwidth of an on-chip optical filter.

#### 4.2.2 Modelling and Optimization of the Filter

There are many parameters of the nanobeam PhC filter that will affect its resonant mode wavelength and band gap, as well as its performance assessed in terms of  $Q$  and  $T$ . These are all the dimensions mentioned earlier:  $a$ ,  $d$ ,  $c$ ,  $w$ ,  $t$ , as well as the number of holes on either side of the cavity,  $n$  (as will be demonstrated later). The effects of these parameters are not independent from each other. For example, if  $a$  is altered, this will affect both the size and wavelength of the photonic band gap as well as the resonant mode wavelength. Therefore, designing a suitable device that fulfils all the filtering specifications outlined above often requires a computationally intensive parameter search. This is particularly challenging as most similar studies reported in the literature are

concerned with longer (telecommunication) wavelength filtering operation (at  $\sim 1500$  nm) [110, 125–127, 129–132]. Therefore, in order to perform a parameter optimization that allows one to find the set that fulfils all the specified design requirements, an initial set of dimensions was first chosen.

As the nanobeam PhC filter was to be made on a typical intrinsic GaAs wafer with a membrane thickness of 140 nm, this provided a fixed requirement for the thickness of the waveguide,  $t$ . Other dimensions chosen as a starting point were based on those used by Chen et al. [125]. These were:  $w_0 = 435$  nm,  $a_0 = 360$  nm,  $d_0 = 258$  nm, and  $c_0 = 503$  nm, where the subscript zero indicates an initial value. FDTD electromagnetic modelling (see Section 3.4.1) was then undertaken in order to determine the propagation of light within the structure. The results of these simulations for a nanobeam PhC filter with the above-mentioned dimensions and  $n = 3$  are shown in Figure 4.3(a). The graph indicates the amount of light with a wavelength in the range of 1000–1200 nm that will be transmitted through the filter from one end to the other. In this case the cavity mode is at  $\sim 1100$  nm, which is  $\sim 170$  nm longer than the target 930 nm. However, the width of the photonic band gap is sufficiently large for the defined filtering requirements.

In order to study systematically the effects of optimizing some of the dimensions of the filter a commonly used design criterion for the nanobeam PhCCs, called the filling fraction (FF) [112], is introduced. This is simply the ratio,  $f$ , of the area of each air hole to the area of the nanobeam waveguide over one PhC period:

$$f = \frac{\pi d^2}{4wa}. \quad (4.3)$$

Therefore, an obvious first step in the parameter optimization is to rescale all the parameters in the same way, so as to keep  $f$  fixed. A scaling factor of 0.8 was found to shift the cavity mode to the required wavelength while keeping the width of the photonic band unchanged matching all the design requirements. The transmissivity,  $T$ , remains at  $\sim 20\%$ . Further optimization of  $a$  and  $c$  then led to a maximization of  $T$  at a value of  $\sim 70\%$  at the required wavelength. The final parameters were as follows:  $t = 140$  nm,  $w = 350$  nm,  $d = 200$  nm,  $a = 263$  nm, and  $c = 413$  nm. The modelling results for several parameter sets used in the optimization, including the final one, are presented in Figure 4.3(b).

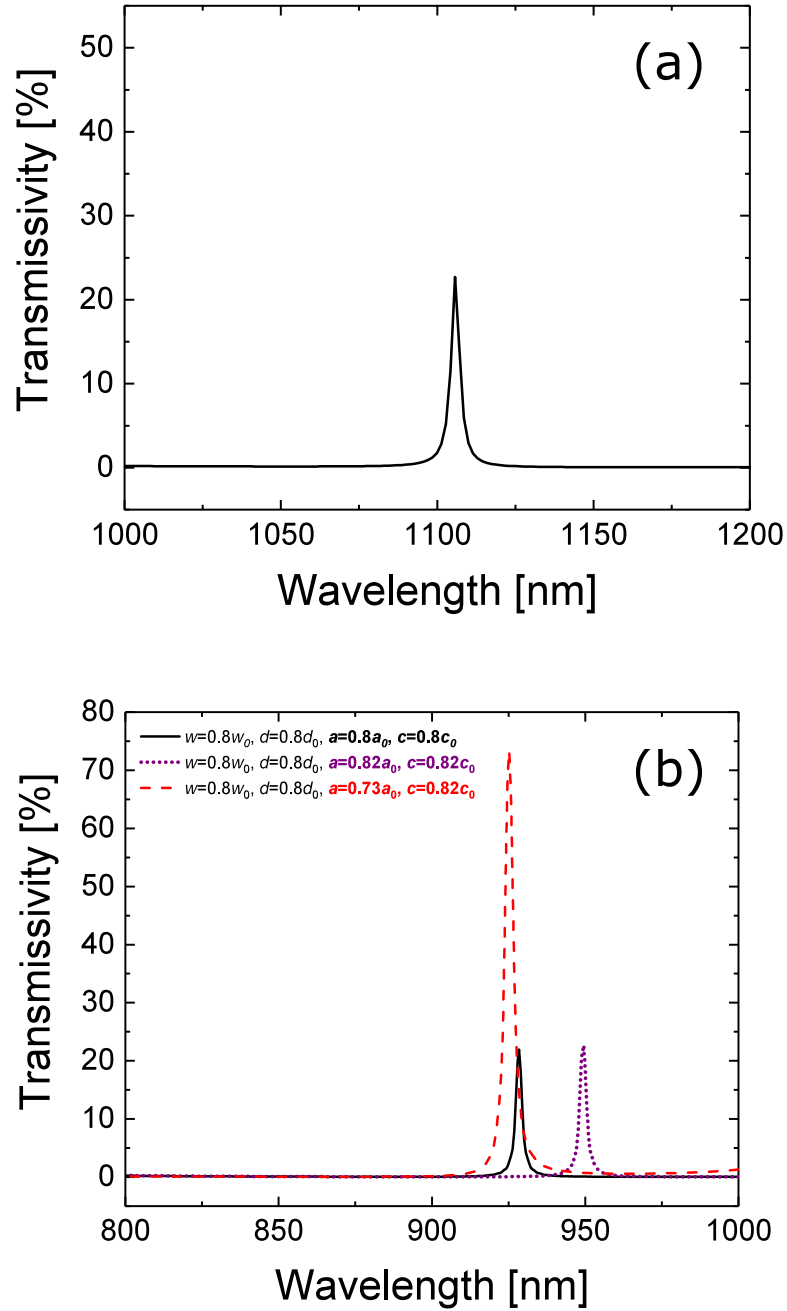


**Figure 4.3:** Simulation results showing the percentage of light with a wavelength range of 200 nm transmitted through nanobeam PhC filters with waveguide thickness  $t = 140$  nm, number of holes on each side of the cavity  $n = 3$ , and (a) other dimensions as chosen by Chen et al. [125], and (b) other dimensions rescaled with respect to the initial values.

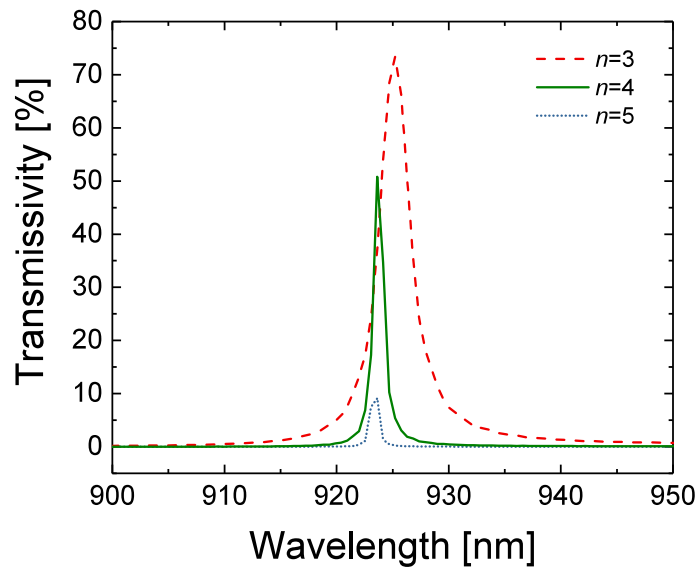


**Figure 4.4:** Simulation results showing the percentage of light with a wavelength range of 900–950 nm transmitted through nanobeam PhC filters with filling fraction,  $f$ , held constant, waveguide thickness  $t = 140$  nm, waveguide width  $w = 350$  nm, diameter of holes  $d = 200$  nm, period  $a = 263$  nm, cavity width  $c = 413$  nm and different number of holes on either side of the cavity  $n = 3, 4, 5$ .

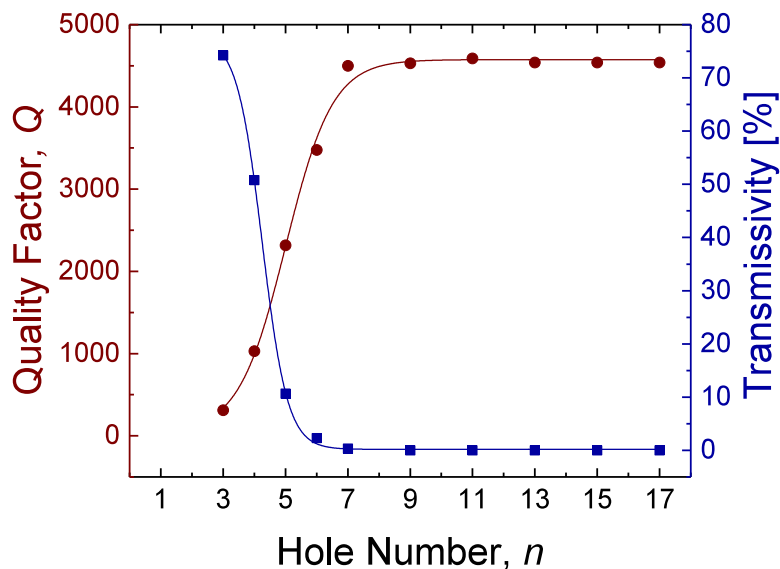


**Figure 4.5:** Simulation results for the designed filter showing how the quality factor of the cavity,  $Q$ , and the maximum transmissivity of light through the filter,  $T$ , vary with respect to the number of holes on each side of the cavity,  $n$ .

As mentioned before, apart from the filtering requirements of the resonant wavelength and the range of the PhC band gap, the important performance indicators of the PhC filter are  $Q$  and  $T$ . The larger is  $Q$ , the smaller is the FWHM of the resonance wavelength peak, and hence the emission from fewer QDs will be transmitted. Therefore, for practical applications in quantum optics, the higher the  $Q$  of the filter the better as ideally one would like for only a single QD emission to be transmitted. One way of attempting to increase  $Q$  is to increase the hole number,  $n$ . The more mirrors are placed on either side of the cavity the stronger will be the light confinement within it. However, this was found to have its own disadvantages, as mentioned before. Due to stronger confinement within the cavity the light resonates inside for a longer period of time. This means that there is more opportunity for the light to scatter out of the waveguide without propagating along it as  $Q_w$  increases.

The effect of  $n$  on both  $Q$  and  $T$  for this filter is presented in Figures 4.4 and 4.5. The graph in Figure 4.4 shows the transmissivity through the filter with  $n = 3, 4, 5$  as a function of wavelength in the range of 900 – 950 nm. It is clear that as  $n$  increases, the FWHM of the resonance peak decreases. For  $n = 3$ ,  $\Delta\omega_{n=3} = 3$  nm, which corresponds to  $Q_{n=3} \approx 310$ ; for  $n = 4$ ,  $\Delta\omega_{n=4} = 0.9$  nm ( $Q_{n=4} \approx 1030$ ); and for  $n = 5$ ,  $\Delta\omega_{n=5} = 0.4$  nm ( $Q_{n=5} \approx 2310$ ). This accompanies the expected decrease in  $T$  from  $\sim 73\%$  for  $n = 3$ , through  $\sim 51\%$  for  $n = 4$  to just  $\sim 10\%$  for  $n = 5$ . This demonstrates a large trade-off between  $Q$  and  $T$ , which is presented clearly in Figure 4.5 for  $n$  between 3 and 17. The relationships between  $Q$  and  $n$  as well as  $T$  and  $n$  are approximately sigmoidal. This is because for  $n = 0$  there is no PhC in the nanobeam waveguide and hence  $T$  should be at its maximum,  $T_{n=0} = 100\%$ , while  $Q$  at its minimum,  $Q_{n=0} = 0$  (as FWHM is a very large wavelength range). As  $n$  increases  $Q$  also increases and then saturates at  $\sim 4500$  for  $n \geq 9$ , while  $T$  decreases to its minimum,  $T_{n \geq 9} \approx 0\%$ . This is caused by the radiation losses in the nanobeam PhCC due to its 2D confinement through total internal reflection. While  $Q_w$  increases exponentially with  $n$ ,  $Q_r$  remains approximately constant. Hence, for larger  $n$ ,  $Q$  is dominated by  $Q_r$  and can no longer increase with increasing  $Q_w$ . For a structure with complete 3D PhC confinement radiation losses would be near zero, and hence  $Q_r \gg Q_w$  resulting in nearly 100% transmission on resonance (according to Equation 4.2) and  $Q$  increasing exponentially with  $n$  without saturation.

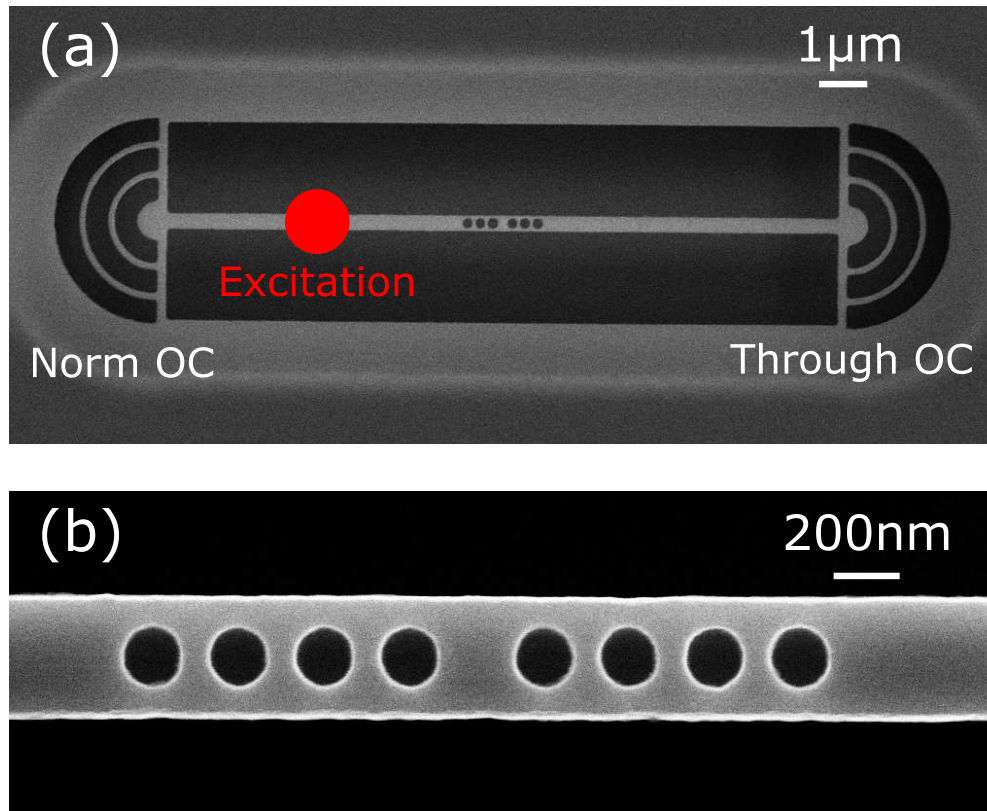


**Figure 4.6:** Top-view scanning electron microscope (SEM) images of typical nanobeam PhC filters with filling fraction,  $f$ , held constant and (a)  $n = 3$ , and (b)  $n = 4$ .

### 4.2.3 Fabrication

Nanobeam PhC filters with a different number of holes on each side of the cavity,  $n = 3, 4, 5$ , were fabricated on an undoped GaAs wafer, using standard techniques together with a  $\text{SiO}_2$  e-beam mask (rather than resist), which was especially developed for these structures (see Section 3.14). The filter was defined within the top GaAs membrane of 140 nm thickness, with InGaAs self-assembled quantum dots (QDs) embedded in its centre, which were used as photon sources for the optical testing of the filter. The nanobeam waveguide containing the filter was terminated on each side with a Bragg output-coupler (OC) to enable out-of-plane collection of the transmitted signal. The GaAs substrate was isolated from the membrane by a 1  $\mu\text{m}$  thick intrinsic  $\text{Al}_{0.6}\text{Ga}_{0.4}\text{As}$  layer, which was removed from beneath the device using an HF etch to create the suspended structure. Scanning electron microscope (SEM) images of typical fabricated devices are shown in Figure 4.6.

#### 4.2.4 Filtering of QD Emission Using Nanobeam PhCCs

##### Experimental Setup

The optical properties of the filters were studied experimentally using micro-photoluminescence ( $\mu$ -PL) spectroscopy with spatially resolved excitation and collection in a continuous flow cryostat at 4.2 K, using a confocal microscope system (see Sections 3.3.2,3.3.1). A He:Ne continuous-wave laser emitting at 633 nm was used for QD excitation via GaAs. The  $\mu$ -PL measurements were performed by exciting QDs in the waveguide on one side of the filter and collecting the emission from both sides consecutively. The light transmitted through the filter was collected from the through OC, while that transmitted through the waveguide without passing through the filter was collected from the normalisation (norm) OC [as indicated in Figure 4.6(a)]. The spectra were recorded using a spectrometer and a liquid N<sub>2</sub> cooled CCD.

##### Results and Discussion

Examples of raw spectra recorded from one of the filters with  $n = 3$  at an excitation laser power of  $\sim 0.5 \mu\text{W}$  are presented in Figure 4.7. The black continuous line shows the emission both from a large ensemble of QDs located inside the waveguide in the wavelength range of  $\sim 920 - 1000 \text{ nm}$ , and from the wetting layer at  $\sim 850 \text{ nm}$ . Under normal circumstances this light will be emitted in both directions along the waveguide to the norm and through OCs with equal probabilities [28]. Therefore, the signal recorded from the norm OC can be used as a reference to assess the performance of the filter. It is clear from the collected data, that the filter suppresses the light propagation in the designed wavelength range, removing both emission from the wetting layer and a large proportion from the QDs, while at the same time it allows for a small bandwidth of wavelengths, inside the PhC band gap, to be transmitted to the through OC.

The wafer used for this experiment had a high density of QDs in the membrane, so that filter modes can be clearly observed and measured. This is why the signal collected from the norm OC is an accumulation of emission from a large ensemble of QDs rather than single and sharp individual QD peaks. The peaks and troughs in that spectrum are caused by the Fabry-Pérot resonances

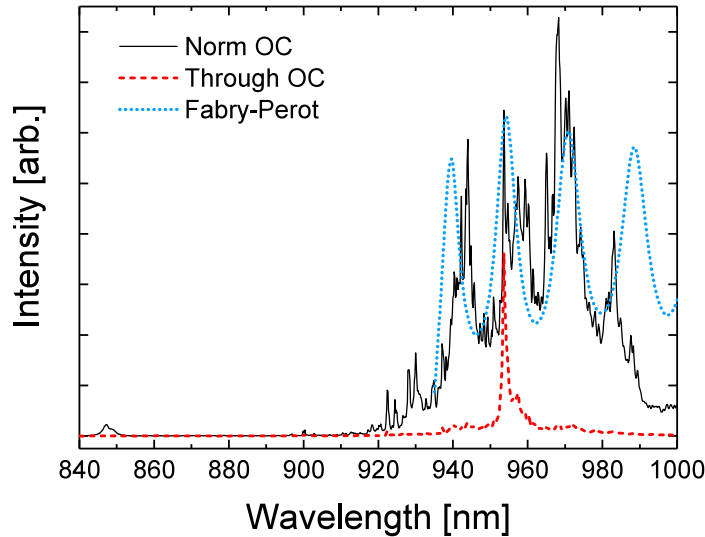


**Figure 4.7:** Experimental results showing the routed QD emission in the wavelength range of 840 – 1000 nm collected from the through and normalisation OCs for a filter with  $n = 3$ . The blue dotted line shows modelled Fabry-Perot resonances within the nanobeam waveguide.

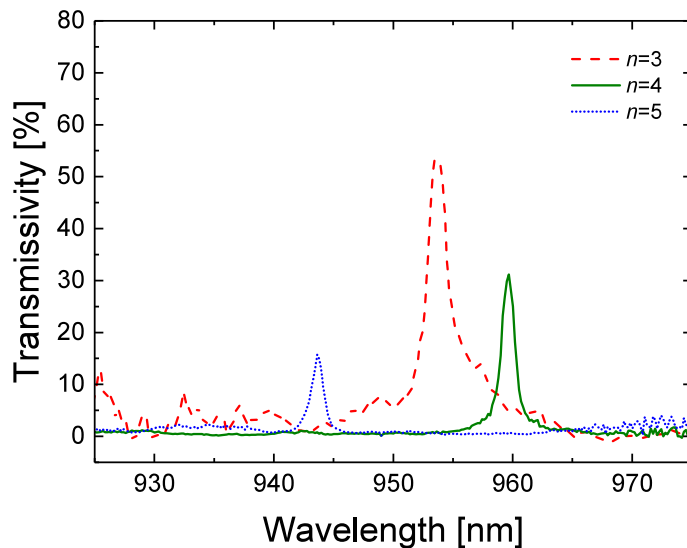


**Figure 4.8:** Experimental results for filters with  $n = 3, 4, 5$ . The data show the percentage of light transmitted to the through OC with respect to that collected from the normalisation OC for the wavelength range of 925 – 975 nm.

within the structure. Both OCs at the ends of the 15  $\mu\text{m}$  long waveguide will cause reflections of the propagating light. The various reflections will interfere with each other and the actual signal, either constructively or destructively, forming resonances within the device. This effect was also modelled using the FDTD electromagnetic simulation software and the results are overlapped on top of the experimental curves in Figure 4.7.

Figure 4.8 shows the normalized transmissivity measurement results for three filters with  $n = 3, 4, 5$  for a wavelength range of 925 – 975. The emission outside of this range is very small causing large errors in the normalization procedure. A comparison of these curves with their theoretical counterparts in Figure 4.4 leads to several findings. Firstly, both the FWHM,  $\Delta\omega$ , and transmissivity,  $T$ , follow the expected trends to decrease as  $n$  is increased. However, most values of  $\Delta\omega$  are larger (and hence the corresponding  $Q$ -factors are smaller) than the modelled values, while most values of  $T$  are smaller than their modelled counterparts. This is likely caused by any roughness and irregularities in the structures resulting from the fabrication processes, which increase scattering losses, and hence reduce  $Q_r$ . Furthermore, the difference between the experimentally determined  $Q$ -factors,  $Q_{\text{exp}}$ , and the simulated values,  $Q_{\text{mod}}$ , is larger for bigger  $n$ . For  $n = 3$ ,  $Q_{\text{exp}} \approx Q_{\text{mod}} \approx 310$  ( $\Delta\omega_{n=3} = 3 \text{ nm}$ ); for  $n = 4$ ,  $Q_{\text{exp}} \approx 0.78Q_{\text{mod}} \approx 800$  ( $\Delta\omega_{n=4} = 1.2 \text{ nm}$ ); and for  $n = 5$ ,  $Q_{\text{exp}} \approx 0.41Q_{\text{mod}} \approx 940$  ( $\Delta\omega_{n=5} = 1 \text{ nm}$ ). As the increase in  $Q$  depends greatly on  $n$ , any fabrication imperfections per each period of the PhC accumulate to cause a slower increase as  $n$  is increased.

Secondly, the resonant wavelengths are considerably longer (even up to 30 nm longer) than designed. They also varied between the measured devices. This shift is most likely caused by the differences in the dimensions of the fabricated filters with respect to those intended. A study of the dependence of waveguide width,  $w$ , and hole diameter,  $d$ , on the wavelength of the cavity mode has been undertaken and the results from the electromagnetic modelling are reported in Figure 4.9. In order for the mode to be shifted by 10 nm towards longer wavelengths, the hole diameter needs to be smaller by only 5 nm, or the waveguide width larger by  $\sim 12 \text{ nm}$ . This indicates that the structure is extremely sensitive to fabrication inaccuracies. The cavity length,  $c$ , and the PhC period,  $a$ , will also have a similar effect on the cavity mode, but these are easier to achieve with higher accuracy during fabrication than sizes

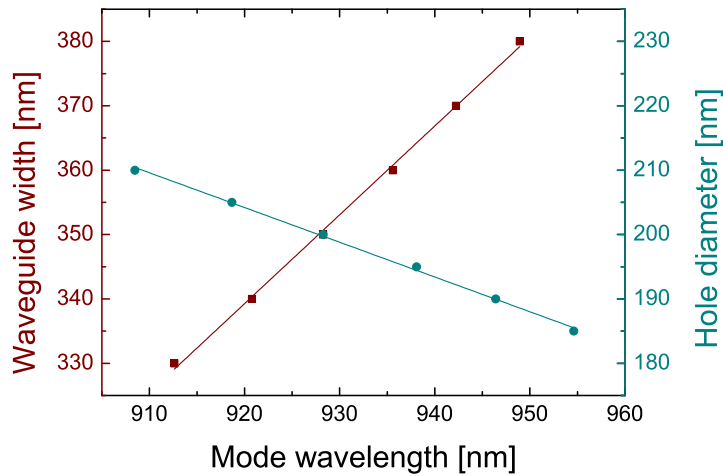


**Figure 4.9:** Modelling results demonstrating how small changes to the waveguide width,  $w$ , and hole diameter,  $d$ , affect the resonance wavelength of the filters.

of structures that depend on a larger number of processing steps. The position of various on-chip elements only depends on the single lithography step that defines them, but the sizes of structures also depend on several etching procedures, which are not straightforward to control to such tight tolerances.

#### 4.2.5 Conclusions and Further Development

In conclusion, an on-chip photonic crystal band-pass filter with a passband of 1 – 3 nm, and a band gap of  $\sim 180$  nm has been both designed and realized experimentally. The filter can be easily integrated into III-V semiconductor quantum optical circuits as it is based on a nanobeam waveguide structure, widely used for light guiding, interferometry, and beam splitting. The passband was in the range of  $\sim 940$  – 960 nm, which was ideal for the QD emission from the investigated wafer. However, the resonance wavelength can be adjusted by slightly altering the dimensions of the device if a shorter filtering wavelength is required. The demonstrated device represents an important step towards realizing fully integrated quantum optical circuits, as it paves the way for single-photon detectors being effectively integrated on a chip [133]. The large trade-off between the transmissivity and the width of the passband of the filter was also studied both through simulations and experimentally. The sensitivity of the device to fabrication imperfections has been found to increase

this trade-off further by increasing the scattering losses. The following section presents ways of maximising the possible values of  $Q$  by studying different designs of the nanobeam photonic crystal cavity. It also reports results from the experimental investigation of the possibility of tuning a single QD emission using QCSE into resonance with a nanobeam PhCC for cQED applications.

### 4.3 Cavity QED Effects

High- $Q$  PhCCs, which have small modal volumes, are of great interest to the quantum optics community as they offer large Purcell enhancement of the emission rate of an emitter within an optical cavity (see Section 2.3). Hence, they offer excellent platforms for studying cQED effects. Tuning of the QD emission using temperature control or QCSE to switch between the weak and strong coupling regimes of the light-matter interaction have been reported in many 2D PhCCs like L3 cavities [134] (see Section 2.6). However, similar studies with nanobeam PhCCs have only so far been attempted with temperature tuning [135], which affects both the cavity mode wavelength as well as that of a QD. It also broadens the QD emission peak due to the reduced confinement potential of the charge carriers. In this section an improved design for a nanobeam PhCC is presented for which experimental  $Q$ -factors are less dependent on any fabrication imperfections. Experimental results from the QCSE tuning of the QD emission inside this cavity are also reported. At the end of this section another cavity design is also presented for which very high  $Q$ -factors can be achieved.

#### 4.3.1 Design Requirements

In order to investigate experimentally the possibility of tuning the QD emission wavelength using QCSE into resonance with the cavity mode of a nanobeam PhCC, the sample is required to be fabricated on a doped GaAs wafer. This allows application of a potential difference across the GaAs membrane with embedded QDs. Thus, the thickness of the waveguide is larger than for the on-chip filter presented in Section 4.2, with  $t = 170$  nm. The QDs on a target wafer emit at slightly shorter wavelengths than before, in the range  $\sim 890 - 940$  nm, and hence the cavity mode should be redesigned accordingly

for  $\sim 915$  nm. The photonic band gap can, therefore, also be slightly narrower, in the range of  $\sim 800 - 960$  nm. Another additional requirement chosen for this iteration of the PhCC design is that the waveguide width should be  $w \approx 280$  nm to ensure operation in a single (TE) polarisation, which is an important requirement for optical QIP applications (see Section 2.2.1). It also ensures compatibility with other on-chip photonic devices based on single-mode nanobeam waveguides, such as the beam splitters reported in Chapter 5.

### 4.3.2 Modelling and Optimization of the Filter

Simply changing the width and the thickness of the nanobeam waveguide in comparison to those presented in Section 4.2, while keeping the remaining PhC parameters ( $a$ ,  $d$ ,  $c$ ) as before, considerably decreases the performance of the device. Figure 4.10 shows the simulated transmission spectra for a nanobeam PhC filter with  $n = 3$ ,  $d = 200$  nm,  $a = 263$  nm, width  $c = 413$  nm, and two sets of different values of  $w$  and  $t$ . Changing the width from  $w = 350$  nm to  $w = 280$  nm and thickness from  $t = 140$  nm to  $t = 170$  nm causes a large decrease in both  $Q$  and  $T$ , which experience decreases of 59% (from 310 to 127) and 77% (from 73% to 17%) respectively. In addition, the photonic band gap shifts towards shorter wavelengths by  $\sim 30$  nm. For this reason, another parameter search is necessary to optimize the remaining dimensions of the filter in order to maximize  $Q$  and  $T$  for the required  $w$  and  $t$ . A device with  $t = 170$  nm,  $w = 280$  nm,  $d = 125$  nm,  $a = 250$  nm,  $c = 335$  nm was found to fulfil the design requirements with the resonant wavelength at  $\sim 911$  nm,  $T = 65\%$ ,  $\Delta\omega = 1.4$  nm and hence  $Q \approx 650$  for  $n = 4$  (see Figure 4.11).

The reason for this simple cavity's performance to be affected strongly by fabrication imperfections with  $Q$ -factor values lower than expected with each period of the PhC (as shown experimentally in Section 4.2.4) is the mismatch of various modes existing within the structure and the abrupt interfaces between them. As the light propagates along the nanobeam waveguide it will arrive at the sudden boundary where the optical mode changes to that of the nanobeam PhC and then again at the cavity interface, and similarly on the way out. Hence there exist two abrupt interfaces in this cavity design: between the waveguide and the PhC, and between the PhC and the cavity. These will affect the waveguide and radiation losses respectively ( $Q_w$  and  $Q_r$ ). It has

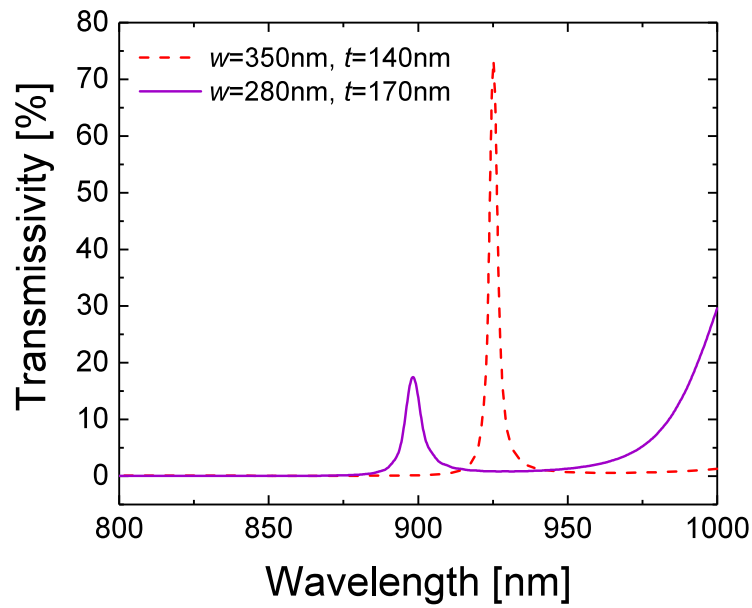


**Figure 4.10:** Simulation results showing the percentage of light within the wavelength range of 800 – 1000 nm transmitted through a nanobeam PhC filter with  $n = 3$ ,  $d = 200$  nm,  $a = 263$  nm,  $c = 413$  nm, and different values of  $w$  and  $t$ .

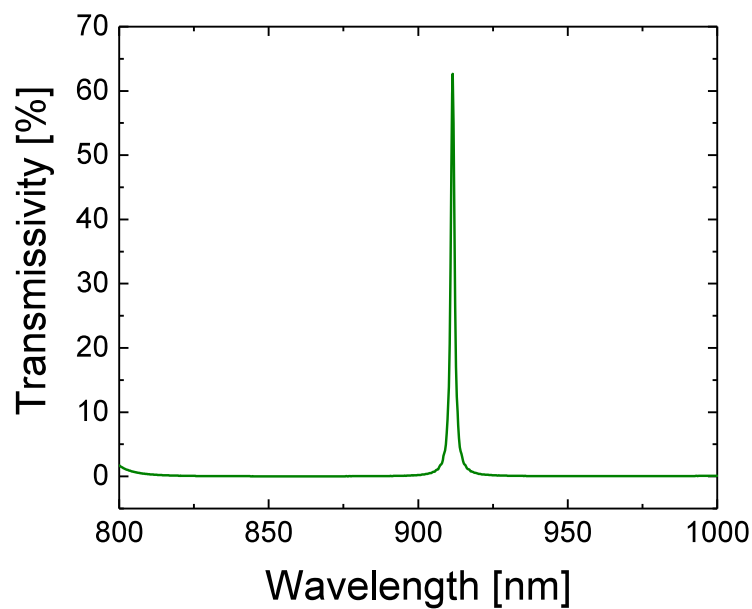


**Figure 4.11:** Simulation results showing the percentage of light within the wavelength range of 800 – 1000 nm transmitted through a nanobeam PhC filter with  $t = 170$  nm,  $w = 280$  nm,  $d = 125$  nm,  $a = 250$  nm,  $c = 335$  nm, and  $n = 4$ .

been shown that by gentler confinement of light within the PhCC a stronger and more imperfection-resistant confinement (with higher  $Q$ -factors) can be achieved [72, 136, 137].

In nanobeam PhCCs better mode matching can be realized through systematic tapering of the filling fraction (FF),  $f$ , along the waveguide. This can be done by altering either the hole diameter, the waveguide width or the PhC period [according to Equation (4.3)]. Even though high  $Q$ -factors have been realised through the PhC period tapering [135] it is considered a less promising method as it also has an effect on the PhC band gap and the wavelength of the cavity mode [112], and hence it is not straightforward to implement effectively. In order to make the interface between the waveguide and the PhC smoother  $f$  should be decreasing from the centre of the device in either direction so that the mirror strength of the PhC structure is systematically reduced at each period towards the waveguide. However, the opposite is true for the mode matching between the cavity (whose  $n_{\text{eff}}$  is that of the waveguide) and the PhC structure, for which  $f$  should be increasing from the centre of the device. Therefore, these two approaches are considered here separately.

As mentioned above, better mode coupling between the PhC structure and the waveguide can be realised by decreasing the FF from the centre of the device. This can be realized by either increasing the waveguide width or decreasing the hole diameter [see Equation (4.3)]. Schematic diagrams of both of these methods are presented in Figure 4.12. The latter approach has two important advantages over the former. Firstly, it is simply easier to realise in practice variations to the hole size along the PhC structure than to the curvature of the waveguide. Secondly, in order for the nanobeam PhCC to be compatible with other photonic elements on-chip for use in QIP, such as beam splitters, the waveguide width needs to remain uniform and in single polarization. For these reasons, the nanobeam PhCC with decreasing hole diameter is investigated here.

A nanobeam PhCC with  $f$  decreasing from the centre of the device has been modelled using the FDTD software Lumerical, as previously. A linear tapering of the FF was realized through changes to the hole diameter. The diameter of the holes closest to the cavity,  $d_0$ , was set to be 125 nm together with the remaining parameters chosen as previously. The FF was decreased by the same amount at each period of the PhC by reduced hole diameter. Simulation re-

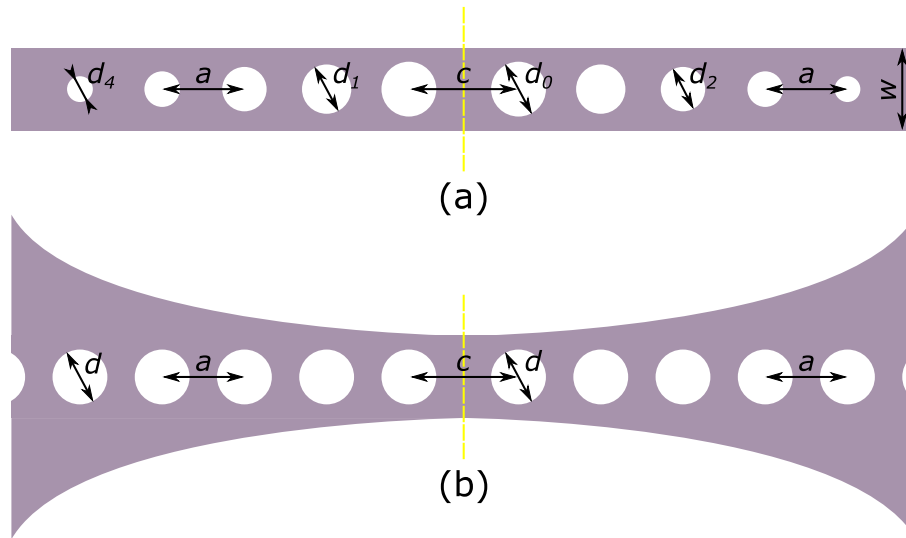


**Figure 4.12:** Schematic diagram of a nanobeam PhC filter with decreasing FF realized through (a) decreasing hole diameter, and (b) increasing waveguide width. The dashed yellow lines indicate the centres of symmetry of the devices.

sults comparing the performance of the cavity in terms of  $Q$  and  $T$  depending on the number of holes,  $n$ , with  $f = \text{const.}$  for all periods and with decreasing  $f$  are presented in Figures 4.13 and 4.14. As could be expected intuitively, in order to achieve similar confinement level ( $Q$ -factor) more periods are necessary in the case of the tapered design, as each individual PhC mirror strength is weaker than in the case of  $f = \text{const.}$  Even though, the value at which  $Q$  saturates does not seem to be affected by the tapered design, it is expected to have a significant impact on the experimentally achievable  $Q$ -factors, as is demonstrated below.

### 4.3.3 Fabrication

Nanobeam PhCCs with  $n = 15$  and decreasing  $f$ , were fabricated on a GaAs wafer with a doped membrane, using standard techniques (see Section 3.2) and a  $\text{SiO}_2$  mask. The filter was defined within the top  $p$ - $i$ - $n$  GaAs membrane of 170 nm thickness, and with a low density of InGaAs self-assembled quantum dots (QDs) embedded in its centre, which were used as photon sources for optical testing of the device. Separate Ni: Au contacts were made to the top  $p$  and the bottom  $n$  layers of the membrane to enable wavelength tuning of the QD emission through QCSE. The nanobeam waveguide was terminated on each

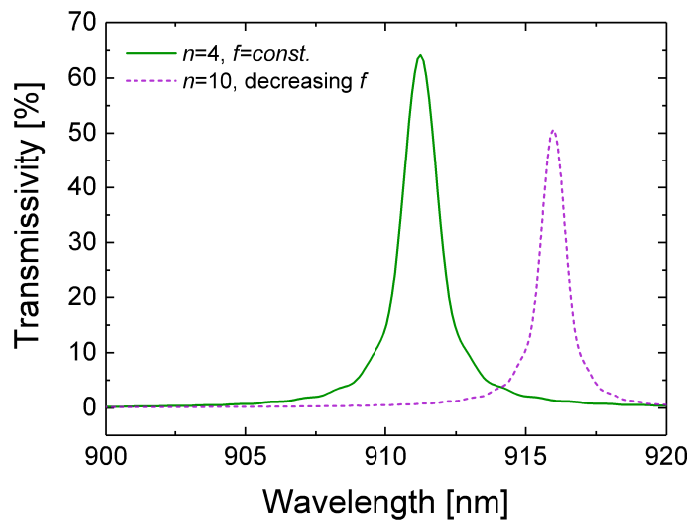


**Figure 4.13:** Simulation results showing the percentage of light within the wavelength range of 900 – 920 nm transmitted through a nanobeam PhC filter with  $t = 170$  nm,  $w = 280$  nm,  $d_0 = 125$  nm,  $a = 250$  nm,  $c = 335$  nm, and either  $n = 4$  with filling fraction,  $f$ , held constant or  $n = 10$  with  $f$  decreasing linearly from the centre of the cavity.

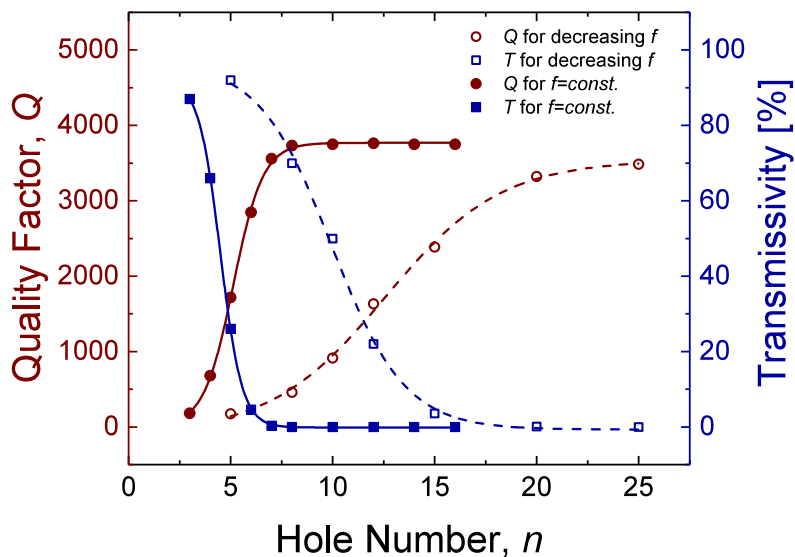


**Figure 4.14:** Simulation results showing the  $Q$ -factor and transmissivity,  $T$ , for a nanobeam PhC filter with  $t = 170$  nm,  $w = 280$  nm,  $d_0 = 125$  nm,  $a = 250$  nm,  $c = 335$  nm, and either filling fraction,  $f$ , held constant or with  $f$  decreasing linearly from the centre of the cavity.

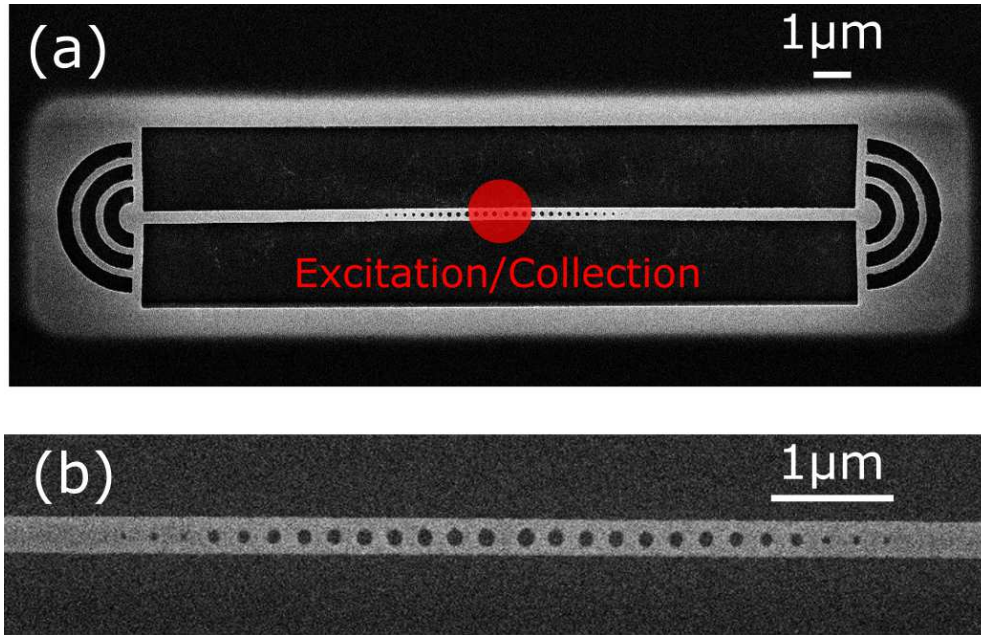


**Figure 4.15:** Top-view scanning electron microscope (SEM) images of typical nano-beam PhC filters with decreasing hole diameter from the centre and  $n = 15$  showing (a) the whole structure with output-couplers and the position of excitation/collection laser spots during experiments, and (b) a close-up of the photonic crystal structure.

side with a Bragg output-coupler (OC) to enable out-of-plane collection of the transmitted signal. The  $n$ -GaAs substrate was isolated from the membrane by a  $1.2 \mu\text{m}$  thick intrinsic  $\text{Al}_{0.6}\text{Ga}_{0.4}\text{As}$  layer, which was removed from beneath the device using an HF etch to create the suspended structure. Scanning electron microscope (SEM) images of typical devices are presented in Figure 4.15.

#### 4.3.4 Cavity QED Effects in Nanobeam PhCCs with Tunable QD Emission

##### Experimental Setup

The optical properties of the nanobeam PhCCs were studied experimentally using micro-photoluminescence ( $\mu$ -PL) spectroscopy with spatially resolved excitation and collection in a bath cryostat at  $\sim 5 \text{ K}$ , using a confocal microscope system (see Sections 3.3.2, 3.3.1). A Ti:Sapphire continuous-wave laser emitting at  $\sim 815 \text{ nm}$  was used for QD excitation via the wetting layer. The  $\mu$ -PL measurements were performed by exciting QDs in the centre of the

device, and thus of the cavity, while collecting the emission from that same position [as indicated in Figure 4.15(a)] with a separate optical path. The signal was recorded using a spectrometer with a liquid N<sub>2</sub> cooled CCD.

## Results and Discussion

Firstly, the fabricated devices were characterized using high-power excitation in order to determine the mode wavelength and the  $Q$ -factor of each cavity. Clear cavity modes were observed for 60% of the measured devices (12/20). The average value of  $Q$  for the working devices was found to be  $Q_{av} \approx 1755$ , 73% of the modelled value of  $Q_{mod} \approx 2400$ , while the highest measured  $Q$  was  $\sim 2020 = 0.84Q_{mod}$  ( $\Delta\omega = 0.47$  nm). This is a significant improvement from the previously studied filter with  $f = const.$ , where the difference between the theoretical and experimental values of  $Q$  was much larger even for the best device whose modelled  $Q$  was slightly lower at 2310 (for  $n = 5$ ). The experimental  $Q$  value was only 41% of the theoretical one in that case. This indicates that due to the gentler mode matching between the PhC structure and the waveguide over a larger number of PhC periods, the performance of the device is less sensitive to fabrication imperfections than in the case of abrupt boundaries between the two. As the devices were deliberately made with a range of hole sizes and waveguide widths in order to increase the probability that some of the cavity modes will overlap with QD emission, the mode wavelengths ranged between 900 nm and 960 nm. Around 50% of the working devices had a cavity mode in the correct wavelength range to match that of the QDs emission. However, due to the low density of QDs on the sample (in contrast with the previously measured filter), only one cavity was found to slightly overlap spectrally with the emission from one QD. Figure 4.16 presents the results for this device.

Figure 4.16(a) shows the raw spectra obtained by exciting and collecting from the cavity at different excitation powers. At low powers of just a few  $\mu$ W only emission from the individual QDs is visible. As the excitation power increases the cavity mode starts to emerge at 933.3 nm, while the intensity of the emission from the QDs increases. At high power the emission intensity from the QDs saturates, while the cavity mode becomes increasingly more pronounced. This phenomenon is captured in Figure 4.16(b), where the integrated

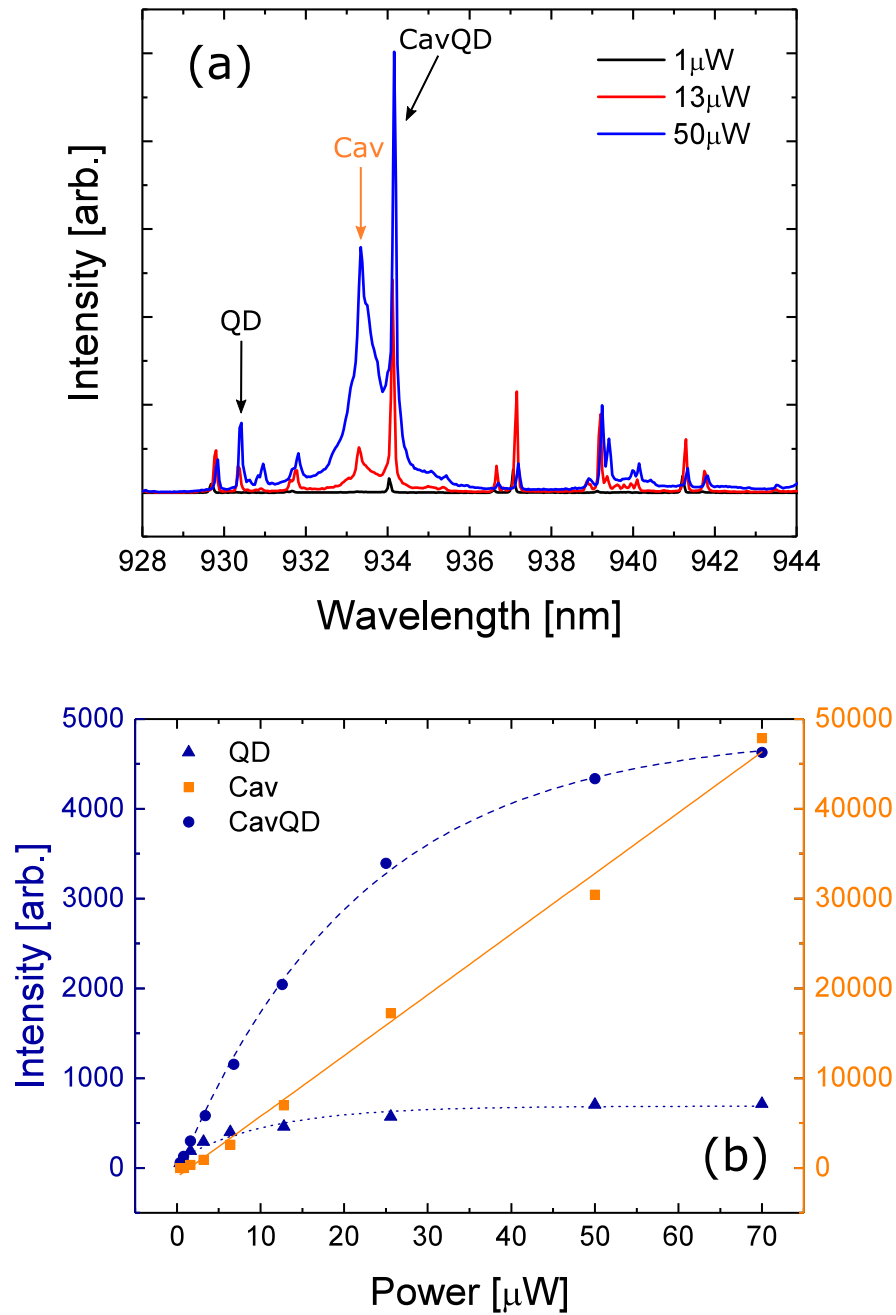


**Figure 4.16:** Results obtained by exciting with different powers and collecting from the centre of one of the devices with a cavity mode (at 933.3 nm) close to the emission wavelength of the QDs. (a) Raw spectra for a wide wavelength range, and (b) integrated peak intensities for the cavity, a typical QD spectrally isolated from the cavity (at 930.4 nm) and a QD which slightly overlaps with the cavity (at 934.1) denoted as CavQD.

peak intensity of the cavity, a typical QD emission not enhanced through the Purcell effect (at 930.4 nm), and a QD emitting at 934.1 nm, which overlaps slightly with the cavity mode (and hence is referred to as CavQD), are plotted against the excitation power. The QD emission increases asymptotically with increasing power and saturates at  $\sim 40 \mu\text{W}$  with an intensity  $\sim 12$  times brighter than at low excitation power, while the cavity emission increases linearly with increasing power, and hence dominates the emission spectrum at high powers. In the case of the CavQD, the intensity of the emission increases much faster than that of a typical QD and saturates at higher power of  $\sim 70 \mu\text{W}$  with intensities  $\sim 300$  times brighter than at low power. Hence, the CavQD is much brighter than other QDs at higher excitation powers. As the Purcell factor depends not only on the Q value of the cavity, but also on the QD's spectral and positional overlap with the modal fields of the cavity, this effect could be greatly increased by, for example, tuning the QD emission wavelength into resonance with the cavity mode. This has been attempted with this sample through QCSE by fabricating the device on a *p-i-n* membrane. The results of this experimental study are presented below.

The IV characteristic of the measured diode is presented in Figure 4.17. The turn-on voltage is  $\sim 8.5$  V. This is much higher than expected ( $\sim 1.5$  V) for a GaAs *p-i-n* structure [134]. However, diodes were fabricated on the same wafer previously and the turn-on voltage was then found to be  $\sim 1.3$  V. This indicates that the problem now lies in the fabrication procedure rather than the wafer itself. For example, if there is any resist still left on the sample when the contacts are deposited, it acts as an insulating layer between the wafer and the contacts. This causes the resistance of the contacts to be much higher than expected, and thus results in a need to apply higher bias than the actual built-in voltage in order to turn the diode on.

Due to the built-in voltage the electronic band structure of the QD/GaAs interface (see Section 2.1.3) is bent to start with, and hence the electrons and holes are allowed to tunnel out from the QD. The bending of the band structure is decreased by the application of a forward bias to the diode structure. This means that only at a certain bias should emission from a large number of QDs be observed. At higher biases their emission wavelength will be blue-shifted. Typical photoluminescence emission spectra obtained by exciting and collecting the signal from the centre of one of the cavities as a function of

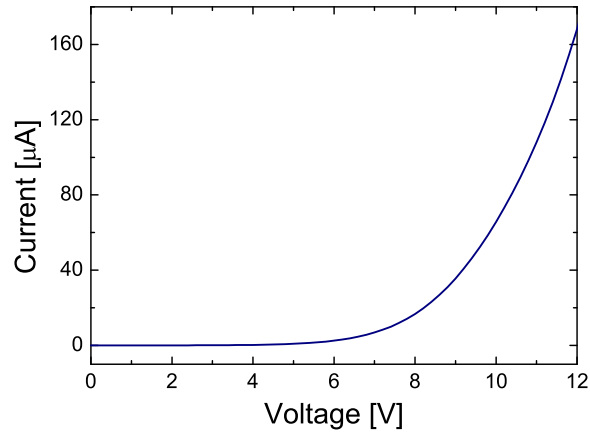


**Figure 4.17:** I-V characteristic of the measured diode structure.

forward bias are shown in Figure 4.18. Figure 4.18(a) shows the effect of the QCSE on the QD emission. At biases up to  $\sim 8.5$  V relatively few QD emission lines are visible due to charge carriers tunnelling out of the QDs. When the diode turns on many more QDs are able to emit single photons. Further increasing the forward bias causes the QD emission to shift towards shorter wavelengths. Overall, a blue-shift of  $\sim 0.2$  nm is achieved when the voltage is increased from 8.5 V to 11.2 V for this sample. Figure 4.18(b) presents these results for a broader range of biases and wavelengths. This particular cavity has a mode at  $\sim 961$  nm, and hence is isolated spectrally from the QD emission. It can be seen that while the QDs experience a shift to shorter wavelengths in their emission, the cavity mode remains unaffected by the application of bias. This demonstrates the potential for tuning the QD emission wavelength into resonance with the nanobeam PhC cavity mode. Unfortunately however, in this case the spectral separation between the cavity mode and the QDs emission is far too large in comparison to the achievable Stark-shift.

In addition, the reproducibility of these results for other cavities was found to have a success rate of only  $\sim 30\%$ . While QCSE could be observed when exciting and collecting from any output-coupler (OC) on the sample, this was not the case for the cavities. This might be due to the fact that by making holes in an already very narrow waveguide, the current flow through the material is greatly suppressed. This leads to no change in the effective field experienced by the QDs in the centre of the cavities with respect to the applied bias, and

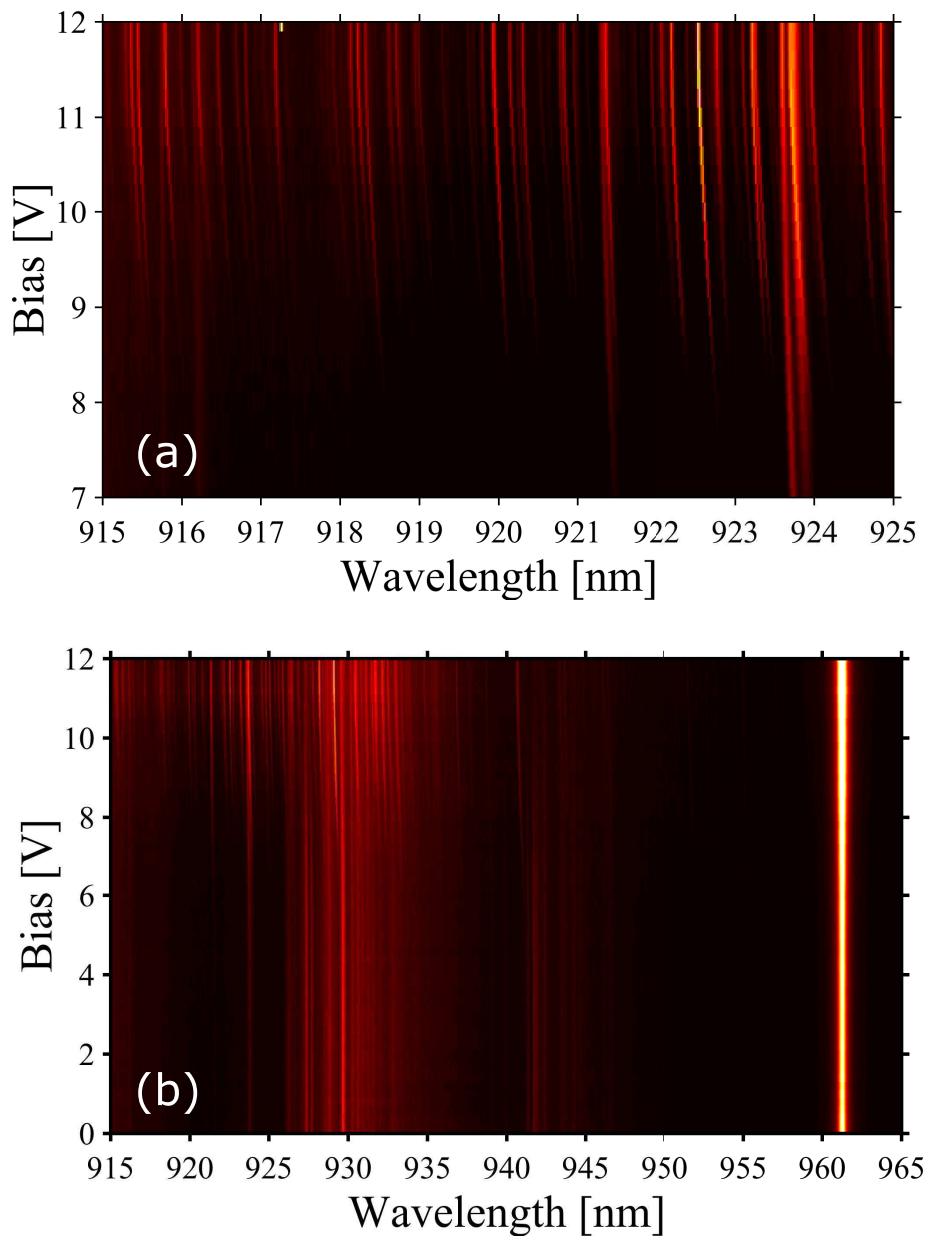


**Figure 4.18:** Photoluminescence emission spectra obtained while exciting and collecting from the centre of one of the cavities, as a function of forward bias applied to the diode structure. The colour map corresponds to emission intensity, with black and red/yellow representing weak and bright signals respectively. Plot (a) focuses on the QDs emission, which appears mostly from a bias of  $\sim 8.5$  V when the diode turns on and is tuned by  $\sim 0.2$  nm through QCSE up to a bias of  $\sim 11.2$  V. Plot (b) shows the position of the cavity mode at  $\sim 961$  nm, the wavelength of which is far away from the QDs emission (visible mostly  $\sim 915 - 935$  nm) and does not change with bias.

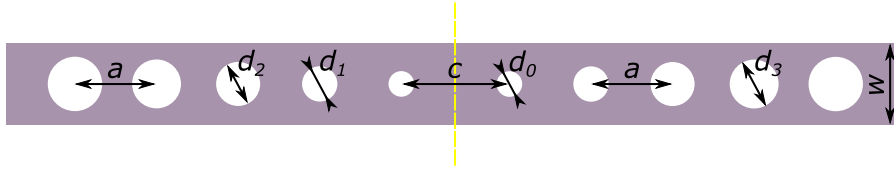


**Figure 4.19:** Schematic diagram of a nanobeam PhCC with filling fraction,  $f$ , increasing from the centre of the cavity, realized through increasing hole diameter. The dashed yellow line indicates the centre of symmetry of the device.

hence no wavelength tuning. This was, for example, the case for the cavity presented earlier in Figure 4.16, whose mode was spectrally much closer to the QD emission wavelength. The small Stark-shift also presents challenges to the demonstration of tuning the QD emission wavelength into resonance with the nanobeam PhCCs using QCSE. However, this can be overcome by designing an appropriate diode structure with AlGaAs barriers as mentioned in Section 2.1.3.

### 4.3.5 High-Q Cavity Design

In the previous section a nanobeam PhCC with better mode matching between the PhC structure and the nanobeam waveguide, realized through decreasing  $f$  from the centre of the cavity, has been presented. Its advantage of being less sensitive to fabrication imperfections with respect to cavities with constant  $f$  manifested itself through higher experimental  $Q$ -factors. However, the maximum theoretical  $Q$ -factors were still only  $\sim 3500$ . Here, a design for nanobeam PhCCs with very high  $Q$ -factors, potentially even reaching values of  $\sim 850,000$ , is presented.

As mentioned before, there is a second interface between the cavity and the PhC structure whose mode mismatch can cause large scattering losses (implying low  $Q_r$  and hence low  $Q$ ). This can be adjusted similarly through a gradual increase of  $f$  from the cavity towards the PhC structure to smooth out this interface. Therefore, a reversed case of a cavity studied in the previous section is investigated here, now with the diameter of the holes *increasing* from the centre towards the waveguide end so that  $f$  changes linearly up to  $d_{\text{end}} = 125 \text{ nm}$  with all the other parameters as before. The schematic diagram of the proposed nanobeam PhCC is presented in Figure 4.19.

The structure was designed so that there were a number of holes,  $n_c$ , over

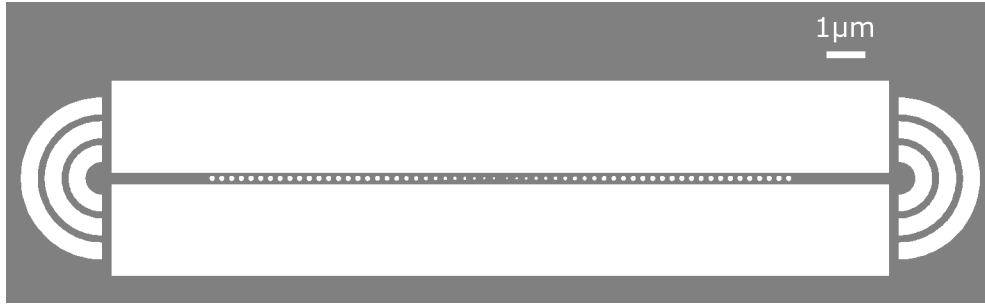


**Figure 4.20:** Digital image of a high-Q nanobeam PhCC with filling fraction,  $f$ , increasing linearly from the centre of the cavity over  $n_c = 15$ , and with a further number,  $n_w = 15$ , of holes with  $f$  held constant at the waveguide end, ready for fabrication.

which the tapering took place, which were followed by a further number,  $n_w = 15$ , of holes with  $d_{\text{end}} = 125$  nm, and hence with  $f = \text{const.}$  in order to increase the mirror strength on the waveguide side. The number  $n_w$  was chosen to be 15 as in the design with  $f = \text{const.}$  over the entire structure 15 holes were enough to reach the maximum  $Q$ -factors for the cavity (see Figure 4.14). This new cavity design is presented in Figure 4.20 in GDSII format with  $n_c = 15$  and  $n_w = 15$ .

The nanobeam PhCC was modelled using the FDTD simulation software Lumerical, as previously. The  $Q$ -factors for designs with various values of  $n_c$  and  $n_w = 15$  are shown in Figure 4.21. This time the  $Q$ -factors saturate at  $\sim 850,000$  for  $n_c \approx 35$ . This indicates that due to the gentler confinement of light between the cavity and the PhC structure, the radiation losses at that interface are greatly decreased, thereby making the confinement much stronger. The tapered design should also make it possible to achieve high  $Q$ -factors experimentally, as demonstrated before. This potentially very high  $Q$  nanobeam PhCC is currently awaiting fabrication for experimental testing.

### 4.3.6 Conclusions and Further Development

In conclusion, two different improved designs of a nanobeam PhCC have been presented. One design was based on improving the mode matching between the PhC structure and the waveguide by systematically *decreasing* the hole diameter from the centre of the device in order to increase the resistance to fabrication imperfections through a longer and softer interface between the two optical modes. This resulted in higher experimental  $Q$ -factors of  $\sim 2000$

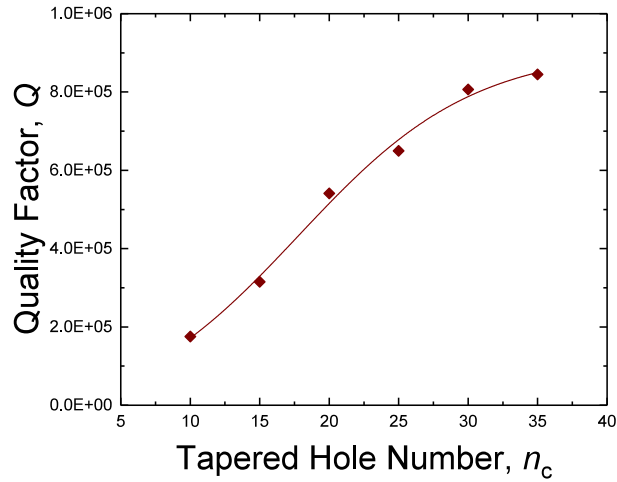


**Figure 4.21:** Simulation results showing the  $Q$ -factor versus the number of holes in the near cavity tapered region,  $n_c$ , for the nanobeam PhCC with filling fraction,  $f$ , increasing linearly from the centre of the device in both directions until  $d_{\text{end}} = 125$  nm, followed by  $n_w = 15$  holes with constant  $f$ .

( $\Delta\omega = 0.47$  nm), 84% of the modelled value, in comparison to just 41% for the original unmodified cavity. Another, reverse design, was also demonstrated, which improves mode matching between the cavity and the PhC structure through a systematic *increase* in the hole diameter from the centre of the device. This decreases scattering losses at that interface, thereby resulting in a much stronger confinement of light in the cavity. It was shown through simulations that such a nanobeam PhCC is capable of achieving  $Q$  factors of around 850,000 ( $\Delta\omega \approx 1$  pm). The experimental studies still need to be carried out on these devices, but they should be fairly resistant to fabrication imperfections due to the tapered design.

Tuning of the QD emission into resonance with the nanobeam PhCC modes using QCSE was also attempted experimentally. However, it was found that for the majority ( $\sim 65\%$ ) of the devices no wavelength tuning was observed for the QDs inside the cavities. This might be caused by a relatively small amount of material remaining in the centre of the nanobeam waveguides with air holes on either side, which would cause the current flow across them to be heavily suppressed. This would result in the band structure at the centre of these devices not to be affected by the application of bias across the diode, and hence also in no change to the confinement potential of those QDs.

## 4.4 Summary and Outlook

In this chapter nanobeam photonic crystal cavities (PhCCs) were studied for on-chip filtering and cQED applications. These devices are highly compatible and easily integrable with other photonic structures essential for QIP, such as the beam splitters that are studied in the next chapter of this thesis. A PhC band-pass filter was first designed and demonstrated experimentally using embedded QDs as light sources. The passbands of the filters were between 1 and 3 nm with a large photonic band gap approaching 200 nm. The large trade-off between the high transmissivity through the filter and its narrow passband was also demonstrated experimentally. These devices pave the way towards fully integrated quantum optical circuits as they make the integration of single photon detectors onto a chip increasingly possible [133].

Nanobeam PhCC designs were further developed in order to decrease the spectral width of the cavity modes, so as to maximise the cavity  $Q$ -factors. This can result in the increased emission rate of the QDs embedded in the cavity if the two overlap well both spectrally and spatially according to the Purcell effect (see Section 2.3). A cavity with an experimental  $Q$ -factor of  $\sim 2000$  ( $\Delta\omega = 0.47$  nm) was achieved through tapering of the hole diameter to aid PhC mode matching with that of a nanobeam waveguide. Tuning of the QD emission wavelength into resonance with the cavity mode was attempted through QCSE in order to study these cQED effects, but was found to be rather unsuccessful, most likely due to the poor current flow across the narrow waveguides with air holes along them. An alternative method is to tune the cavity mode wavelength instead, and this is the topic of Chapter 6 of this thesis. Finally, a nanobeam PhCC design that is theoretically capable of reaching  $Q$ -factors of  $\sim 850,000$  ( $\Delta\omega \approx 1$  pm) through tapering of the hole diameter to aid cavity mode matching with that of a PhC was demonstrated through modelling. This is a very promising approach that is particularly recommended for further experimental study.

## Chapter 5

# Electro-Mechanical Control of an On-Chip Optical Beam Splitter

Micro-opto-electro-mechanical systems (MOEMS) have been widely studied for a variety of applications in semiconductor integrated photonic circuits. The vast majority of work has been carried out on silicon where on-chip tuning of the optical properties of essential circuit components is possible by displacing them mechanically with the application of an electrostatic field. Lateral displacement has been used in phase modulators [138, 139], resonance tuning of nanobeam photonic-crystal cavities (PhCCs) [129, 140] and micro-toroid resonators [141]. More complicated structures such as comb-drive actuators [142–146] have also been developed to allow for the larger displacements that are attractive for optical switching applications [147–151]. Recently, scalable out-of-plane actuation methods based on a cantilever geometry have also been demonstrated at room temperature [152].

MOEMS based on III-V semiconductors are now emerging for applications in quantum information processing (QIP). Initial work has focused on tuning PhCC modes into resonance with quantum emitters in order to enhance their emission. In-plane [153] as well as double-membrane out-of-plane actuation methods [154–156] have been reported, both of which offer small displacements. Beam splitters, realized on chip using directional couplers (DCs), are another vital component of integrated linear quantum optical circuits, with post-fabrication control of their optical properties likely required for efficient QIP applications [7, 157]. In this context the electro-mechanical tuning of DCs

has so far only been considered theoretically [158].

In this chapter the electro-mechanical control of an on-chip optical beam splitter containing an embedded single photon source is demonstrated at low temperature. The beam splitter is tuned reversibly from the initial state, with output from both arms of the beam splitter, to a final state, with photons routed into a single arm, by electro-mechanical actuation of a cantilever, with achievable out-of-plane displacements of over 400 nm [159]. The proposed device can operate as either an optical router or a fine-tuning element of other individual photonic elements, such as PhCCs or Mach-Zehnder interferometers, in III-V semiconductor integrated quantum optical circuits.

The chapter begins with a short discussion of how the device operates and presents the results of optical as well as electro-mechanical modelling of the system, before discussing its fabrication. It then continues with both room- and low-temperature electro-mechanical testing of the device before presenting the results of opto-electro-mechanical and autocorrelation measurements. The chapter concludes with a summary of the work achieved and a discussion of future improvements to the sample design.

## **5.1 Principle of Operation**

The routing of single photons is achieved by electro-mechanical tuning of the splitting ratio of an optical beam splitter in the form of a nanobeam waveguide directional coupler (DC). One of the two waveguides forming the DC is located at the free end of a cantilever, which can be displaced vertically downwards by applying an actuation voltage,  $V_{\text{act}}$ , between the cantilever and the substrate. The resulting out-of-plane separation between the waveguides is used to control the splitting ratio of the DC. In the measured device, in the absence of an actuation voltage, photons emitted by a chosen InGaAs self-assembled QD embedded within the fixed arm of the device are split  $\sim 83:17$  between the co-planar through and drop ports of the DC respectively. This initial state is dependent upon the dimensions of the fabricated structure, as discussed further in the following section. As  $V_{\text{act}}$  is applied the drop port displaces downwards by over 400 nm causing the splitting ratio to approach 100:0.

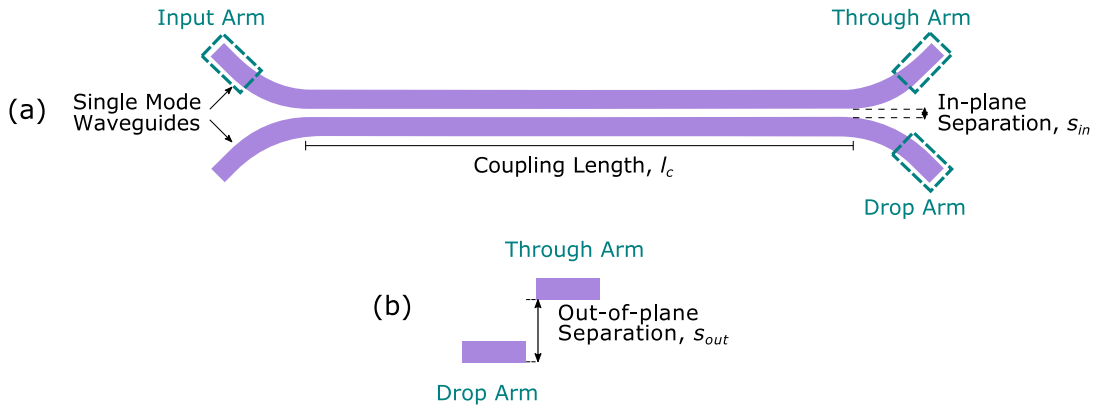


**Figure 5.1:** (a) Top- and (b) side- view schematic diagram of a directional coupler consisting of two single-mode waveguides separated by distance  $s_{in}$  laterally and  $s_{out}$  vertically in the coupling region of length  $l_c$ .

## 5.2 Modelling of the System

### 5.2.1 Modelling of a Directional Coupler

The schematic diagram of a DC consisting of two single-mode waveguides is presented in Figure 5.1. The DC acts as an optical beam splitter for light entering the input arm, due to evanescent light coupling between the two waveguides in the coupling region. Depending on the dimensions of the waveguides, the wavelength of the light, and both in-plane and out-of-plane separations between the waveguides, the light will split differently between the through and drop arms. The splitting ratio (SR) of a DC is defined as the output power from the through arm to the output power from the drop arm. In this chapter tuning of the SR is demonstrated by controlling the out-of-plane waveguide separation,  $s_{out}$ , by electro-mechanical actuation of a cantilever.

Modelling of the optical properties of the DC was performed using MIT Photonic-Bands, a freely available eigenmode solver (see Section 3.4.1). For the simulation the coupling length,  $l_c$ , was set to  $7 \mu\text{m}$  and the thickness of the waveguides to  $160 \text{ nm}$  (the membrane thickness of the wafer used for the experiments). The waveguide width was set to  $280 \text{ nm}$  in order to ensure an operation that is as lossless as possible in a single (TE) polarization. The in-plane waveguide separation,  $s_{in}$ , in the coupling region was chosen to be  $40 \text{ nm}$  so that the initial SR at  $s_{out} = 0$  of the DC is close to 50:50 for a range of emission wavelengths of typical SAQDs ( $890 - 940 \text{ nm}$ ). The results of the modelling

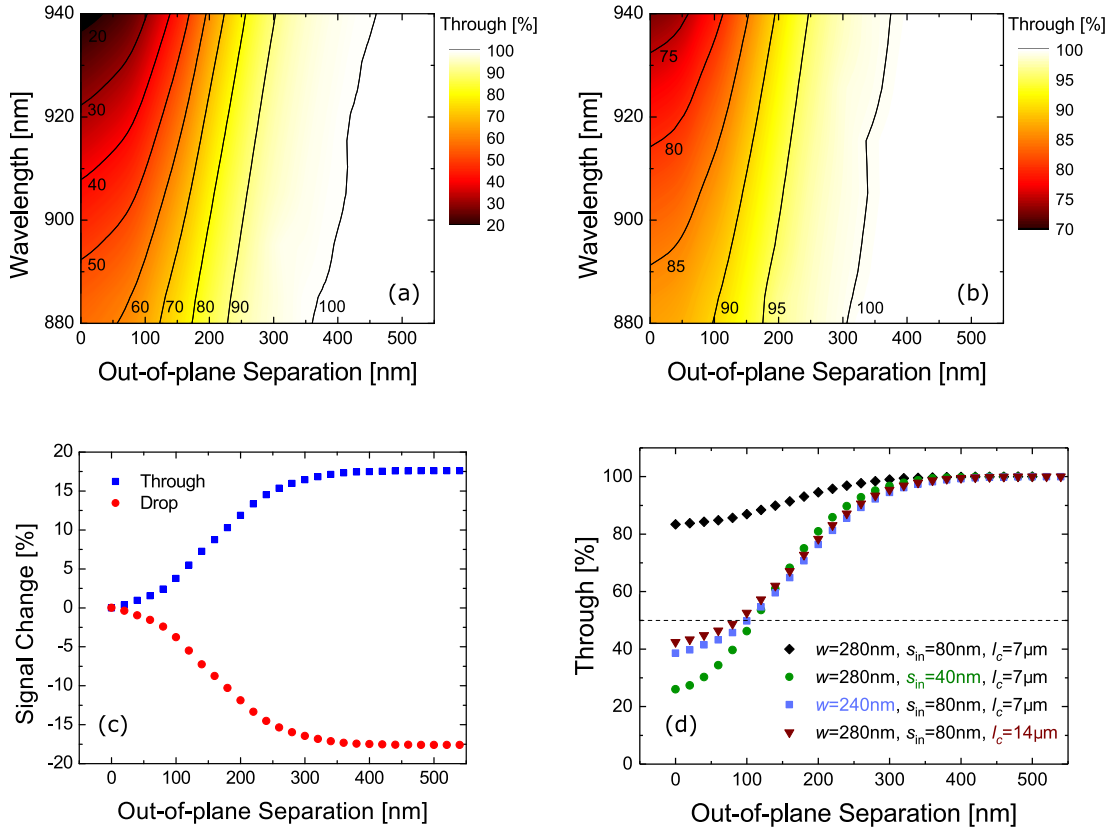


**Figure 5.2:** Results of the optical modelling of a directional coupler consisting of 160 nm thick and 280 nm wide waveguides with a 7  $\mu$ m long coupling region. (a) The contour plot shows how the fraction of light evanescently coupled from one channel to the other depends on the wavelength of the transmitted light and the out-of-plane separation between the waveguides separated laterally by  $s_{in} = 40$  nm. (b) Similar contour plot as in (a) but for increased in-plane waveguide separation of  $s_{in} = 80$  nm. (c) Changes to the signal transmitted in the fixed arm (through) and coupled to the moving arm (drop) as a function of out-of-plane displacement for a wavelength of 910 nm and  $s_{in} = 80$  nm. (d) Increase in the overall percentage of light (for a wavelength of 910 nm) transmitted to the through arm for various parameters of the directional coupler as the out-of-plane separation between the waveguides is increased to over 500 nm.

of a DC, with a light source located in the fixed arm of the DC, are shown in Figure 5.2. Depending on the wavelength of the light transmitted through the DC of the dimensions discussed above and the out-of-plane separation between its arms (introduced through the electro-mechanical actuation of a cantilever) the SR will change, varying the percentage of signal exiting the through arm [see Figure 5.2(a)]. It is clear that in a broad QD emission wavelength range, the DC can be tuned from an overcoupled state, when more light is coupled to the drop than the through arm, to a decoupled state, when all the light is transmitted to the through arm, as  $s_{\text{out}}$  is increased to an achievable 400 nm. This demonstrates the potential of the proposed device, which allows the SR to be switched between the commonly required 50:50 and that corresponding to an output into a single arm, 100:0. Unfortunately, the device studied experimentally had in-plane waveguide separation  $\sim 40$  nm larger than the target value of 40 nm giving  $s_{\text{in}} = 80 \pm 5$  nm. This is caused by fabrication inaccuracies, which are more pronounced for smaller separations. Figure 5.2(b) shows the theoretical output from the through arm of the DC with these dimensions as  $s_{\text{out}}$  is increased. The larger  $s_{\text{in}}$  considerably decreases the range of achievable tuning to  $\sim 15 - 20\%$  as the as-fabricated device is undercoupled. The relative signal change at the through and drop ports of this DC for an operation wavelength of 910 nm (the emission wavelength of the single QD studied experimentally) is shown in Figure 5.2(c).

Further optimization of the dimensions of the DC can overcome the difficulties in achieving small enough in-plane separations during fabrication, which are needed in the reported device for larger tuning range covering the commonly required 50:50 splitting. Figure 5.2(d) shows the comparison of SR tuning ranges for various DC parameter sets. Reducing the width of the waveguides is one possible solution, as it enhances the evanescent light coupling between them. 240 nm wide waveguides (40 nm narrower than current) would enable tuning of the SR over 60%. A coupling region with twice the length of the present one ( $l_c = 14 \mu\text{m}$ ) would triple the potential tuning range of the SR. However, the downside of this method might be a more fragile structure prone to breaking while handling or resulting in waveguides not being parallel along the entire coupling region, which can also have an effect on the optical properties of the DC.

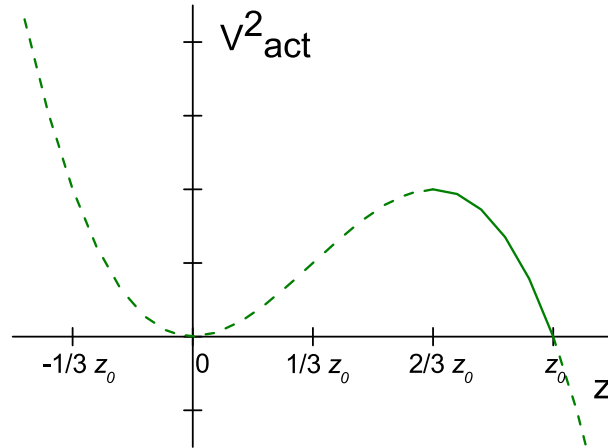


**Figure 5.3:** Relationship between the square of the actuation voltage and the distance between the cantilever and the substrate derived from Equation (5.2). The cantilever collapses down onto the substrate ( $z = 0$ ), when a pull-in voltage is applied for which the cantilever displacement,  $d$ , is  $z_0/3$ .

### 5.2.2 Modelling of a Cantilever

Applying an actuation voltage,  $V_{\text{act}}$ , between the cantilever and the substrate results in a capacitive force, which causes the cantilever to deflect towards the substrate, according to the following equation, which balances the capacitive force with the restoring force of the cantilever:

$$\frac{\epsilon_0 A}{2z^2} V_{\text{act}}^2 = k_s (z_0 - z), \quad (5.1)$$

where  $z$  and  $z_0$  are the current and the initial distance between the cantilever and the substrate respectively, where the cantilever displacement is  $d = z_0 - z$ ,  $\epsilon_0$  is the permittivity of free space,  $A$  is the surface area of the cantilever ( $A = wL$ , where  $w$  is the width and  $L$  the length of the cantilever), and  $k_s$  is a fitting parameter corresponding to an average stiffness of the cantilever. Rearranging for  $V_{\text{act}}$  gives:

$$V_{\text{act}}^2 = \frac{(z_0 - z)z^2}{X^2}, \quad (5.2)$$

where  $X = \sqrt{\epsilon_0 A / 2k}$ . This function, plotted in Figure 5.3, with a minimum at  $z = 0$  and a maximum at  $z = 2/3 z_0$  explains the electro-mechanical behaviour of the cantilever. As  $V_{\text{act}}$  is increased, the cantilever will deflect downwards from  $z = z_0$  at  $V_{\text{act}} = 0$  to  $z = 2/3 z_0$  (corresponding to a cantilever displacement of  $d_{\text{pull}} = 1/3 z_0$ ) at the so-called pull-in voltage,  $V_{\text{pull}}$ . At this point, the

capacitive force becomes greater than the restoring force and the free end of the cantilever collapses down onto the substrate ( $z = 0$ ), as is evident from Figure 5.3. This introduces surface adhesion forces between the cantilever and the substrate. If these forces are smaller than the restoring force, the cantilever will be able to lift back up from the substrate as  $V_{\text{act}}$  is then decreased to a value less than  $V_{\text{pull}}$  creating a hysteresis behaviour [150, 160, 161].

Modelling of the electro-mechanical behaviour of a cantilever with different dimensions was performed using the FEA software (see Section 3.4.2), the results of which are presented in Figure 5.4. Changes to the width and length of the cantilever as well as to the initial separation between the cantilever and the substrate were investigated. It was found that varying the width of the cantilever does not affect the displacement-voltage relationship, while halving its length increases the voltage necessary for achieving the same displacement by a factor of four. In addition, as  $z_0$  doubles, the maximum stable displacement also doubles, which is in accord with the graph shown in Figure 5.3. The former dependencies are in agreement with Equations 5.1 and 5.2. If the cantilever is assumed to act as a linear spring, the stiffness of the cantilever can be written as:

$$k_s = \frac{Ywt^3}{4L^3}, \quad (5.3)$$

where  $t$  is the thickness, and  $Y$  is the Young's modulus of the cantilever. Equation 5.1 then becomes:

$$V_{\text{act}}^2 = \frac{Yt^3}{2\epsilon_0L^4}d(z_0 - d)^2, \quad (5.4)$$

with no dependency on  $w$  as the factor coming from the area cancels out with the one from the stiffness. The discussed relationship between  $V_{\text{act}}$  and  $L$  is also immediately apparent.

As a GaAs cantilever is an intrinsically fragile device to fabricate, the possibility of adding support struts on either side of its free end was also examined (see Figure 5.8). 300 nm wide and 9  $\mu\text{m}$  long supports were added to the FEA model in order to study how their presence will affect the electro-mechanical behaviour of the cantilever. Comparison of the results for a cantilever with and without the struts is shown in Figure 5.5. Even such thin and long struts cause the required voltage to increase dramatically, with 25 V giving a displacement of only 200 nm, which displacement a cantilever without struts can

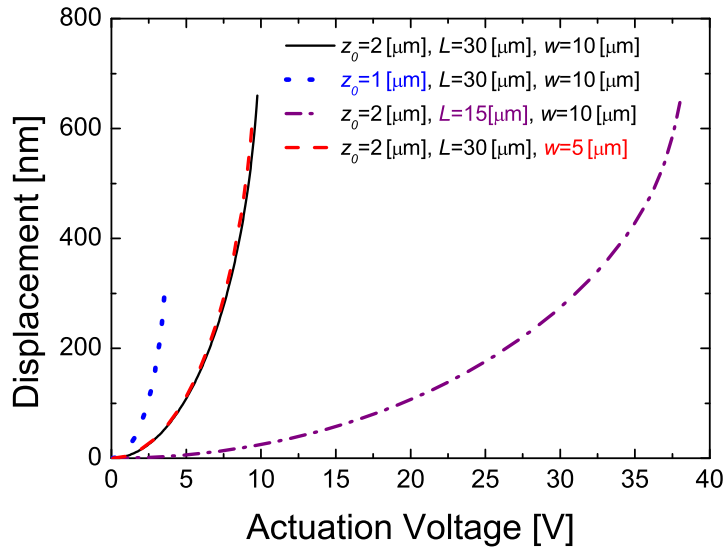


**Figure 5.4:** Displacement of the free end of a cantilever with different dimensions  $z_0$ ,  $L$  and  $w$  as the actuation voltage is increased, found using FEA.

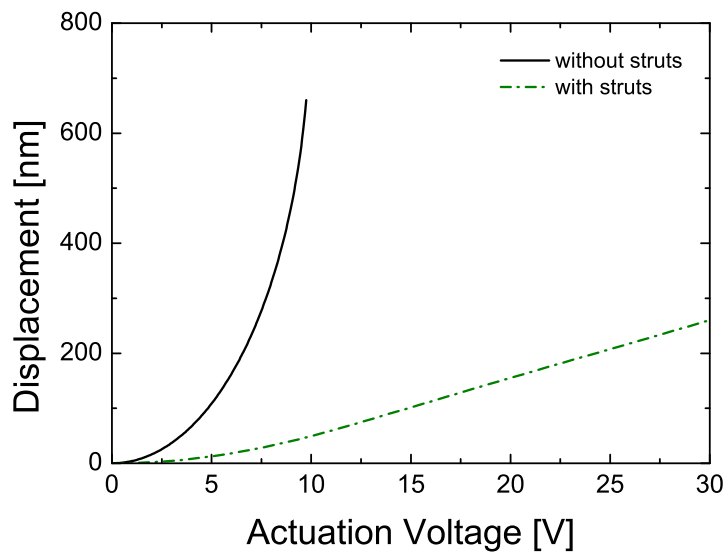


**Figure 5.5:** Displacement of the free end of a  $30\ \mu\text{m}$  long,  $10\ \mu\text{m}$  wide, and  $160\ \text{nm}$  thick cantilever with  $z_0 = 2\ \mu\text{m}$  with and without  $9\ \mu\text{m}$  long and  $300\ \text{nm}$  wide supportive struts, located on either side of the end of the cantilever, as the actuation voltage is increased, found using FEA.

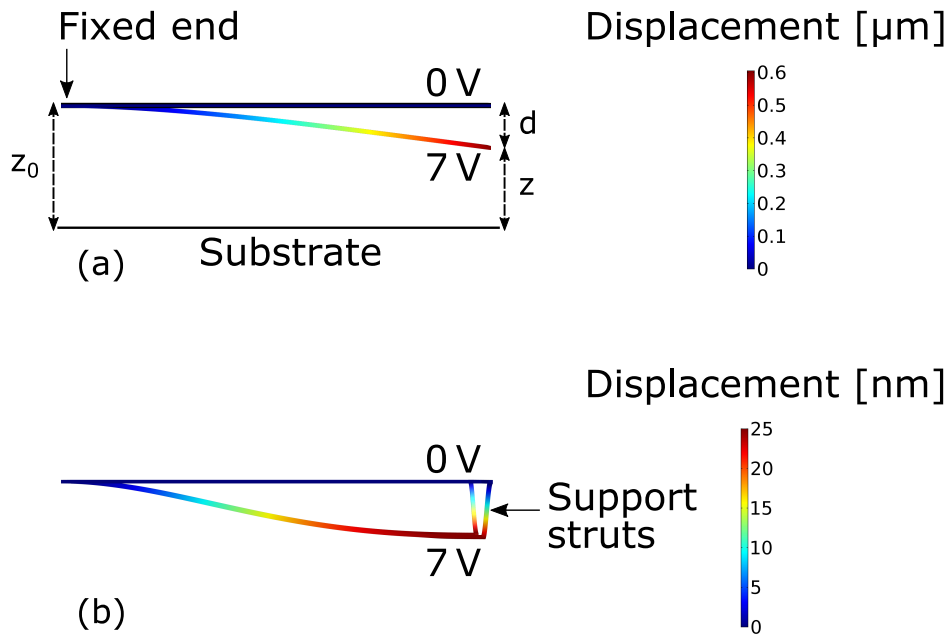


**Figure 5.6:** The profile and deformation of a cantilever as modeled using the FEA software at  $V_{\text{act}} = 0\text{ V}$  and  $V_{\text{act}} = 7\text{ V}$  for (a) a cantilever without struts, (b) a cantilever with  $9\ \mu\text{m}$  long and  $300\text{ nm}$  wide struts.

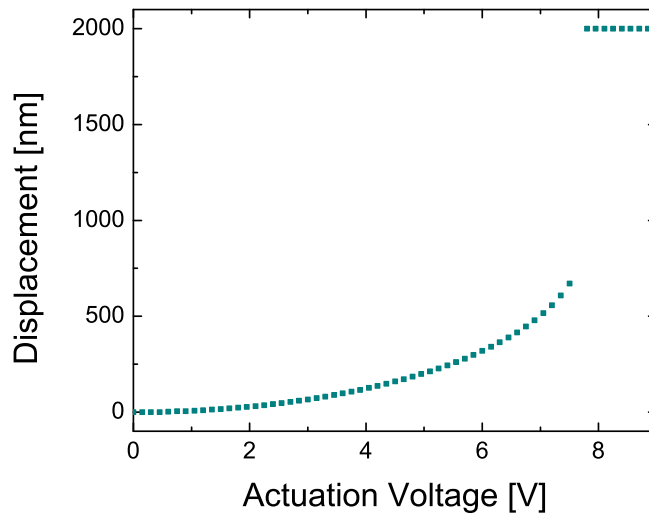


**Figure 5.7:** Displacement of the free end of the  $35\ \mu\text{m}$  long,  $7.5\ \mu\text{m}$  wide, and  $160\text{ nm}$  thick cantilever with  $z_0 = 2\ \mu\text{m}$  as actuation voltage is increased, calculated using analytical modelling.

reach with just 7 V. Therefore, operation of the device with supporting struts is not viable. However, the struts can be detached post-fabrication using local laser ablation (discussed later). This enables protection of the device during fabrication, transport and installation in a cryostat, while still taking advantage of the more efficient actuation without them. The profiles and displacements of the cantilever with and without support struts at  $V_{\text{act}} = 0 \text{ V}$  and  $V_{\text{act}} = 7 \text{ V}$  obtained from this analysis are presented in Figure 5.6.

The electro-mechanical behaviour of the cantilever without support struts with the dimensions used for the fabricated device was modelled using both FEA and an analytical model, which determines the displacement for a given  $V_{\text{act}}$  by minimizing the total energy of the system (comprising restoring and electrostatic energies). The model assumes that the cantilever's vertical displacement is a quadratic function of position along its length [162]. For the simulation the cantilever thickness was set to 160 nm, width to  $7.5 \mu\text{m}$ , length to  $35 \mu\text{m}$ ,  $z_0$ , to  $2 \mu\text{m}$ , and the Young's modulus to 85.5 GPa [163]. Figure 5.7 shows the expected displacement of the free end of the cantilever as  $V_{\text{act}}$  is increased, calculated using the analytical model. For this system  $V_{\text{pull}}$  is calculated to occur at 7.5 V, when the discontinuity in the (filled squares) curve is observed between the displacement of about 667 nm and 2000 nm (corresponding to  $z_0/3$  and  $z_0$ ). The FEA modelling gave a similar result of  $V_{\text{pull}} = 7 \text{ V}$ .

## 5.3 Device Design and Fabrication

### 5.3.1 Device Design

The device, shown in Figure 5.8, consists of a nanobeam waveguide DC, and a cantilever with dimensions  $35 \mu\text{m}$  in length,  $7.5 \mu\text{m}$  in width and 160 nm in thickness. One arm of the DC is fixed to the bulk of the sample, while the other is located on the free end of the cantilever. Single photons incoming from the input arm of the fixed waveguide are split by the DC between the through and drop arms. This occurs due to evanescent coupling between the waveguides in the  $7 \mu\text{m}$  long coupling region, in which the in-plane separation of the arms of the DC is about 80 nm. The nanobeam waveguides of the DC are designed to be 280 nm wide and 160 nm thick. Each arm of the DC is terminated with a Bragg output-coupler (OC) to enable out-of-plane collection of the transmitted

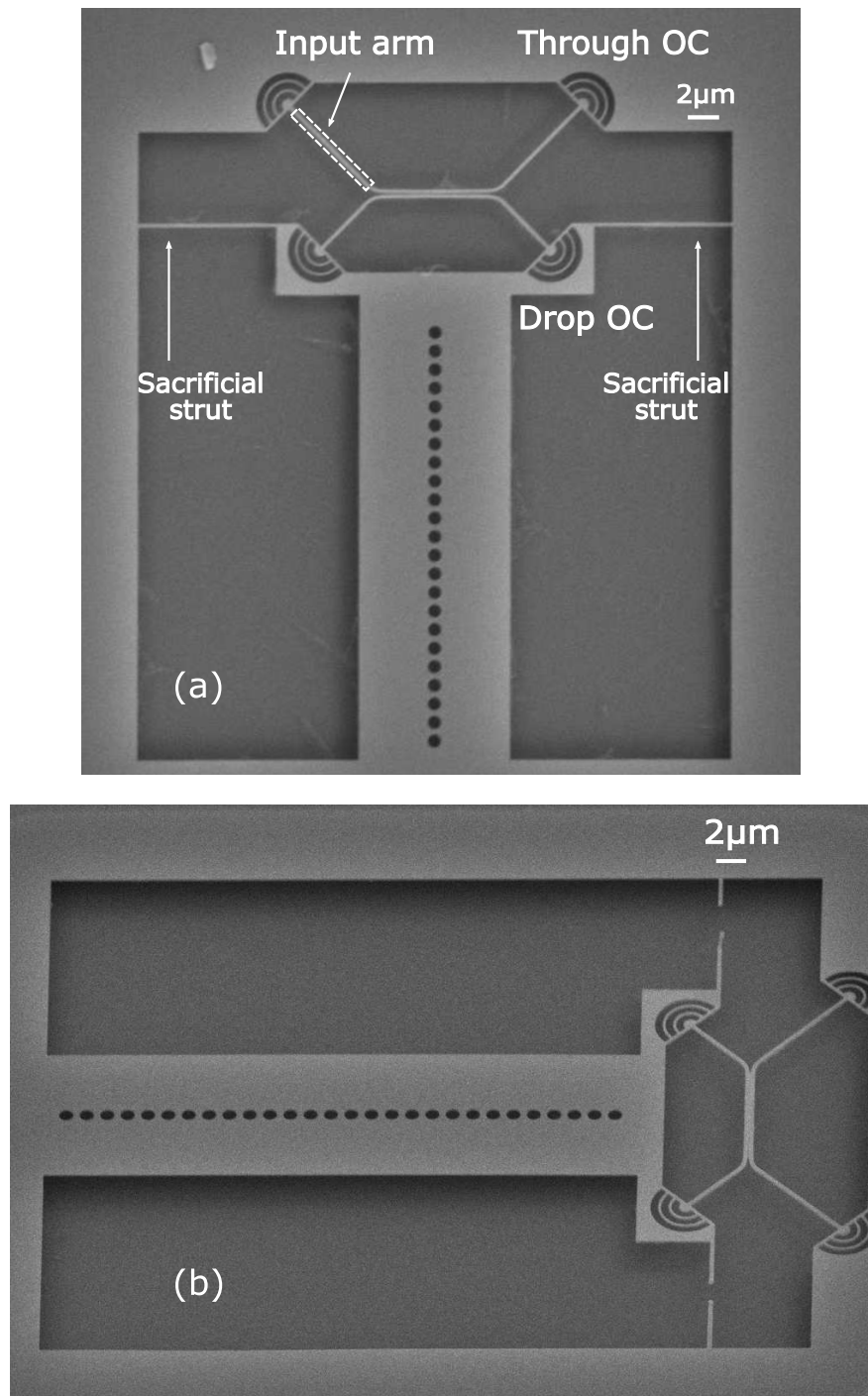


**Figure 5.8:** (a) Top-view scanning electron microscope (SEM) image of a typical opto-electro-mechanical system used for tuning of an on-chip beam splitter. (b) Angled SEM image of the system after sacrificial struts were removed at low temperature before commencing the opto-electro-mechanical measurements.

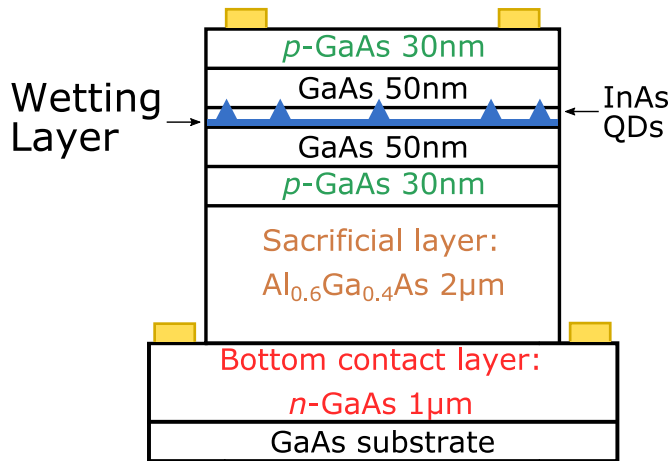


**Figure 5.9:** Schematic diagram of the wafer structure used. The position of the Ni:Au contacts is marked by gold rectangles.

photons. The free end of the cantilever is supported on either side with a 300 nm wide sacrificial strut during sample fabrication and transport. The struts are removed at cryogenic temperature using a high power (20 mW) CW laser emitting at 770 nm before measurements commence. It is focused to a spot of 2 μm diameter on the strut for a duration of about 3 s. This ablates a small part of the strut, thereby releasing the cantilever [see Figure 5.8(b)].

### 5.3.2 Sample Fabrication

The device was fabricated on a *p-i-p-i-n* diode, the schematic of which is presented in Figure 5.9, using standard techniques (see Section 3.2). The DC and the cantilever were defined within the top *p-i-p* GaAs membrane of 160 nm thickness. The intrinsic region of this membrane contained InGaAs self assembled quantum dots (QDs) that are used as embedded single photon sources to probe the optical response of the system. The *n*-GaAs substrate was isolated from the membrane by a 2 μm thick intrinsic Al<sub>0.6</sub>Ga<sub>0.4</sub>As layer, which was removed from beneath the device using an HF etch to create the suspended structure. Ni:Au contacts were made to the top *p*- and the bottom *n*-GaAs layers in order to allow for electro-mechanical control of the cantilever. The row of holes in the centre of the device (see Figure 5.8) allowed for faster under-etching of the cantilever.

## 5.4 Electro-Mechanical Testing of the Device

### 5.4.1 Room Temperature Testing

The electro-mechanical behaviour of the cantilever was first tested at room temperature in the SEM at the National Epitaxy Facility. The SEM images of the actuated device are shown in Figure 5.10. The dashed orange lines indicate the horizontal position of the cantilever at  $V_{\text{act}} = 0$  V [Figure 5.10(a)]. It is clear from Figure 5.10(b), that the free end of the cantilever deflected downwards towards the substrate at  $V_{\text{act}} = 16$  V as expected. The resulting lighter image in comparison to that at  $V_{\text{act}} = 0$  V is indicative of the change in the charge on the surface of the sample. As positive bias is applied to the top  $p$ -layer, the holes move away from the surface, resulting in a negatively charged area. This increases both the scattering of the secondary electrons from the surface and the potential difference between the positively charged detector and the surface, thus enhancing the collection of secondary electrons, which results in a brighter image [164]. Figure 5.10(c) shows the failure mode of the cantilever at  $V_{\text{act}} = 16.5$  V. At room temperature the current flow through the  $2\ \mu\text{m}$  intrinsic AlGaAs layer is greatly enhanced in comparison to that at cryogenic temperatures and causes the sample to heat up. This results in the cantilever breaking away at the point of highest strain and lowest heat dissipation - close to the attachment point to the rest of the membrane. In this particular device, the two arms of the DC became joined during fabrication, and hence, when the cantilever collapsed onto the substrate it pulled the fixed arm of the DC down as well. However, in a working device (as demonstrated later), the two waveguides should be totally independent from each other, and when the cantilever collapses the fixed arm should remain stationary.

### 5.4.2 Cryogenic Temperature Testing

The electro-mechanical behaviour of the cantilever was studied experimentally using white light illumination of the sample in a bath cryostat (see Section 3.3.1) at  $\sim 5$  K, using a confocal microscope system and an infrared camera (see Section 3.3.2). Figure 5.11 shows the images of the device taken as  $V_{\text{act}}$  was increased and then decreased. The free end of the cantilever was observed to collapse onto the substrate at  $V_{\text{pull}} = 13$  V, which is indicated by the end of

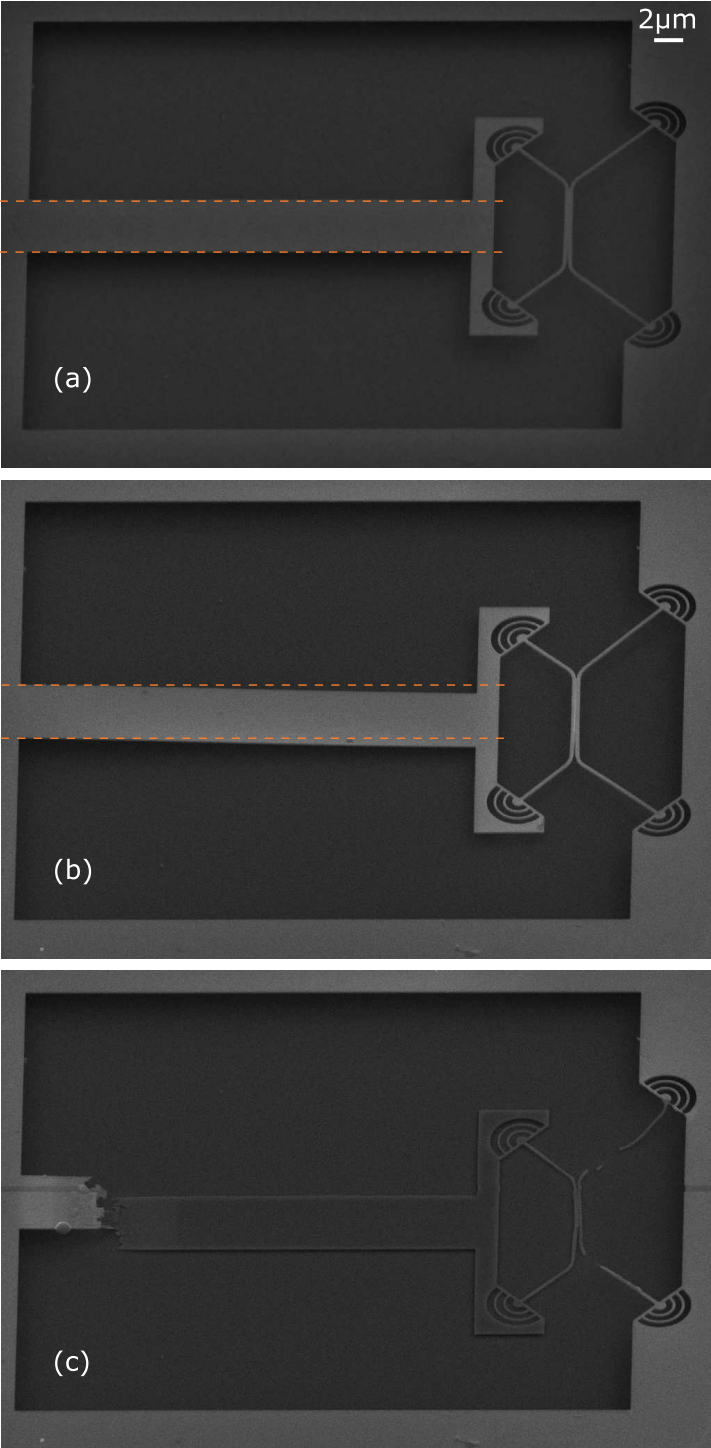


**Figure 5.10:** SEM image of a device actuated electro-mechanically at room temperature at (a) 0 V, (b) 16 V, and (c) 16.5 V.

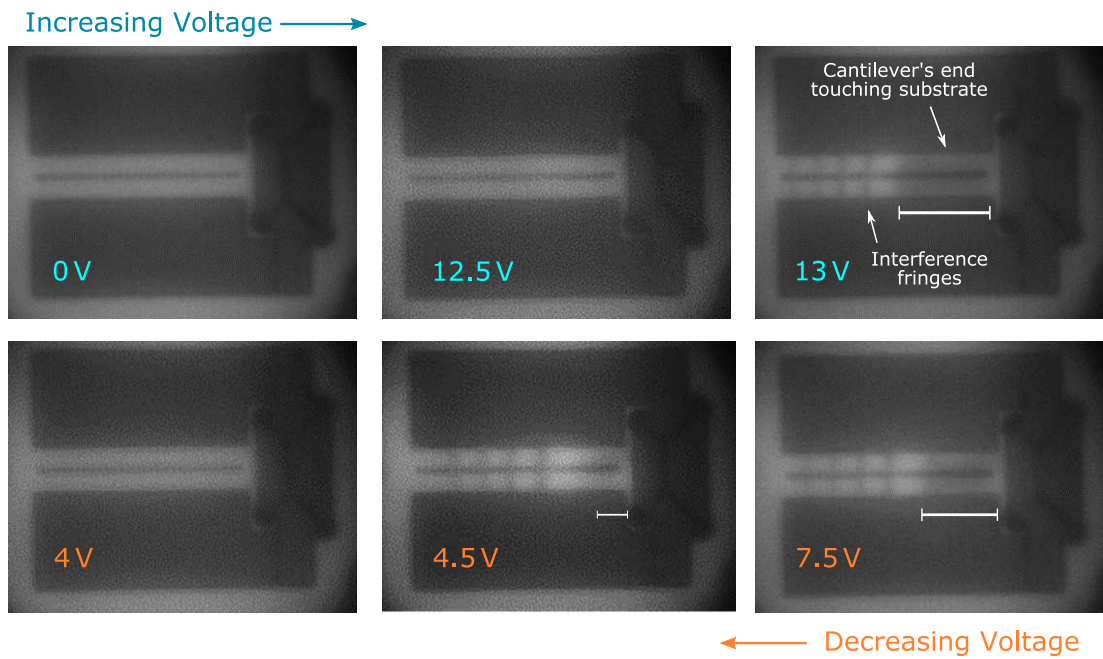


**Figure 5.11:** Images of the device actuated electro-mechanically at cryogenic temperature as the  $V_{act}$  is increased up to 13 V and then decreased back to 0 V, demonstrating the hysteresis behaviour of the cantilever.

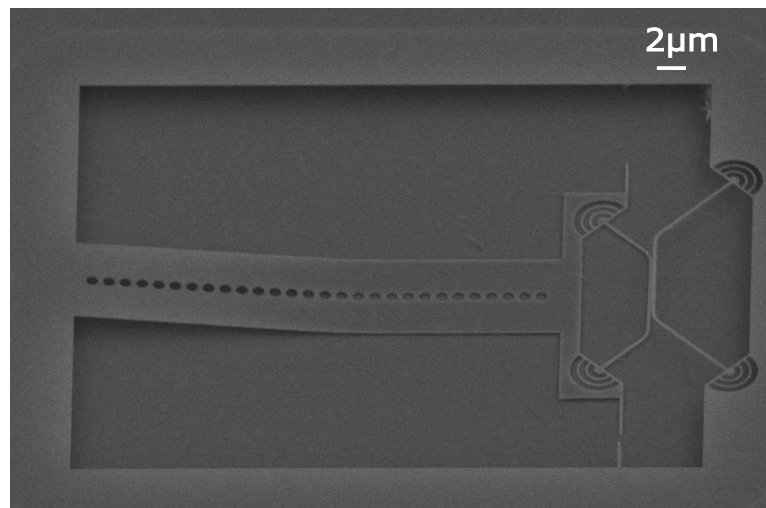


**Figure 5.12:** SEM image of the device which collapsed irreversibly at cryogenic temperature.

the cantilever looking darker and the appearance of interference fringes along the cantilever's length. As  $V_{\text{act}}$  was decreased the cantilever was observed to slowly peel away from the surface (visible through interference fringes moving along the cantilever, and the shortening of the dark end) before finally totally lifting back up at  $V_{\text{act}} = 4\text{ V}$ . This demonstrates the expected hysteresis in the electro-mechanical behaviour of the cantilever (see Section 5.2.2) and allowed for multiple measurements to be performed. The fact that the value of  $V_{\text{pull}}$  found experimentally was larger compared to the modelled value could simply be related to the resistance of the contacts, which was not taken into account in the simulation. The value of  $V_{\text{pull}}$  at  $\sim 5\text{ K}$  is lower and the failure mode is different compared to room temperature operation. Figure 5.12 shows an SEM image of the device, which collapsed irrevocably at cryogenic temperature due to an accidental voltage discharge in the system. At  $\sim 5\text{ K}$  the cantilever does not break away from the membrane when  $V_{\text{pull}}$  is reached, but simply collapses down onto the substrate, which allows it to lift back up when  $V_{\text{act}}$  is decreased. This is due to the absence of current flow, and hence heat, through the  $2\text{ }\mu\text{m}$  intrinsic AlGaAs layer at cryogenic temperature compared to room temperature. Figure 5.12 also demonstrates the correct operation of the device, where the two arms of the DC are independent from each other. It is clear from the image that when the cantilever collapses down onto the substrate, the moving arm of the DC also collapses, but the fixed arm remains stationary at its initial level.

## 5.5 Tuning of the Optical Properties of a Directional Coupler by Electro-Mechanical Control of a Cantilever

### 5.5.1 Experimental Setup

The system was studied experimentally using micro-photoluminescence ( $\mu\text{-PL}$ ) spectroscopy with spatially resolved excitation and two collections in a bath cryostat at  $\sim 5\text{ K}$ , using a confocal microscope system (see Sections 3.3.2, 3.3.1). A Ti:Sapphire continuous-wave laser emitting at  $840\text{ nm}$  was used for QD excitation via the wetting layer. The voltage-dependent  $\mu\text{-PL}$  measure-

ments were performed by exciting QDs through the input OC and collecting the emission from the through and drop OCs simultaneously using two independent collection paths. The spectra from the two paths were then recorded using two spectrometers and two liquid N<sub>2</sub> cooled CCDs.

The  $\mu$ -PL maps obtained for a single value of  $V_{\text{act}}$  involved exciting the chosen QD through the input OC and collecting emission from the entire device by raster scanning a single collection path using a motorised mirror. The signal was filtered through one of the spectrometers with a bandwidth of 80  $\mu\text{m}$  and detected by an APD.

For the autocorrelation measurements (see Section 3.3.3), the chosen QD was excited from above and the emission was collected from the input OC using two separate collection paths. The signal from the two paths was then filtered through the two spectrometers separately and detected by two APDs.

## 5.5.2 Results and Discussion

A bright and spectrally isolated QD embedded within the input arm of the DC, emitting at 910.6 nm was chosen for the measurements. Figure 5.13 shows the emission spectra obtained while exciting QDs through the input OC and collecting the emission at the input, through and drop OCs. The chosen QD emission is marked on the figure.

Figure 5.14 shows two  $\mu$ -PL maps, with the device contour overlaid, obtained by raster scanning the collection across the device while spectrally filtering at the QD wavelength. Figure 5.14(a) was obtained from the device with  $V_{\text{act}} = 0\text{ V}$ , where emission can be seen from three OCs: input, through and drop, as well as from the location of the QD within the input arm. As QDs emit light in both directions along the waveguide the signal also reaches the input OC. The emission in the other direction will be split between the through and drop OCs as discussed in Section 5.2.1. The  $\mu$ -PL map in Fig. 5.14(b) was acquired for the device operated with  $V_{\text{act}} = 12.5\text{ V}$ . The emission from the drop OC is now observed to be heavily suppressed, while that from the through OC increases, in comparison to the previous case. This is exactly as expected from the modelling, as when  $V_{\text{act}}$  is applied the cantilever deflects downwards, thereby increasing the out-of-plane separation between the waveguides, which causes the evanescent coupling between them to decre-

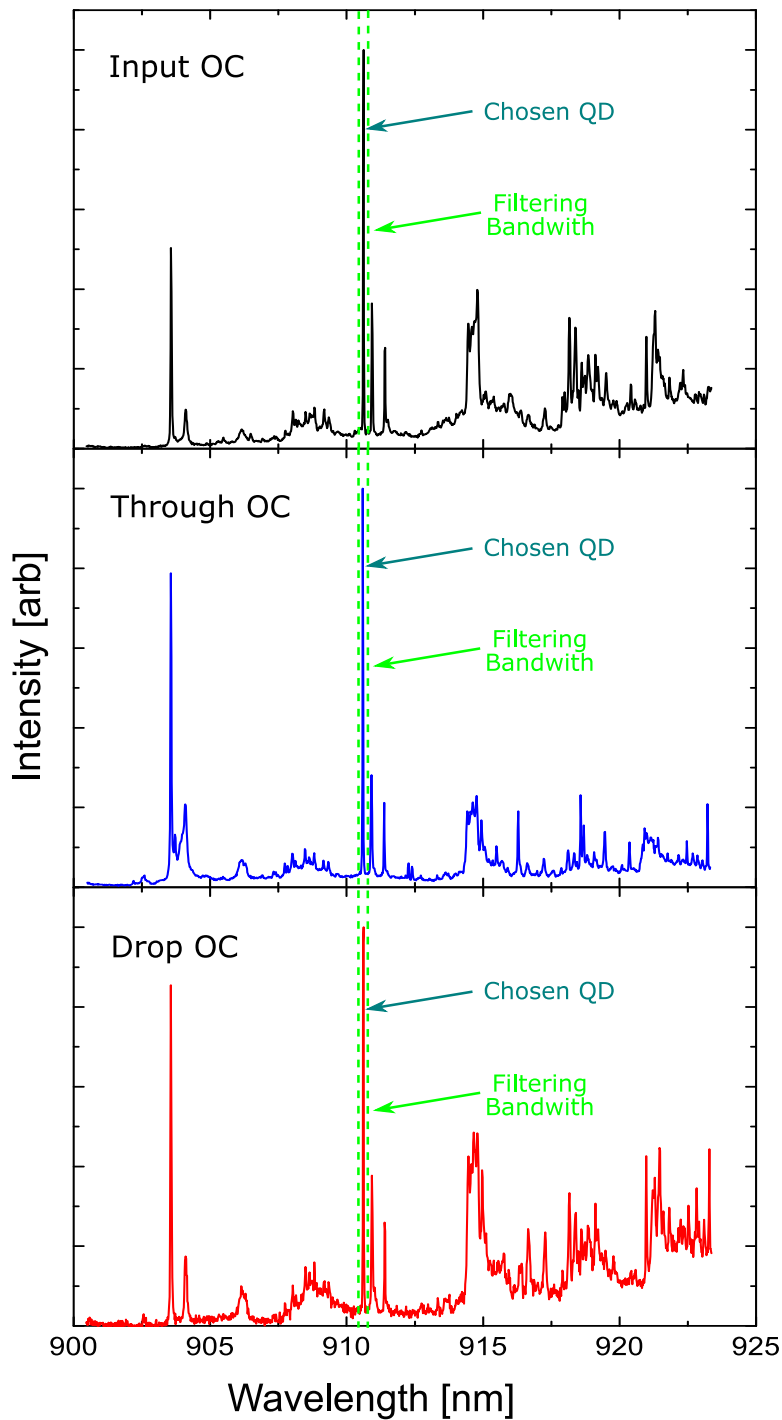


**Figure 5.13:** QD  $\mu$ -PL emission spectra obtained when exciting the wetting layer at the input OC and collecting signal from the input, through and drop OCs. All spectra are normalised to the chosen QD emission line.

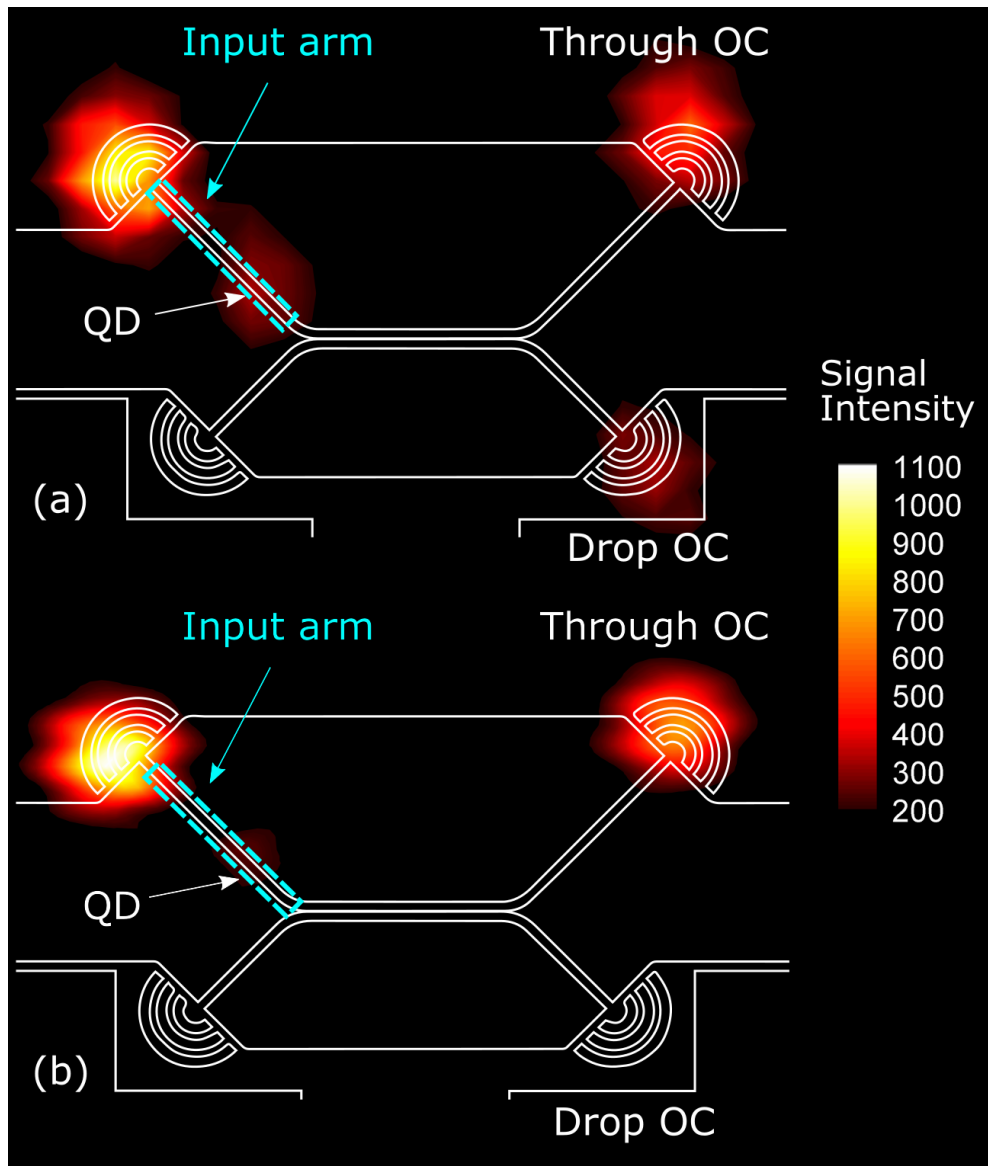


**Figure 5.14:** Filtered  $\mu$ -PL collection maps of the device with an overlaid device contour with (a)  $V_{act} = 0$  V, and (b)  $V_{act} = 12.5$  V.

ase. Hence, all of the light is observed to be routed to the through OC when  $V_{\text{act}} = 12.5 \text{ V}$ .

The single-photon nature of the emission from this QD was verified by performing an on-chip Hanbury Brown and Twiss experiment (see Section 3.3.3), which consisted of cross-correlating the photons at the QD wavelength collected by two separate paths from the input OC. The results, shown in Figure 5.15, yield a normalized value of  $g^{(2)}(0) = 0.25 \pm 0.02$ . By deconvoluting the experimental data with the temporal response of the detection system used (Gaussian, with a FWHM =  $874 \pm 4 \text{ ps}$ ) a value of  $g^{(2)}(0) = 0.00 \pm 0.01$  was obtained, which indicates that the source is strongly antibunched.

To characterize the device at increasing out-of-plane waveguide separation, the routed QD emission was measured simultaneously from the through (fixed) and the drop (moving) OCs using two independent collection paths as  $V_{\text{act}}$  was increased. The SR for the device at  $V_{\text{act}} = 0 \text{ V}$  was measured to be SR = 80:20. The absolute percentage change to the collected signal is shown in Figure 5.16 for the through and drop OCs separately. The signal is normalized to the total signal collected from both OCs at  $V_{\text{act}} = 0 \text{ V}$ . The change in the QD emission collected from the through OC increases monotonically until it saturates at  $\sim 17\%$  for  $V_{\text{act}} > 11 \text{ V}$ . The signal at the drop OC decreases initially as expected, but then recovers and peaks at  $V_{\text{act}} \approx 11.5 \text{ V}$  before decreasing again. This is caused by the downward movement of the drop OC as  $V_{\text{act}}$  is applied. It results in changes to the optical interference between the signal emitted from the OC and that reflected from the substrate. This effect has been modelled using the TMM (see Section 3.4.1), the result of which is presented in Fig. 5.17. The graph reflects the changes to the signal with respect to that at zero displacement ( $V_{\text{act}} = 0 \text{ V}$ ). As the cantilever displaces downwards when  $V_{\text{act}}$  is applied the signal that can be collected from the drop OC decreases quickly until it reaches a minimum at about 140 nm displacement. The signal then starts to increase until it reaches a maximum at about 360 nm displacement before decreasing again. The peaks and troughs expected from the changing interference effect during the movement of the drop OC explain the presence of them in the measured data. However, the movement of the drop OC (with increasing  $V_{\text{act}}$ ) will also induce some collection efficiency changes due to the varying collection angle, which are much more difficult to quantify.

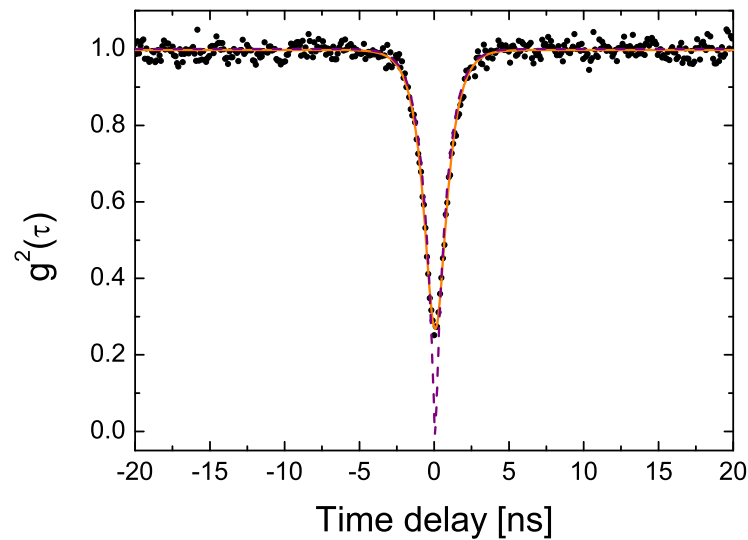


**Figure 5.15:** Normalized second-order correlation function obtained by exciting the QD from above and collecting the spectrally filtered  $\mu$ -PL signal from the input OC using two separate collection paths. The orange continuous line is a fit to the experimental data (black points), while the dashed purple line represents a fit that takes into account the time response of the measurement system.

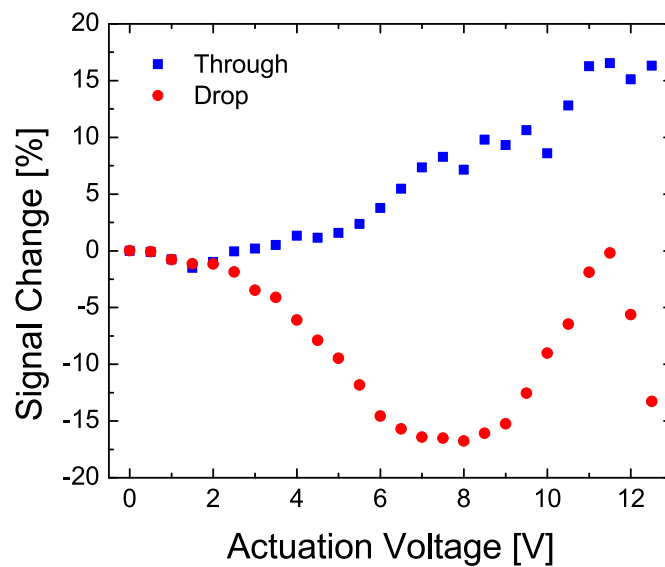


**Figure 5.16:** Measured changes to the QD signal collected from the through (fixed) and drop (moving) OCs independently, as the actuation voltage is increased. The signal is normalized to the total signal recorded from both OCs at  $V_{\text{act}} = 0$  V.

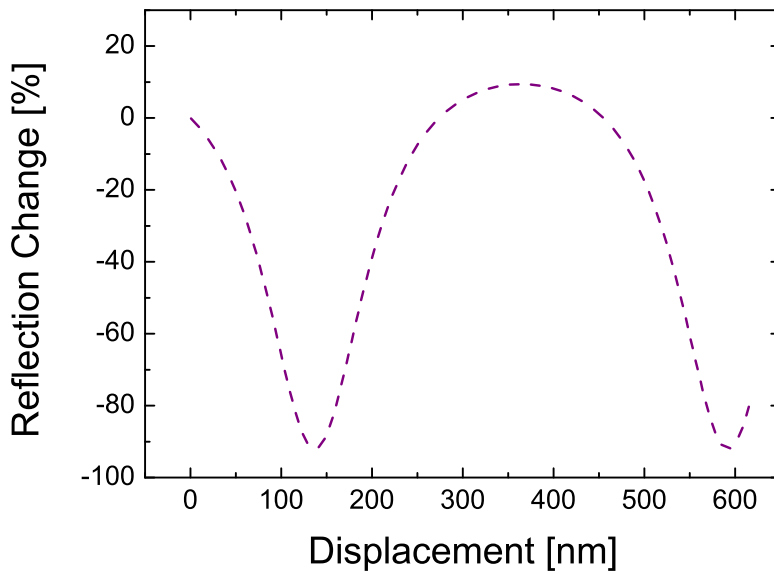


**Figure 5.17:** Theoretical changes to the reflection from an OC as its distance from the substrate decreases (with increasing displacement), based on the TMM.

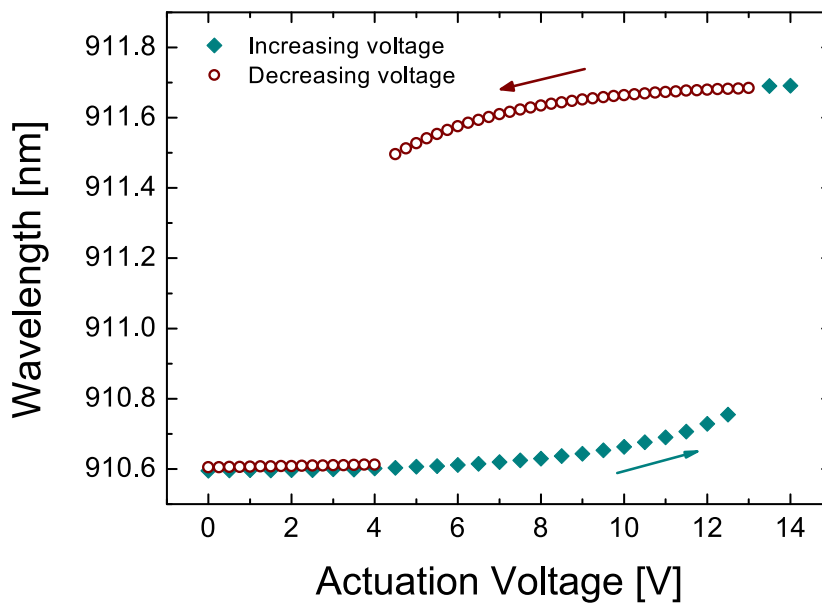


**Figure 5.18:** Measured changes to the emission wavelength of the QD as the actuation voltage is increased (filled squares) and then decreased (empty circles), demonstrating the hysteresis in the electro-mechanical behaviour of the cantilever.

The measurement with increasing  $V_{\text{act}}$  has also revealed a wavelength shift of the QD emission, which is plotted in Figure 5.18. This is clearly caused by the QCSE (see Section 2.1.3), even though the biasing of the QD is unintentional. Since the bottom  $p$ -layer in the membrane is contactless it remains at a certain potential that cannot be controlled. As  $V_{\text{act}}$  is applied to the top  $p$ -layer a potential difference between the two layers is created, which results in the QCSE (see Figure 5.9 for the wafer structure used). The resulting wavelength red-shift is small, less than 0.2 nm, up to  $V_{\text{act}} = 12.5$  V. Once  $V_{\text{act}}$  reaches the value  $V_{\text{pull}} = 13$  V, when the cantilever collapses down onto the substrate the emission wavelength red-shifts considerably by another 0.9 nm. When the cantilever touches the substrate a path is created for current to flow freely between the grounded  $n$ -substrate and the actuated top  $p$ -layer with a large potential difference of 13 V, and hence the QCSE has a much bigger influence on the QD. When the voltage is then decreased the same hysteresis in the QD emission wavelength is observed as in the electro-mechanical behaviour of the cantilever. The wavelength blue-shift is small at first as  $V_{\text{act}}$  is decreased since the cantilever slowly peels away from the substrate (see Figure 5.11). When  $V_{\text{act}}$  reaches 4 V, which is exactly the lifting point of the cantilever, the wavelength blue-shifts by 0.9 nm back to the original value of 910.6 nm.

In order to directly compare the controlled optical properties of the DC with the modelling (shown in Figure 5.2),  $V_{\text{act}}$  was converted to cantilever displacement, by rearranging Equation (5.2) to obtain:

$$V_{\text{act}} = \frac{(z_0 - d)\sqrt{d}}{X}, \quad (5.5)$$

The parameter  $X$  was found based on the pull-in point of the cantilever, which occurs at  $d = z_0/3 = d_{\text{pull}} = 667$  nm. As the value of  $V_{\text{pull}}$  determined through the modelling was different from the experimentally observed value, two parameters can be used here. By first using the theoretical  $V_{\text{pull}}$ , the proposed approach of relating  $V_{\text{act}}$  to cantilever displacement can be compared to the modelling. The values of  $V_{\text{pull}}$  were found to be 7.5 V using analytical modeling (see Figure 5.7), and 7 V using the FEA method (see Section 3.4.2). Choosing a mean value of 7.25 V for  $V_{\text{pull}}$  gives  $X_{\text{mod}} = 4750 \text{ (nm)}^{3/2}\text{V}^{-2}$ . Figure 5.19 shows the comparison of the displacement of the cantilever (up to the pull-in point) as a function of  $V_{\text{act}}$  for the three methods that were used to find this

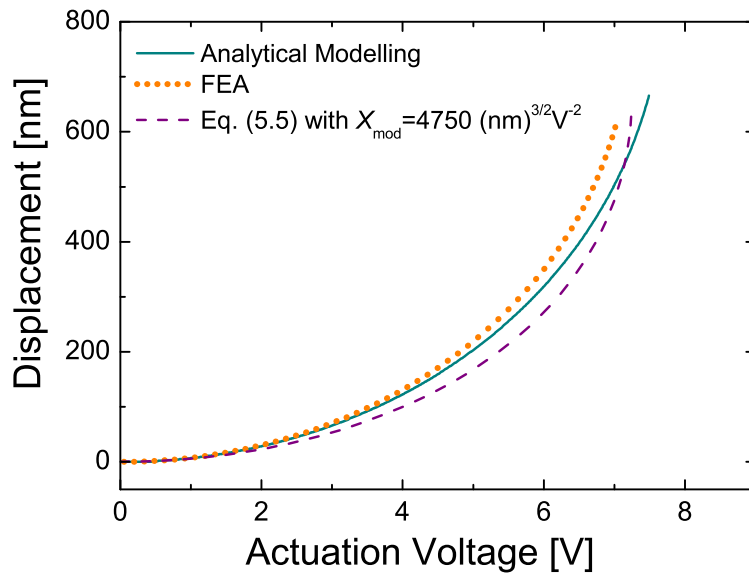


**Figure 5.19:** Comparison of the cantilever displacement as a function of actuation voltage (up to the pull-in displacement of  $z_0/3$ ), found using: analytical modelling (solid line) as shown previously in Figure 5.7, FEA (dotted line), and that derived using Equation (5.5) with  $X_{\text{mod}} = 4750 \text{ (nm)}^{3/2} \text{V}^{-2}$  (dashed line).

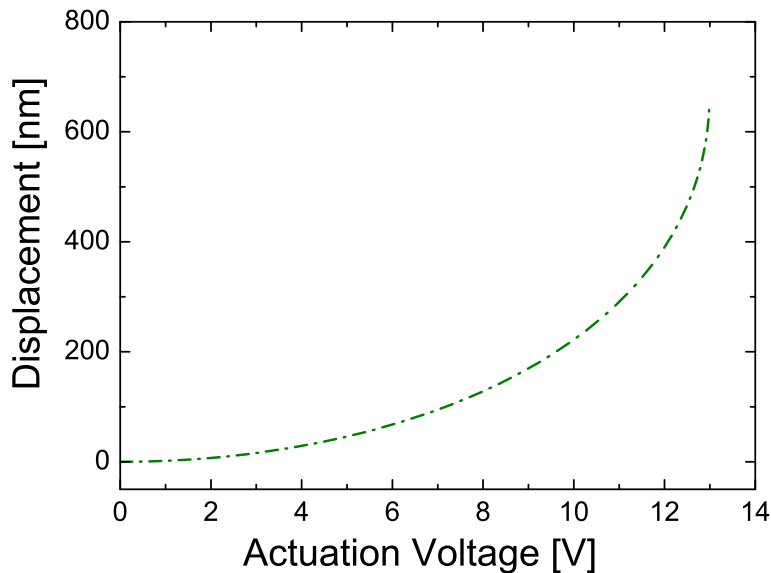


**Figure 5.20:** Estimated experimental cantilever displacement as a function of actuation voltage based on the observed pull-in voltage of 13 V.

relationship (analytical modelling, FEA, and Equation (5.5) with  $X = X_{\text{mod}}$ ). The three curves give similar results, which validates the proposed conversion method.

As the value of  $V_{\text{pull}}$  found experimentally for the device was 13 V the parameter  $X$  for the measured system is  $X_{\text{exp}} = 2650 \text{ (nm)}^{3/2}\text{V}^{-2}$ . Using this value  $V_{\text{act}}$  can then be converted to the actual cantilever displacement observed in the measured device using Equation (5.5) with  $X_{\text{exp}}$ . The resulting relationship is plotted in Figure 5.20.

By converting cantilever displacement to  $V_{\text{act}}$  using this relationship, the variation in signal due to the interference effect on the drop OC can be directly compared to the measured signal. Figure 5.21 shows the changes to the recorded emission from the drop OC (previously shown in Figure 5.16) with respect to the signal at  $V_{\text{act}} = 0 \text{ V}$ , and the interference effect changes (previously shown in Figure 5.17 as a function of cantilever displacement) as a function of  $V_{\text{act}}$ . The large peak and trough, which dominate the changes observed from the drop OC, match well those expected from the modelled changes to the interference effect. This again supports the validity of the method used to convert  $V_{\text{act}}$  into cantilever displacement. It also validates the reason proposed for the results obtained from the drop OC.

As the measured data from the drop OC are dominated by the interference effect changes it is unreliable to determine the changes to the SR due to the electro-mechanical actuation of the cantilever based on this OC. Therefore, the SR changes need to be found using the through OC only. By converting  $V_{\text{act}}$  to cantilever displacement the QD emission routed to the through OC can be compared with that calculated using the eigenmode solver [see Figure 5.2(b)]. The experimental curve is in the best agreement with the theoretical curve for  $s_{\text{in}} = 82 \text{ nm}$ , presented in Figure 5.22 as a function of cantilever displacement. The two curves demonstrate a monotonic increase of the QD signal until saturation at 17% for displacements of over 300 nm. This demonstrates the control of the SR of the DC from 83:17 to 100:0 using electro-mechanical actuation of the cantilever. The initial SR based on the measured signal change in the through OC, 83:17, is in good agreement with that measured by comparing the QD emission from the through and drop OCs,  $\text{SR}_{\text{both}} = 80:20$ . The small difference between the two ratios is likely to be related to the uncertainty in aligning the two collection paths over the through and drop OCs with the

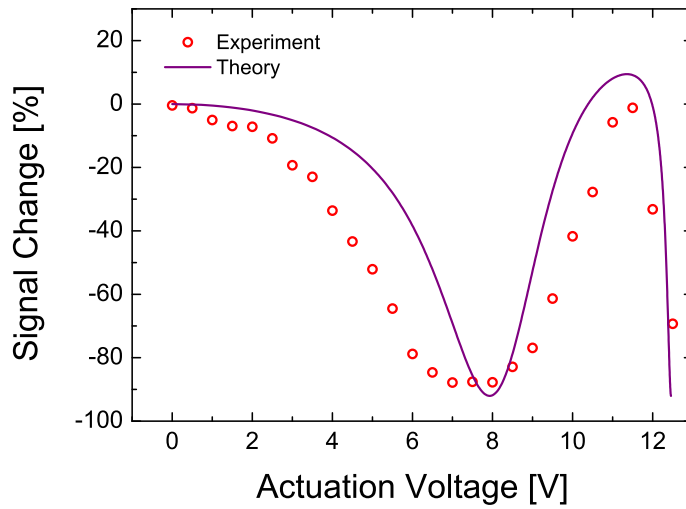


**Figure 5.21:** Percentage change of the QD signal collected from the drop OC with respect to the signal recorded from that OC at 0 V (red empty circles). The continuous purple line shows the expected reflection changes (already shown in Figure 5.17) but as a function of actuation voltage (converted from displacement using the derived relationship in Figure 5.20).

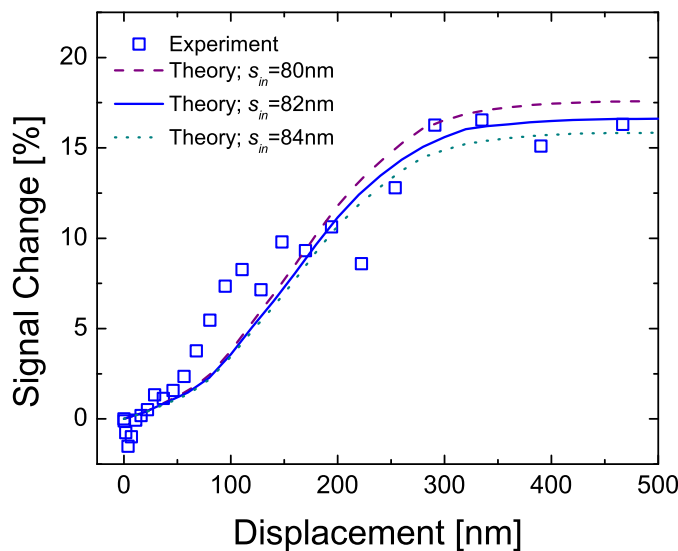


**Figure 5.22:** Experimental results (empty squares) for the through OC from the graph in Figure 5.16 as a function of displacement converted from actuation voltage using the relationship in Figure 5.20. The other three lines are theoretical curves for  $s_{in}$  of 80, 82, and 84 nm normalized to the initial signal at zero displacement.

same efficiency for the  $SR_{\text{both}}$  measurement. The achieved displacement of the cantilever was found to be over 400 nm, which is considerably larger than demonstrated in any other GaAs-based MOEMS.

## 5.6 Summary and Outlook

In conclusion, electro-mechanical control of an on-chip beam splitter operating at low temperature using out-of-plane actuation, with large achievable displacements of over 400 nm, has been demonstrated. Emission from an embedded QD was used to probe the optical response of the system. The splitting ratio of the on-chip optical beam splitter was tuned from  $\sim 83:17$  at  $V_{\text{act}} = 0$  V (zero displacement) up to  $\sim 100:0$  at  $V_{\text{act}} = 11$  V (300 nm displacement). The single photon nature of the quantum emitter was confirmed through auto-correlation measurements. The proposed device operates as a fine-tuning element and can be adapted to control other on-chip photonic elements for QIP applications, such as nanobeam PhCC modes, or Mach-Zehnder interferometers. It represents a significant step towards reconfigurable integrated III-V semiconductor quantum optical circuits with embedded single photon sources using compact, easy-to-fabricate and scalable structures.

Greater versatility and scalability of the system can be achieved through some improvements to the sample design, including the elimination of the problem arising from the movement of the drop OC during the cantilever actuation [152]. This could enable the device to operate as an optical router. Further optimization of the dimensions of the DC can overcome the difficulties in achieving small enough in-plane separations needed in the reported device for a larger tuning range covering the commonly required 50:50 splitting. Increasing the coupling length of the DC or decreasing the cross section of the waveguides are examples of promising approaches that are worth investigating. Fabricating this structure on a *p-i-n-i-n* diode and depositing a third contact on the middle *n*-layer would enable tuning of the QD emission wavelength using the QCSE [27], at the same time as controlling the beam splitter electro-mechanically. The actuation voltage could also be decreased by using either a longer cantilever or a thinner AlGaAs sacrificial layer, thus reducing the initial distance between the two electrodes. A suggested improved wafer structure is shown in Figure 5.23.

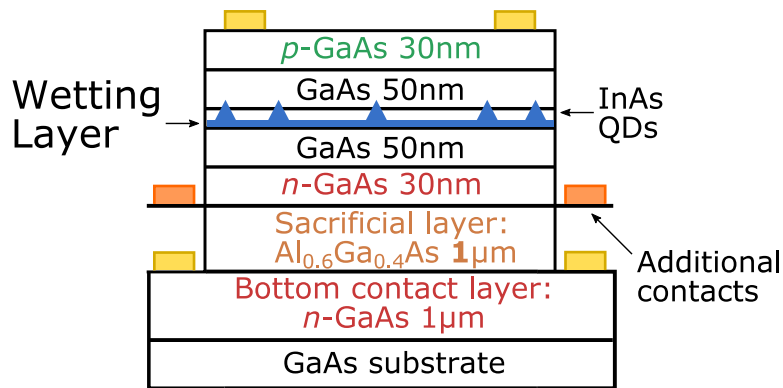


**Figure 5.23:** Schematic diagram of the suggested improved wafer structure. The position of the Ni:Au contacts is marked by (gold for existing and orange for additional) rectangles.

## Chapter 6

# Development of Electro-Mechanical In-Plane Actuators for the On-Chip Tuning of Photonic Devices

On-chip electro-mechanical actuation can be used to tune the optical properties of photonic devices, as discussed and demonstrated in Chapter 5. The benefits of such control can be utilized in many aspects of the physical realizations of integrated quantum optical circuits (IQOCs) [165]. Examples include correcting for fabrication imperfections [159], routing of light on a chip [113], optical switching [147–151] and alternating between the strong and weak coupling regimes of light-matter interaction for cavity quantum electro-dynamics (cQED) applications (see Section 2.3) [153].

In the previous chapter the design, fabrication and testing of a cantilever-based electro-mechanical actuator was presented. The proposed system operated by displacing one of the waveguides out-of-plane with respect to the other, thereby allowing to tune the splitting ratio of a beam splitter. While this was the first demonstration of such control on a GaAs substrate with embedded InAs quantum dots (QDs) acting as single-photon sources, the device has some limitations. In particular, a cantilever displacement of about 300 nm was required to achieve maximum control over the splitting ratio, necessitating a rather large actuation voltage of 11 V. Whilst the actuation voltage could be decreased in this system by reducing the initial distance between the electrodes, this would also diminish the maximum achievable displacement of the

cantilever, and hence the amount of optical tuning. In addition, issues with fabricating nanobeam waveguides in close proximity to each other, in order to enhance the coupling between them, limited the range of achievable control over the splitting ratio. In this chapter these shortcomings are addressed by proposing electro-mechanical systems that offer in-plane rather than out-of-plane actuation.

So far the majority of reported studies of micro-opto-electro-mechanical systems (MOEMS) on GaAs have focused on out-of-plane actuation methods, and hence in-plane actuation is a novel approach in this platform. Nevertheless, this has been the preferred mechanism for Si-based devices as it offers better control over the photonic properties for similar electro-mechanical performance of the systems. This is demonstrated through the optical modelling of a directional coupler that is presented in the following section. By utilising variation in the in-plane separation between the waveguides, less than 150 nm displacement is required to achieve the maximum control over the splitting ratio of a beam splitter. This is half the distance needed when using the out-of-plane approach presented in Chapter 5. In addition, using an in-plane actuation method could circumvent the need to fabricate two nanobeam waveguides in close proximity in order to gain maximum control over the optical properties of the structures. By designing an actuation system that brings the two waveguides closer together the fabricated in-plane separation can be large and still not affect the amount of achievable tuning. Such structures could bring a single-photon GaAs optical switch a step closer to realization.

In this chapter electro-magnetic modelling of two specific photonic systems is first presented in order to demonstrate the amount of control over the optical properties that can be achieved by changing the in-plane separation between the structures. The two systems chosen are a directional coupler and one that allows the tuning of a photonic crystal cavity (PhCC) mode. By controlling the resonant wavelength, the propagation of QD emission through a PhC filter could be turned on and off, thereby effectively acting as an optical switch. Alternatively, the tuning could be used to alter between the weak and strong coupling regimes of light-matter interaction for cQED applications. The design, fabrication and development of two different types of electro-mechanical in-plane actuators that could be used to realize this tuning is then presented. These are the so-called metal rail and comb-drive actuators. This

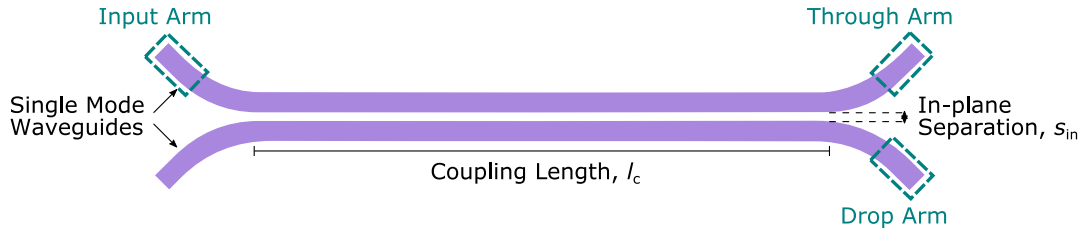


**Figure 6.1:** Schematic diagram of a directional coupler consisting of two single-mode waveguides separated laterally by distance  $s_{in}$  in the coupling region of length  $l_c$ .

is followed by a summary of the achieved progress and a discussion of recommended further developments that are likely to lead to very promising experimental results.

## 6.1 Control of Optical Properties Using In-Plane Actuation

### 6.1.1 Directional Couplers

A schematic diagram of a directional coupler (DC) acting as a beam splitter [previously shown in Figure 5.1(a)] is presented again in Figure 6.1. In Section 5.2.1 results of the electro-magnetic modelling of this structure as a function of the out-of-plane separation of the waveguides were presented and discussed for two in-plane separations,  $s_{in}$ , between the waveguides. By contrast, Figure 6.2 now presents simulation results for coplanar waveguides of the same dimensions for a range of values of  $s_{in}$ . The modelling was likewise undertaken using MIT Photonic-Bands (see Section 3.4.1). As observed previously, the larger is the in-plane separation between the waveguides the more light is transmitted to the through arm of the DC. Therefore, by controlling this parameter electro-mechanically an optical switch can be realized on a chip. Figure 6.2(b) demonstrates this behaviour for a single wavelength of 910 nm, as previously. One sees clearly that displacing the drop arm of a DC in-plane by  $\sim 120$  nm from a separation of 30 nm to 150 nm would allow one to tune the operation of a beam splitter from highly overcoupled, with only  $\sim 5\%$  of light transmitted to the through arm, to completely decoupled, with  $\sim 100\%$  of signal reaching the through arm, through the commonly re-

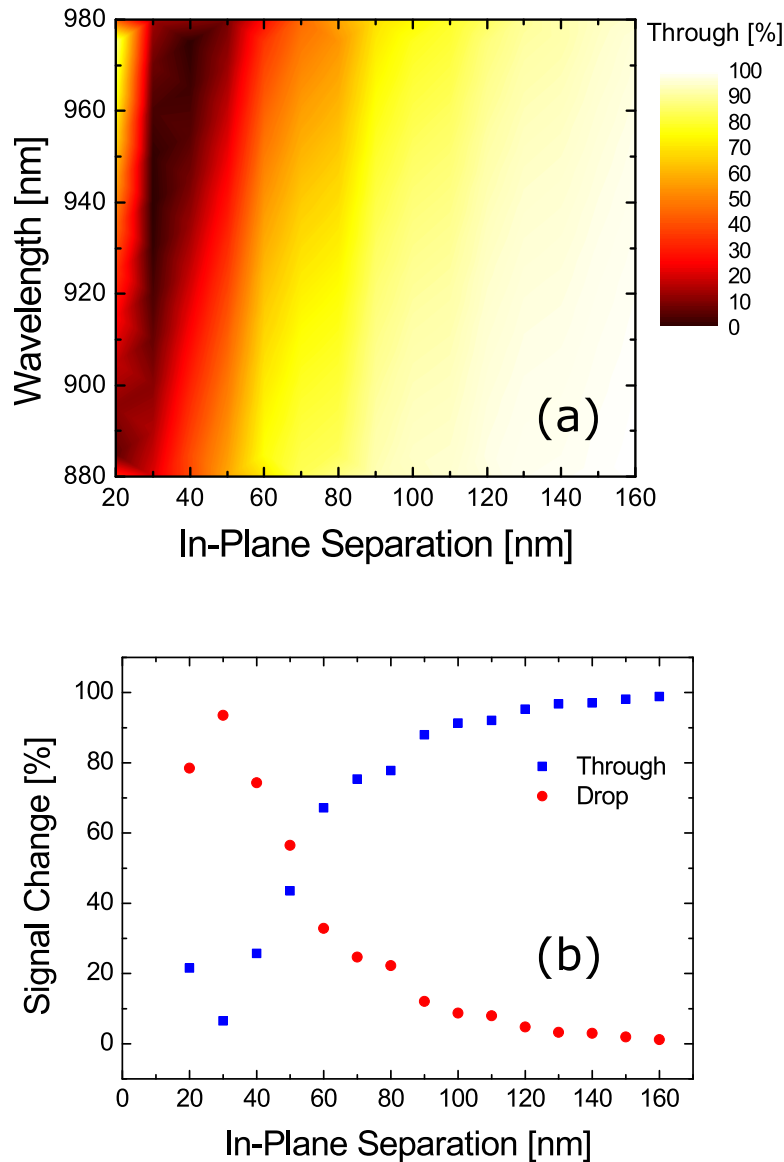


**Figure 6.2:** Results of the optical modelling of a directional coupler consisting of 160 nm thick and 280 nm wide coplanar waveguides with a  $7 \mu\text{m}$  long coupling region. (a) The contour plot shows how the fraction of light evanescently coupled from one channel to the other depends on the wavelength of the transmitted light and the in-plane separation between the waveguides. (b) Changes to the signal transmitted in the fixed arm (through) and coupled to the moving arm (drop) as a function of in-plane displacement for a wavelength of 910 nm.

quired 50:50 splitting in between at  $s_{\text{in}} \approx 50$  nm. By using a QD emitting at slightly longer wavelength, for example 920 nm, a full 100 % tuning range necessary for optical routing and switching applications could be reached using this approach. This is a much more efficient way of controlling the splitting ratio than through the out-of-plane actuation, which required a displacement of  $\sim 300$  nm to achieve a tuning range of just under 20 %.

### 6.1.2 Nanobeam Photonic Crystal Cavities

As discussed in Section 2.6 PhCCs are Fabry-Perot type optical resonators, which allow resonant tunnelling of wavelengths that satisfy the following condition:

$$\lambda = 2n_{\text{eff}}L, \quad (6.1)$$

where  $n_{\text{eff}}$  is the effective refractive index of the modes within the medium and  $L$  is the length of the optical cavity. Therefore, in order to tune the resonant wavelength of a physical nanobeam PhCC one can take two approaches. One of them is to change  $L$  by, for example, stretching the device. The disadvantage of using this method is that the resulting stresses within the membrane will affect the electronic structure of quantum dots (see Section 2.1.1) embedded in its centre [166–169]. The other approach is through modifying  $n_{\text{eff}}$ . Various techniques of achieving this have been proposed and reported in the literature, each having their own advantages and disadvantages. They can be classified into two types: direct, caused by internal perturbation; and indirect, caused by the change in overlap of the optical mode with the structure [170].

Examples of direct tuning methods include the thermo-optic [171, 172], electro-optic [173, 174] and acousto-optic [175, 176] effects. However, controlling  $n_{\text{eff}}$  through temperature, for example, often requires high operating powers (of tens or hundreds of mW), which can cause problems with heat dissipation on the chip [177, 178]. On the other hand, both the electro-optic and acousto-optic approaches suffer from the fact that they require a relatively large device footprint (of the order of a few millimetres in linear dimension) due to the range of tuning that can be achieved with these methods [179, 180].

Therefore, indirect methods for tuning the parameter  $n_{\text{eff}}$  of optical on-chip cavities offer promising alternatives. In order to modify the amount of

overlap of the optical resonator mode with the structure, the device has to be displaced mechanically. This can be achieved by using either optical or electrical forces leading to opto-mechanical and electro-mechanical reconfiguration techniques respectively. While the opto-mechanical approach requires a steady-state hold power for a reconfigured state, the unavoidable introduction of the electrical contacts demanded by the electro-mechanical method also increases the footprint of the devices. Therefore, in this chapter, two different in-plane electro-mechanical actuators are presented that allow the on-chip tuning of a PhCC mode by controlling the overlap of the mode with the device.

The two proposed device designs that are first investigated through electromagnetic modelling are presented in Figure 6.3. Both of them consist of a nanobeam PhC filter (similar to those studied in Chapter 4) and a perturbing nanobeam structure in a coplanar configuration and separated laterally by a distance  $s_{in}$ . This in-plane separation between the two elements will determine the amount of overlap of the filter mode with the perturbing structure, and hence also  $n_{eff}$  and the resonant wavelength of the PhCC.

A structure similar to that shown in Figure 6.3(a) has been studied for cQED applications by Ohta et al. [153]. Placing a nanobeam waveguide next to a PhCC allows for a part of the optical power of the resonator to couple to the waveguide due to evanescent coupling between the two, just as in the case of two nanobeam waveguides forming a beam splitter that was discussed earlier and in Chapter 5. This means that the light will leak from the PhCC into the waveguide, thereby decreasing the resonator strength and hence also the Q-factor. Tuning the Q-factor of a PhCC can allow switching between the weak and strong coupling regimes of light-matter interaction (see Section 2.3). However, if the aim now is to tune the PhCC mode wavelength to match that of a QD emission to allow its transmission through a nanobeam filter then the challenge is to retain the highest possible Q-factor. For this reason a variation of this configuration is also studied. By using a nanobeam PhC instead of a waveguide as the perturbing element [as demonstrated in Figure 6.3(b)] the transfer of the optical power to the perturbing structure is suppressed. A nanobeam PhC of the same dimensions as the filter, but without the displacement defect between the two centre holes that creates an optical cavity, exhibits an optical band gap over the same wavelength range but includes the resonant wavelength of the filter. This allows to diminish the decrease in the

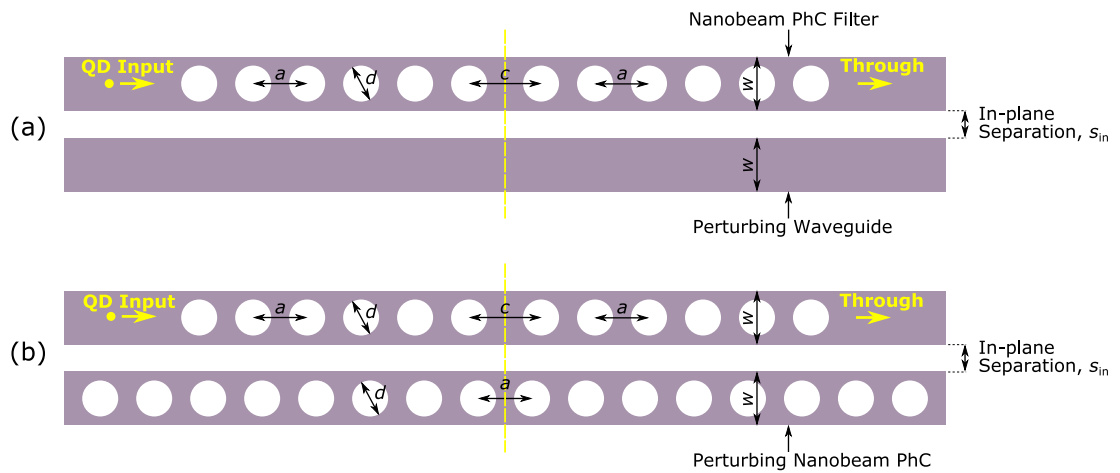


**Figure 6.3:** Schematic diagrams of the proposed systems for the tuning of a nanobeam photonic crystal cavity by varying the in-plane separation,  $s_{in}$ , between the device and (a) a perturbing nanobeam waveguide, and (b) a perturbing nanobeam PhC.

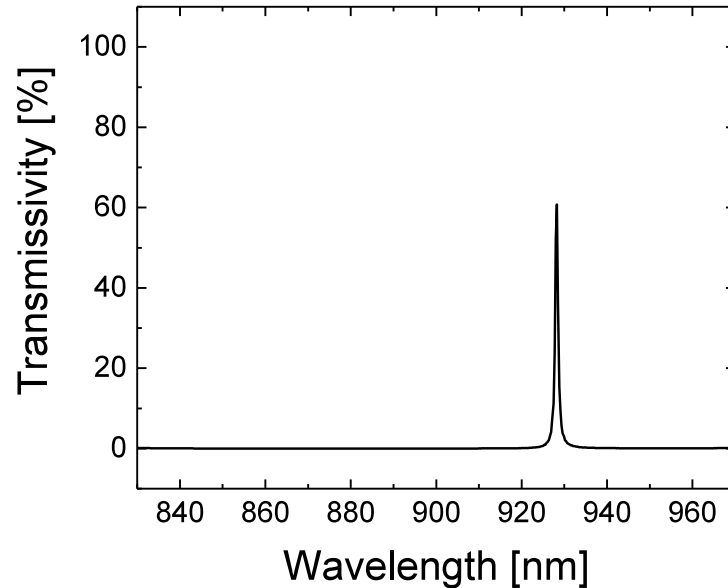


**Figure 6.4:** Transmissivity of light through a PhC filter (with the following parameters:  $t = 140$  nm,  $w = 280$  nm,  $a = 240$  nm,  $d = 100$  nm,  $c = 360$  nm and  $n = 6$ ) versus wavelength.

Q-factor of the filter for smaller in-plane separations between the filter and the perturbing structure.

The parameters of the PhC filter studied through FDTD electromagnetic simulations (see Section 3.4.1) are as follows: thickness  $t = 140$  nm, width  $w = 280$  nm, PhC period  $a = 240$  nm, hole diameter  $d = 100$  nm, distance between the two centre holes  $c = 360$  nm and the number of holes on either side of the cavity  $n = 6$ . Figure 6.4 presents transmissivity results for the filter without any perturbing structure present, when light is injected from one side of the device to the other as indicated in Figure 6.3 as QD Input and Through respectively. The designed mode wavelength is  $\sim 928.3$  nm with a full-width at half-maximum (FWHM) of  $\sim 0.74$  nm and a Q-factor of  $\sim 1250$ .

The results of the FDTD electromagnetic modelling of the two systems that allow tuning of the PhC filter mode are presented in Figures 6.5-6.9. Figure 6.5 illustrates the relationship between the filter mode wavelength and the in-plane separation,  $s_{in}$ , between the filter and each of the perturbing structures. As  $s_{in}$  decreases the resonant wavelength experiences a red shift for both perturbing structures. However, the maximum wavelength shift is appreciably larger when the nanobeam PhC is used as the perturbing device rather than the nanobeam waveguide. The former causes an 8.1 nm change to the filter's wavelength when  $s_{in}$  varies between 40 nm and 180 nm, while the latter tunes it by 5.9 nm over the same range of  $s_{in}$ . Most of this 2.2 nm difference between the two shifts occurs for the smaller in-plane separations of 40 – 80 nm. This is rather intuitive, as the closer is the perturbing structure to the filter the more will the filter mode overlap and interact with it. At larger separations the mode overlap diminishes to zero and hence its wavelength approaches that of a individual PhC filter at  $\sim 928$  nm. This causes larger shifts for smaller separations. It also explains the larger shift observed for the PhC in comparison to the waveguide. At smaller separations the field overlaps more with the periodic hole structure of the PhC, which acts as a mirror for the optical mode of the filter, unlike the waveguide, which supports the propagating wavelength. At larger separations this overlap decreases and hence the difference in the red shift is also suppressed. This is illustrated in Figure 6.7, which shows the  $E_y$  component of the electromagnetic mode of the filter at two different in-plane separations of 40 nm and 120 nm from the two perturbing structures.

Figure 6.6 demonstrates the dependence of the FWHM of the cavity mode

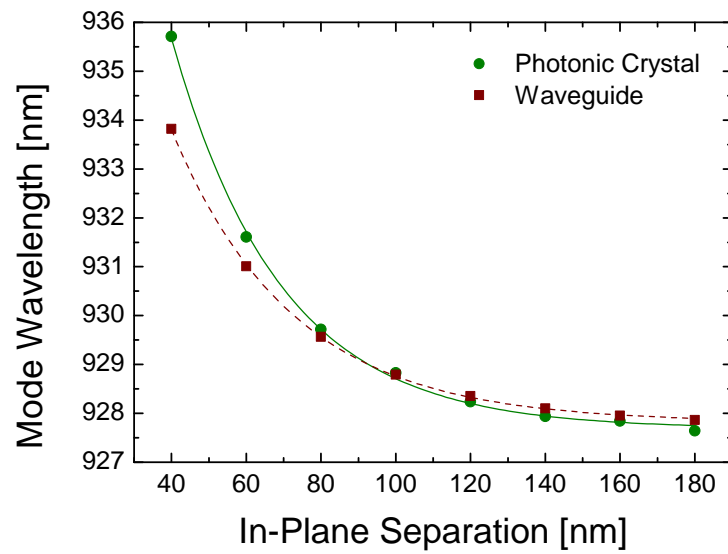


**Figure 6.5:** Simulation results showing how the mode wavelength of the nanobeam photonic crystal filter varies with respect to the in-plane separation,  $s_{in}$ , from both a perturbing nanobeam photonic crystal and a perturbing nanobeam waveguide.

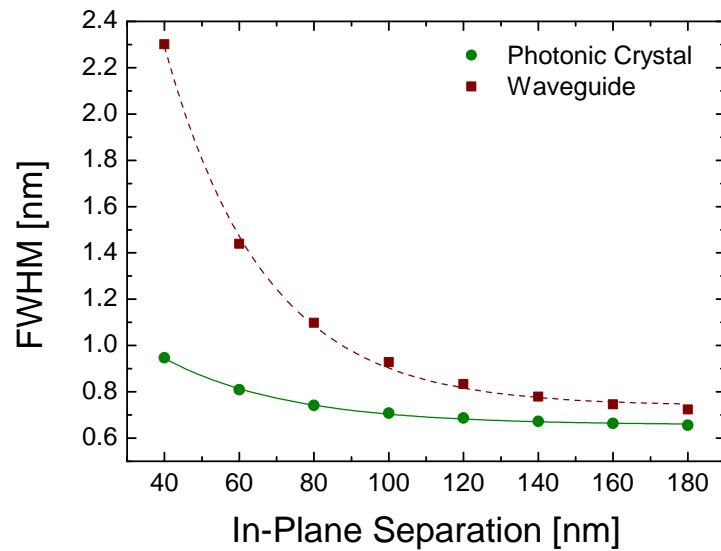


**Figure 6.6:** Simulation results demonstrating how the full-width at half-maximum of the spectral peak of the nanobeam photonic crystal filter varies with respect to the in-plane separation,  $s_{in}$ , from both a perturbing nanobeam photonic crystal and a perturbing nanobeam waveguide.

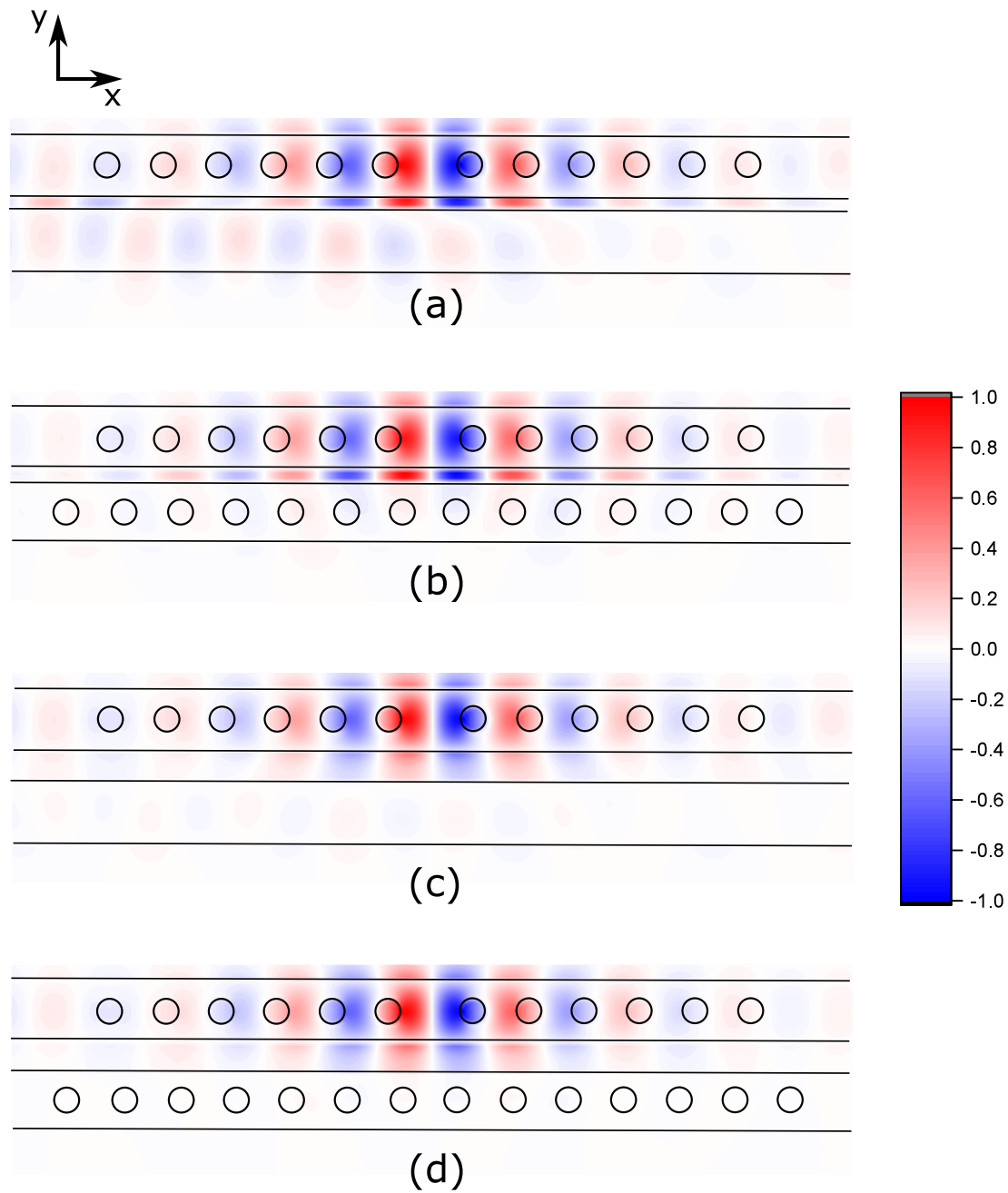


**Figure 6.7:** Modelling results for the  $E_y$  component of the electromagnetic mode of the PhC filter separated laterally from a coplanar nanobeam (a) waveguide by  $s_{in} = 40 \text{ nm}$ , (b) PhC by  $s_{in} = 40 \text{ nm}$ , (c) waveguide by  $s_{in} = 120 \text{ nm}$ , and (d) PhC by  $s_{in} = 120 \text{ nm}$ .

spectrum on the in-plane separation between the filter and the two perturbing nanobeam structures. As the separation decreases the FWHM increases as evanescent coupling from the filter to the perturbing structure increases. This time the larger effect is observed for the nanobeam waveguide, with the FWHM increasing from 0.75 nm by 1.54 nm to a value of 2.29 nm when  $s_{\text{in}}$  decreases from 180 nm to 40 nm, in comparison to the smaller increase of 0.28 nm for the nanobeam PhC. As discussed in Section 2.3, the FWHM is directly related to the photon loss rate of the cavity. Therefore, as evanescent coupling of light is stronger when the two structures are closer together, more photons escape from the PhCC to the perturbing device, thereby increasing the FWHM. This is exacerbated when the nanobeam waveguide is the perturbing device which, by contrast to the nanobeam PhC that has a photonic band gap at these wavelengths, allows light to propagate along it. This means that more photons will be allowed to leak out from the filter into the nanobeam waveguide than into the nanobeam PhC.

As mentioned in Section 2.3 and examined in detail in Chapter 4, the  $Q$ -factor, which relates the mode wavelength to the FWHM, is the figure of merit for optical cavities. Therefore, the  $Q$ -factor of the PhC filter is plotted against  $s_{\text{in}}$  for both perturbing structures in Figure 6.8. As expected, the  $Q$ -factor reduces with decreasing in-plane separation, but the undesirable change is smaller for the PhC than for the waveguide as the perturbing element. While the  $Q$ -factor experiences a reduction as high as 70 % between values of  $s_{\text{in}}$  of 180 nm and 40 nm for the waveguide, when the PhC is used instead that decrease is only about 30 %. This is a considerable improvement on this important figure of merit. Interestingly, the  $Q$ -factor does not saturate at the same values for both perturbing structures as  $s_{\text{in}}$  is increased. While for the system with a perturbing waveguide the  $Q$ -factor approaches that of a single PhC filter of  $\sim 1250$  for  $s_{\text{in}} = 180$  nm, the device with a perturbing PhC reaches a higher  $Q$ -factor of  $\sim 1400$ . This may be caused by the fact that the mode is *forbidden* to scatter out of the PhCC to one side by the presence of the nanobeam PhC there which acts as a mirror, thereby decreasing radiation losses from the filter.

Similar benefits are observed when transmissivity through the filter is studied (see Figure 6.9). While the transmissivity approaches  $\sim 60$  % (similar to the single filter) at large  $s_{\text{in}}$  for the waveguide, the same value for the perturbing PhC is  $\sim 70$  %. The transmissivity at smaller separations is also consi-

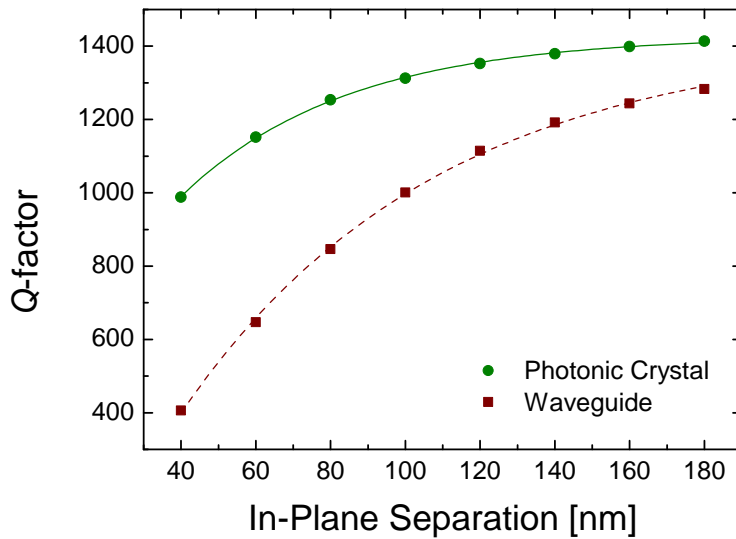


**Figure 6.8:** Simulation results showing the dependency of the Q-factor of the nanobeam photonic crystal cavity on the in-plane separation,  $s_{in}$ , from both a perturbing nanobeam photonic crystal and a perturbing nanobeam waveguide.

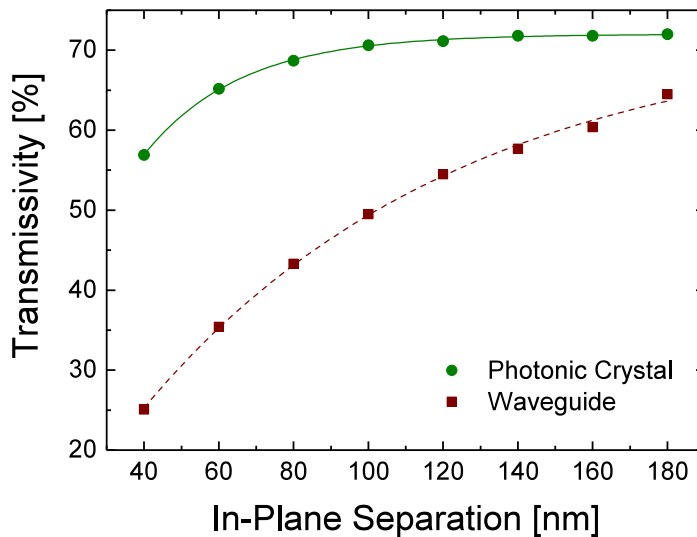


**Figure 6.9:** Simulation results showing the relationship between the transmissivity of resonant light through the nanobeam photonic crystal filter and its in-plane separation,  $s_{in}$ , from both a perturbing nanobeam photonic crystal and a perturbing nanobeam waveguide.

derably improved when the PhC, rather than the waveguide, is used for filter mode tuning. The reduction in transmissivity for the PhC is only  $\sim 20\%$  when  $s_{\text{in}}$  decreases from 180 nm to 40 nm while that for the waveguide is as high as 60% over the same range of  $s_{\text{in}}$ . Likewise, this is due to the evanescent field coupling between the two nanobeam structures, which is suppressed in the case of a PhC, which acts as a mirror for the resonant wavelength of the filter. This results in considerably more light coupling to the nanobeam waveguide (approaching directional coupler behaviour) than to the PhC, and hence much less light being transmitted through the filter.

In conclusion, using in-plane displacement of a nanobeam structure for tuning the wavelength of a PhC filter is a very promising approach to control single-photon propagation on a chip. It can provide several nanometers shift for relatively small displacements. Much better performance of the system is achieved when a nanobeam PhC is used as a perturbing device in comparison to a waveguide. Displacing the structure by  $\sim 140$  nm can achieve a wavelength shift of  $\sim 8$  nm with a corresponding reduction in the Q-factor and transmissivity of only 30% and 20% respectively. This large tuning would be more than enough to tune the resonant wavelength of a filter (with a FWHM of  $\sim 0.74$  nm) away from the QD emission, so that the propagation can be turned off (and back on), effectively making an optical switch.

## 6.2 Metal Rail Actuators

Perhaps the simplest way of displacing two nanobeam structures closer together using the electro-mechanical reconfiguration method is to apply an electrostatic potential difference between them. The resulting Coulomb attraction will then cause them to bend towards each other, effectively decreasing the distance between them. This approach has been used in the in-plane geometry for phase shifting in Si [138] as well as for the tuning of coupled PhCCs on GaAs [129]. However, this method has its disadvantages for integration with the quantum nano-photonic devices presented in this thesis. Firstly, any internal stresses within the waveguides caused by their direct bending can affect the QD emission. Secondly the profile of the bent waveguides means that the two would no longer be parallel to each other, *i.e.*, they would be closest to

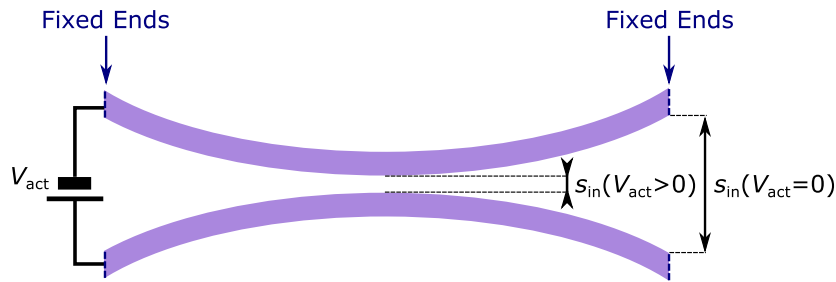


**Figure 6.10:** Schematic diagram of the profile of the two fixed-fixed nanobeam structures with an actuation voltage applied between them.

each other in their centre and furthest apart at the fixed ends (see Figure 6.10). This in turn may affect the mode coupling between the waveguides.

Even though this is a similar approach to that demonstrated in Chapter 5, these drawbacks were avoided in that system by using an out-of-plane cantilever geometry. Instead of a waveguide bending, the cantilever absorbed the stresses caused by deflection, and the waveguides remained parallel to each other during the electro-mechanical displacement. Likewise, researchers have been developing systems that would isolate the photonic device of interest from the electro-mechanical in-plane mechanism. One of the studied methods for phase shifting and tuning of the  $Q$ -factor of a nanobeam PhCC utilizes thin metal electrodes (*rails*) deposited on other pliable parts of the device so that their movement caused in-plane displacement of the nano-photonic structure indirectly [139, 153]. The design and development of electro-mechanical platforms for the tuning of DCs and PhCCs using this approach is discussed below.

### 6.2.1 Electro-Mechanical Modelling

Modelling of the electro-mechanical behaviour of a nanobeam with a metal rail has been performed using Comsol Multiphysics (see Section 3.4.2). In the simulation a thin and long GaAs waveguide (in a fixed-fixed beam configuration) with a metal rail on top of it was placed in close proximity to a much wider GaAs structure also covered in metal (see Figure 6.11). The wider structure was assumed to be fixed, as one of the electrodes would be attached to the bulk of the sample in an actual device. The Young's modulus material property used in the model was 85.5 GPa for GaAs [163] and 79 GPa for the

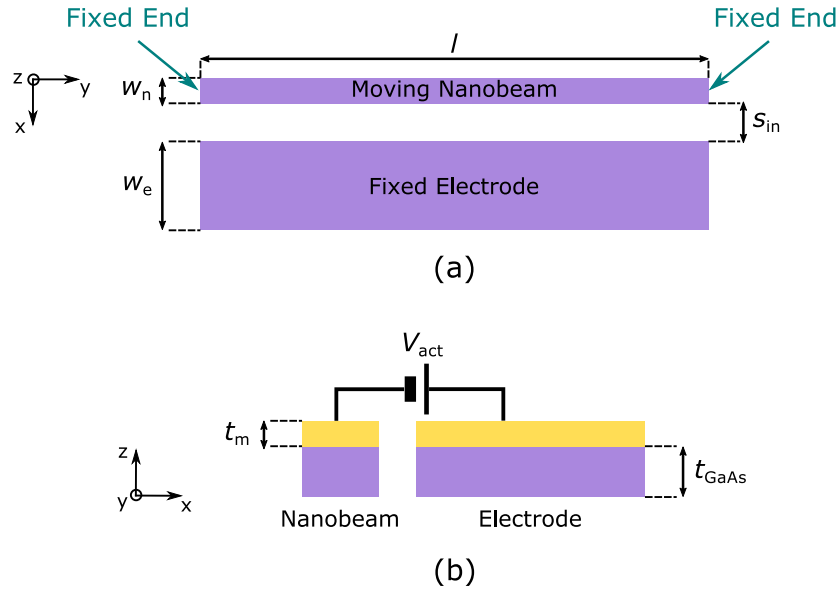


**Figure 6.11:** (a) Bottom- and (b) side-view schematic diagrams of the modelled electro-mechanical metal rail system. GaAs structures are marked in violet, while metal layers are shown in gold.

metal (gold) [181]. The thickness of the GaAs was set to be  $t_{\text{GaAs}} = 140 \text{ nm}$  (a typical membrane thickness for undoped wafers), the width of the electrode  $w_e = 1 \text{ }\mu\text{m}$  and the remaining dimensions for the initial model were as follows: length of both structures  $l = 40 \text{ }\mu\text{m}$ , width of the nanobeam  $w_n = 300 \text{ nm}$ , in-plane separation  $s_{\text{in}} = 150 \text{ nm}$  and thickness of the metal  $t_m = 100 \text{ nm}$ . The displacement of the nanobeam with grounded rail was monitored as actuation voltage,  $V_{\text{act}}$ , was applied to the wider electrode. The results are presented in Figure 6.12.

Figure 6.12(a) demonstrates the profile of the nanobeam with initial dimensions for  $V_{\text{act}} = 3 \text{ V}$ , with the horizontal axis indicating the distance from one end of the rail to the other ( $y$  direction in Figure 6.11), and the vertical axis showing the in-plane displacement of the nanobeam towards the electrode ( $x$  direction in Figure 6.11). It is clear that the maximum displacement occurs half way along the nanobeam.

Figure 6.12(b) presents the simulation results of the in-plane displacement at that point versus  $V_{\text{act}}$  for the model with the initial parameters as well as individually altered dimensions of  $l$ ,  $w_n$ ,  $s_{\text{in}}$  and  $t_m$ . The pull-in behaviour of the electro-mechanical device discussed in Section 5.2.2 applies to any such system [182], and hence the maximum controllable in-plane displacement for

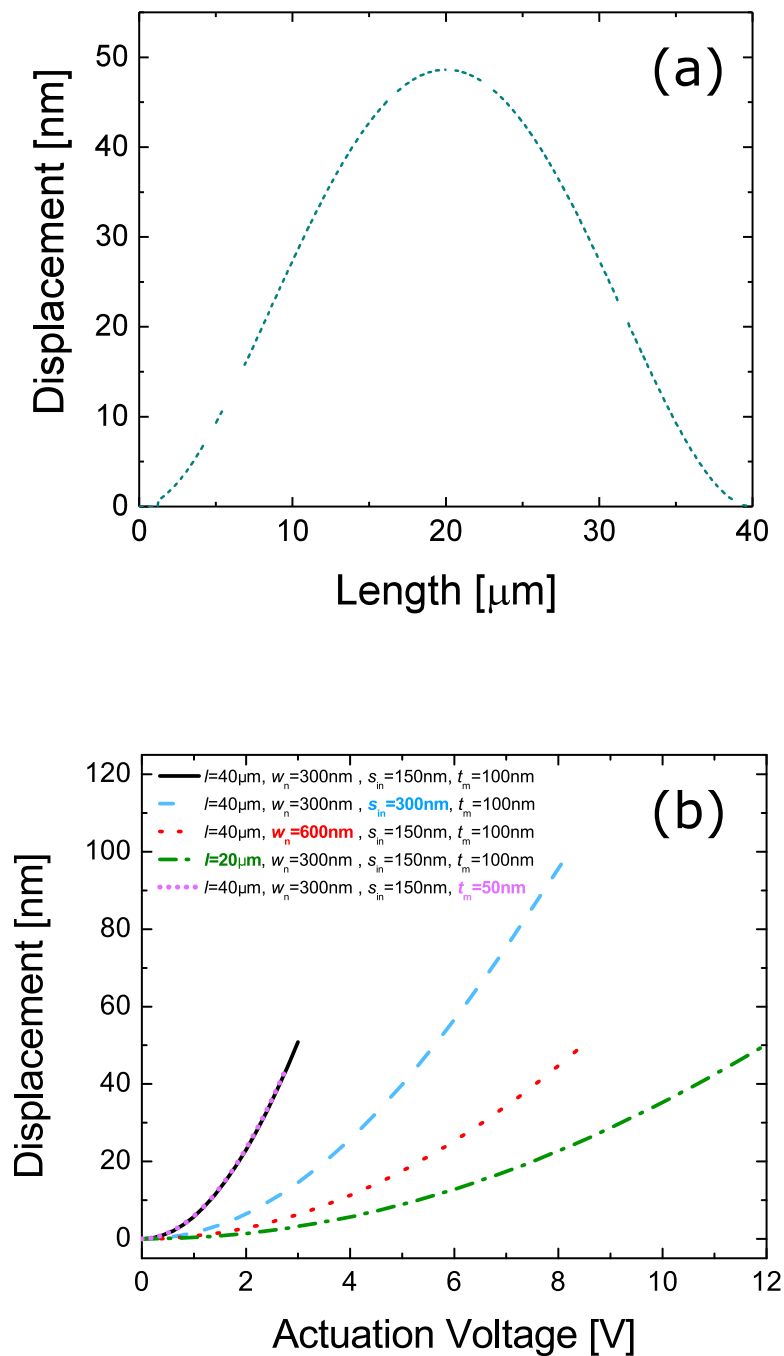


**Figure 6.12:** Results of the electro-mechanical simulations of the rail system presented in Figure 6.11. (a) In-plane displacement of the nanobeam versus position along its length for the model with initial dimensions and an actuation voltage,  $V_{\text{act}} = 3 \text{ V}$ . (b) Maximum in-plane displacement of the nanobeam versus actuation voltage for models with various dimensions.

this device is  $d = 50$  nm for  $s_{\text{in}} = 150$  and  $d = 100$  nm for  $s_{\text{in}} = 300$  nm. Doubling the initial in-plane separation between the two structures doubles their maximum possible displacement but also doubles the value of  $V_{\text{act}}$  required to achieve the same amount of movement. Altering the thickness of the metal contact has been found not to affect the displacement-voltage relationship. This is similar to the cantilever case, where its behaviour was observed to be independent of its width (see Section 5.2.2). In this system the width of the cantilever was the parallel dimension of the surface of the capacitor plate. In the in-plane nanobeam device discussed here, the corresponding dimension is the thickness of the structures. Similarly to the previous case, halving the length of the nanobeam increases  $V_{\text{act}}$  necessary to achieve the same displacement by a factor of 4. On the other hand, doubling the width of the nanobeam increases  $V_{\text{act}}$  by a factor of about 3 to achieve the same displacement.

## 6.2.2 Device Design, Fabrication and Testing

Our first design of an electro-mechanical in-plane metal rail actuator for controlling the splitting ratio of a directional coupler (DC) was based on experimental work of Winger *et al.* [139]. Their system was used on Si for phase-shifting an electromagnetic mode of a PhC waveguide. An adjusted design that meets the needs of the work discussed earlier in this chapter is presented in Figure 6.13(a) in a GDSII format used for fabrication (see Section 3.2.1). The grey areas represent the top GaAs membrane, while white ones indicate the etched regions. The metal rails are marked in yellow, while the green arrows indicate the direction of movement for each nanobeam.

The device consists of two separate flexible platforms that house each of the two waveguides of the beam splitter. These platforms are suspended and connected to the bulk of the wafer through two thin struts at each end. A thin metal rail is designed to run along the outside strut forming a fixed-fixed nanobeam. The nanobeam rail is then slowly widened as it reaches the bulk of the wafer in order to avoid using unnecessarily thin rails that, as will be discussed later, cause problems during fabrication. While the wider electrode is situated in close proximity to the nanobeam rail, the two are separated by an etched-away air gap. The electrode is rounded at the corners in order to avoid discontinuities in the electric potential between the two rails when  $V_{\text{act}}$

is applied. An air gap is also included on the outside of each vertical part of the electrode (running along the horizontal axis) to avoid current leakage through the intrinsic GaAs membrane between the electrode and the nanobeam. The air gaps are more visible in Figure 6.13(b), which shows an SEM image of one of the best fabricated devices.

As the two nanobeams are kept grounded and  $V_{act}$  is applied to both electrodes, both platforms should move towards their corresponding electrodes, effectively increasing the in-plane separation of the waveguides of the DC. The system used by Winger *et al.* with a strut length of  $3\ \mu\text{m}$  (excluding the length of the platform) achieved about 15 nm displacement of each of the platforms for  $V_{act} = 19\ \text{V}$ . The displacement should be larger for a GaAs device, which is more flexible than Si (whose Young's modulus is twice as large), and can be easily increased further by making the struts longer.

Our device was fabricated on an intrinsic GaAs wafer, using standard techniques (see Section 3.2). The DC structure was first created on a GaAs membrane of 140 nm thickness. Then Ti:Au rails were deposited on top of the device. The  $1\ \mu\text{m}$  thick sacrificial  $\text{Al}_{0.6}\text{Ga}_{0.4}\text{As}$  layer separating the membrane from the substrate was finally removed from underneath the structure using an HF etch to create the suspended system. While Figure 6.13(b) shows an almost perfect fabricated system, it is the best-looking device that has been achieved. Unfortunately, it was not possible to measure it experimentally due to problems with the metal bond pads that allow application of  $V_{act}$ .

The majority of other fabrication trials of these devices were unsuccessful due to other recurring issues. Figure 6.14 demonstrates the two most common problems. One of them is the breakage of the nanobeam rail in the under-etched region of the bulk wafer [see Figure 6.14(a)], before the rail widens. It is not obvious why this area should be particularly prone to contacts failing. However, by consulting the literature, it was found that Ti, which is mainly used to enhance adhesion between GaAs and Au, is affected by HF acid used for etching away the sacrificial AlGaAs layer [183, 184]. This has probably not been a problem in the past for standard fabrication as only larger contacts were used in previous electrical samples. Ni is another metal that was reported to enhance adhesion between Au and GaAs creating uniform contacts [185], while at the same time demonstrating corrosion resistance to HF acid [186, 187]. Hence, tests were performed to check that diode structures

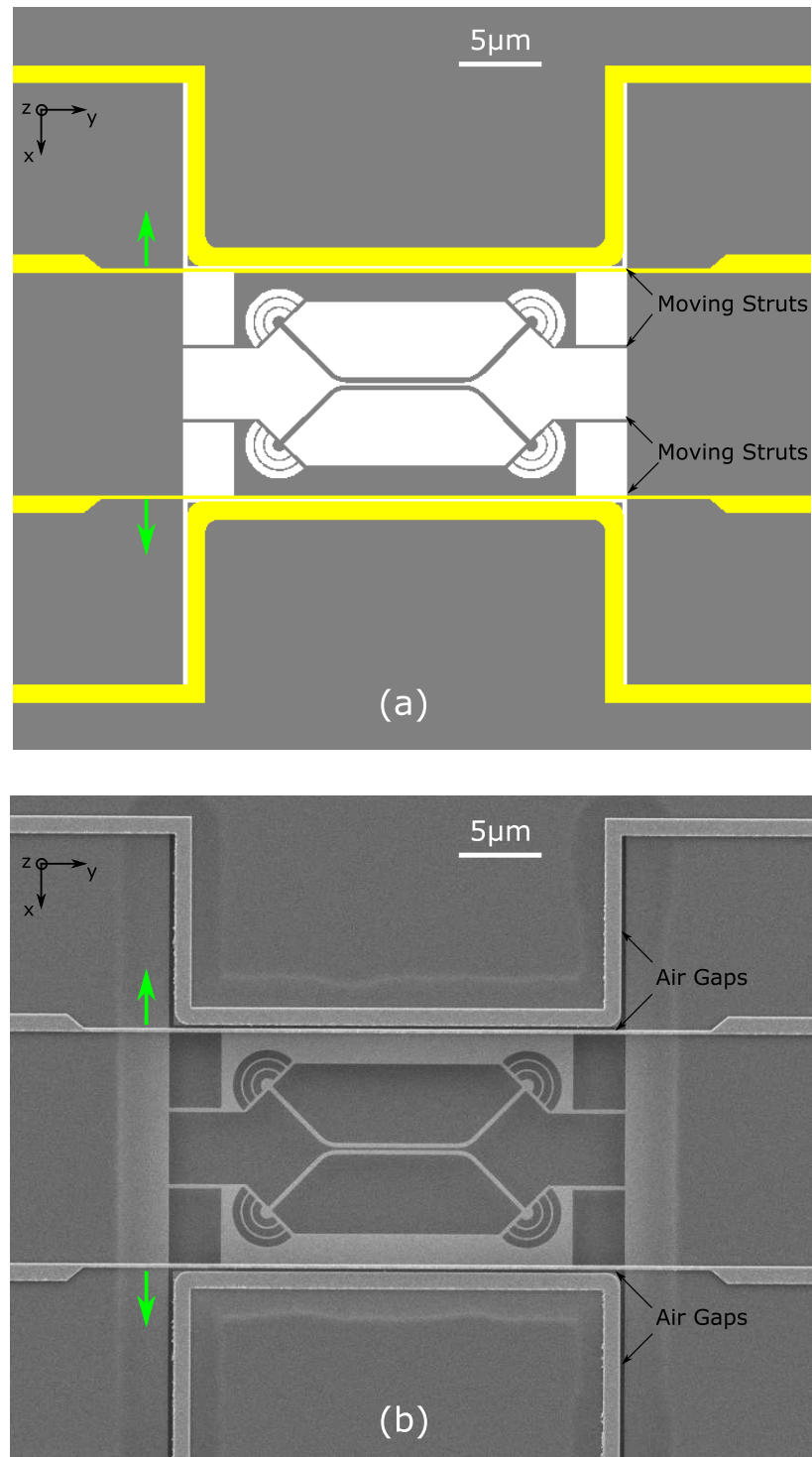


**Figure 6.13:** (a) Original design of a metal rail actuator for the tuning of directional couplers, in GDSII format. Grey areas indicate the GaAs membrane structure, while white regions represent etched features. Metal contacts are marked in yellow. (b) SEM image of the fabricated system. Green arrows indicate the direction of movement of the nanobeam rail.

(on doped wafers) with Ni:Au contacts exhibited similar electrical properties to those with Ti:Au contacts. Therefore, Ni:Au has been used instead in all later fabrications, not only for the thin rails but also for large metal bond pads and other contacts. In addition, for the next iteration of this system's design, the thin metal rails were made to widen almost immediately after they reach the bulk wafer to avoid the breakage.

The second typical issue observed during fabrication of this system was the unintended joining of the two rails (nanobeam and electrode) together at various positions along their lengths [see Figure 6.14(b)]. This of course shorts the contacts and makes the device unusable. A possible reason for this to happen is misalignment of the rail pattern with respect to that of the GaAs. This system requires very high-precision positioning of the two patterns on top of each other of an order of 10 nm during EBL, which is not trivial to achieve. In order to minimise this issue, the metal rails were made slightly thinner than the GaAs nanobeams for the next fabrication trials. This offered somewhat more room for error in the alignment procedure. Another possible solution was to make the metal rail pattern first followed by the GaAs one, rather than the other way round. This could also help with the metal lift-off process after deposition.

For the rail fabrication e-beam resist is used to mask the regions of the sample that are not to be covered with metal. Then metal is deposited on the whole sample, and removed from the masked areas together with the resist using acetone. It is not easy to remove metal from small areas in general (as will be illustrated later), but it is extremely difficult to remove it from nanometre-sized dips that are the etched air gaps between the rails (if these are fabricated first). By patterning the rails first the thin strip of metal between the rails is not buried inside the GaAs membrane and hence acetone can access it easier for removal.

Another issue with the system was that devices with longer struts tended to sag, increasing the initial in-plane separation of the devices, which is highly undesirable since this system is designed to only increase it further during electro-mechanical actuation. Hence, the next design iteration included holes in the flexible platforms in order to minimise their weight.

The improved design of the metal rail in-plane actuator for the tuning of the SR of a DC is presented in GDSII format in Figure 6.15. Figure 6.15(a)

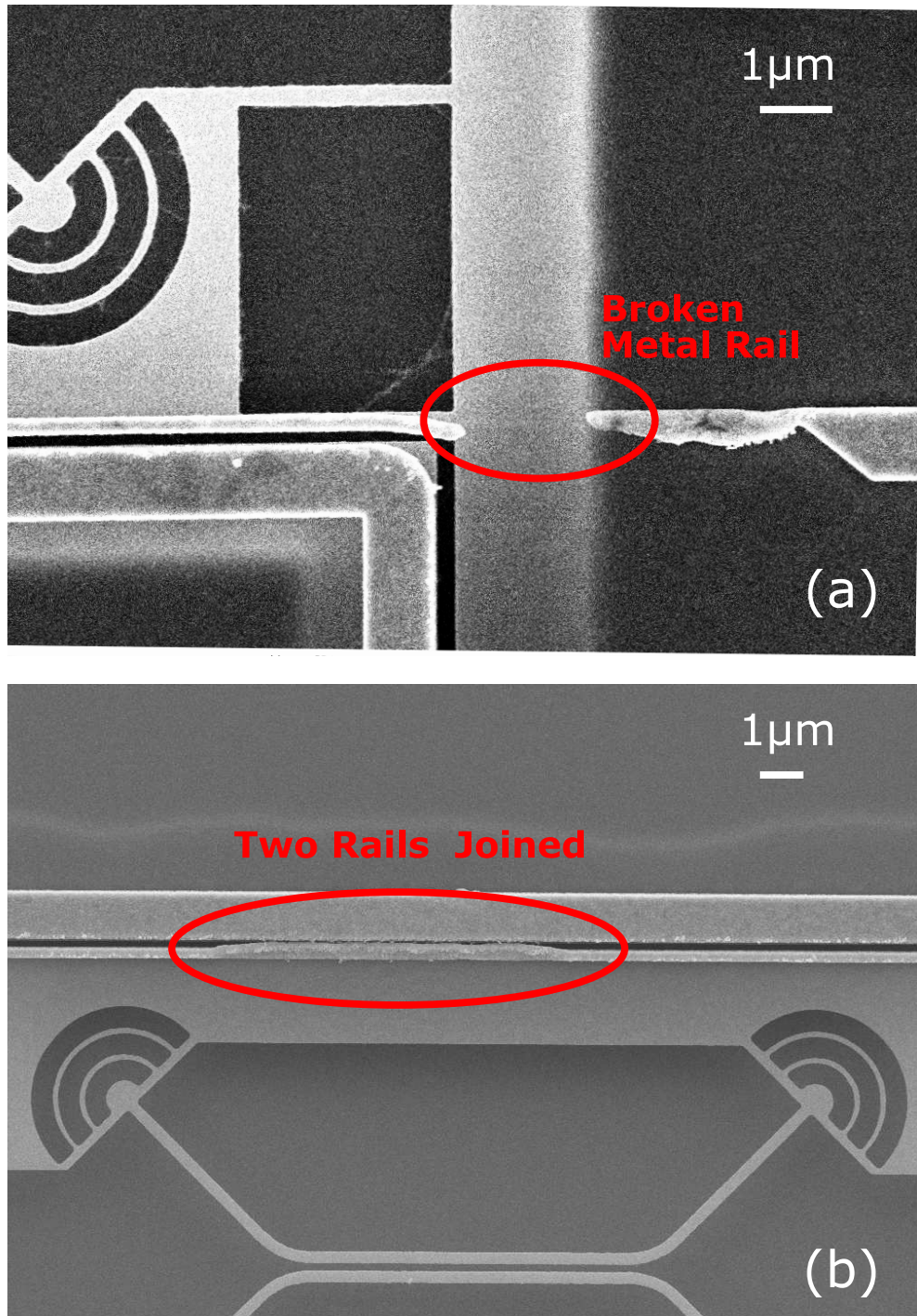


**Figure 6.14:** SEM images showing examples of problems occurring during fabrication of the original metal rail actuator for the tuning of directional couplers. (a) The thin metal rail has broken above the suspended region in the bulk. (b) Two metal rails (belonging to the nanobeam and the electrode) have become joined.

shows the close-up of one of the devices, while Figure 6.15(b) demonstrates the full sample layout on a chip including bond pads (marked in blue) that allow application of  $V_{\text{act}}$  to the metal rails. The notable adjustments discussed above include the nanobeam metal rail widening immediately after it reaches the bulk GaAs on either side of the structure, and the inclusion of holes in the platforms holding each waveguide of the DC. The number of devices using the same metal rails for their operation was also reduced to just two, so that there is less chance of the contacts being shorted, thereby making a lot of devices unusable. Of course this increased the surface area required for the system as more large metal bond pads are needed for the same number of devices on a chip. Figure 6.16 shows SEM images of some of the fabrication attempts of the new design. While devices with shorter struts appear to be coplanar [Figure 6.16(a)], those with longer struts are still sagging [Figure 6.16(b)], resulting in an in-plane separation between the waveguides of the DC of the order of 300 nm, and hence making any tuning of the SR impossible. The quality of the metal rails was definitely improved with respect to the previous design, but the overall success rate for the devices was still low.

In order to minimise the amount of possible failure regions in this metal rail system it was subsequently redesigned for the tuning of a photonic crystal cavity (PhCC) so that there is only one movable strut and the in-plane separation,  $s_{\text{in}}$ , can be either increased or decreased. This is a considerable improvement from the metal rail system for the tuning of the SR of a DC, where the two waveguides could only be moved apart. One thin metal rail instead of two also reduces opportunities for fabrication errors. The device design, which is completely original, is presented in Figure 6.17(a) in a GDSII format. By depositing electrode on either side of the movable strut a bidirectional movement is achieved (as indicated by purple arrows). Applying  $V_{\text{act}}$  to the top bond pad (and hence top electrode) will result in a decrease of  $s_{\text{in}}$ , while an increase of  $s_{\text{in}}$  can be achieved by applying  $V_{\text{act}}$  to the bottom bond pad (and hence bottom electrode). However, as the top electrode is in close proximity to the strut over a shorter distance along its length than the bottom electrode, the decrease in  $s_{\text{in}}$  is expected to be smaller than its increase for the same  $V_{\text{act}}$ .

Figure 6.17(b) shows an SEM image of one of the fabricated devices. The most common failure mode of this system was the strut bending towards, and consequently sticking to, the bottom electrode. It might be that a value of  $V_{\text{act}}$

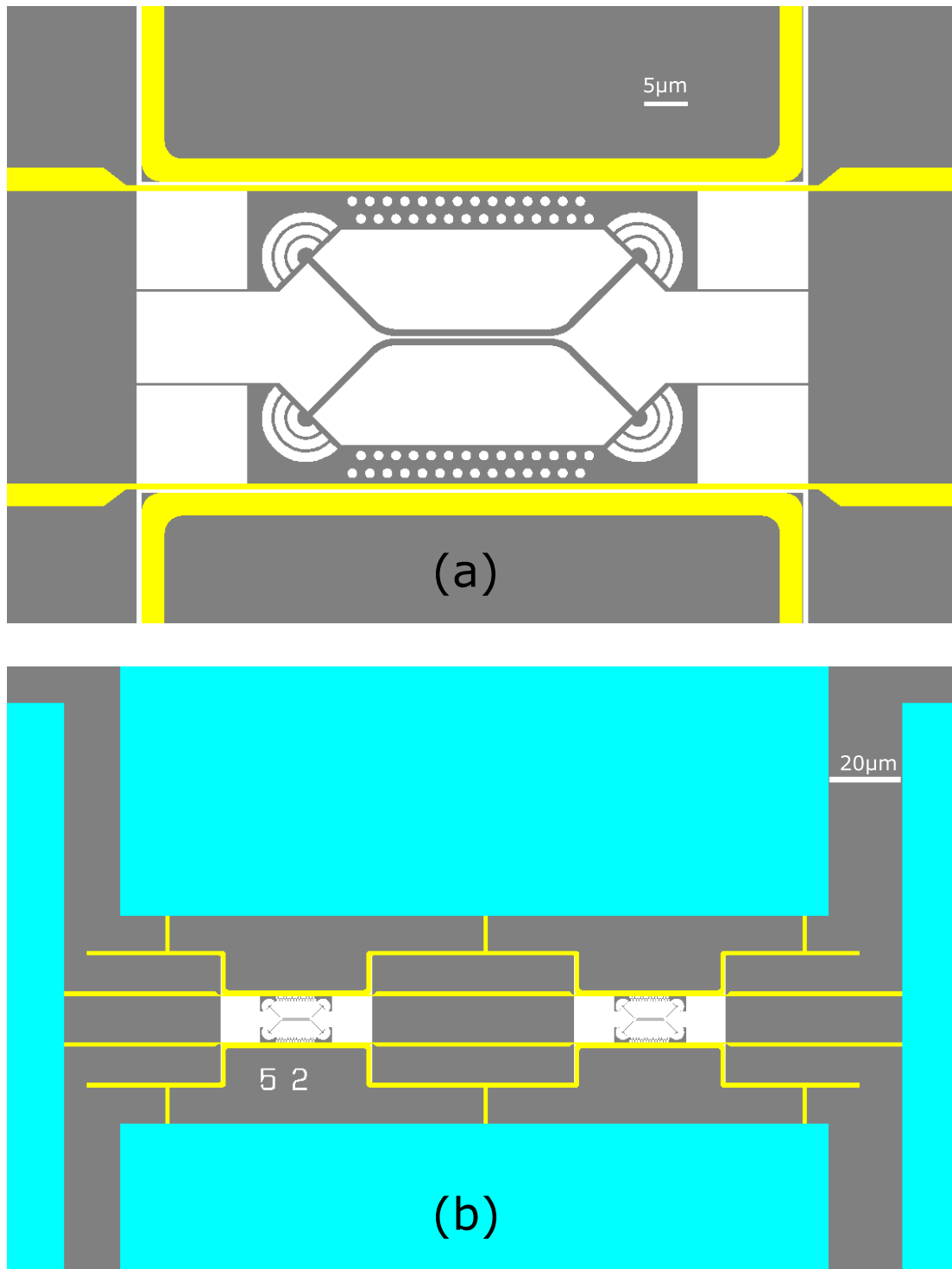


**Figure 6.15:** Improved design of a metal rail actuator for the tuning of directional couplers, in GDSII format. (a) Close-up image of a single device. (b) Sample design with two devices and electrical contact pads marked in blue.

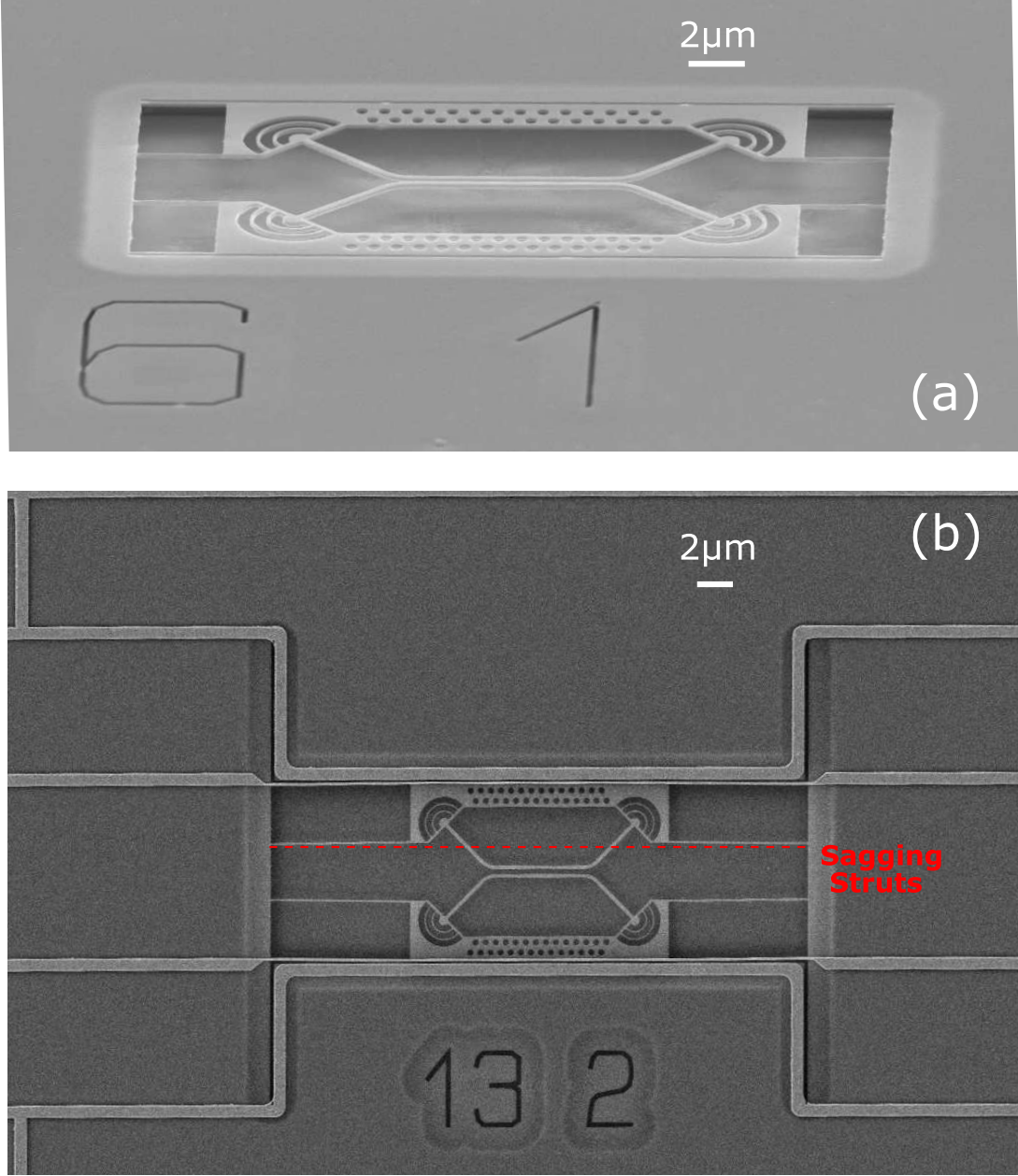


**Figure 6.16:** SEM images of the improved metal rail actuator for the tuning of directional couplers. (a) Angled image of the coplanar rail structure with short struts. (b) Top-down image of the fabricated device with longer struts.

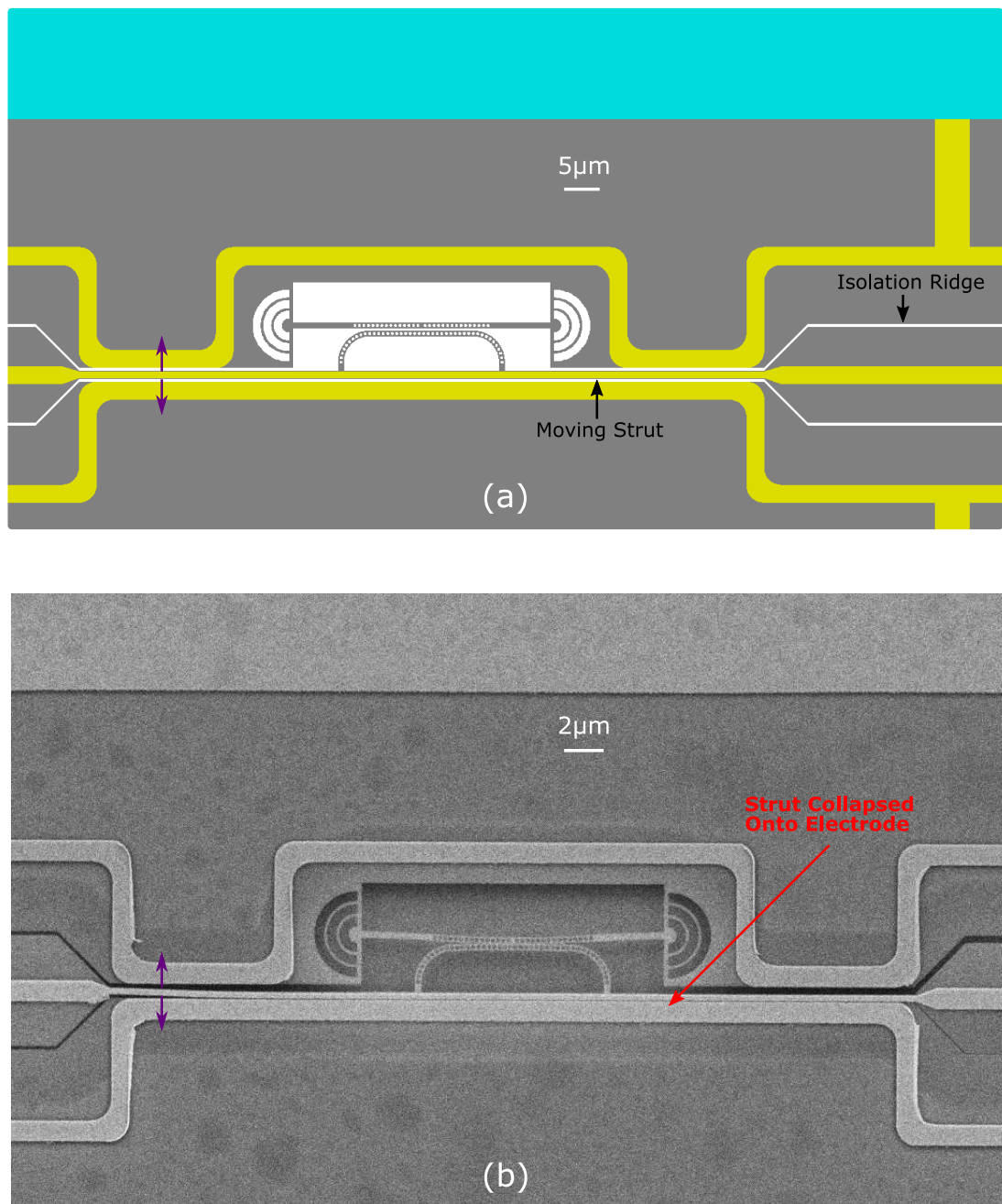


**Figure 6.17:** Images of the electro-mechanical in-plane actuator for the tuning of a nanobeam photonic crystal cavity. Purple arrows indicate the two possible movement directions for the strut. (a) System designed in GDSII format. (b) SEM image of a fabricated device, the movable nanobeam strut of which has collapsed onto the bottom electrode.

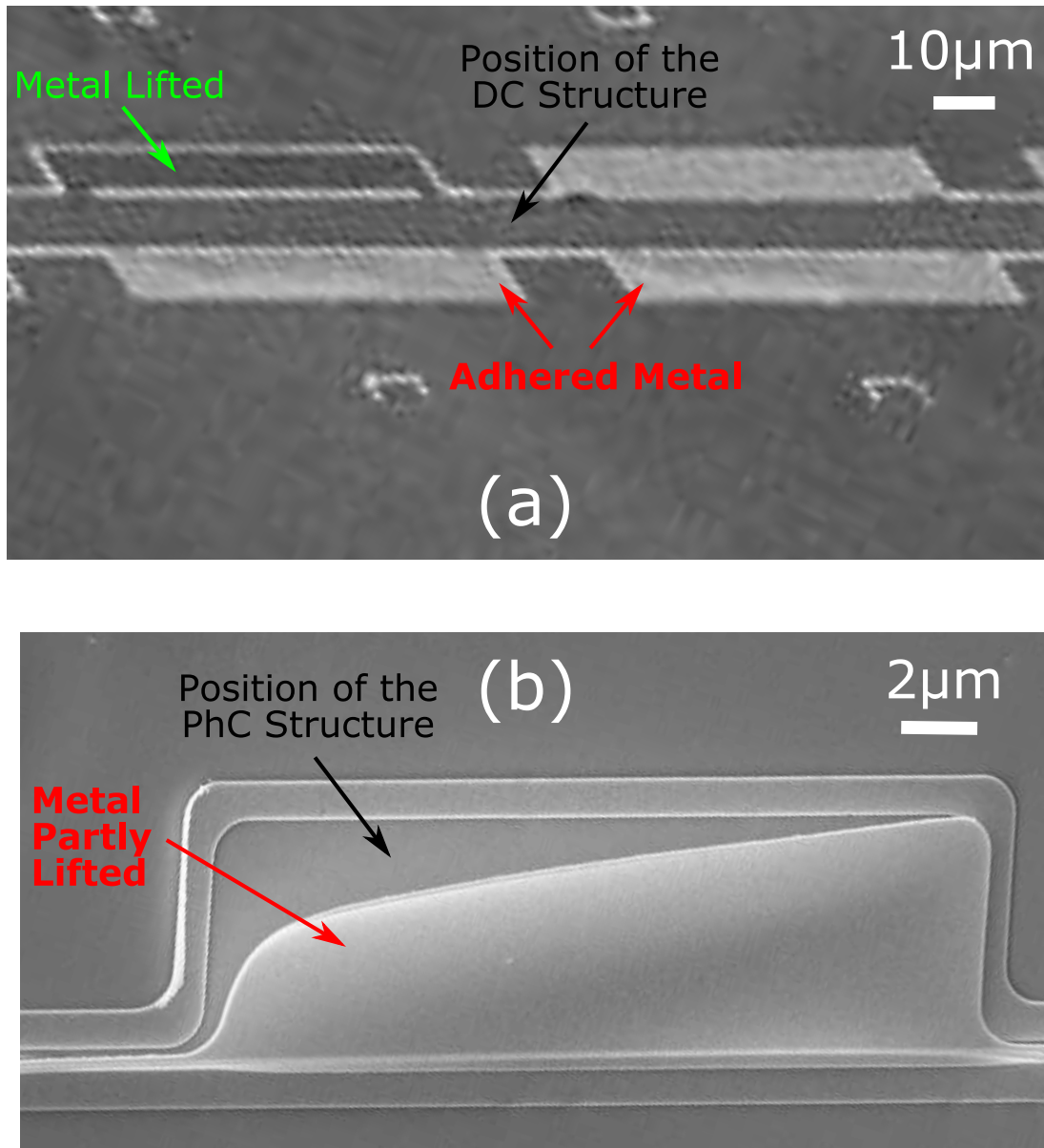


**Figure 6.18:** Images of the fabricated metal rail actuators showing problems with lifting the metal off the sample from in between rails for the tuning of (a) a directional coupler, and (b) a nanobeam photonic crystal cavity.

of only  $\sim 2$  V between the strut and the bottom electrode (as indicated by the electro-mechanical simulations of the system with the initial conditions) is too low to operate the device in a controllable manner. Charge build-up on the metal contacts is possible both during sample handling and also when using SEM to image the structure. If that occurs and causes the nanobeam rail to be at a different potential to that of one of the electrodes it is possible for the device to be actuated accidentally. Making the struts shorter might resolve this sensitivity issue. However, having an asymmetric electrode structures might turn out still to cause problems. In this case an inclusion of sacrificial struts, similar to those used for the cantilever system reported in Chapter 5, which would hold the nanobeam rail in place during fabrication and may be removed prior to measurements using laser ablation, could be considered.

Furthermore, the issue with the metal contacts not peeling off easily after deposition still remains unresolved. Even with fabricating contacts prior to the GaAs structure and using acetone slightly above room temperature to aid dissolution of the e-beam resist, this step is highly unreliable. Figure 6.18 shows SEM images of both rail systems after contact deposition and lift off (but before GaAs device patterning), which demonstrate this problem. Figure 6.18(a) demonstrates the difficulty in lifting off the metal from in between the two rail contacts in the DC tuning system, even in the large areas between individual devices where they are much further apart. Figure 6.18(b) illustrates the failing metal removal process from the PhCC tuning system, where it has only partly lifted off from the region where the GaAs PhC structure should be positioned.

Overall the metal rail systems that have been investigated here appear to be extremely fragile and difficult to fabricate reliably. Therefore, comb-drive actuators, which offer larger in-plane displacements and are easier to design for the actuation to decrease  $s_{in}$ , were also investigated. The findings from this study are reported below.

## 6.3 Comb-Drive Actuators

Comb-drive actuators (CDAs) are electro-mechanical actuators, which have been well studied on Si platforms thanks to advanced Si micro-fabrication

technologies. They have found many applications in a variety of fields from electronic oscillators [188] and tunable lasers [189], through inkjet printing to automobile sensors [190], biosensors and drug delivery systems [191]. They are capable of providing large in-plane displacements of tens of micrometers [192]. Even though GaAs has been identified as a good mechanical material [193, 194] with selective etching of III-V compounds enabling it to host electro-mechanical structures [195, 196], only few such devices have been demonstrated on GaAs to date. CDAs have so far not been reported for use with integrated quantum optical devices on GaAs, and hence are a very interesting and challenging prospect to study in this context.

CDAs consist of two *comb* structures whose *teeth* are facing each other in an interlocking fashion, as shown in Figure 6.19. One of the combs is fixed to the substrate and is usually referred to as a stator, while the other is attached to a flexible suspension and is typically called a rotor. When an actuation voltage,  $V_{act}$ , is applied between the two combs, the electrostatic attraction causes the rotor to travel towards the stator and the rotor's teeth slide further between the stator's teeth, keeping the teeth parallel. By attaching a photonic device to the rotor, its in-plane position can be controlled on a chip.

### 6.3.1 Electro-Mechanical Modelling

Applying  $V_{act}$  between the rotor and the stator causes electrical charge to build up between adjacent interlocking teeth of the CDA. To simplify the electro-mechanical modelling of the system a one-dimensional parallel-plate capacitor model between the engaged parts of the comb teeth can be used. Therefore, effects such as fringing fields, fields between the teeth ends and the combs, as well as out-of plane fields are neglected [197, 198]. In order to simulate fully the whole system a finite-element analysis modelling tool, such as Comsol Multiphysics (see Section 3.4.2), would have to be used. However, this is extremely computationally intensive for such large and complex systems. Therefore, a simplified model is presented here. The capacitance between the teeth can be expressed as follows:

$$C = \frac{2n\epsilon_0 t(L_0 + x)}{g}, \quad (6.2)$$

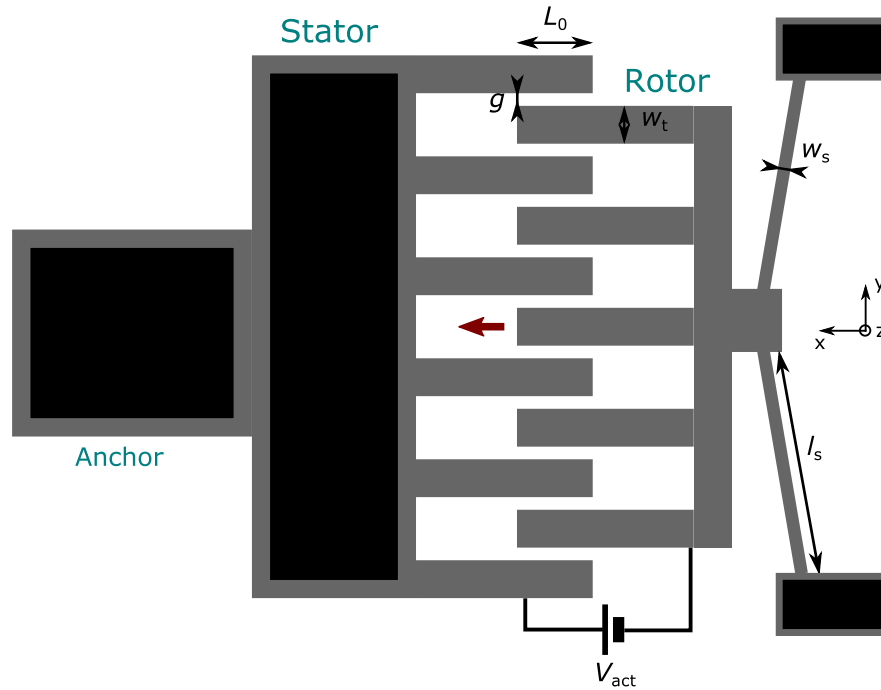


**Figure 6.19:** Schematic diagram of a comb-drive actuator. The red arrow indicates the direction of movement of the rotor.

where  $n$  is the number of teeth in the shorter comb (in Figure 6.19 the rotor),  $\epsilon_0$  is the permittivity of free space,  $t$  is the thickness of the teeth (in the out-of-plane  $z$  direction),  $L_0$  is the length of the initial overlap between the opposite teeth,  $g$  is the air gap between the opposing teeth and  $x$  is the displacement of the rotor.

The electrostatic force between the stator and the rotor can then be written as:

$$F = \frac{1}{2} \frac{dC}{dx} V_{\text{act}}^2 = \frac{n\epsilon_0 t}{g} V_{\text{act}}^2. \quad (6.3)$$

Since the rotor acts as a spring, its displacement due to the electrostatic force can be derived from Hooke's law as follows:

$$x = \frac{n\epsilon_0 t}{gk_s} V_{\text{act}}^2, \quad (6.4)$$

where  $k_s$  is the stiffness constant of the spring. For a fixed-fixed beam, such as the one supporting the rotor at its centre through two struts, the spring constant is given by [142]:

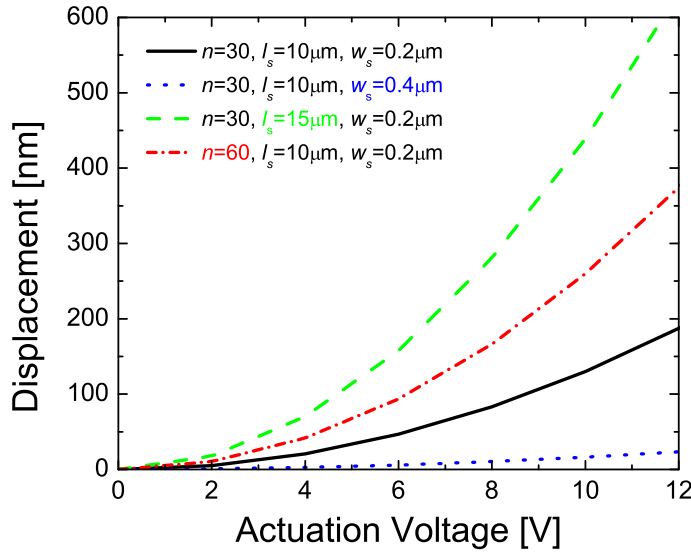


**Figure 6.20:** Displacement of the rotor versus actuation voltage for comb-drive actuators with an air gap between the opposing teeth of  $g = 150$  nm, for various values of the parameters  $n$ ,  $l_s$  and  $w_s$ .

$$k_s = \frac{2Ytw_s^3}{l_s^3}, \quad (6.5)$$

where  $Y$  is the Young's modulus of the comb's material (here GaAs),  $w_s$  and  $l_s$  are the width and the length of the struts. The displacement of the rotor can then be derived to be:

$$x = \frac{n\epsilon_0 l_s^3}{2Ygw_s^3} V_{\text{act}}^2. \quad (6.6)$$

Once again the thickness of the structure is found not to affect the electro-mechanical behaviour of the in-plane actuator. While the travel range of the rotor depends linearly on the number of teeth, and is inversely proportional to the distance between them and the Young's modulus of the material, the dimensions of the struts have a cubic or inverse cubic effect. Therefore, in order to achieve larger displacements it is most effective to increase the length or decrease the width of the struts. Figure 6.20 demonstrates the expected electro-mechanical behaviour of a GaAs CDA (for which  $Y = 85.5$  GPa) for a range of realistic parameter sets. One sees clearly that a CDA with  $n = 30$ ,

$l_s = 10 \mu\text{m}$ ,  $w_s = 200 \text{ nm}$  and  $g = 150 \text{ nm}$  is expected to achieve over 180 nm in-plane displacement for  $V_{\text{act}} = 12 \text{ V}$ , which would be more than sufficient to demonstrate maximum control over the SR of a DC and to achieve more than 10 nm tuning of a PhCC mode wavelength. Increasing the length of the struts by just  $5 \mu\text{m}$  to  $l_s = 15 \mu\text{m}$  extends the travel range to over 600 nm for  $V_{\text{act}} = 12 \text{ V}$ . If the width of the struts were too thin to support the rotor structure, this can be increased at the same time as increasing the strut length to achieve identical electro-mechanical performance of the device.

### 6.3.2 Device Design, Fabrication and Testing

Our first comb-drive actuator design was based on that demonstrated by Chew *et al.* [144] for the tuning of coupled PhCCs on Si. Figure 6.21 illustrates the device design (in GDSII format) that allows the control of the SR of a DC on a GaAs substrate according to the electro-mechanical behaviour discussed above. The stator is designed to be fixed to the GaAs substrate, while the rotor is suspended through a so-called tilted-folded beam suspension arrangement. The slight tilting of the struts with respect to  $y$  axis has been reported to extend the stable travel range of the rotor [143]. The suspension is connected to the bulk of the wafer through support columns fixed to the substrate at both ends. The holes in the rotor's suspension increase the etch rate of the sacrificial AlGaAs layer underneath it to ensure the rotor is fully suspended, while at the same time the stator and the fixed columns are attached to the GaAs substrate through the AlGaAs layer. The holes also decrease the weight of the device. One waveguide of the DC is attached to the rotor, while the other is fixed to the bulk of the wafer.

When  $V_{\text{act}}$  is applied between the two combs, the rotor will travel in the  $x$  direction (as indicated in Figure 6.21 by the red arrow), and hence decrease the in-plane separation,  $s_{\text{in}}$ , between the waveguides, which in turn changes the SR of the DC. In order to avoid the pull-in of the rotor to the substrate due to electrostatic attraction between the two, they should be kept at the same potential. Therefore,  $V_{\text{act}}$  is applied individually to the stator, while both the rotor and the substrate are grounded. The isolation ridge, marked in green in Figure 6.21, allows electrical isolation between the stator's and rotor's contacts.  $V_{\text{act}}$  is applied to the stator through the contacting bond pad marked in blue.

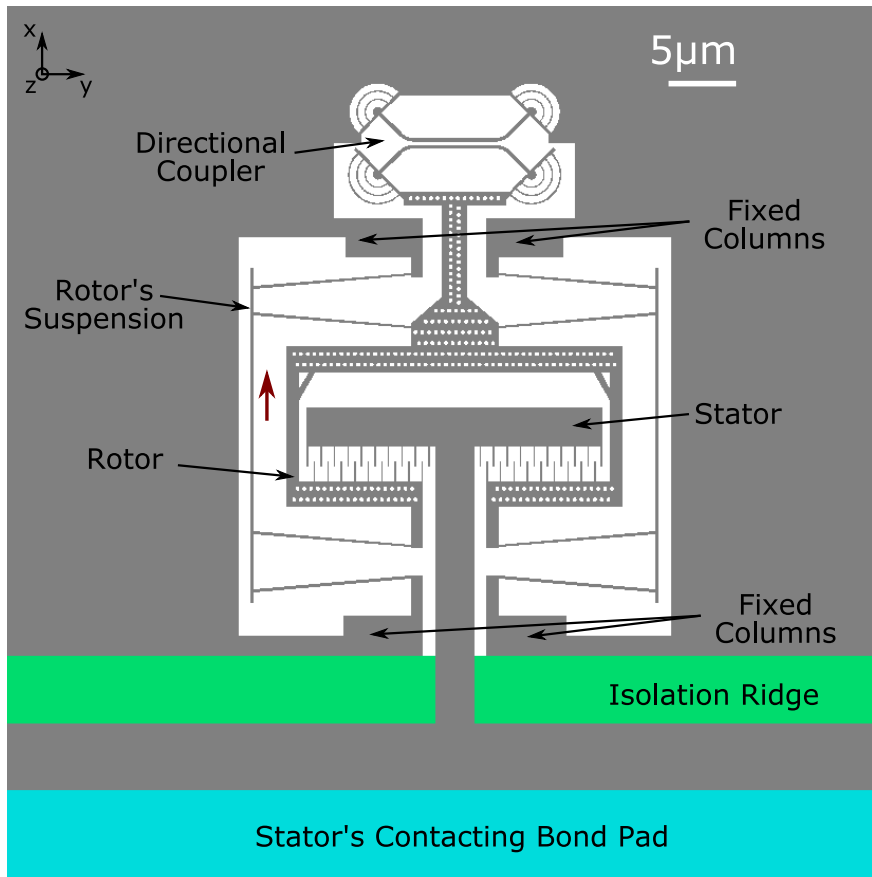


**Figure 6.21:** Digital image (in GDSII format) of an initial design of a comb-drive actuator for controlling the SR of a DC. The direction of travel of the rotor is indicated by a red arrow.

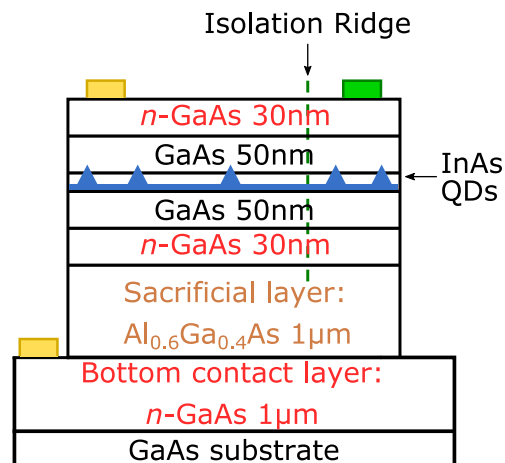


**Figure 6.22:** Schematic diagram of the wafer structure used for comb-drive actuators. The position of the Ni:Au contacts at the same ground potential for the substrate and the rotor are marked by gold rectangles. The isolated stator's contact, for applying  $V_{act}$ , is indicated in green.

Two separate contacts for the grounding of the rotor and the substrate, which can be common to several CDAs on a chip, are not shown here.

A variety of these devices with different dimensions were fabricated on an *n-i-n-i-n* diode, the schematic of which is presented in Figure 6.22, using standard techniques (see Section 3.2). The DC and the CDA structure were defined within the top *n-i-n* GaAs membrane of 160 nm thickness. The intrinsic region of this membrane contained InGaAs self assembled quantum dots (QDs). The *n*-GaAs substrate was isolated from the membrane by a 1  $\mu$ m thick intrinsic Al<sub>0.6</sub>Ga<sub>0.4</sub>As layer, which was removed from beneath the device using an HF etch to create the suspended rotor and DC structure. Two electrically isolated Ni: Au contacts were made to the top layer and one to the bottom *n*-GaAs layer in order to allow for electro-mechanical control of the CDA.

SEM images of two such fabricated devices are shown in Figure 6.23. Figure 6.23(a) shows a device without the stator's contact. The inset demonstrates how well-resolved are the teeth of the combs. The whole structure looks exceptionally good for the first fabrication trial of such a complex system. However, the support columns for the rotor's suspension under-etched during the HF etch step, indicating their size was not large enough to prevent it. Figure 6.23(b) shows another commonly observed issue. Most of the rotor structures were seen drooping towards the substrate at the DC end, slightly displacing the moving waveguide out-of-plane with respect to the fixed one. As discussed in detail in Chapter 5 if this distance from horizontal is large enough it will prevent the coupling of light between the two waveguides, and hence make the device inoperable. Some of the fabricated devices, like the one shown in the image, have totally collapsed down onto the substrate at that end, resulting in the moving waveguide touching the ground. Therefore, this was a major issue that had to be resolved for the CDA to operate as expected.

Two distinct solutions were implemented simultaneously in the second CDA design. One of them consisted of exchanging the holes in the rotor for a triangular mesh structure that would further reduce the weight of the rotor by removing more material, while keeping the structural rigidity of the device. This, however, increased the complexity of the fabrication process as smaller features had to be resolved. The other, more radical approach, involved completely changing the rotor's design at the DC end to decrease the amount of cantilever-type load exerted on the suspension at this location.

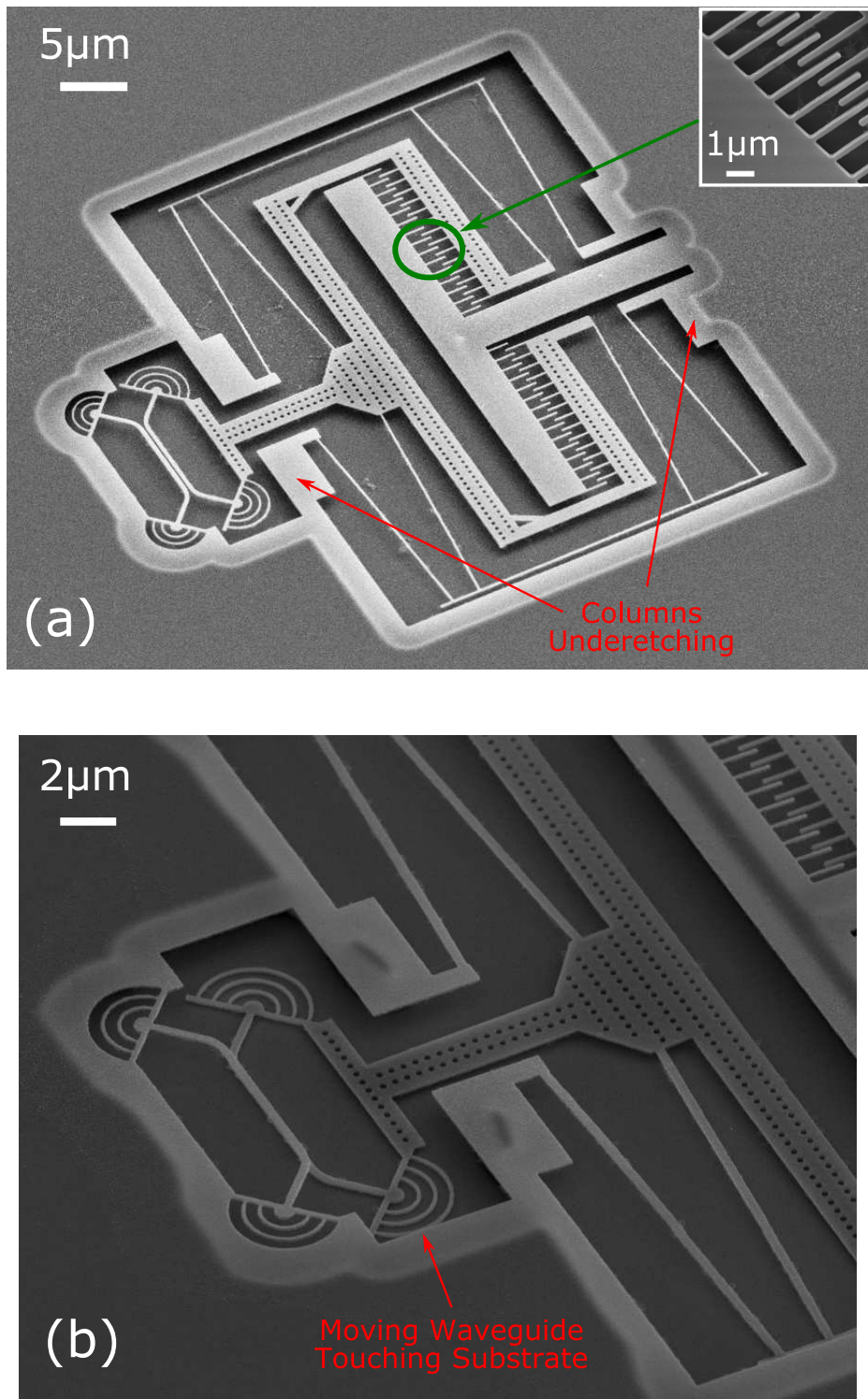


**Figure 6.23:** Angled SEM images showing fabricated comb-drive actuators. (a) A CDA with a suspended rotor and well-resolved teeth structure (see the inset), but slightly under-etched columns. (b) A CDA whose rotor is drooping towards the substrate with the moving waveguide of the DC in contact with the ground.

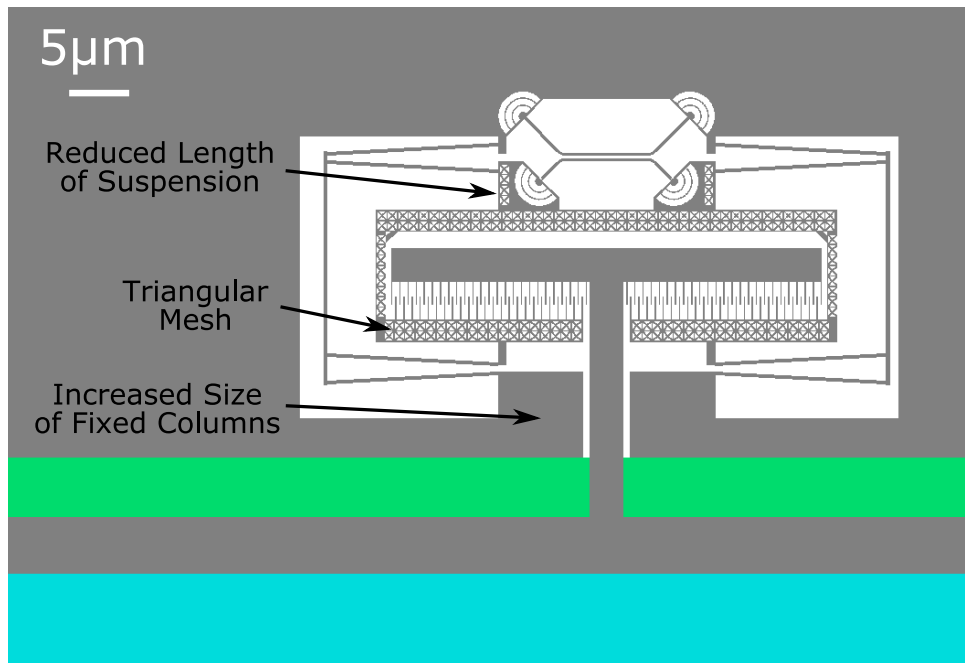


**Figure 6.24:** Digital image (in GDSII format) of an improved design of a comb-drive actuator for controlling the SR of a DC.

The improved CDA design is shown in Figure 6.24. The moving waveguide is now attached directly to the rotor's body, which removes the torque associated with the previous design. The reduced size of the suspension also decreases its weight. In addition, the improved design eliminates the need for the support columns at that (DC) end, as the struts are connected directly to the bulk of the wafer in this layout. The size of the fixed columns at the other end of the rotor were also doubled to ensure they remain attached to the substrate during an HF etch. To further reduce the weight of the rotor the triangular mesh structure is implemented throughout the rotor's body.

A range of these CDAs was fabricated once again on an *n-i-n-i-n* wafer, the structure of which is shown in Figure 6.22, using identical procedures to those used previously. SEM images of two such fabricated devices are shown in Figure 6.25. This time the support columns clearly remained attached to the substrate and the triangular mesh structure was very well-resolved [see inset in Figure 6.25(a)]. In addition, the rotor structure including the DC end was completely suspended without visible drooping present. This is particularly clear from the angled SEM image in Figure 6.25(b) and demonstrates a considerable improvement on the initial CDA design.

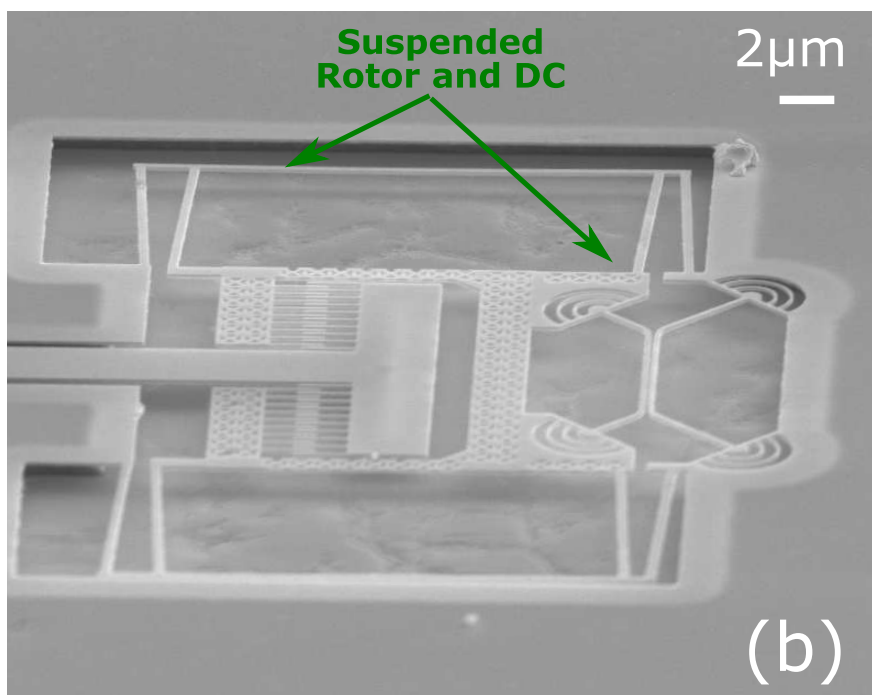
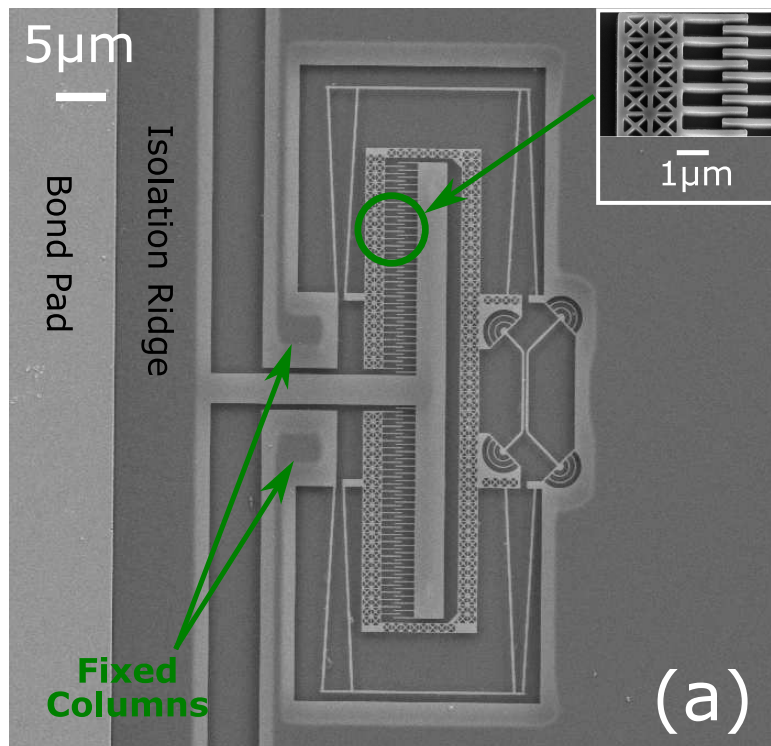


**Figure 6.25:** SEM images showing fabricated improved comb-drive actuators. (a) Top-down view of the complete device with the rotor support columns fixed to the substrate and well-resolved triangle pattern (see insert). (b) Angled view of a fully suspended CDA.

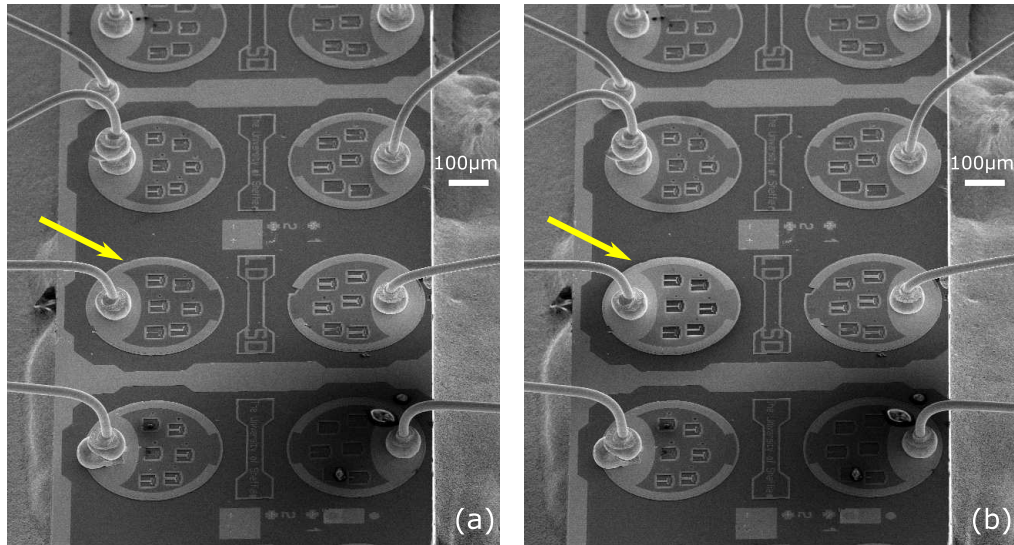


**Figure 6.26:** SEM images of the electro-mechanical diode structure reported in Chapter 5 with six cantilevers actuated through one contact. The yellow arrow indicates the biased diode with (a)  $V_{\text{act}} = 0 \text{ V}$  and (b)  $V_{\text{act}} = 3 \text{ V}$ . The applied voltage clearly increases the brightness of the actuated contact.

The CDA sample was first tested electro-mechanically in the SEM, which has the capability of applying a voltage to the devices whilst imaging. Unfortunately, no movement of the rotor was observed. However, the problem was most likely associated with the actual electrical contacts rather than the CDA itself. As discussed briefly in Section 5.4.1, application of a voltage to a conductive surface causes change in the brightness of its image. Figure 6.26 demonstrates this behaviour on the working sample of an electro-mechanical system reported in Chapter 5. The actuated diode is indicated with a yellow arrow. Figure 6.26(a) shows the image of the sample with  $V_{\text{act}} = 0 \text{ V}$ , while Figure 6.26(b) presents the same image with  $V_{\text{act}} = 3 \text{ V}$ . The brightness of the biased contact clearly increases with the applied voltage. No such changes to the brightness of the actuated CDAs were observed, which indicates that there was no electrical connection between the contact and the GaAs surface. This might have been caused by the quality of the deposited contacts. Occasionally during fabrication, there might be a thin layer of resist remaining on the sample when contacts are deposited, which consequently acts as an insulating layer between the GaAs surface and the metal contact. Therefore, it is highly likely that any future fabrication attempts would be successful and result in the first demonstration of a GaAs-based CDA allowing to control the SR of a

single-photon beam splitter containing an embedded quantum emitter.

The CDA structure is also very versatile as it can be easily adapted to tune other photonic devices on a chip. By making holes in the waveguides of the DC, a desired PhC structure can be created for the tuning of the PhCC mode wavelength, as discussed earlier. In fact, any other photonic structure can be easily exchanged with the DC to allow the control of its optical properties. Using a CDA for the on-chip tuning of optical properties of GaAs devices for QIP applications is a very promising field of research, and hence it is expected that it will surely be continued further by other researchers in the group.

## **6.4 Summary and Outlook**

In conclusion, an in-plane movement of photonic devices was shown through modelling to be much more effective in controlling their optical properties than the out-of-plane displacement demonstrated in Chapter 5. Two distinct electro-mechanical in-plane actuators that would allow such tuning were designed, fabricated, tested and developed. The metal rail system was more compact than the CDA. However, it offered smaller displacements for the same nominal actuation voltage. In addition, it was extremely fragile and unreliable to fabricate due to the required dimensions and proximity of the metal rail contacts. It was also less effective, as the original design permitted only an increase in the in-plane separation between the structures. The optical tuning effect is the most efficient for small separations, which are difficult to achieve during fabrication. Adapting the device to offer the reduction in the separation instead is not straightforward and adds to the complexity of the system. On the other hand, the CDA is less compact and more complex to start with. However, it offers much larger displacements that reduce the in-plane separation between the photonic devices and can be easily adapted to tune a variety of on-chip optical elements for QIP applications. Its fabrication was easier than was first expected, and perhaps the only reason for it not being able to operate was the quality of the contacts on the particular sample. Overall, a CDA structure is the system that is more likely to be successfully fabricated and demonstrated to work with embedded single-photon sources, and hence is the one recommended for further study.

# Chapter 7

## Summary and Future Directions

### 7.1 Summary

This thesis has focused on the development and experimental demonstration of a variety of nanophotonic elements integrated in a GaAs planar architecture, and with self-assembled quantum dots as single photon sources, for the first time in the LDS group at the University of Sheffield. The reported devices represent significant steps towards the realization of fully integrated III-V semiconductor quantum optical circuits.

Chapter 1 introduced the intriguing subject of quantum information processing and discussed its proposed solid-state implementation using III-V semiconductors and quantum dots (QDs). This was followed in Chapter 2 by a presentation of the basic concepts that form the underpinning of the research undertaken for this thesis. Both the experimental and the computational methods of study, the results of which form a basis for the work reported in this thesis, were then discussed in Chapter 3.

The use of nanobeam photonic crystal cavities (PhCCs) for on-chip spectral filtering and cavity quantum electrodynamics (cQED) applications was investigated in Chapter 4. Nanobeam PhC filters with a passband of  $\Delta\omega = 1 - 3$  nm ( $Q = 300 - 1000$ ) have been both modelled and demonstrated experimentally. The trade-off between a high transmissivity and a narrow bandwidth of these devices was explained and then demonstrated through spectral measurements. Various design improvements to the PhCC design, which result in higher  $Q$ -factors were also explored, with one device achieving  $Q \approx 2000$

( $\Delta\omega = 0.45$  nm) experimentally, and another shown through modelling to be capable of reaching  $Q = 850,000$  ( $\Delta\omega = 1$  pm). Tuning of the QD emission wavelength using the quantum-confined Stark effect was also attempted, but found unsuccessful, most likely due to the reduced current flow through the nanobeam PhC structure.

For the first time in-situ electro-mechanical control of an on-chip optical beam splitter operating at the single photon level was demonstrated in detail in Chapter 5, using a cantilever geometry. The splitting ratio was reversibly tuned from an initial value of 83:17 at 0 V (0 displacement) to  $\sim 100:0$  at 11 V (300 nm displacement). The cantilever was capable of both achieving displacements of over 400 nm and overcoming the surface adhesion forces between it and the substrate when the electro-mechanical pull-in occurred.

Finally, in Chapter 6 it was shown through modelling that controlling the beam splitter electro-mechanically using in-plane rather than out-of-plane actuation is much more efficient and can greatly enhance the amount of tuning that was achieved using a cantilever, as presented in Chapter 5. Similarly, the concept of tuning a PhCC mode wavelength into resonance with a QD emission was also discussed. The development, fabrication and testing of two distinct in-plane actuators, namely a metal rail system and a comb-drive actuator (CDA), both of which could enable such tuning, was then reported. The CDA structure was found to be easier to fabricate and design to decrease the in-plane separation between the on-chip structures. This makes CDAs more promising systems for the demonstration of increased control over the optical properties of the integrated nanophotonic devices studied in this thesis.

## 7.2 Further Work

The main purpose of the research undertaken for this thesis was to further the integration of single-photon devices on a III-V semiconductor chip, as well as to design systems that will allow in-situ control of their optical properties so that quantum optical information processing circuits can be realized. In this context, there are several possible future research directions that stem directly from the work presented here.

As discussed in Chapter 4, non-resonant QD excitation results in a large emission spectrum from the wafer. For this reason filtering of the signal from a single QD and detecting it on-chip is the obvious next step in achieving a fully integrated quantum optical circuit. Superconducting nanowire single-photon detectors (SNSPDs) are promising contenders for realizing this goal as they are well suited to the planar circuit geometry. They can be installed by positioning superconducting nanowire on top of a nanobeam waveguide. This makes a nanobeam PhC filter ideal for integration with a SNSPD [123, 199, 200]. In addition, the two elements could also be integrated further with the electroluminescence excitation of QDs, as reported by Bentham *et al.* [122]. This would result in single-photon generation, filtering and detection all performed on-chip.

The system presented in Chapter 5 that enabled electro-mechanical control of a splitting ratio of an optical beam splitter through out-of-plane actuation of a cantilever could be further developed in order to realize single-photon routers or Mach-Zehnder interferometers on-chip. It could also be used to tune the optical mode of a nanobeam PhCC for cQED applications. Some of these configurations are currently under joint investigation with Joseph Maguire. If correctly designed, this control method could also be integrated with the other circuit components mentioned above.

However, the in-plane electro-mechanical actuation methods presented in Chapter 6 offer greater control over the optical properties of photonic elements. Comb-drive actuators are particularly promising and considerable progress has already been made, as reported in this thesis, towards their realization on a III-V semiconductor circuit. These systems should also be more reliable in the longer term, as problems with the pull-in effect between the two electrodes are easier to circumvent in comparison to the out-of-plane actuation methods. Their integration with other on-chip elements should also be more straightforward.



## Appendix: List of Wafers

Chapter	Device	Wafer ID	Structure from Top to Bottom
4	On-Chip Filter: 3-hole 4 & 5-hole	VN2009 VN2777 (rotation stop)	70 nm GaAs 0.7 nm InAs 70 nm GaAs 1 $\mu\text{m}$ $\text{Al}_{0.6}\text{Ga}_{0.4}\text{As}$ 200 nm GaAs
4	Nanobeam Cavity (15-hole)	SF1100	30 nm $p$ -GaAs 55 nm GaAs 0.7 nm InAs 55 nm GaAs 30 nm $n$ -GaAs 200nm $n$ - $\text{Al}_{0.6}\text{Ga}_{0.4}\text{As}$ 1 $\mu\text{m}$ $\text{Al}_{0.6}\text{Ga}_{0.4}\text{As}$ 300nm $n$ -GaAs
5	On-Chip Beam Splitter	VN2103 (rotation stop)	30 nm $p$ -GaAs 50 nm GaAs 0.7 nm InAs 50 nm GaAs 30 nm $p$ -GaAs 2 $\mu\text{m}$ $\text{Al}_{0.6}\text{Ga}_{0.4}\text{As}$ 1 $\mu\text{m}$ $n$ -GaAs

*Appendix: List of Wafers*

---

<b>Chapter</b>	<b>Device</b>	<b>Wafer ID</b>	<b>Structure from Top to Bottom</b>
6	Comb-Drive Actuator	SF1102	30 nm <i>n</i> -GaAs 50 nm GaAs 0.7 nm InAs 50 nm GaAs 30 nm <i>n</i> -GaAs 200nm <i>n</i> -Al <sub>0.6</sub> Ga <sub>0.4</sub> As 1 μm Al <sub>0.6</sub> Ga <sub>0.4</sub> As 300nm <i>n</i> -GaAs

# Bibliography

- [1] R. P. Feynman, “Simulating physics with computers,” *Int. J. Theor. Phys.* **21**, 467–488 (1982).
- [2] P. W. Shor, “Algorithms for quantum computation: discrete logarithms and factoring,” in *Proc. 35th Annual Symposium on Foundations of Computer Science* (IEEE, Santa Fe, NM, USA, 1994) pp. 124–134.
- [3] L. K. Grover, “A fast quantum mechanical algorithm for database search,” in *Proc. 28th Annual ACM Symposium on Theory of Computing* (ACM, New York, NY, USA, 1996) pp. 212–219.
- [4] D. P. DiVincenzo, “The physical implementation of quantum computation,” *Fortschr. Phys.* **48**, 771–783 (2000).
- [5] T. D. Ladd, F. Jelezko, R. Laflamme, Y. Nakamura, C. Monroe, and J. L. O’Brien, “Quantum computers,” *Nature* **464**, 45–53 (2010).
- [6] J. L. O’Brien, “Optical quantum computing,” *Science* **318**, 1567–1570 (2007).
- [7] E. Knill, R. Laflamme, and G. J. Milburn, “A scheme for efficient quantum computation with linear optics,” *Nature* **409**, 46–52 (2001).
- [8] The Nobel Foundation, “*The Nobel Prize in Physics 2000*,” (2014).
- [9] J. Y. Marzin, J. M. Gérard, A. Izraël, D. Barrier, and G. Bastard, “Photoluminescence of single InAs quantum dots obtained by self-organized growth on GaAs,” *Phys. Rev. Lett.* **73**, 716–719 (1994).
- [10] A. Milnes and A. Polyakov, “Indium arsenide: a semiconductor for high speed and electro-optical devices,” *Mater. Sci. Eng. B-Adv.* **18**, 237–259 (1993).

- [11] B. Lounis, H. Bechtel, D. Gerion, P. Alivisatos, and W. Moerner, “Photon antibunching in single CdSe/ZnS quantum dot fluorescence,” *Chem. Phys. Lett.* **329**, 399–404 (2000).
- [12] K. Sebald, P. Michler, T. Passow, D. Hommel, G. Bacher, and A. Forchel, “Single-photon emission of CdSe quantum dots at temperatures up to 200 K,” *Appl. Phys. Lett.* **81**, 2920–2922 (2002).
- [13] F. Tinjod, B. Gilles, S. Moehl, K. Kheng, and H. Mariette, “II–VI quantum dot formation induced by surface energy change of a strained layer,” *Appl. Phys. Lett.* **82**, 4340–4342 (2003).
- [14] K. Brunner, “Si/Ge nanostructures,” *Rep. Prog. Phys.* **65**, 27–72 (2002).
- [15] P. Michler, A. Kiraz, C. Becher, W. V. Schoenfeld, P. M. Petroff, L. Zhang, E. Hu, and A. Imamoglu, “A quantum dot single-photon turnstile device,” *Science* **290**, 2282–2285 (2000).
- [16] V. Zwiller, H. Blom, P. Jonsson, N. Panev, S. Jeppesen, T. Tsegaye, E. Goobar, M.-E. Pistol, L. Samuelson, and G. Björk, “Single quantum dots emit single photons at a time: Antibunching experiments,” *Appl. Phys. Lett.* **78**, 2476–2478 (2001).
- [17] C. Santori, D. Fattal, J. Vučković, G. S. Solomon, and Y. Yamamoto, “Single-photon generation with InAs quantum dots,” *New J. Phys.* **6**, 89 (2004).
- [18] S. Strauf, N. G. Stoltz, M. T. Rakher, L. A. Coldren, P. M. Petroff, and D. Bouwmeester, “High-frequency single-photon source with polarization control,” *Nat. Photonics* **1**, 704–708 (2007).
- [19] S. Guha, A. Madhukar, and K. C. Rajkumar, “Onset of incoherency and defect introduction in the initial stages of molecular beam epitaxial growth of highly strained  $\text{In}_x\text{Ga}_{1-x}\text{As}$  on GaAs(100),” *Appl. Phys. Lett.* **57**, 2110–2112 (1990).
- [20] G. A. Narvaez, G. Bester, and A. Zunger, “Dependence of the electronic structure of self-assembled (In,Ga)As/GaAs quantum dots on height and composition,” *J. Appl. Phys.* **98**, 043708 (2005).

- [21] W. Sheng and J.-P. Leburton, “Electron-hole alignment in InAs/GaAs self-assembled quantum dots: Effects of chemical composition and dot shape,” *Phys. Rev. B* **63**, 161301 (2001).
- [22] A. Zrenner, “A close look on single quantum dots,” *J. Chem. Phys.* **112**, 7790–7798 (2000).
- [23] S. W. da Silva, Y. A. Pusep, J. C. Galzerani, D. I. Lubyshv, P. P. González-Borrero, and P. Basmaji, “Photoluminescence study of spin-orbit-split bound electron states in self-assembled InAs and  $\text{In}_{0.5}\text{Ga}_{0.5}\text{As}$  quantum dots,” *J. Phys.: Condens. Matter* **9**, L13–L17 (1997).
- [24] P. W. Fry, I. E. Itskevich, S. R. Parnell, J. J. Finley, L. R. Wilson, K. L. Schumacher, D. J. Mowbray, M. S. Skolnick, M. Al-Khafaji, A. G. Cullis, M. Hopkinson, J. C. Clark, and G. Hill, “Photocurrent spectroscopy of InAs/GaAs self-assembled quantum dots,” *Phys. Rev. B* **62**, 16784–16791 (2000).
- [25] M. Bayer, G. Ortner, O. Stern, A. Kuther, A. A. Gorbunov, A. Forchel, P. Hawrylak, S. Fafard, K. Hinzer, T. L. Reinecke, S. N. Walck, J. P. Reithmaier, F. Klopff, and F. Schäfer, “Fine structure of neutral and charged excitons in self-assembled In(Ga)As/(Al)GaAs quantum dots,” *Phys. Rev. B* **65**, 195315 (2002).
- [26] B. Urbaszek, R. J. Warburton, K. Karrai, B. D. Gerardot, P. M. Petroff, and J. M. Garcia, “Fine structure of highly charged excitons in semiconductor quantum dots,” *Phys. Rev. Lett.* **90**, 247403 (2003).
- [27] C. Bentham, I. E. Itskevich, R. J. Coles, B. Royall, E. Clarke, J. O’Hara, N. Prtljaga, A. M. Fox, M. S. Skolnick, and L. R. Wilson, “On-chip electrically controlled routing of photons from a single quantum dot,” *Appl. Phys. Lett.* **106**, 221101 (2015).
- [28] R. J. Coles, D. M. Price, J. E. Dixon, B. Royall, E. Clarke, P. Kok, M. S. Skolnick, A. M. Fox, and M. N. Makhonin, “Chirality of nanophotonic waveguide with embedded quantum emitter for unidirectional spin transfer,” *Nat. Commun.* **7**, 11183 (2016).

- [29] R. M. Thompson, R. M. Stevenson, A. J. Shields, I. Farrer, C. J. Lobo, D. A. Ritchie, M. L. Leadbeater, and M. Pepper, “Single-photon emission from exciton complexes in individual quantum dots,” *Phys. Rev. B* **64**, 201302 (2001).
- [30] O. Benson, C. Santori, M. Pelton, and Y. Yamamoto, “Regulated and entangled photons from a single quantum dot,” *Phys. Rev. Lett.* **84**, 2513–2516 (2000).
- [31] R. M. Stevenson, R. J. Young, P. Atkinson, K. Cooper, D. A. Ritchie, and A. J. Shields, “A semiconductor source of triggered entangled photon pairs,” *Nature* **439**, 179–182 (2006).
- [32] M. Ward, M. Dean, R. Stevenson, A. Bennett, D. Ellis, K. Cooper, I. Farrer, C. Nicoll, D. A. Ritchie, and A. J. Shields, “Coherent dynamics of a telecom-wavelength entangled photon source,” *Nat. Commun.* **5**, 3316 (2014).
- [33] Y. Benny, S. Khatsevich, Y. Kodriano, E. Poem, R. Presman, D. Galushko, P. M. Petroff, and D. Gershoni, “Coherent optical writing and reading of the exciton spin state in single quantum dots,” *Phys. Rev. Lett.* **106**, 040504 (2011).
- [34] W. B. Gao, P. Fallahi, E. Togan, J. Miguel-Sanchez, and A. Imamoglu, “Observation of entanglement between a quantum dot spin and a single photon,” *Nature* **491**, 426–430 (2012).
- [35] A. J. Ramsay, “A review of the coherent optical control of the exciton and spin states of semiconductor quantum dots,” *Semicond. Sci. Technol.* **25**, 103001 (2010).
- [36] P. Michler, *Single Quantum Dots* (Springer, Berlin, Germany, 2003).
- [37] D. A. B. Miller, D. S. Chemla, T. C. Damen, A. C. Gossard, W. Wiegmann, T. H. Wood, and C. A. Burrus, “Band-edge electroabsorption in quantum well structures: The quantum-confined stark effect,” *Phys. Rev. Lett.* **53**, 2173–2176 (1984).

- [38] B. Alén, J. Bosch, D. Granados, J. Martínez-Pastor, J. M. García, and L. González, “Oscillator strength reduction induced by external electric fields in self-assembled quantum dots and rings,” *Phys. Rev. B* **75**, 045319 (2007).
- [39] A. J. Bennett, R. B. Patel, J. Skiba-Szymanska, C. A. Nicoll, I. Farrer, D. A. Ritchie, and A. J. Shields, “Giant Stark effect in the emission of single semiconductor quantum dots,” *Appl. Phys. Lett.* **97**, 031104 (2010).
- [40] R. J. Warburton, C. Schäfflein, D. Haft, F. Bickel, A. Lorke, K. Karrai, J. M. Garcia, W. Schoenfeld, and P. M. Petroff, “Optical emission from a charge-tunable quantum ring,” *Nature* **405**, 926–929 (2000).
- [41] J. P. Reithmaier, G. Sęk, A. Löffler, C. Hofmann, S. Kuhn, S. Reitzenstein, L. V. Keldysh, V. D. Kulakovskii, T. L. Reinecke, and A. Forchel, “Strong coupling in a single quantum dot-semiconductor microcavity system,” *Nature* **432**, 197–200 (2004).
- [42] E. Peter, P. Senellart, D. Martrou, A. Lemaître, J. Hours, J. M. Gérard, and J. Bloch, “Exciton-photon strong-coupling regime for a single quantum dot embedded in a microcavity,” *Phys. Rev. Lett.* **95**, 067401 (2005).
- [43] R. B. Patel, A. J. Bennett, I. Farrer, C. A. Nicoll, D. A. Ritchie, and A. J. Shields, “Two-photon interference of the emission from electrically tunable remote quantum dots,” *Nat. Photonics* **4**, 632–635 (2010).
- [44] P. Lodahl, S. Mahmoodian, and S. Stobbe, “Interfacing single photons and single quantum dots with photonic nanostructures,” *Rev. Mod. Phys.* **87**, 347–400 (2015).
- [45] P. Stepanov, A. Delga, X. Zang, J. Bleuse, E. Dupuy, E. Peinke, P. Lalanne, J.-M. Gérard, and J. Claudon, “Quantum dot spontaneous emission control in a ridge waveguide,” *Appl. Phys. Lett.* **106**, 041112 (2015).
- [46] E. Yablonovitch, “Inhibited spontaneous emission in solid-state physics and electronics,” *Phys. Rev. Lett.* **58**, 2059–2062 (1987).
- [47] J. D. Joannopoulos, S. G. Johnson, J. N. Winn, and R. D. Meade, *Photonic Crystals: Molding the Flow of Light*, 2nd ed. (Princeton University Press, Woodstock, 2008).

- [48] J. D. Joannopoulos, P. R. Villeneuve, and S. Fan, “Photonic crystals: putting a new twist on light,” *Nature* **386**, 143–149 (1997).
- [49] S. Y. Lin, J. G. Fleming, D. L. Hetherington, B. K. Smith, R. Biswas, K. M. Ho, M. M. Sigalas, W. Zubrzycki, S. R. Kurtz, and J. Bur, “A three-dimensional photonic crystal operating at infrared wavelengths,” *Nature* **394**, 251–253 (1998).
- [50] A. Faraon, A. Majumdar, D. Englund, E. Kim, M. Bajcsy, and J. Vučković, “Integrated quantum optical networks based on quantum dots and photonic crystals,” *New J. Phys.* **13**, 055025 (2011).
- [51] T. F. Krauss, “Slow light in photonic crystal waveguides,” *J. Phys. D: Appl. Phys.* **40**, 2666–2670 (2007).
- [52] J. B. Khurgin, “Optical buffers based on slow light in electromagnetically induced transparent media and coupled resonator structures: comparative analysis,” *J. Opt. Soc. Am. B* **22**, 1062–1074 (2005).
- [53] A. Y. Petrov and M. Eich, “Zero dispersion at small group velocities in photonic crystal waveguides,” *Appl. Phys. Lett.* **85**, 4866–4868 (2004).
- [54] L. H. Frandsen, A. V. Lavrinenko, J. Fage-Pedersen, and P. I. Borel, “Photonic crystal waveguides with semi-slow light and tailored dispersion properties,” *Opt. Express* **14**, 9444–9450 (2006).
- [55] M. Notomi, K. Yamada, A. Shinya, J. Takahashi, C. Takahashi, and L. Yokohama, “Extremely large group-velocity dispersion of line-defect waveguides in photonic crystals slabs,” *Phys. Rev. Lett.* **87**, 253902 (2001).
- [56] M. L. Povinelli, S. G. Johnson, and J. D. Joannopoulos, “Slow-light, band-edge waveguides for tunable time delays,” *Opt. Express* **13**, 7145–7159 (2005).
- [57] Y. A. Vlasov, M. O’Boyle, H. F. Hamann, and S. J. McNab, “Active control of slow light on a chip with photonic crystal waveguides,” *Nature* **438**, 65–69 (2005).
- [58] J. T. Mok and B. J. Eggleton, “Expect more delays,” *Nature* **433**, 811–812 (2005).

- 
- [59] J. Khurgin, “Adiabatically tunable optical delay lines and their performance limitations,” *Opt. Lett.* **30**, 2778–2780 (2005).
- [60] A. V. Kavokin, J. J. Baumberg, G. Malpuech, and F. P. Laussy, *Microcavities* (Oxford University Press, New York, NY, USA, 2007).
- [61] J. T. Robinson, C. Manolatou, L. Chen, and M. Lipson, “Ultrasmall mode volumes in dielectric optical microcavities,” *Phys. Rev. Lett.* **95**, 143901 (2005).
- [62] E. M. Purcell, “Spontaneous emission probabilities at radio frequencies,” *Phys. Rev. B* **69**, 674 (1946).
- [63] J. M. Gérard, B. Sermage, B. Gayral, B. Legrand, E. Costard, and V. Thierry-Mieg, “Enhanced spontaneous emission by quantum boxes in a monolithic optical microcavity,” *Phys. Rev. Lett.* **81**, 1110–1113 (1998).
- [64] I. I. Rabi, “Space quantization in a gyrating magnetic field,” *Phys. Rev.* **51**, 652–654 (1937).
- [65] E. T. Jaynes and F. W. Cummings, “Comparison of quantum and semi-classical radiation theories with application to the beam maser,” *Proc. IEEE* **51**, 89–109 (1963).
- [66] J. J. Hopfield, “Theory of the contribution of excitons to the complex dielectric constant of crystals,” *Phys. Rev.* **112**, 1555–1567 (1958).
- [67] A. Kiraz, P. Michler, C. Becher, B. Gayral, A. Imamoglu, L. Zhang, E. Hu, W. V. Schoenfeld, and P. M. Petroff, “Cavity-quantum electrodynamics using a single InAs quantum dot in a microdisk structure,” *Appl. Phys. Lett.* **78**, 3932–3934 (2001).
- [68] T. Yoshie, A. Scherer, J. Hendrickson, G. Khitrova, H. M. Gibbs, G. Rupper, C. Ell, O. B. Shchekin, and D. G. Deppe, “Vacuum Rabi splitting with a single quantum dot in a photonic crystal nanocavity,” *Nature* **432**, 200–203 (2004).
- [69] K. Hennessy, A. Badolato, M. Winger, D. Gerace, M. Atatue, S. Gulde, S. Fält, E. L. Hu, and A. Imamoglu, “Quantum nature of a strongly coupled single quantum dot–cavity system,” *Nature* **445**, 896–899 (2007).

- [70] G. Cui and M. G. Raymer, “Quantum efficiency of single-photon sources in the cavity-QED strong-coupling regime,” *Opt. Express* **13**, 9660–9665 (2005).
- [71] D. Press, S. Götzinger, S. Reitzenstein, C. Hofmann, A. Löffler, M. Kamp, A. Forchel, and Y. Yamamoto, “Photon antibunching from a single quantum-dot-microcavity system in the strong coupling regime,” *Phys. Rev. Lett.* **98**, 117402 (2007).
- [72] Y. Akahane, T. Asano, B.-S. Song, and S. Noda, “High-Q photonic nanocavity in a two-dimensional photonic crystal,” *Nature* **425**, 944–947 (2003).
- [73] M. Shirane, S. Kono, J. Ushida, S. Ohkouchi, N. Ikeda, Y. Sugimoto, and A. Tomita, “Mode identification of high-quality-factor single-defect nanocavities in quantum dot-embedded photonic crystals,” *J. Appl. Phys.* **101**, 073107 (2007).
- [74] M. Notomi, A. Shinya, K. Nozaki, T. Tanabe, S. Matsuo, E. Kuramochi, T. Sato, H. Taniyama, and H. Sumikura, “Low-power nanophotonic devices based on photonic crystals towards dense photonic network on chip,” *IET Circ. Device Syst.* **5**, 84–93 (2011).
- [75] A. Nötzel, “Self-organized growth of quantum-dot structures,” *Semicond. Sci. Technol.* **11**, 1365–1379 (1996).
- [76] A. Wojs, P. Hawrylak, S. Fafard, and L. Jacak, “Electronic structure and magneto-optics of self-assembled quantum dots,” *Phys. Rev. B* **54**, 5604–5608 (1996).
- [77] O. Gywat, H. J. Krenner, and J. Berezovsky, *Spins in Optically Active Quantum Dots: Concepts and Methods* (WILEY, Weinheim, 2010).
- [78] I. N. Stranski and L. Krastanow, “Zur Theorie der orientierten Ausscheidung von Ionenkri,” *Akad. Wissen. Wien (Iib)* **146**, 797–810 (1938).
- [79] W. J. Schaffer, M. D. Lind, S. P. Kowalczyk, and R. W. Grant, “Nucleation and strain relaxation at the InAs/GaAs(100) heterojunction,” *J. Vac. Sci. Technol. B* **1**, 688–695 (1983).

- [80] L. Goldstein, F. Glas, J. Y. Marzin, M. N. Charasse, and G. L. Roux, "Growth by molecular beam epitaxy and characterization of InAs/GaAs strained-layer superlattices," *Appl. Phys. Lett.* **47**, 1099–1101 (1985).
- [81] L. E. Black, *Surface Recombination Theory. In: New Perspectives on Surface Passivation: Understanding the Si-Al<sub>2</sub>O<sub>3</sub> Interface*. (Springer, Cham, 2016).
- [82] G. B. Stringfellow, *Organometallic Vapor-Phase Epitaxy* (Academic Press, 1999).
- [83] A. Cho and J. Arthur, "Molecular beam epitaxy," *Prog. Solid State Ch.* **10**, 157–191 (1975).
- [84] J. A. C. Bland and B. Heinrich, *Ultrathin Magnetic Structures III* (Springer, Berlin, 2005).
- [85] R. Braive, L. L. Gratiet, S. Guilet, G. Patriarche, A. Lemaître, A. Beveratos, I. Robert-Philip, and I. Sagnes, "Inductively coupled plasma etching of GaAs suspended photonic crystal cavities," *J. Vac. Sci. Technol. B* **27**, 1909–1914 (2009).
- [86] J. W. Lee, M. W. Devre, B. H. Reelfs, D. Johnson, J. N. Sasserath, F. Clayton, D. Hays, and S. J. Pearton, "Advanced selective dry etching of GaAs/AlGaAs in high density inductively coupled plasmas," *J. Vac. Sci. Technol. A* **18**, 1220–1224 (2000).
- [87] R. J. Shul, G. B. McClellan, R. D. Briggs, D. J. Rieger, S. J. Pearton, C. R. Abernathy, J. W. Lee, C. Constantine, and C. Barratt, "High-density plasma etching of compound semiconductors," *J. Vac. Sci. Technol. A* **15**, 633–637 (1997).
- [88] P. Kumar, S. Kanakaraju, and D. DeVoe, "Sacrificial etching of Al<sub>x</sub>Ga<sub>1-x</sub>As for III–V MEMS surface micromachining," *Appl. Phys. A* **88**, 711–714 (2007).
- [89] A. L. Cohen, *Scanning Electron Microscope II*, Vol. 11 (1979) pp. 302–322.

- [90] J. J. Gannon and C. J. Nuese, “A chemical etchant for the selective removal of GaAs through SiO<sub>2</sub> masks,” *J. Electrochem. Soc.* **121**, 1215–1219 (1974).
- [91] F. Grazioso, B. R. Patton, and J. M. Smith, “A high stability beam-scanning confocal optical microscope for low temperature operation,” *Rev. Sci. Instrum.* **81**, 093705 (2010).
- [92] I. Itskevich, S. Stoddart, S. Rybchenko, I. Tartakovskii, L. Eaves, P. Main, M. Henini, and S. Parnell, “Electroluminescence from individual InAs self-assembled quantum dots,” *Phys. Status Solidi A* **178**, 307–311 (2000).
- [93] R. Heitz, M. Veit, N. N. Ledentsov, A. Hoffmann, D. Bimberg, V. M. Ustinov, P. S. Kop’ev, and Z. I. Alferov, “Energy relaxation by multiphonon processes in InAs/GaAs quantum dots,” *Phys. Rev. B* **56**, 10435–10445 (1997).
- [94] C. Santori, D. Fattal, J. Vučković, G. S. Solomon, and Y. Yamamoto, “Indistinguishable photons from a single-photon device,” *Nature* **419**, 594–597 (2002).
- [95] S. Sauvage, P. Boucaud, R. P. S. M. Lobo, F. Bras, G. Fishman, R. Prazeres, F. Glotin, J. M. Ortega, and J.-M. Gérard, “Long polaron lifetime in InAs/GaAs self-assembled quantum dots,” *Phys. Rev. Lett.* **88**, 177402 (2002).
- [96] E. A. Zibik, L. R. Wilson, R. P. Green, J.-P. R. Wells, P. J. Phillips, D. A. Carder, J. W. Cockburn, M. S. Skolnick, M. J. Steer, H. Y. Liu, and M. Hopkinson, “Polaron relaxation channel in InAs/GaAs self-assembled quantum dots,” *Semicond. Sci. Technol.* **19**, S316–S318 (2004).
- [97] A. Muller, E. B. Flagg, P. Bianucci, X. Y. Wang, D. G. Deppe, W. Ma, J. Zhang, G. J. Salamo, M. Xiao, and C. K. Shih, “Resonance fluorescence from a coherently driven semiconductor quantum dot in a cavity,” *Phys. Rev. Lett.* **99**, 187402 (2007).

- 
- [98] K. Kuroda, T. Kuroda, K. Watanabe, T. Mano, K. Sakoda, G. Kido, and N. Koguchi, “Final-state readout of exciton qubits by observing resonantly excited photoluminescence in quantum dots,” *Appl. Phys. Lett.* **90**, 051909 (2007).
- [99] G. Kiršanskė, H. Thyrrerstrup, R. S. Daveau, C. L. Dreeßen, T. Pregnolato, L. Midolo, P. Tighineanu, A. Javadi, S. Stobbe, R. Schott, A. Ludwig, A. D. Wieck, S. I. Park, J. D. Song, A. V. Kuhlmann, I. Söllner, M. C. Löbl, R. J. Warburton, and P. Lodahl, “Indistinguishable and efficient single photons from a quantum dot in a planar nanobeam waveguide,” *Phys. Rev. B* **96**, 165306 (2017).
- [100] A. M. Fox, *Quantum Optics: An Introduction* (Oxford University Press, New York, 2006).
- [101] M. Strauß, M. Placke, S. Kreinberg, C. Schneider, M. Kamp, S. Höfling, J. Wolters, and S. Reitzenstein, “Photon-statistics excitation spectroscopy of a single two-level system,” *Phys. Rev. B* **93**, 241306 (2016).
- [102] A. Taflove and S. C. Hagness, *Computational Electrodynamics: The Finite-Difference Time-Domain Method*, 3rd ed. (Artech House Inc., London, 2005).
- [103] Lumerical Inc., “Lumerical FDTD Solutions,” (2018).
- [104] S. G. Johnson and J. D. Joannopoulos, “Block-iterative frequency-domain methods for Maxwell’s equations in a planewave basis,” *Opt. Express* **8**, 173–190 (2001).
- [105] S. G. Johnson and J. D. Joannopoulos, “MIT Photonic Bands,” (2018).
- [106] B. E. A. Saleh and M. C. Teich, *Fundamentals of Photonics*, 2nd ed. (John Wiley & Sons, Inc., Hoboken, New Jersey, 2007).
- [107] O. S. Heavens, “Optical properties of thin films,” *Rep. Prog. Phys.* **23**, 1–65 (1960).
- [108] S. Byrnes, “Python tmm package,” (2018).

- [109] Comsol Multiphysics Inc., “MEMS Module,” (2018).
- [110] P. B. Deotare, M. W. McCutcheon, I. W. Frank, M. Khan, and M. Lončar, “High quality factor photonic crystal nanobeam cavities,” *Appl. Phys. Lett.* **94**, 121106 (2009).
- [111] S. Noda, M. Fujita, and T. Asano, “Spontaneous-emission control by photonic crystals and nanocavities,” *Nat. Photonics* **1**, 449–458 (2007).
- [112] Q. Quan, P. B. Deotare, and M. Lončar, “Photonic crystal nanobeam cavity strongly coupled to the feeding waveguide,” *Appl. Phys. Lett.* **96**, 203102 (2010).
- [113] P. B. Deotare, L. C. Kogos, I. Bulu, and M. Lončar, “Photonic crystal nanobeam cavities for tunable filter and router applications,” *IEEE J. Sel. Top. Quant.* **19**, 3600210 (2013).
- [114] S. Koseki, B. Zhang, K. De Greve, and Y. Yamamoto, “Monolithic integration of quantum dot containing microdisk microcavities coupled to air-suspended waveguides,” *Appl. Phys. Lett.* **94**, 051110 (2009).
- [115] C. Baker, C. Belacel, A. Andronico, P. Senellart, A. Lemaitre, E. Galopin, S. Ducci, G. Leo, and I. Favero, “Critical optical coupling between a GaAs disk and a nanowaveguide suspended on the chip,” *Appl. Phys. Lett.* **99**, 151117 (2011).
- [116] J. Moosburger, M. Kamp, A. Forchel, U. Oesterle, and R. Houdré, “Transmission spectroscopy of photonic crystal based waveguides with resonant cavities,” *J. Appl. Phys.* **91**, 4791–4794 (2002).
- [117] H. Takano, Y. Akahane, T. Asano, and S. Noda, “In-plane-type channel drop filter in a two-dimensional photonic crystal slab,” *Appl. Phys. Lett.* **84**, 2226–2228 (2004).
- [118] M. K. Chhipa and L. K. Dusad, “Dual curved photonic crystal ring resonator based channel drop filter using two-dimensional photonic crystal structure,” *AIP Conf. Proc.* **1728**, 020226 (2016).

- [119] R. Sathyadevaki, A. S. Raja, and D. S. Sundar, “Photonic crystal-based optical filter: a brief investigation,” *Photonic Netw. Commun.* **33**, 77–84 (2017).
- [120] B.-S. Song, S. Noda, T. Asano, and Y. Akahane, “Ultra-high-Q photonic double-heterostructure nanocavity,” *Nat. Mater.* **4**, 207–210 (2005).
- [121] J. M. Gerard and B. Gayral, “Strong Purcell effect for InAs quantum boxes in three-dimensional solid-state microcavities,” *J. Lightwave Technol.* **17**, 2089–2095 (1999).
- [122] C. Bentham, D. Hallett, N. Prtljaga, B. Royall, D. Vaitiekus, R. J. Coles, E. Clarke, A. M. Fox, M. S. Skolnick, I. E. Itskevich, and L. R. Wilson, “Single-photon electroluminescence for on-chip quantum networks,” *Appl. Phys. Lett.* **109**, 161101 (2016).
- [123] R. H. Hadfield, “Single-photon detectors for optical quantum information applications,” *Nat. Photonics* **3**, 696–705 (2009).
- [124] C. P. Dietrich, A. Fiore, M. G. Thompson, M. Kamp, and S. Höfling, “GaAs integrated quantum photonics: Towards compact and multifunctional quantum photonic integrated circuits,” *Laser Photonics Rev.* **10**, 870–894 (2016).
- [125] J. C. Chen, H. A. Haus, S. Fan, P. R. Villeneuve, and J. D. Joannopoulos, “Optical filters from photonic band gap air bridges,” *J. Lightwave Technol.* **14**, 2575–2580 (1996).
- [126] J. S. Foresi, P. R. Villeneuve, J. Ferrera, E. R. Thoen, G. Steinmeyer, S. Fan, J. D. Joannopoulos, L. C. Kimerling, H. I. Smith, and E. P. Ippen, “Photonic-bandgap microcavities in optical waveguides,” *Nature* **390**, 144–145 (1997).
- [127] K. Lim, D. J. Ripin, G. S. Petrich, L. A. Kolodziejski, E. P. Ippen, M. Mondol, H. I. Smith, S. F. Villeneuve, and J. D. Joannopoulos, “Photonic band-gap waveguide microcavities: Monorails and airbridges,” *J. Vac. Sci. Technol. B* **17**, 1171–1174 (1999).

- [128] M. Notomi, E. Kuramochi, and H. Taniyama, “Ultra-high-Q nanocavity with 1D photonic gap,” *Opt. Express* **16**, 11095–11102 (2008).
- [129] I. W. Frank, P. B. Deotare, M. W. McCutcheon, and M. Lončar, “Programmable photonic crystal nanobeam cavities,” *Opt. Express* **18**, 8705–8712 (2010).
- [130] Y. Zhang, M. Khan, Y. Huang, J. Ryou, P. Deotare, and M. Lončar, “Photonic crystal nanobeam lasers,” *Appl. Phys. Lett.* **97**, 051104 (2010).
- [131] Q. Quan and M. Lončar, “Deterministic design of wavelength scale, ultra-high Q photonic crystal nanobeam cavities,” *Opt. Express* **19**, 18529–18542 (2011).
- [132] A. R. M. Zain, N. P. Johnson, M. Sorel, and R. M. De La Rue, “Ultra high quality factor one dimensional photonic crystal/photonic wire microcavities in silicon-on-insulator (SOI),” *Opt. Express* **16**, 12084–12089 (2008).
- [133] G. E. Digeronimo, M. Petruzzella, S. Birindelli, R. Gaudio, S. Fattah Poor, F. W. van Otten, and A. Fiore, “Integration of single-photon sources and detectors on GaAs,” *Photonics* **3**, 55 (2016).
- [134] A. Laucht, F. Hofbauer, N. Hauke, J. Angele, S. Stobbe, M. Kaniber, G. Böhm, P. Lodahl, M.-C. Amann, and J. J. Finley, “Electrical control of spontaneous emission and strong coupling for a single quantum dot,” *New J. Phys.* **11**, 023034 (2009).
- [135] R. Ohta, Y. Ota, M. Nomura, N. Kumagai, S. Ishida, S. Iwamoto, and Y. Arakawa, “Strong coupling between a photonic crystal nanobeam cavity and a single quantum dot,” *Appl. Phys. Lett.* **98**, 173104 (2011).
- [136] C. Sauvan, G. Lecamp, P. Lalanne, and J. P. Hugonin, “Modal-reflectivity enhancement by geometry tuning in photonic crystal microcavities,” *Opt. Express* **13**, 245–255 (2004).
- [137] C. Sauvan, P. Lalanne, and J. P. Hugonin, “Slow-wave effect and mode-profile matching in photonic crystal microcavities,” *Phys. Rev. B* **71**, 165118 (2005).

- 
- [138] K. Van Acoleyen, J. Roels, P. Mechet, T. Claes, D. Van Thourhout, and R. Baers, “Ultracompact phase modulator based on a cascade of NEMS-operated slot waveguides fabricated in silicon-on-insulator,” *IEEE Photonics J.* **4**, 779–788 (2012).
- [139] M. Winger, T. D. Blasius, T. P. Alegre, A. H. Safavi-Naeini, S. Meehan, J. Cohen, S. Stobbe, and O. Painter, “A chip-scale integrated cavity-electro-optomechanics platform,” *Opt. Express* **19**, 24905–24921 (2011).
- [140] P. B. Deotare, M. W. McCutcheon, I. W. Frank, M. Khan, and M. Lončar, “Coupled photonic crystal nanobeam cavities,” *Appl. Phys. Lett.* **95**, 031102 (2009).
- [141] C. G. Baker, C. Bekker, D. L. McAuslan, E. Sheridan, and W. P. Bowen, “High bandwidth on-chip capacitive tuning of microtoroid resonators,” *Opt. Express* **14**, 20400–20412 (2016).
- [142] R. Legtenberg, A. W. Groeneveld, and M. Elwenspoek, “Comb-drive actuators for large displacements,” *J. Micromech. Microeng.* **6**, 320–329 (1996).
- [143] G. Zhou and P. Dowd, “Tilted folded-beam suspension for extending the stable travel range of comb-drive actuators,” *J. Micromech. Microeng.* **13**, 178–183 (2003).
- [144] X. Chew, G. Zhou, F. S. Chau, J. Deng, X. Tang, and Y. C. Loke, “Dynamic tuning of an optical resonator through MEMS-driven coupled photonic crystal nanocavities,” *Opt. Lett.* **35**, 2517–2519 (2010).
- [145] X. Chew, G. Zhou, H. Yu, F. S. Chau, J. Deng, Y. C. Loke, and X. Tang, “An in-plane nano-mechanics approach to achieve reversible resonance control of photonic crystal nanocavities,” *Opt. Express* **18**, 22232–22244 (2010).
- [146] P. Shi, G. Zhou, J. Deng, F. Tian, and F. S. Chau, “Tuning all-optical analog to electromagnetically induced transparency in nanobeam cavities using electromechanical system,” *Sci. Rep.* **5**, 14379 (2015).

- [147] E. Bulgan, Y. Kanamori, and K. Hane, “Submicron silicon waveguide optical switch driven by microelectromechanical actuator,” *Appl. Phys. Lett.* **92**, 101110 (2008).
- [148] Y. Akihama, Y. Kanamori, and K. Hane, “Ultra-small silicon waveguide coupler switch using gap-variable mechanism,” *Opt. Express* **19**, 23658–23663 (2011).
- [149] Y. Akihama and K. Hane, “Single and multiple optical switches that use freestanding silicon nanowire waveguide couplers,” *Light: Sci. Appl.* **1**, e16 (2012).
- [150] J. O. Lee, Y.-H. Song, M.-W. Kim, M.-H. Kang, J.-S. Oh, H.-H. Yang, and J. B. Yoon, “A sub-1-volt nanoelectromechanical switching device,” *Nat. Nanotechnol.* **8**, 36–40 (2013).
- [151] Y. Munemasa and K. Hane, “A compact 1x3 silicon photonic waveguide switch based on precise investigation of coupling characteristics of variable-gap coupler,” *Jpn. J. Appl. Phys.* **52**, 06GL15 (2013).
- [152] S. Han, T. J. Seok, N. Quack, B. W. Yoo, and M. C. Wu, “Large-scale silicon photonic switches with movable directional couplers,” *Optica* **2**, 370–375 (2015).
- [153] R. Ohta, Y. Ota, H. Takagi, N. Kumagai, K. Tanabe, S. Ishida, S. Iwamoto, and Y. Arakawa, “Electro-mechanical Q factor control of photonic crystal nanobeam cavity,” *Jpn. J. Appl. Phys.* **52**, 04CG01 (2013).
- [154] L. Midolo, P. J. van Veldhoven, M. A. Dündar, R. Nötzel, and A. Fiore, “Electromechanical wavelength tuning of double-membrane photonic crystal cavities,” *Appl. Phys. Lett.* **98**, 211120 (2011).
- [155] L. Midolo, S. N. Yoon, F. Pagliano, T. Xia, F. W. M. van Otten, M. Lerner, S. Höfling, and A. Fiore, “Electromechanical tuning of vertically-coupled photonic crystal nanobeams,” *Opt. Express* **20**, 19255–19263 (2012).
- [156] M. Petruzzella, T. Xia, F. Pagliano, S. Birindelli, L. Midolo, Z. Zobenica, L. H. Li, E. H. Linfield, and A. Fiore, “Fully tuneable, Purcell-enhanced solid-state quantum emitters,” *Appl. Phys. Lett.* **107**, 141109 (2015).

- [157] H. J. Kimble, “The quantum internet,” *Nature* **453**, 1023–1030 (2008).
- [158] T. Liu, F. Pagliano, and A. Fiore, “Nano-opto-electro-mechanical switch based on a four-waveguide directional coupler,” *Opt. Express* **25**, 10166–10176 (2017).
- [159] Z. K. Bishop, A. P. Foster, B. Royall, C. Bentham, E. Clarke, M. S. Skolnick, and L. R. Wilson, “Electro-mechanical control of an on-chip optical beam splitter containing an embedded quantum emitter,” *Opt. Lett.* **43**, 2142–2145 (2018).
- [160] O. Buchnev, N. Podoliak, T. Frank, M. Kaczmarek, L. Jiang, and V. A. Fedotov, “Controlling stiction in nano-electro-mechanical systems using liquid crystals,” *ACS Nano* **10**, 11519–11524 (2016).
- [161] M. Petruzzella, Ž. Zobenica, M. Cotrufo, V. Zardetto, A. Mameli, F. Pagliano, S. Koelling, F. W. M. van Otten, F. Roozeboom, W. M. M. Kessels, R. W. van der Heijden, and A. Fiore, “Anti-stiction coating for mechanically tunable photonic crystal devices,” *Opt. Express* **26**, 3882–3891 (2018).
- [162] S. Tsuchitani and R. Kaneko, “Theoretical analysis of cantilever motion under electrostatic force,” *T. IEE Japan* **118**, 6–13 (1998).
- [163] S. M. Sze and K. K. Ng, *Physics of Semiconductor Devices*, 3rd ed. (Wiley-Interscience, 2007).
- [164] K. H. Kim, Z. Akase, T. Suzuki, and D. Shindo, “Charging effects on SEM/SIM contrast of metal/insulator system in various metallic coating conditions,” *Mater. Trans.* **51**, 1080–1083 (2010).
- [165] L. Midolo, A. Schliesser, and A. Fiore, “Nano-opto-electro-mechanical systems,” *Nat. Nanotechnol.* **13**, 11–18 (2018).
- [166] W. Jaskólski, M. Zieliński, G. W. Bryant, and J. Aizpurua, “Strain effects on the electronic structure of strongly coupled self-assembled InAs/GaAs quantum dots: Tight-binding approach,” *Phys. Rev. B* **74**, 195339 (2006).

- [167] S. Seidl, M. Kroner, A. Högele, K. Karrai, R. J. Warburton, A. Badolato, and P. M. Petroff, “Effect of uniaxial stress on excitons in a self-assembled quantum dot,” *Appl. Phys. Lett.* **88**, 203113 (2006).
- [168] J. Beetz, T. Braun, C. Schneider, S. Höfling, and M. Kamp, “Anisotropic strain-tuning of quantum dots inside a photonic crystal cavity,” *Semicond. Sci. Tech.* **28**, 122002 (2013).
- [169] S. Sun, H. Kim, G. S. Solomon, and E. Waks, “Strain tuning of a quantum dot strongly coupled to a photonic crystal cavity,” *Appl. Phys. Lett.* **103**, 151102 (2013).
- [170] S. G. Johnson, M. Ibanescu, M. A. Skorobogatiy, O. Weisberg, J. D. Joannopoulos, and Y. Fink, “Perturbation theory for Maxwell’s equations with shifting material boundaries,” *Phys. Rev. E* **65**, 066611 (2002).
- [171] J. Pan, Y. Huo, K. Yamanaka, S. Sandhu, L. Scaccabarozzi, R. Timp, M. L. Povinelli, S. Fan, M. M. Fejer, and J. S. Harris, “Aligning microcavity resonances in silicon photonic-crystal slabs using laser-pumped thermal tuning,” *Appl. Phys. Lett.* **92**, 103114 (2008).
- [172] I. Fushman, E. Waks, D. Englund, N. Stoltz, P. Petroff, and J. Vučković, “Ultrafast nonlinear optical tuning of photonic crystal cavities,” *Appl. Phys. Lett.* **90**, 091118 (2007).
- [173] P. Buchmann, H. Kaufmann, H. Melchior, and G. Guekos, “Broadband y-branch electro-optic gaas waveguide interferometer for 1.3  $\mu\text{m}$ ,” *Appl. Phys. Lett.* **46**, 462–464 (1985).
- [174] L. Midolo, S. L. Hansen, W. Zhang, C. Papon, R. Schott, A. Ludwig, A. D. Wieck, P. Lodahl, and S. Stobbe, “Electro-optic routing of photons from a single quantum dot in photonic integrated circuits,” *Opt. Express* **25**, 33514–33526 (2017).
- [175] M. M. de Lima, M. Beck, R. Hey, and P. V. Santos, “Compact mach-zehnder acousto-optic modulator,” *Appl. Phys. Lett.* **89**, 121104 (2006).
- [176] S. Ayalew Tadesse and M. Li, “Sub-optical wavelength acoustic wave modulation of integrated photonic resonators at microwave frequencies,” *Nat. Commun.* **5**, 5402 (2014).

- [177] Q. Lai, W. Hunziker, and H. Melchior, “Low-power compact 2x2 thermo-optic silica-on-silicon waveguide switch with fast response,” *IEEE Photonics Technol. Lett.* **10**, 681–683 (1998).
- [178] J. Yang, Q. Zhou, and R. T. Chen, “Polyimide-waveguide-based thermal optical switch using total-internal-reflection effect,” *Appl. Phys. Lett.* **81**, 2947–2949 (2002).
- [179] T. H. Stievater, D. Park, W. S. Rabinovich, M. W. Pruessner, S. Kanakaraju, C. J. K. Richardson, and J. B. Khurgin, “Enhanced electro-optic phase shifts in suspended waveguides,” *Opt. Express* **18**, 885–892 (2010).
- [180] C. S. Tsai, B. Sun, and A. Kar-Roy, “Guided-wave acousto-optic Bragg diffraction in indium gallium arsenide phosphide waveguides,” *Appl. Phys. Lett.* **70**, 3185–3187 (1997).
- [181] W. D. Callister and D. G. Rethwisch, *Materials Science and Engineering*, 9th ed. (John Wiley & Sons Inc., 2014).
- [182] L. Midolo and A. Fiore, “Design and optical properties of electromechanical double-membrance photonic crystal cavities,” *IEEE J. Quantum Elect.* **50**, 404–414 (2014).
- [183] K. R. Williams and R. S. Muller, “Etch rates for micromachining processing,” *J. Microelectromech. S.* **5**, 256–269 (1996).
- [184] V. B. Verma, M. J. Stevens, K. L. Silverman, N. L. Dias, A. Garg, J. J. Coleman, and R. P. Mirin, “Photon antibunching from a single lithographically defined InGaAs/GaAs quantum dot,” *Opt. Express* **19**, 4182–4187 (2011).
- [185] N. Braslau, J. B. Gunn, and J. L. Staples, “Metal-semiconductor contacts for GaAs bulk effect devices,” *Solid-State Electron.* **10**, 381 – 383 (1967).
- [186] R. B. Rebak, J. R. Dillman, P. Crook, and C. V. V. Shawber, “Corrosion behavior of nickel alloys in wet hydrofluoric acid,” *Mater. Corros.* **52**, 289–297 (2001).

- [187] X. Zhang, K. N. Tu, Y. H. Xie, and C. H. Tung, "High aspect ratio nickel structures fabricated by electrochemical replication of hydrofluoric acid etched silicon," [Electrochem. Solid-State Lett.](#) **9**, C150–C152 (2006).
- [188] J. T. M. van Beek and R. Puers, "A review of MEMS oscillators for frequency reference and timing applications," [J. Micromech. Microeng.](#) **22**, 013001 (2012).
- [189] A. Q. Liu and X. M. Zhang, "A review of MEMS external-cavity tunable lasers," [J. Micromech. Microeng.](#) **17**, R1 (2007).
- [190] M. Tanaka, "An industrial and applied review of new MEMS devices features," [Microelectron. Eng.](#) **84**, 1341 – 1344 (2007).
- [191] A. C. R. Grayson, R. S. Shawgo, A. M. Johnson, N. T. Flynn, Y. LI, M. J. Cima, and R. Langer, "A BioMEMS review: MEMS technology for physiologically integrated devices," [Proc. IEEE](#) **92**, 6–21 (2004).
- [192] Y. Gao, Z. You, and J. Zhao, "Electrostatic comd-drive actuator for MEMS relays/switches with double-tilt comb fingers and tilted parallelogram beams," [J. Micromech. Microeng.](#) **25**, 045003 (2015).
- [193] K. Hjort, "Gallium arsenide micromechanics. A comparison to silicon and quartz," in [GAAS](#) (Turin, Italy, 1994) pp. 65–72.
- [194] K. Hjort, J. Söderkvist, and J. Schweitz, "Gallium arsenide as a mechanical material," [J. Micromech. Microeng.](#) **4**, 1–13 (1994).
- [195] K. Hjort, "Sacrificial etching of III - V compounds for micromechanical devices," [J. Micromech. Microeng.](#) **6**, 370 (1996).
- [196] J. Leclercq, R. Ribas, J. Karam, and P. Viktorovitch, "III–V micromachined devices for microsystems," [Microelectr. J.](#) **29**, 613 – 619 (1998).
- [197] W. C. Tang, M. G. Lim, and R. T. Howe, "Electrostatic comb drive levitation and control method," [J. Microelectromech. Syst.](#) **1**, 170–178 (1992).
- [198] E. Gallagher and W. Moussa, "A study of the effect of the fringe fields on the electrostatic force in vertical comb drives," [Sensors](#) **14**, 20149–20164 (2014).

- [199] G. Reithmaier, S. Lichtmannecker, T. Reichert, P. Hasch, K. Müller, M. Bichler, R. Gross, and J. J. Finley, “On-chip time resolved detection of quantum dot emission using integrated superconducting single photon detectors,” *Sci. Rep.* **3**, 1901 (2013).
- [200] G. Reithmaier, M. Kaniber, F. Flassig, S. Lichtmannecker, K. Müller, A. Andrejew, J. Vučković, R. Gross, and J. J. Finley, “On-chip generation, routing, and detection of resonance fluorescence,” *Nano Lett.* **15**, 5208–5213 (2015).